Metal Pincers as Antiviral Agents Targeting SARS-CoV-2 Spike Protein

Submitted in fulfilment of the requirements for the degree of

Master of Science

By

Matthew L. Bracken



UNIVERSITY OF THE
WITWATERSRAND,
JOHANNESBURG



March 2023

School of Chemistry

University of the Witwatersrand

Johannesburg

Declaration

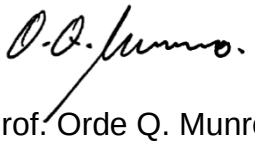
I declare that this dissertation is my own, unaided work. It is being submitted for the Degree of Master of Science at the University of the Witwatersrand, Johannesburg. It has not been submitted before for any degree or examination at any other University. This dissertation does not contain other persons' data, text, writing, graphs or figures and any other persons' contributing information has been properly cited in the references at the end of each chapter. Figures created with the use of BioRender, Maestro, Mercury, ChemDraw, and Inkscape.

Signed: 

Matthew L. Bracken

On this day 7 August 2023 in Cape Town

I hereby certify that this is correct.

Signed: 

Prof. Orde Q. Munro

Abstract

The purpose of this work was to prove the concept that complexes of bioavailable metal ions may be designed to target specific solvent-exposed amino acid residues on therapeutic protein targets. The complexes synthesized and studied were novel Zn(II) and Cu(II) NNN amide pincers. The chelates were designed by *in silico* methods to target solvent-exposed tyrosine residues on the receptor binding domain of SARS-CoV-2. These tyrosine residues are crucial for binding host cell receptors and by targeting these groups, the metal pincers may potentially act as antiviral fusion inhibitors for the treatment of COVID-19. Biophysical studies were carried out to determine the binding affinity between the chelate and phenolic residues. These studies identified the most likely binding site for the metal complex on the SARS-CoV-2 spike protein epitope. The novel chelates were crystalized and found to adopt hexameric metallocycle architecture.

Acknowledgments

I would like to acknowledge my supervisor Prof. Orde Munro for conceptualizing this MSc project. Orde has really created a world-class lab at Wits and it was a pleasure being able to work under his guidance. I remember our very first meeting almost three years ago, and from then on, it has been a fruitful relationship with many scientific discoveries. Orde's enthusiasm for research is contagious and his high standards have made me a better scientist. I am grateful for the experience I have had in the bioinorganic lab. Thanks Prof!

I would also like to acknowledge Prof. Manuel Fernandes for his guidance in the X-ray lab. The crystals studied were generally poor quality and Manuel's supervision during data collection and refinement was invaluable. Manuel and I spent countless hours finding the best crystals, shooting X-rays, and refining final solutions for the structures. The sheer volume of Chapter 5 would not have been possible without Prof. Fernandes.

I would also like to acknowledge my colleagues in the bioinorganic lab for their advice. I would like to thank Mark Blow for his tips regarding computers and spectrometers. I would also like to thank Sheldon Sookai for his advice regarding protein chemistry. Without these two people, I would have been one man in a world-class lab.

I thank the National Institute for Communicable Diseases for gifting us with purified viral proteins. Dr Thandeka Moyo-Gwete and Dr Frances Ayres expressed SARS-CoV-2 RBD protein at the NICD and the final biophysical assays would not have been possible without this contribution.

I also acknowledge the Centre for High Performance Computing for providing us access to the Lengau cluster. The CHPC is an indispensable resource and the computational chemistry presented in this work would not have been possible without access to supercomputing infrastructure.

Finally, I would like to acknowledge funding granted by Prof. Munro, the National Research Foundation, and Wits University.

Contents

Master of Science 1

Declaration 2

Abstract 3

Acknowledgments 4

List of Figures 10

List of Tables 28

Abbreviations 32

Chapter 1 33

Introduction 33

1. Medicinal Inorganic Chemistry 33

1.1 Advantages of the Metal Ion 33

1.2 Metallodrugs 35

1.2.1 Platinum 35

1.2.2 Gold 37

1.2.3 Ruthenium 39

1.2.4 Iron 41

1.3 Antiviral Metal Complexes 43

2. Metal Pincers 47

3. SARS-CoV-2 & COVID-19 54

4. Aims & Objectives 61

5. References 62

Chapter 2 69

2.1 General Methods 69

2.2 Instrumentation 69

2.2.1 NMR Spectrometer 69

2.2.2 Mass Spectrometer 69
2.2.3 FTIR Spectrometer 69
2.2.4 X-ray Diffractometer 70
2.2.5 UV-Vis Spectrometer 70
2.3 Ligand Synthesis 71
2.3.1 Synthesis of 5,5'-[(pyridine-2,6-dicarbonyl)bis(azanediyl)]dinicotinic acid, H_4L1 73
2.3.2 Synthesis of 3,3'-[(pyridine-2,6-dicarbonyl)bis(azanediyl)]dibenzoic acid, H_4L2 74
2.3.3 Synthesis of 4,4'-[(pyridine-2,6-dicarbonyl)bis(azanediyl)]dibenzoic acid, H_4L3 75
2.3.4 Synthesis of 2,2'-[((pyridine-2,6-dicarbonyl)bis(azanediyl))bis(4,1-phenylene)]diacetic acid, H_4L4 76
2.3.5 Synthesis of N^2,N^6-bis[3-(dimethylcarbamoyl)phenyl]pyridine-2,6-dicarboxamide, H_2L5 77
2.3.6 Synthesis of N^2,N^6-bis[3-(isopropylcarbamoyl)phenyl]pyridine-2,6-dicarboxamide, H_4L6 78
2.3.7 Synthesis of N^2,N^6-bis(1,3-dioxoisoindolin-6-yl)pyridine-2,6-dicarboxamide, H_4L7 79
2.3.8 Synthesis of N^2,N^6-bis(3-(ethylcarbamoyl)phenyl)pyridine-2,6-dicarboxamide, H_4L8 80
2.3.9 Synthesis of N^2,N^6-bis(3-acetamidophenyl)pyridine-2,6-dicarboxamide, H_4L9 81
2.3.10 Synthesis of N^2,N^6-bis(3-cyanophenyl)pyridine-2,6-dicarboxamide, H_2L10 82
2.3.11 Synthesis of N^2,N^6-bis(3-(phenylcarbamoyl)phenyl)pyridine-2,6-dicarboxamide, H_4L11 83
2.4 Metal Chelate Synthesis 84
2.4.1 Zinc and the Carboxylic Catastrophe 85
2.4.1.1 Zn(H_2L1) 85
2.4.1.2 Zn(H_2L2) 86
2.4.1.3 Zn(H_2L3) 88
2.4.1.4 Zn(H_2L4) 90
2.4.2 Copper and the Carboxylic Catastrophe 91
2.4.2.1 Cu(H_2L1) 91

2.4.2.2 $Cu_2(H_2L2)_2$ 92
2.4.2.3 $Cu_2(L3)$ 94
2.4.2.4 $Cu(H_2L4)$ 95
2.4.3 Zinc Pincers 96
2.4.3.1 $Zn(L5)(H_2O)_2$ 96
2.4.3.2 $Zn(H_2L6)$ 98
2.4.3.3 $Zn(H_2L7)$, $Zn(H_2L8)$, $Zn(H_2L9)$ and $Zn(L10)$ 98
2.4.4 Copper Pincers 99
2.4.4.1 $Cu(L5)(H_2O)$ 99
2.4.4.2 $Cu(H_2L6)$(MeOH) 102
2.4.4.3 $Cu(H_2L7)$ 104
2.4.4.4 $Cu(H_2L8)(H_2O)$ 105
2.4.4.5 $Cu(H_2L9)(H_2O)$ 107
2.4.4.6 $Cu(L10)(H_2O)$ 109
2.4.4.7 Cu(L11)(MeOH) 111
References 113
Chapter 3 115
1. Introduction 115
2. Methods 116
2.1 Protein Preparation 116
2.2 Ligand Preparation 117
2.3 Molecular Docking 117
2.4 Molecular Dynamics 119
3. Results and Discussion 120
3.1 MD Analysis of RBD-ACE2 Complex 120
3.2 HTVS Molecular Docking & Dynamics 123
3.3 SP Molecular Docking & Dynamics 127

3.4 XP Molecular Docking & Dynamics 134
3.5 Synthesized Chelate Docking (RBD) 142
3.6 Synthesized Chelate Docking (Epitope) 145
4. Conclusion 148
References 149
Chapter 4 152
1. Introduction 152
2. Methods 157
2.1 NMR Spectroscopy 157
2.2 Mass Spectroscopy 157
2.3 CD Spectroscopy 157
2.4 Fluorescence Spectroscopy 158
3. Results and Discussion 159
3.1 Biomimetic Models 159
3.2 SARS-CoV-2 Delta RBD 172
3.3 Solution Behavior of Cu(II) Pincers 179
4. Conclusion 182
References 183
Chapter 5 185
Crystallography 185
1. Introduction 185
2. Methods 189
3. Results & Analysis 190
3.1 CuL2 “blue” 190
3.2 CuL2 “green” 193
3.3 CuL3 197
3.4 CuL5 201

3.5 Cu(H_2L6) “kinetic”.....209
3.6 Cu(H_2L6) “thermodynamic”.....215
3.7 Cu(H_2L8) “kinetic”.....220
3.8 Cu(H_2L8) “thermodynamic”.....225
3.9 Cu(H_2L9) “kinetic”.....231
3.10 Cu(H_2L9) “thermodynamic”.....236
3.11 CuL10.....242
4. Discussion & Conclusion.....248
References.....260
Chapter 6.....261
Conclusion.....261

List of Figures

Figure 1.1: The advantages of the metal ion. From square planar metal complexes that bind DNA, to yet undiscovered coordination compounds that fill the 3D pharmacophore of protein targets. Numerous oxidation states are available to the metal that facilitate versatile redox chemistry. The bond strengths of ligands may be controlled by stereoelectronic effects allowing fine-tuned reactivity of the bioactive metal complex. Outer coordination-sphere chemistry is available upon metal-protein complex formation. 34
Figure 1.2: The X-ray crystal structure of TriplatinNC bound to dsDNA. The metallodrug binds the DNA phosphate backbone through electrostatic forces thereby disrupting replication and repair processes. Ligand carbons shown in green, nitrogen blue, and platinum grey. 35
Figure 1.3: The octahedral Pt(IV) metallodrug Satraplatin. The complex is reduced to square planar Pt(II) in hypoxic environments, releasing potentially bioactive ligands for dual mechanistic action. The nucleobase guanine then attacks the metal centre, displacing chloride and becoming covalently linked to the metallodrug. 36
Figure 1.4: The chemical structure of Auranofin is shown, the metallodrug serves as a delivery vehicle for the Au(I) ion. The crystal structure of Au(I) bound to the active site of TGR is shown. The Au(I) ion inhibits the enzyme by preventing the reducing action of the flavin in the active site. 37
Figure 1.5: The chemical structure of AuMesoIX and its reaction with thiol-containing enzymes. The cysteine residue of Peroxiredoxin III found in the active site of the enzyme has been shown to covalently bind AuMesoIX under physiological conditions. The Au(III) ion increases the electrophilicity of the *meso* carbon, allowing nucleophilic attack by the thiol. The cysteine-porphyrin adduct is then easily oxidized to re-establish the electronic conjugation that extends throughout the macrocycle. 38
Figure 1.6: The X-ray structure of Staurosporine bound to the active site of GSK-3. The metallodrug Ru-Staurosporine targets the same protein kinase with improved specificity and activity. ATP-mimetics need to be highly specific for cancer proliferating proteins as off-target effects are common. While the indolocarbazole moiety is mostly the same between drugs, the Ru(II) ion can fill the 3D space of the active site to form a coordination sphere involving the protein residues. 39
Figure 1.7: The chemical structure of RM175 and the metallodrug mechanism of action. 40
Figure 1.8: The structure of sodium nitroprusside and its interaction with thiol groups of erythrocytes and albumins in the bloodstream. The release of NO from SNP results in vasodilation and reduced blood pressure. 41

Figure 1.9: The dual mechanistic action of Ferroquine prevents the formation of Fe(III) hematin crystals and generates ROS causing lipid peroxidation in the digestive vacuole of *Plasmodium falciparum.* 42
Figure 1.10: The mechanism of HIV NCp7 ZnF inhibition by Au(bnpy)Cl_2. 43
Figure 1.11: The structure of Doxovir, a lead antiviral metallodrug candidate. Doxovir shows broad-spectrum inhibition of enveloped viruses such as HSV and acts in a post-attachment phase of infection. The Co(III) complex prevents cell-to-cell infection of herpes viruses, but its exact mechanism of action has not yet been delineated. 44
Figure 1.12: The crystal structure of the influenza M2 channel blocked by AMT. The Cu(II) derivative is shown to block the channel by coordinating at the H37 cluster. 45
Figure 1.13: The crystal structure of Zn(II) bound to the catalytic dyad of SARS-CoV-2 Mpro…46
Figure 1.14: The stock price in US dollars of major biopharmaceutical companies over the worst period of the COVID-19 pandemic. Companies that focused on vaccine development saw the largest percentage increase in their stock prices with incredible investment during vaccine roll-out. Moderna showed an astonishing 1140% increase in stock value compared to the pre-pandemic market. The larger “Big Pharma” players such as Pfizer and Johnson & Johnson did not see such steep percentage increases because the relative investment has less impact on the evaluation of the company and demand for shares. In July 2022, Moderna and J&J were trading at $176.23 and $178.28 per share respectively. 55
Figure 1.15: Some structural proteins of SARS-CoV-2 that represent suitable therapeutic targets. The E protein functions as an ion channel that may be inhibited by channel blockers such as AMT. The N protein is shown bound to mRNA and is instrumental to virion assembly, hence it serves as a suitable molecular target for vaccine and drug design. The S protein is shown with two RBDs in the “up” position and bound to the human ACE2 receptor. 57
Figure 1.16: S protein-mediated viral attachment and the life cycle of SARS-CoV-2. 58
Figure 1.17: The structural alignment of WT, Delta, and Omicron RBDs bound to human ACE2. The tyrosine residues of the RBD have been conserved among CoVs indicating the importance of these contacts concerning ACE2 receptor recognition. The design of novel metallodrugs that specifically target the phenolic side chains of the RBD may result in the development of a universal fusion inhibitor that targets new and emerging CoVs. 60

Figure 2.1: Structure and atom labelling of 5,5'-[(pyridine-2,6-dicarbonyl)bis(azanediyl)]dinicotinic acid.....73

Figure 2.2: Structure and atom labelling of 3,3'-[(pyridine-2,6-dicarbonyl)bis(azanediyl)]dibenzoic acid. 74
Figure 2.3: Structure and atom labelling of 4,4'-[(pyridine-2,6-dicarbonyl)bis(azanediyl)]dibenzoic acid. 75
Figure 2.4: Structure and atom labelling of 2,2'-[((pyridine-2,6-dicarbonyl)bis(azanediyl))bis(4,1-phenylene)]diacetic acid. 76
Figure 2.5: Structure and atom labelling of N^2,N^6-bis[3-(dimethylcarbamoyl)phenyl]pyridine-2,6-dicarboxamide. 77
Figure 2.6: Structure and atom labelling of N^2,N^6-bis[3-(isopropylcarbamoyl)phenyl]pyridine-2,6-dicarboxamide. 78
Figure 2.7: Structure and atom labelling of N^2,N^6-bis(1,3-dioxoisoindolin-6-yl)pyridine-2,6-dicarboxamide. 79
Figure 2.8: Structure and atom labelling of N^2,N^6-bis(3-(ethylcarbamoyl)phenyl)pyridine-2,6-dicarboxamide. 80
Figure 2.9: Structure and atom labelling of N^2,N^6-bis(3-acetamidophenyl)pyridine-2,6-dicarboxamide. 81
Figure 2. 10: Structure and atom labelling of N^2,N^6-bis(3-cyanophenyl)pyridine-2,6-dicarboxamide. 82
Figure 2.11: Structure and atom labelling of N^2,N^6-bis(3-(phenylcarbamoyl)phenyl)pyridine-2,6-dicarboxamide. 83
Figure 2.12: Structure and atom labelling of $Zn_2(H_2L2)_2(H_2O)_4$. 86
Figure 2.13: Structure and atom labelling of $Zn_2(H_2L3)_2(H_2O)_8$. 88
Figure 2. 14: The structure of $Cu_2(H_2L2)_2$ when crystallized from pyridine. 92
Figure 2. 15: The structure of Cu_2(L3) when crystallized from pyridine. 94
Figure 2.16: Structure and atom labelling of Zn(L5)$(H_2O)_2$. 96
Figure 2.17: The structure of Cu(L5) in aqueous solution. 99
Figure 2.18: The structure of Cu(H_2L6) in aqueous solution. 102
Figure 2.19: The structure of Cu(H_2L8) in aqueous solution. 105
Figure 2.20: The structure of Cu(H_2L9) in aqueous solution. 107
Figure 2.21: The structure of Cu(L10) in aqueous solution. 109
Figure 2.22: The structure of Cu(H_2L11) in aqueous solution. 111

Figure 3.1: The Root Mean Square Deviation plot of the RBD-ACE2 complex over 50 ns. The RMSD measures the average change in displacement of atoms in each frame with respect to a

reference frame. The RMSD analysis identifies structural conformational changes and RMSD values between 1 and 3 Å are normal for proteins. The C_α trace follows the backbone trajectory exactly and hence is not visible on the plot. 120
Figure 3.2: The Root Mean Square Fluctuation plot of RBD-ACE2 complex over 50 ns. The regions highlighted in red show that the α-helical secondary structure is maintained over 70% of the simulation time, and those regions highlighted in blue indicate β-strand secondary structure. The RMSF is used to indicate local changes in the protein chain and the peaks represent areas of high fluctuation. Secondary structure elements like α-helices are typically more rigid than loop, C-, and N-terminal regions of the protein. The C_α and backbone trajectory are exactly overlapped. 121
Figure 3.3: The MD trajectory analysis snapshots of the interfacial region of the SARS-CoV-2 spike protein RBD-ACE2 complex at 0, 25 and 50 ns. ACE2 is coloured red-orange and the RBD is coloured blue-green. 122
Figure 3.4: The top-scoring compound from HTVS docked against the RBD of SARS-CoV-2. The ligand is coloured magenta and the geometry around the copper centre is square-pyramidal with Y453 forming part of the inner coordination sphere. There are some residues omitted for clarity. 125
Figure 3.5: The RMSD plot of RBD-HTVS1 complex over 100 ns. The plot indicates that the dynamic system is stable in solution. The docked chelate undergoes conformational changes at 20 ns where the organic framework rearranges and binds more favourable residues at 60 ns. This binding pocket is maintained until 100 ns where the MD simulation has equilibrated. Despite rearrangement of the organic framework in solution, the Cu(II) centre remains coordinated to Y453 over the full trajectory period. 126
Figure 3.6: The protein-ligand interaction timeline of the RBD-HTVS1 complex showing the number of contacts per residue over 100 ns. 126
Figure 3.7: The G-scores obtained from docking entries *SP1* through *SP37* against 6M0J. 128
Figure 3.8: The G-scores obtained from docking entries *SP1* through *SP37* against 7DK5 and 7KJ5. 129
Figure 3.9: The best-ranked chelate, *SP22*, docked against the RBD of SARS-CoV-2 (6M0J). There are multiple hydrogen-bonding interactions between the chelate and RBD, stabilizing the protein-ligand complex. The Zn(II) centre is distorted square-pyramidal with Y505 forming part of the inner coordination sphere. 132
Figure 3.10: The protein-ligand contacts between *SP22* and the RBD over 100 ns. 132

Figure 3.11: MD trajectory snapshots over 100 ns for the RBD-SP34 complex. *SP34* was initially docked against Y453 as shown at 0 ns. The dynamic fluctuations of the protein result in *SP34* departing the original binding site at Y453 and coordinating to Y449. The chelate then remains bound to solvent-exposed Y449 for 50 ns before leaving this binding site at 87 ns. The chelate then coordinates Y489 towards the end of the trajectory indicating that this is the more favourable binding site as the MD simulation has equilibrated. 133
Figure 3.12: The G-scores obtained from docking entries XP1 through XP56 against 6M0J. ..134
Figure 3.13: The G-scores obtained from docking entries XP1 through XP56 against 7DK5 and 7KJ5. 135
Figure 3.14: The best-ranked chelate from XP docking, *XP56*, after 100 ns MD equilibration. The ligand is coloured magenta and intermolecular interactions are listed in the legend. As was noted in the methods for docking, an anionic charge was given to each tyrosine suspected to serve as a binding site, i.e., Y453, Y449, Y489, and Y505. This was done to introduce “decoy” targets as the receptor grid was large enough to encompass the entire receptor binding motif. This gives more freedom to the docking run and does not constrain chelate binding to any particular tyrosine residue. Electrostatic forces then direct binding to the more favourable tyrosine target. 138
Figure 3.15: RBD-XP56 interaction timeline over 100 ns. 139
Figure 3.16: The best-docked chelates with substituents in the 4-position, *XP40* is coloured magenta, *XP42* is yellow, *XP38* is green and *XP41* is red. The Zn(II) ions have been coloured grey while Cu(II) is brown. The metal centres are all 5-coordinate with a single water molecule making the square plane and Y453 bound in the axial position. The residues on the RBD have been labelled, although some have been omitted for clarity. Y489 and Y449 were given an anionic charge to serve as “decoy” targets so that electrostatic forces were used to direct chelate binding to the most favourable residue. 140
Figure 3.17: Interactions fraction and protein-ligand contacts between *XP38* and the RBD over 100 ns. 141
Figure 3.18: The G-scores for synthesized chelates docked against the RBD of SARS-CoV-2. 142
Figure 3.19: The best-ranked copper complex, Cu(H_2L8), docked against Y489 of the RBD (6M0J). The ligand is coloured magenta, and the black dashed lines are primary interactions with the protein. The copper centre is square pyramidal with Y489 making up the square plane and an aqua ligand bound in the axial position. The chelate donates two hydrogen bonds to the protein, one to the backbone at G485 and one to the side chain of N487. The ligand is further

stabilized by hydrophobic forces between surrounding residues shown in Figure 3.20 below. As was noted in the methods for docking, positional constraints were used to dock the synthesized chelates. This constraint was shown by NMR to be valid. Hence, these docking runs served to delineate the binding mode between the synthesized chelates and the RBD. 144
Figure 3.20: Ligand interaction diagram showing forces between Cu(H_2L8) and the RBD. Hydrophobic forces are coloured green, polar forces are blue, electrostatic forces are red, and hydrogen bonds are indicated by magenta arrows. 144
Figure 3.21: The RMSD plot for Cu(L5) and the peptide epitope. The system struggles to equilibrate and the fluctuations for the peptide RMSD indicate that the α-helical structure is unstable under the force field parameters. 146
Figure 3.22: Cu(L5) docked against the peptide RBD epitope. The tyrosine is coordinated to the copper center making up the square plane of the square pyramidal metal complex. The binding is stabilized by hydrophobic forces between the aryl rings of the ligand and the phenolic residue. The hydrophobic interactions fraction is also shown and was used to determine the ranking for the chelates. 147

Figure 4.1: I_0 is the horizontally orientated excitation beam with thickness s. The path length of the exciting radiation d = 1 cm and g is the distance from the edge of the sample beam to the edge of the cuvette. This reduces to g = 0 cm because the entire 0.2 cm emission pathlength is illuminated by the excitation beam and hence s = 0.2 cm.....155
Figure 4.2: The biomimetics used to model the SARS-CoV-2 RBD. The small molecule *p*-cresol is the simplest model for tyrosine and was used to determine the Cu(II) NNN pincers' coordinative affinity for the phenol side chain. The peptide epitope used to model the RBD has the sequence GVGYQP and corresponds to G502-V503-G504-Y505-Q506-P507 on the RBD of SARS-CoV-2. The peptide epitope has been shown on the RBD as ball-and-stick structures along with solvent-exposed Y453 and Y489 which are also potential binding sites for the Cu(II) pincers studied here.....156
Figure 4.3: The NMR spectrum of the free peptide at a concentration of 6 mM is shown in black, the spectrum of the free complex CuL5 at 3 mM is shown in green, and the spectrum of peptide-chelate mixture is shown in red with [peptide] = 6 mM and [CuL5] = 3 mM. 159
Figure 4.4: The NMR spectrum of the free peptide at a concentration of 6 mM is shown in black, the spectrum of the free complex Cu(H_2L6) at 800 μM is shown in green, and the spectrum of the peptide-chelate mixture is shown in red with [peptide] = 6 mM and [Cu(H_2L6)] = 800 μM..160

Figure 4.5: The FTIR spectra of CuL10 shown in green, the lyophilized peptide epitope shown in red, and the peptide-CuL10 lyophilized mixture shown in blue. There is a slight change in polarization of the hydroxyl stretch of the tyrosine upon coordination of the Cu(II) pincer. There is significant perturbation of the aromatic C–H stretching vibrations of the peptide upon CuL10 binding. Hence, the FTIR spectra show distinct binding specificity between tyrosine on the epitope and the Cu(II) NNN pincer. 161
Figure 4.6: The MS detected peptide-CuL5 complex species. $[M + H]^+$: calc 1181.43501 Da; found 1181.41589 Da. The elemental formula is thus $CuN_{13}O_{13}C_{55}H_{68}$. The data confirm that the binding stoichiometry is 1:1. 162
Figure 4.7: The CD spectra of the free peptide epitope and Cu(H_2L8) bound peptide. The [peptide] was kept constant at 50 μM while the [Cu(H_2L8)] was increased from 0 to 120 μM...163
Figure 4.8: The fluorescence emission spectra of *p*-cresol at various concentrations of Cu(H_2L9). The [*p*-cresol] was kept constant at 100 μM while the [Cu(H_2L9)] was varied from 0.00 to 536 μM. The *p*-cresol fluorophore is quenched by increasing concentration of Cu(H_2L9). The inset shows the plot of the modified double-log Stern-Volmer equation where n = 1.00 and logK = 3.82. The deviation from linearity at high concentrations is due to dynamic quenching being observed. 166
Figure 4.9: The Hill plot obtained from fluorescent intensity values at 308 nm. The [Cu(H_2L9)] was varied from 536 μM to 1.00 μM while the [*p*-cresol] was kept constant at 100 μM. The error bars are reported as the standard deviation of the intensity value at 308 nm for three independent samples. 167
Figure 4.10: The plot of K_{app} vs [Cu(H_2L9)] obtained by titrating Cu(H_2L9) against *p*-cresol showing that dual quenching mechanisms are being observed at high concentrations of copper complex. The deviation from linearity at low [Cu(H_2L9)] indicates that only static quenching is being observed in this region. The K_{app} plot yields ($K_D + K_s$) = 5510 ± 110 M^{-1} and K_DK_S = $1.44\times10^7 \pm 4.89\times10^5$ M^{-1}. The inset shows the Stern-Volmer plot with the straight line plotted for low concentration data only. The SV plot yields a slope of 6920 ± 164 M^{-1} which is the K_{SV} and furthermore, the equilibrium association constant, K_a. The deviation from linearity observed for the SV plot at high concentrations of copper complex is due to dynamic quenching processes. 168
Figure 4.11: The fluorescence emission spectra of the SARS-CoV-2 peptide epitope at various concentrations of Cu(H_2L9). The [peptide] was kept constant at 100 μM while the [Cu(H_2L9)] was varied from 0.00 to 500 μM. The peptide fluorophore is quenched by increasing concentration of Cu(H_2L9). The inset shows the plot of the modified double-log Stern-Volmer

equation where n = 0.995 and logK = 3.79. The deviation from linearity at high concentrations is due to dynamic quenching being observed. 169
Figure 4.12: The Hill plot obtained from fluorescent intensity values at 308 nm. The [Cu(H_2L9)] was varied from 500 μM to 1.00 μM while the [peptide] was kept constant at 100 μM. The error bars are reported as the standard deviation of the intensity value at 308 nm for three independent samples. 170
Figure 4.13: The plot of K_{app} vs [Cu(H_2L9)] obtained by titrating Cu(H_2L9) against the peptide epitope showing that dual quenching mechanisms are being observed at high concentrations of copper complex. The deviation from linearity at low [Cu(H_2L9)] indicates that only static quenching is being observed in this region. The K_{app} plot yields (K_D + K_s) = 5470 ± 81.7 M^{-1} and K_DK_S = 1.04×10^7 ± 2.56×10^5 M^{-1}. The inset shows the Stern-Volmer plot with the straight line plotted for low concentration data only. The SV plot yields a slope of 6790 ± 574 M^{-1} which is the K_{SV} and furthermore, the equilibrium association constant, K_a. The deviation from linearity observed for the SV plot at high concentrations of copper complex is due to dynamic quenching processes. 171
Figure 4.14: The CD spectra of SARS-CoV-2 Delta RBD in the presence of copper complex CuL5. The [RBD] was kept constant at 15 μM while titrating aliquots of CuL5 into the protein solution. The secondary structure of the protein is perturbed upon addition of the copper chelate indicating that the compound binds the biomolecule. There is a weak induced CD signal at 550 nm which indicates that the copper complex is stable and has not demetalated in the presence of RBD. Furthermore, the weak induced signal indicates that CuL5 is surface bound so that it may potentially act as a fusion inhibitor. The inset shows Cu(H_2L8) docked against Y489 of the RBD; this solvent exposed residue is the most likely target as determined by *in silico* methods. 172
Figure 4.15: The DFT ONIOM calculated spectra and experimental CD and UV-Vis spectra of Delta RBD in complex with CuL5 (cam-b3lyp/sdd, TD-DFT n=60, with empirical dispersion correction gd3bj). The copper chelate was docked against Y489 of the Delta RBD (PDB:7V8B) either with 4-coordinate (4CN) geometry or 5-coordinate (5CN) geometry where the fourth and fifth ligands are tyrosine and water. Simulations were also calculated for Y505, Y449, and Y473, with CuL5 4CN, 5CN, and anionic (S4.58). However, the results for CuL5 docked against Y489 produced the best correlation between calculated and experimental results. The DFT calculated CD wavelengths for 5CN data were corrected by –19 nm while 4CN data was corrected by –38 nm. The DFT calculated UV-Vis data was only normalized. There is good overlap between all three CD spectra, and hence cannot comment on coordination geometry, but it is highly likely

that Y489 is the binding site on the RBD. However, the UV-Vis data suggests that CuL5 is bound with 5-coordinate geometry (S4.59). The severe noise for experimental UV-Vis data is due to the dilute solutions producing absorbance values below 0.1. Experimental UV-Vis data excluded between 750 and 760 nm for normalization between 450 and 800 nm.....173
Figure 4.16: The fluorescence emission spectra of SARS-CoV-2 Delta RBD in the presence of $Cu(H_2L8)$. The $[Cu(H_2L8)]$ was varied from 500 nM to 5.38 μM while the [RBD] was kept constant at 3.11 μM or 0.08 mg/mL. The RBD fluorophore is quenched by increasing $[Cu(H_2L8)]$.....174
Figure 4.17: The Hill plot obtained from fluorescent intensity values at 335 nm. The $[Cu(H_2L8)]$ was varied from 500 nM to 5.38 μM while the [RBD] was kept constant at 3.11 μM. The error bars are reported as the standard deviation of the intensity value at 335 nm for two independent samples. 175
Figure 4.18: The SV plot obtained from fluorescence quenching of SARS-CoV-2 Delta RBD by $Cu(H_2L8)$. The K_{SV} of 62900 ± 172 M^{-1} may be equated to K_a, the equilibrium association constant. The fit is excellent with $R^2 = 1$ despite so much scatter.....176
Figure 4.19: The modified double-log SV plot obtained from fluorescence quenching of SARS-CoV-2 Delta RBD by $Cu(H_2L8)$. The straight line yields a slope of 0.887 ± 0.09 which is n, the binding stoichiometry. This suggests that the stoichiometry is approximately 1:1 $Cu(H_2L8)$:RBD. The plot yields an intercept of 4.25 ± 0.5 which is the value of logK. 176
Figure 4.20: The absorbance values at 640 nm for a solution of CuL5 with 1 and 3 equivalents of glutathione (GSH). GSH is present in high concentrations in living cells and it is important that the Cu(II) chelates are GSH stable. Upon sample preparation, the solution changes from green to colourless before returning to a green colour over time.....180

Figure 5.1: The crystal structures of a Cu(II) NNN amide pincer coordinated to various phenols. The structures have been labelled with their CSD reference codes. The phenol group serves as a biomimetic model for tyrosine and indicates the possible binding mode when the chelate has bound the solvent exposed residue on the SARS-CoV-2 receptor binding domain. The phenol coordinates in the equatorial position such that there is overlap of the paramagnetic $3d_{x^2-y^2}$ orbital and the aromatic π-system. This has been observed by NMR and was presented in Chapter 4. Additional stability is afforded by hydrophobic interactions between the phenol and the aryl rings present on the chelate. 186
Figure 5.2: The Cu(II) hexamer published by Lloyd *et al.*[4] with the coordination pattern shown as ball-and-stick models. The cyclic coordination follows the pattern Cu(II)–C=O_{amide}–Cu(II).

Standard colours have been used for atoms, i.e., grey for carbon, red for oxygen, blue for nitrogen, bronze for copper. 187
Figure 5.3: The copper metallocycle published by Hossain *et al.*[5] with the cyclic coordination pattern Cu(II)–N_{diazo}–Cu(II) shown as ball-and-stick models. Standard colours have been used for atoms, i.e., grey for carbon, red for oxygen, blue for nitrogen, bronze for copper. 187
Figure 5.4: The Cu(II) superstructure published by Fu *et al.*[6] with the coordination pattern shown as ball-and-stick models. The (1*H*-benzimidazol-1-yl)acetic acid moiety serves as a bridging group between metal centres. Standard colours have been used for atoms, i.e., grey for carbon, red for oxygen, blue for nitrogen, bronze for copper. 188
Figure 5.5: The hexanuclear cyclic assembly published by Higa *et al.*[7] with the coordination pattern Cu(II)–$N_{imidazole}$–Cu(II) shown as ball-and-stick models. Standard colours have been used for atoms, i.e., grey for carbon, red for oxygen, blue for nitrogen, bronze for copper. 188
Figure 5.6: Crystals of CuL2 “blue” grown by evaporating a saturated pyridine solution. 190
Figure 5.7: The asymmetric unit of CuL2 “blue” showing the dinuclear cage structure and co-crystallized solvent molecules. The square pyramidal copper centers have been shown as polyhedrons. There are six water molecules and four pyridines, two have been omitted for clarity. The internal H-bond network has been shown as cyan cylinders. 191
Figure 5.8: The intermolecular forces and unit cell of CuL2 “blue”. The C–H···π, C–H···O, and π···π interactions have been shown as space-fill models while the H-bonding network has been shown as cyan cylinders. There are additional, and numerous, close contacts that further facilitate packing of the cage structure into the crystal lattice. 192
Figure 5.9: Crystals of CuL2 “green” grown from a saturated pyridine solution. 193
Figure 5.10: The dinuclear cage structure of CuL2 “green” has co-crystalized with three water molecules. A single water molecule is shown that acts as a H-bond donor to the carbonyl of a neighboring chelate and facilitates packing of the complexes into the lattice. 194
Figure 5.11: (Top) The molecular overlay of computed structure (shown in yellow) and X-ray crystal structure, R^2 = 0.86 Å. (Bottom) The spin-density plot for CuL2 “green” shows significant $3d_{x^2-y^2}$ character and occupies the square plane of the metal center. 195
Figure 5.12: The unit cell and packing of CuL2 “green” is shown with neighboring cage structures colored differently. The H-bonding network extends between three water molecules that occupy the cage cavity and the carbonyl of an adjacent chelate. These strong intermolecular interactions result in efficient crystal packing as no voids are present in the lattice. 196
Figure 5.13: Crystals of CuL3 grown from a saturated pyridine solution. 197

Figure 5.14: The asymmetric unit of CuL3 is described by a tetramer of the MOF polymer. 197
Figure 5.15: The unit cell of CuL3 showing the 2D MOF polymer. There is metal coordination that extends the polymer parallel to the crystallographic b- and c-axes while close contacts facilitate packing parallel to the a-axis. The unit cell is viewed down the a-axis (left), b-axis (top), and c-axis (bottom). 199
Figure 5.16: The voids that extend through the lattice of CuL3 as infinite channels parallel to the crystallographic c-axis. 200
Figure 5.17: Crystals of CuL5 viewed under the microscope. 201
Figure 5.18: The coordination pattern that generates the 24-membered hexanuclear copper carboxamide macrocycle with S_2 symmetry. The metal centers are 5-coordinate square pyramidal and are shown as polyhedrons. The mean plane for the hexamer lies in the plane of the six nitrogens that make up the cyclic pattern. There are three Cu(II) centers that lie in a plane above the mean plane (solid green) and three Cu(II) centers that lie in a plane below the mean plane (dashed green). The asymmetric unit is shown on the right. 201
Figure 5.19: A single monomer of CuL5 that makes up the metallocycle hexamer. The inner coordination sphere is square pyramidal and donor nitrogens are labelled where N_{pyr} is the pyridine nitrogen and N_{amide} is the amide anionic nitrogen. The label $N_{amide\text{-}Cu}$ refers to the anionic nitrogen that forms the amide that is coordinated to a neighboring complex of CuL5. The carbonyls that make up the chelate ring are distinguished as C=O and $C{=}O_{Cu}$ where the latter refers to the carbonyl that acts as a bridge between metal centers of the hexamer. 203
Figure 5.20: The inner coordination sphere of CuL5 is shown in the top left, and the only symmetry element is a vertical mirror plane, σ_V. The mirror plane defines the Cartesian z-axis as the principal z-axis is collinear with the highest symmetry element. As a result, the x-axis is perpendicular to the z-axis and collinear with highest number of identical atoms, i.e., the two N_{amide}. That leaves the y-axis to pass through N_{pyr} and $O_{carbonyl}$. The bridging carbonyl interaction is then shown on the top right. The bonding involves predominately σ-overlap of the metal-based $3d_{x^2-y^2}$ atomic orbital and σ* molecular orbital of the carbonyl. There is additional bonding involving π-overlap of the metal-based $3d_{xy}$ atomic orbital and the π* molecular orbitals of the carbonyl. This donation of electron density from the metal-based orbitals into antibonding orbitals of the carbonyl causes the bond length to increase for the bridging moiety. This was confirmed with DFT, as the spin-density plot in the bottom left of the figure shows significant $3d_{x^2-y^2}$ character as well as σ-overlap between copper and the carbonyl. The π-overlap between carbonyl π* molecular orbitals and the atomic $3d_{xy}$ orbital was observed for the LUMO of the asymmetric unit of CuL5. Additionally, the axially coordinated solvent molecule shows

significant $3d_z^2$ character, substantiating the claim that the z-axis is collinear with the axial position. 204
Figure 5.21: The geometry of C–H···π and d···π interactions. The centroid of the aromatic ring is marked “x” and the normal to the aromatic plane is shown as a solid black line. The atom-to-centroid distances are marked by solid red lines while atom-to-plane distances are marked by dashed red lines. The angles that define the interaction have been marked in red. The C–H···π interaction has optimal overlap when the angle at hydrogen ∠C–H–X approaches 180°. The metal d···π interaction has optimal overlap when the angle at the centroid ∠C–X–M approaches 90°. The angle is defined by selecting the atom in the aromatic ring closest to the metal centre, the centroid of the ring, and the metal centre itself. When the d···π interaction has optimal overlap all angles ∠C–X–M will approach 90° as the d_z^2 orbital approaches the centroid of the aromatic ring. When the d···π interaction angle ∠C–X–M is acute, but greater than 45°, the d_{xz} and d_{yz} orbitals are orientated for favourable overlap with the π molecular orbitals of the aromatic ring. Hence, C–H···π interactions will be described by the atom-to-plane distance between the hydrogen atom and the aromatic plane as well as the angle at hydrogen ∠C–H–X. Furthermore, d···π interactions will be described by the atom-to-plane distance in angstroms between the metal centre and the aromatic plane as well as the angle at the centroid ∠C–X–M. 205
Figure 5.22: The intramolecular interactions stabilizing the CuL5 metallocycle hexamer. The repeating coordination pattern has been shown in yellow while H-bonds are shown as dashed cyan cylinders. The Cu(II) triad that lies above the mean plane of the macrocycle has been shown as space-fill model with C–H···π and d···π interactions to aromatic rings of adjacent chelates shown. There are numerous disordered van der Waals interactions, one interaction has been shown at the green-highlighted methyl groups.....206
Figure 5.23: The bond lengths and angles of the intramolecular C–H···π and d···π interactions that stabilize the CuL5 cyclic assembly. 207
Figure 5.24: The unit cell of CuL5 as viewed down the crystallographic b-axis. The intermolecular forces that stabilize the packing of hexamers in the lattice are shown as space-fill models. The voids present in the crystal are also shown and these extend as infinite channels parallel to the crystallographic a-axis. 208
Figure 5.25: Crystals of Cu(H_2L6) grown over 6 weeks and viewed under the microscope. 209
Figure 5.26: The coordination pattern that generates the 24-membered hexanuclear copper carboxamide metallocycle with S_2 symmetry. The metal centers are 5-coordinate square pyramidal or 4-coordinate square planar and are shown as polyhedrons. The mean plane for the

hexamer lies in the plane of the six nitrogens that make up the cyclic pattern. There are three Cu(II) centers that lie in a plane above the mean plane (solid green) and three Cu(II) centers that lie in a plane below the mean plane (dashed green). Each Cu(II) triad has two neighboring metal centers square pyramidal with the third being square planar. Asymmetric unit shown on the right. 209
Figure 5.27: The intramolecular interactions stabilizing the Cu(H_2L6) “kinetic” metallocycle hexamer. The repeating coordination pattern has been shown in yellow while H-bonds are shown as dashed cyan cylinders. The Cu(II) triad that lies above the mean plane of the macrocycle has been shown as space-fill model with C–H···π and d···π interactions to aromatic rings of adjacent chelates shown. 212
Figure 5.28: The bond lengths and angles of the intramolecular C–H···π and d···π interactions that stabilize the Cu(H_2L6) cyclic assembly. The H-bonds that prevent C–H···π bond formation have been shown as cyan cylinders with the H-bond bond length and angle. 213
Figure 5.29: (Top) The unit cell of Cu(H_2L6) as viewed down the crystallographic a-axis. The intermolecular forces that stabilize the packing of hexamers in the lattice are shown as space-fill models for van der Waals forces and cyan cylinders for the H-bonding network. (Bottom) The voids as viewed down the crystallographic c-axis extend as infinite channels through the lattice. 214
Figure 5.30: Crystals of Cu(H_2L6) grown over 6 months and viewed under the microscope. ... 215
Figure 5.31: The coordination pattern that generates the 24-membered hexanuclear copper carboxamide metallocycle with S_2 symmetry. The metal centers are 5-coordinate square pyramidal or 4-coordinate square planar and are shown as polyhedrons. The mean plane for the hexamer lies in the plane of the six nitrogens that make up the cyclic pattern. There are three Cu(II) centers that lie in a plane above the mean plane (solid green) and three Cu(II) centers that lie in a plane below the mean plane (dashed green). Each Cu(II) triad has two neighboring metal centers square planar with the third being square pyramidal. Asymmetric unit shown on the right. 215
Figure 5.32: The intramolecular interactions stabilizing the Cu(H_2L6) “thermodynamic” metallocycle hexamer. The repeating coordination pattern has been shown in yellow while H-bonds are shown as dashed cyan cylinders. The Cu(II) triad that lies above the mean plane of the macrocycle has been shown as space-fill model with C–H···π and d···π interactions to aromatic rings of adjacent chelates shown. 217
Figure 5.33: The bond lengths and angles of the intramolecular C–H···π and d···π interactions that stabilize the Cu(H_2L6) “thermodynamic” cyclic assembly 218

Figure 5.34: (Top) The unit cell of Cu(H_2L6) “thermodynamic” as viewed down the crystallographic b-axis. The short contacts between hexamers are shown as dashed red cylinders while C–H···O and van der Waals interactions between supermolecules in the *bc* plane have been shown as space-fill models. (Bottom) The unit cell viewed down the crystallographic c-axis shown with the voids that exist as doughnut-shaped pockets in the lattice. Also shown as space-fill models are the intermolecular interactions in the *ac* plane between the co-crystallized methanol of one unit cell H-bonded to the carbonyl of a chelate in the adjacent unit cell.....219
Figure 5.35: A single crystal of Cu(H_2L8) “kinetic” grown from an ethanol/methanol mixture. ..220
Figure 5.36: The coordination pattern for Cu(H_2L8) “kinetic” that generates the cyclic hexamer. The asymmetric unit is shown on the right. 220
Figure 5.37: The intramolecular interactions imparting the tensegrity observed for the Cu(H_2L8) “kinetic” supermolecule. The cyclic coordination pattern has been shown in yellow while intramolecular H-bonds between ethylamide groups are shown as cyan cylinders. The C–H···π and d···π interactions have been shown as space-fill models.....222
Figure 5.38: The C–H···π and d···π interactions observed for Cu(H_2L8) “kinetic” with the relevant bond lengths and angles. 223
Figure 5.39: The unit cell of Cu(H_2L8) “kinetic” as viewed down the crystallographic a-axis. The intermolecular forces that facilitate packing of the hexamers have been shown as space-fill models and comprise of H-bonding and van der Waals forces. 224
Figure 5.40: The voids present in the lattice of Cu(H_2L8) “kinetic” occupy the corners of the triclinic unit cell. 224
Figure 5.41: Crystals of Cu(H_2L8) grown from methanol overnight and stored for 6 months before data collection. 225
Figure 5.42: The coordination pattern for Cu(H_2L8) “thermodynamic” that generates the cyclic hexamer. The asymmetric unit is shown on the right with co-crystalized solvent. 225
Figure 5.43: The intramolecular forces stabilizing the Cu(H_2L8) cyclic assembly. The coordination pattern has been highlighted in yellow while C–H···π and d···π interactions have been shown as space-fill models. The intramolecular H-bonding between ethylamide groups has been shown as cyan cylinders while H-bonding to co-crystalized water has been shown as green cylinders. The H-bonding network between the hexamer and water molecules is shown to extend from an axially coordinated solvent molecule and H-bond through waters before bonding carbonyls on adjacent chelates. 227
Figure 5.44: The C–H···π and d···π interaction bond lengths and angles for Cu(H_2L8) “thermodynamic”. 228

Figure 5.45: The unit cell of Cu(H_2L8) “thermodynamic” as viewed down the crystallographic c-axis. The adjacent supermolecules have been colored differently. The extensive H-bonding network has been shown as cyan cylinders and exists between co-crystalized solvent molecules and neighboring hexamers. The network enables efficient packing as the unit cell volume is only 0.1% void volume. 229
Figure 5.46: The hypothesized annealing process for Cu(H_2L8) “thermodynamic” and the FTIR spectrum confirming that water enters the crystal over time. The FTIR spectrum shows Cu(H_2L8) powder sample in red, while crystals grown overnight are shown in green and crystals stored for 6 months are shown in pink. The peak at 1696 cm^{-1} indicates O–H wagging from water that has entered the lattice and co-crystalized. The annealing process begins in the top left of the figure, where kinetic crystals of Cu(H_2L8) grown overnight are suspected to possess large voids that extend as infinite channels. The annealing process then compresses the voids into amorphous pockets that trap solvent. As the process continues, these pockets compress further into small spheres that occupy only 0.1% of the unit cell volume. After the thermodynamic process has completed, the crystal is packed efficiently, and the potential energy of the solid-state system has been lowered. The structure of the kinetic crystals grown overnight was never elucidated and hence the annealing process is speculative. The voids shown as infinite channels are drawn from the structure of Cu(H_2L6) “kinetic”, which differs from Cu(H_2L8) by only a single methyl group on the chelate and was grown from methanol. The voids shown as amorphous pockets have been drawn from Cu(H_2L8) “kinetic” which was grown from an ethanol/methanol mixture. The voids for Cu(H_2L8) “thermodynamic” have been presented and the crystal was grown from a methanol solution. 230
Figure 5.47: Crystals of Cu(H_2L9) “kinetic” grown from an ethanol solution over 6 weeks. 231
Figure 5.48: The coordination pattern that generates the 24-membered hexanuclear copper carboxamide macrocycle with S_2 symmetry. The metal centers are 5-coordinate square pyramidal or 4-coordinate square planar and are shown as polyhedrons. The mean plane for the hexamer lies in the plane of the six nitrogens that make up the cyclic pattern. There are three Cu(II) centers that lie in a plane above the mean plane (solid green) and three Cu(II) centers that lie in a plane below the mean plane (dashed green). Each Cu(II) triad has two neighboring metal centers square pyramidal with the third being square planar. The asymmetric unit is shown on the right.....231
Figure 5.49: The intramolecular forces stabilizing the cyclic assembly of Cu(H_2L9) “kinetic”. The coordination pattern has been highlighted yellow while H-bonds between acetamide groups of neighboring chelates have been shown as cyan cylinders. The C–H···π and d···π intramolecular

interactions have been shown as space-fill models. Additionally, there are numerous disordered van der Waals forces that exist between monomers of the supermolecule.....233
Figure 5.50: The C–H···π and d···π bond lengths and angles for the Cu(H_2L9) "kinetic" cyclic superstructure. The most significant d···π interaction is observed for the square planar chelate which has an atom-to-plane distance of 2.8 Å and indicates that in the absence of an axially coordinated ligand, the metal centre may approach closer to the π-system for more favourable overlap of atomic d-orbitals and molecular orbitals of the aromatic ring.....234
Figure 5.51: The unit cell of Cu(H_2L9) as viewed down the crystallographic a-axis. The H-bonding between the acetamide of one supermolecule and the carbonyl of another is shown as space-fill models and exist along the *ac* plane. The H-bonding network between co-crystalized solvent molecules and neighboring supermolecules has been shown as cyan cylinders and exist along the *ab* plane. Additional close contacts have been shown as red cylinders. The void volume has been shown in yellow and is considerable at 29% of the unit cell volume. The voids extend through the lattice as infinite channels in two dimensions parallel to the crystallographic a- and b-axes.....235
Figure 5.52: Crystals of Cu(H_2L9) "thermodynamic" grown by vapor diffusion of DCM into a methanol solution over 6 months. 236
Figure 5.53: The coordination pattern that generates the 24-membered hexanuclear copper carboxamide macrocycle with S_6 symmetry. The metal centers are 5-coordinate square pyramidal and are shown as polyhedrons. The mean plane for the hexamer lies in the plane of the six nitrogens that make up the cyclic pattern. There are three Cu(II) centers that lie in a plane above the mean plane (solid green) and three Cu(II) centers that lie in a plane below the mean plane (dashed green). The asymmetric unit shown on the right.....236
Figure 5.54: The intramolecular interactions stabilizing the Cu(H_2L9) "thermodynamic" supermolecular assembly. The coordination pattern has been shown as yellow atoms and follows the sequence Cu(II)–N–C=O_{amide}–Cu(II). There are C–H···π and d···π interactions which have been shown as space-fill models for one of the Cu(II) triads. The interactions are related to the second Cu(II) triad by inversion through the centroid of the metallocycle. Additional stabilization of the assembly is afforded by van der Waals interactions (shown in green) between acetyl groups of neighbouring chelates. Notably, intramolecular H-bonding is absent and instead the H-bond donors and acceptors participate in intermolecular recognition and packing of supermolecules into the crystal lattice.....238

Figure 5.55: The C–H···π and d···π interaction bond lengths and angles. The bond parameters for each interaction are identical for the Cu(II) triad and reflects the symmetry of the crystal. The d···π interactions are significant with an atom-to-plane distance of 2.834 Å. 239
Figure 5.56: The microstructure of the supermolecule is observed for the macrostructure of the crystal. 240
Figure 5.57: (Top) The unit cell of Cu(H_2L9) “thermodynamic” viewed down the crystallographic c-axis. (Middel) The H-bonding network between acetamide moieties of neighboring supermolecules and co-crystallized water that extends through all dimensions of the lattice. (Bottom) The monomer that describes the asymmetric unit H-bonded to four water molecules and two adjacent chelates of a hexamer. 241
Figure 5.58: Crystals of CuL10 grown by evaporation from a methanol/ethyl acetate mixture. 242
Figure 5.59: The coordination pattern for CuL10 that results in S_2 symmetry for the metallocycle. The asymmetric unit is shown on the right with the coordinating bond that results in an extended polymeric crystal structure.....242
Figure 5.60: The intramolecular interactions stabilizing the CuL10 metallocycle. The coordination pattern has been shown as yellow atoms and follows the sequence Cu(II)–N–C=O_{amide}–Cu(II). There are C–H···π and d···π interactions which have been shown as space-fill models for one of the Cu(II) triads. The interactions are related to the second Cu(II) triad by inversion through the centroid of the metallocycle. 245
Figure 5.61: The C–H···π and d···π bond lengths and angles for CuL10. 245
Figure 5.62: Space-filling model of the CuL10 metallocycle highlighting the various van der Waals forces imparting tensional integrity to the cyclic assembly. Additional π···π stacking is evident between aromatic pyridine rings and adjacent aryl groups. 246
Figure 5.63: The centroid-to-centroid and centroid-to-plane distances between aromatic groups participating in π···π stacking within the CuL10 supermolecule. 246
Figure 5.64: The unit cell and packing of CuL10 supermolecules in the crystal lattice. The intermolecular interactions have been shown as space-fill models and comprise of coordinating bonds that extend the hexamers as infinite polymers through the lattice. Additional C–H···O and H-bonding interactions further facilitate packing of the complex. The voids present in the crystal have also been shown and exist at the corners of the unit cell. 247
Figure 5.65: The asymmetric unit of CuL5 optimized at the B3LYP/LanL2DZ level of theory. The structure was computed with quartet multiplicity and the paramagnetic spin density was found to be located at each of the three Cu(II) centres that make up the asymmetric unit. The

paramagnetic spin density is localized in the square plane of the metal centre and shows significant $3d_{x^2-y^2}$ character. Alpha spin is blue and beta spin is green. 248
Figure 5.66: The CuL5 metallocycle hexamer shown with paramagnetic spin density orbitals. The spin density is located at each of the six copper centers and shows significant $3d_{x^2-y^2}$ character. The delocalization of this reactive orbital into vacant orbitals of the equatorially coordinated ligand is instrumental to metallocycle formation. The figure was created from the optimized asymmetric unit and crystal structure of CuL5.....249
Figure 5.67: The molecular overlay of DFT calculated structures (yellow) and crystal structure. The dissolution mechanism has been shown as water may substitute at the Cu(II) center and release monomers into solution. The experimental UV-vis spectrum (red) shows excellent agreement with the DFT calculated spectrum (black). The HOMO→LUMO transition at 640 nm has also been shown. The DFT wavelength data was adjusted by –152 nm.....251
Figure 5.68: The steric requirements for Cu(II) NNN amide pincer metallocycle formation. When the aryl ring is substituted in the 4-position there are no steric repulsions, and the structure may adopt cyclic hexameric coordination as reported by Lloyd *et al*.[4] Substitution in the 2- and 6-position results in steric hinderance and metallocycles do not form, while substitution at the 2-position only results in intramolecular recognition at the Cu(II) center which prevents hexamer formation. The aryl ring substituted in the 3-position permits cyclic assembly but not when the 3- and 5-positions are substituted. 254
Figure 5.69: The general coordination mode for the Cu(II) NNN amide pincer. The metal center requires an available coordination site for the metallocycle to form and the ligand should not sterically hinder hexamer assembly. The electronic requirements of the metal center must be met through a finely balanced interplay between σ- and π-effects. 256

List of Tables

Table 1.1: NNN metal pincers and their inhibitory concentrations against various cancer cell lines. Cell cultures were incubated between 24 and 72 hours at 37°C with 5% CO_2. 49

Table 2.1: List of yields for synthesized ligands.....71

Table 3.1: The G-score and interaction profile of the top five hits obtained from HTVS. 123
Table 3.2: The structures and druglikeness parameters for the top five HTVS hits.....124
Table 3.3: The best-ranked entries from SP docking as determined by ECR and summation. 130
Table 3.4: The structures and druglikeness parameters for the top five SP docking hits. 131
Table 3.5: The best-ranked entries from XP docking as determined by ECR and summation. 136
Table 3.6: The structures and druglikeness parameters for the top 10 XP hits. As was noted in the methods for ligand preparation, the current force fields employed by Schrodinger are not parameterized for metal-containing ligands. Consequently, ionization states could not be generated for the chelates and represents a current limitation in the accuracy of docking in Glide. While ionization states for carboxylic acids and guanadinium groups may affect the *in silico* affinity for the RBD, the purpose of docking was to determine ideal substitution patterns for the chelates. Hence, the docking results are valid for determining favourable substitution patterns on the aryl rings of the chelate but the final G-score may be affected by ionization states. 136
Table 3.7: The G-scores for top-ranking entries when docked against Y453 of 6M0J. 140
Table 3.8: The ECR and summation rankings of the five synthesized copper chelates. 143
Table 3.9: G-scores for the binding of five synthesized Cu(II) chelates to the RBD target peptide epitope, the fraction of hydrophobic interactions to tyrosine over a 100 ns MD simulation, and the experimental association constant. 145
Table 3.10: The rankings of the chelates based on experimental K_a, G-score, and the hydrophobic fraction of interactions. 145

Table 4.1: Fluorescence quenching parameters of *p*-cresol in the presence of copper complexes. The data were obtained in MOPS aqueous buffer 10% DMSO (v/v) at pH 7.4 and 37 °C. The parameters highlighted in green are obtained from the Hill model. Those highlighted in blue are obtained from the modified double-log SV equation. The parameters highlighted in orange are obtained from the SV equation. The logK value is the logarithm of the association

constant, K_a; n is the stoichiometry of binding; R^2 is the square of the correlation coefficient of the model; and $\boldsymbol{kq}$ is the bimolecular quenching rate constant. The errors are obtained as the estimated standard deviation of the model and from the rules of propagation of uncertainty in measurement. 164
Table 4.2: Fluorescence quenching parameters of the peptide epitope in the presence of copper complexes. The data were obtained in MOPS aqueous buffer 10% DMSO (v/v) at pH 7.4 and 37 °C. The parameters highlighted in green are obtained from the Hill model. Those highlighted in blue are obtained from the modified double-log SV equation. The parameters highlighted in orange are obtained from the SV equation. The logK value is the logarithm of the association constant, K_a; n is the stoichiometry of binding; R^2 is the square of the correlation coefficient of the model; and $\boldsymbol{kq}$ is the bimolecular quenching rate constant. The errors are obtained as the estimated standard deviation of the model and from the rules of propagation of uncertainty in measurement. 165
Table 4.3: Fluorescence quenching parameters of the SARS-CoV-2 Delta RBD in the presence of Cu(H_2L8). The data were obtained in 3 mM HEPES, 150 mM NaCl, 0.02% NaN_3 aqueous buffer at pH 7.4 and 37 °C. The parameters highlighted in green are obtained from the Hill model. Those highlighted in blue are obtained from the modified double-log SV equation. The parameters highlighted in orange are obtained from the SV equation. The logK value is the logarithm of the association constant, K_a; n is the stoichiometry of binding; R^2 is the square of the correlation coefficient of the model; and $\boldsymbol{kq}$ is the bimolecular quenching rate constant. The errors are obtained as the estimated standard deviation of the model and from the rules of propagation of uncertainty in measurement. 174
Table 4.4: The solubility of the copper complexes in water as determined by UV-Vis at 25 °C. The complexes are water soluble with CuL5 saturating water at 3 mM. The solubility was not determined for Cu(H_2L9) as the complex demetallates in pure water and solubility was not determined for CuL10 because the complex is very poorly water soluble. 179
Table 4. 5: The complex Cu(H_2L9) was observed to demetallate in water and its percent demetallation was determined by UV-Vis spectroscopy. The complex is not stable in pure water and decomposes by 6% over 24 hours. However, the complex is stable in MOPS buffer at pH 7.4 over 24 hours. 179
Table 4.6: The stability of CuL5 was tested in the presence of GSH. Solutions of CuL5 were preprepared in MOPS buffer at pH 7.4 with 1 and 3 equivalents of GSH and monitored by UV-Vis spectroscopy over time. Upon sample preparation, the solution changes from green to colourless. It is suspected that GSH reduces the Cu(II) NNN pincer to a negatively charged

Cu(I)L5-GSH complex before dissolved oxygen oxidizes the chelate back to its Cu(II) form. The re-oxidation process was monitored over 1.5 hours, and with 1 eq GSH, 65% of the Cu(II) chelate remains in solution while 3 eq resulted in only 33% Cu(II) chelate remaining. The experiment was run with the cuvette properly sealed and it was suspected that equilibrium was established for the oxidation process. Hence, the experiment was repeated with 7 eq of GSH but molecular oxygen was bubbled through the solution before leaving it for ∞ time and again before recording the UV-Vis spectrum. At 7 eq GSH with the solution oxygenated, the CuL5 concentration returned to 79% of its initial concentration. There were no signs of demetallation and hence it is suspected that an equilibrium exists where the Cu(I)L5-GSH complex is stable and present in measurable quantities (the difference between initial and final Cu(II) pincer concentration). The GSH stability was also tested in HEPES, NaCl buffer but resulted in instant and irreversible demetallation. Finally, the Cu(II) chelates were tested for a suitable buffer. Cu(H_2L9) was only stable in MOPS buffer, while the complex demetallated in PBS, TBS, HEPES and TA. CuL5 was stable in HEPES, MOPS, TA, and TBS but demetallated in PBS. The Cu(II) NNN pincers are highly sensitive to demetallation in HCl with compounds decomposing in 0.01M $HCl_{(aq)}$. Hence, it is unlikely the copper chelates would survive *in vitro* cell cultures and live virus data was never collected.....181

Table 5.1: The inner coordination bond lengths in Angstroms for the CuL3 tetramer. The bond lengths have been reported with the estimated standard deviation of the least significant digits given in parenthesis. Cu4 has been omitted due to the disorder at this metal center. 199
Table 5.2: The bond lengths for the inner coordination sphere of CuL5 as well as carbonyl bonds that make up the tridentate chelate ring. The asymmetric unit of the crystal contains three Cu(II) centers, and the bond lengths are presented as the average with the error reported as the standard deviation of three independent bond length measurements.....203
Table 5.3: The bond lengths for the inner coordination sphere of Cu(H_2L6) as well as carbonyl bonds that make up the tridentate chelate ring system. The asymmetric unit of the crystal contains three Cu(II) centers, and the bond lengths are presented as the average with the error reported as the standard deviation of three independent bond length measurements or two independent measurements for bonds to axially coordinated solvent.....211
Table 5.4: The bond lengths for the inner coordination sphere of Cu(H_2L6) “thermodynamic” as well as carbonyl bonds that make up the tridentate chelate ring. The asymmetric unit of the crystal contains three Cu(II) centers, and the bond lengths are reported for the square planar geometry as the average and standard variation of two independent bond measurements. There

is only one Cu(II) center with square pyramidal geometry and its inner sphere bond lengths have also been presented. 217
Table 5.5: The inner coordination sphere bond lengths for Cu(H_2L8) “kinetic” are reported as the average and standard deviation for two bond measurements at the square pyramidal metal centers. The bond lengths for the square planar chelate monomer has been reported with the error of the X-ray measurement. 222
Table 5.6: The inner coordination sphere bond lengths for Cu(H_2L8) “thermodynamic”. The square pyramidal bond lengths have been reported as the average and standard deviation of two independent measurements in the asymmetric unit. The square planar bond lengths have been reported with the error of the X-ray measurement. 227
Table 5.7: Bond lengths for the inner coordination sphere of Cu(H_2L9) “kinetic” as well as carbonyl bonds that make up the tridentate chelate ring. The asymmetric unit of the crystal contains three Cu(II) centers, and the bond lengths are reported for the square pyramidal geometry as the average and standard variation of two independent bond measurements. There is only one Cu(II) center with square planar geometry and its inner sphere bond lengths have also been presented....233
Table 5.8: Bond lengths that make up the inner coordination sphere for Cu(H_2L9) “thermodynamic”. The bond lengths have been reported with the standard deviation of the X-ray measurement. 239
Table 5.9: The inner coordination sphere bond lengths for CuL10 have been reported as the average of three measurements at each metal center that describes the asymmetric unit. The bond lengths for the axially coordinated ligands have been reported with the standard deviation of the X-ray measurement. 244
Table 5.10: CSD results upon submission of the search query. The aryl substitution positions have been labelled on the query structure. Reference codes highlighted in green represent structures that possess H-bond donors on the chelate. 252
Table 5.11: Crystal data, refinement details, and structural aspects for metallocycles CuL5, Cu(H_2L6), and Cu(H_2L8) “kinetic”. The metal centers are reported as “4×5CN 2×4CN” which is read as “four 5-coordinate geometry and two 4-coordinate geometry”. 257
Table 5.12: Crystal data, refinement details, and structural aspects for metallocycles Cu(H_2L8) “thermodynamic”, Cu(H_2L9), and CuL10. The metal centers are reported as “4×5CN 2×4CN” which is read as “four 5-coordinate geometry and two 4-coordinate geometry”. 257

Abbreviations

cHex	Cyclohexane
CSD	Cambridge Structural Database
DCM	Dichloromethane
DMF	Dimethylformamide
DMSO	Dimethyl sulfoxide
Et_2O	Diethyl ether
Et_3N	Triethylamine
EtOAc	Ethyl acetate
EtOH	Ethanol
FTIR	Fourier Transform Infrared
GSH	Glutathione
HEPES	4-(2-hydroxyethyl)-1-piperazineethanesulfonic acid
HTVS	High-Throughput Virtual Screening
iPrOH	Isopropanol
MD	Molecular Dynamics
MeCN	Acetonitrile
MeOH	Methanol
MOF	Metal-organic framework
MOPS	3-morpholinopropane-1-sulfonic acid
MS	Mass Spectrometry
NMR	Nuclear Magnetic Resonance
PBS	Phosphate Buffer Saline
PTFE	Polytetrafluoroethylene
PTSA	p-Toluenesulfonic acid
PVDF	Polyvinylidene difluoride
TA	Tris-acetate
TBS	Tris-buffered saline
THF	Tetrahydrofuran
XRD	X-ray Diffraction

Chapter 1

Introduction

1. Medicinal Inorganic Chemistry

1.1 Advantages of the Metal Ion

Medicinal bioinorganic chemistry considers the effect of metal ions and metal complexes on biological systems with a special focus on therapeutic relief from diseased states. Metals have been used to treat disease since antiquity and these metal ions still provide advantages in modern medicine. Metals may act as Lewis acids or bases that interact directly with target molecules to form coordination complexes embedded in protein scaffolds, the protein host environment then defines a second outer-coordination sphere for the metal complex. The diverse stereochemistry and variable coordination numbers of metal complexes allow them to specifically target 3D pharmacophores.[1] This allows more diverse binding modes when compared to organic molecules. The binding geometry of organic molecules is determined by the sp, sp^2, and sp^3 hybridization of carbon, while the geometry of metals spans square planar, square pyramidal, octahedral, and even more complex geometries when coordination numbers exceed six. In addition to the unique geometries of metals, the coordinated ligands will still display binding based on the principles of hybridization.

The pharmacological properties of bioactive organic molecules may be improved by metal ion coordination, metal complexes of organic drugs often display better solubility, lipophilicity, and specificity, and overcome challenges of acquired drug resistance.[2] The specificity of metallodrugs can be attributed to their targeted activation in biological systems and changes in pH may facilitate ligand exchange to produce the bioactive metal complex at the target site. Additionally, variable redox environments of the cell may activate the metallodrugs upon reduction or oxidation, promoting highly specific activity in different cellular environments. The redox chemistry of metal complexes is an attractive avenue for producing novel therapeutic effects by mechanisms of action unavailable to fundamentally drab organic molecules.

The tuneable oxidation states of metal complexes allow them to mimic metalloenzymes and carry out catalytic redox activity[3]. Various redox couples are accessible under physiological conditions[4], such as the Fe^{III}/Fe^{II}, Cu^{II}/Cu^{I}, Mn^{III}/Mn^{II}, and Ru^{III}/Ru^{II} redox couple. This redox

chemistry allows the generation of reactive oxygen species (ROS) in specific target organelles and provides therapeutic relief by modulating the cellular redox equilibrium which ultimately results in the apoptosis of cancerous cells or the death of parasites.[5] The stereoelectronic properties of the metal may be fine-tuned for desirable bioactivity. The synergistic effects of σ- and π-bonding allow ligands to be tailored such that the reactivity of the metal complex is modulated. This allows the lability of coordinated ligands to be controlled such that desirable ligand exchange is achieved at the target site, or alternatively, that the metal complex is inert under biological conditions. Finally, radionuclides are common for metals and thus provide additional mechanisms of action.[6] Metallodrugs may be synthesized with radioactive isotopes that emit ionizing radiation at the target which provides a therapeutic effect by destroying malignant cells. Today, the bestselling radio imaging agents that specifically target diseased cells are metal-based. The advantages of the metal ion in medicinal chemistry are reflected in Figure 1.1

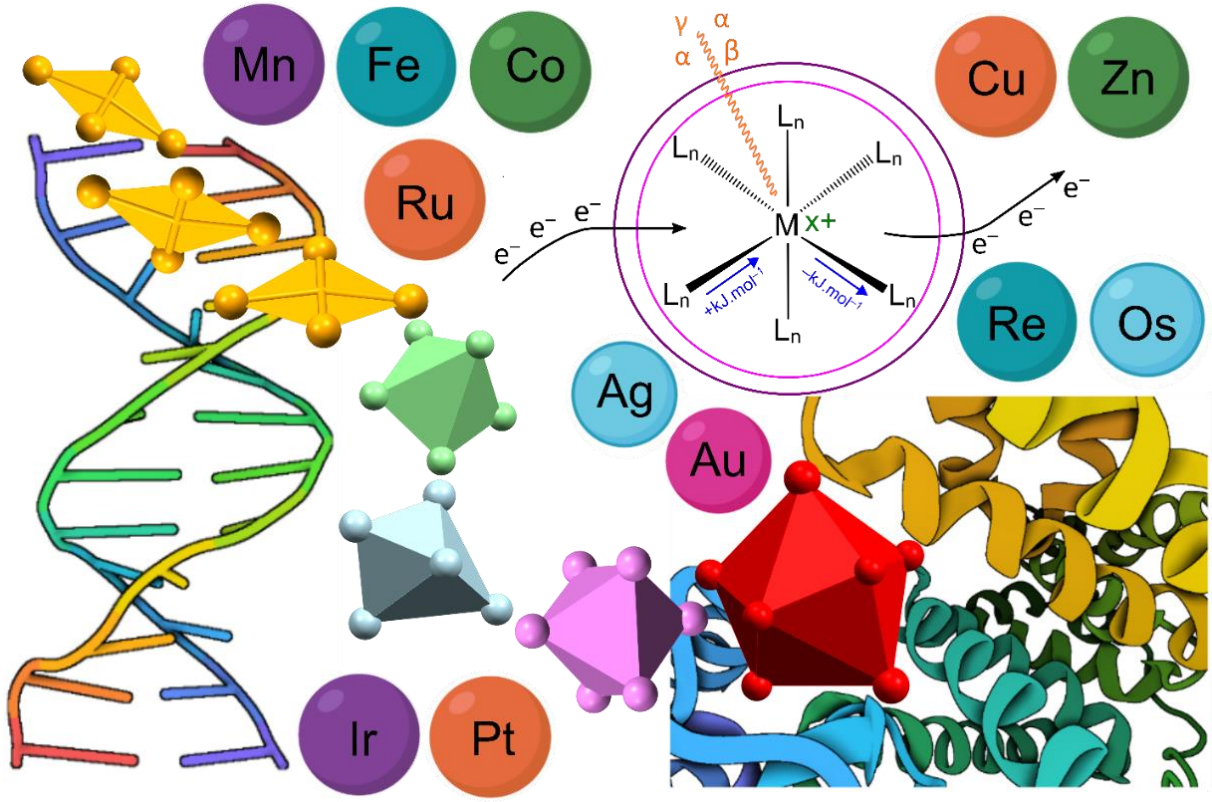


Figure 1.1: The advantages of the metal ion. From square planar metal complexes that bind DNA, to yet undiscovered coordination compounds that fill the 3D pharmacophore of protein targets. Numerous oxidation states are available to the metal that facilitate versatile redox chemistry. The bond strengths of ligands may be controlled by stereoelectronic effects allowing fine-tuned reactivity of the bioactive metal complex. Outer coordination-sphere chemistry is available upon metal-protein complex formation.

1.2 Metallodrugs

The present review will focus on some metallodrugs that are currently sold on the pharmaceutical market or are presently in active clinical trials. These compounds serve to emphasize the exciting possibilities that metallodrugs have to offer based on the unique chemistry of the metal ion. Then, we will turn our attention to antiviral metal complexes- the main focus of this work.

1.2.1 Platinum

TriplatinNC is a DNA-binding ligand with anticancer properties.[7] The metallodrug consists of three cationic square planar Pt(II) centres tethered together through amino alkyl chains with the formula $[\{trans\text{-}Pt(NH_3)_2(NH_2(CH_2)_6(NH_3^+)\}_2\text{-}\mu\text{-}\{trans\text{-}Pt(NH_3)_2\text{-}(NH_2(CH_2)_6NH_2)_2\}]^{8+}$. The high cationic charge on the complex allows targeted delivery to cancer cells with a high dependence on inorganic cations. The metallodrug is able to wrap around the DNA phosphate backbone acting as a clamp that prevents nuclear processes such as replication and transcription. TriplatinNC surrounds the DNA and tightly binds through electrostatic interactions between the cationic Pt(II) centres and anionic phosphates of the DNA backbone. The crystal structure[8] of TriplatinNC bound to DNA is shown in Figure 1.2.

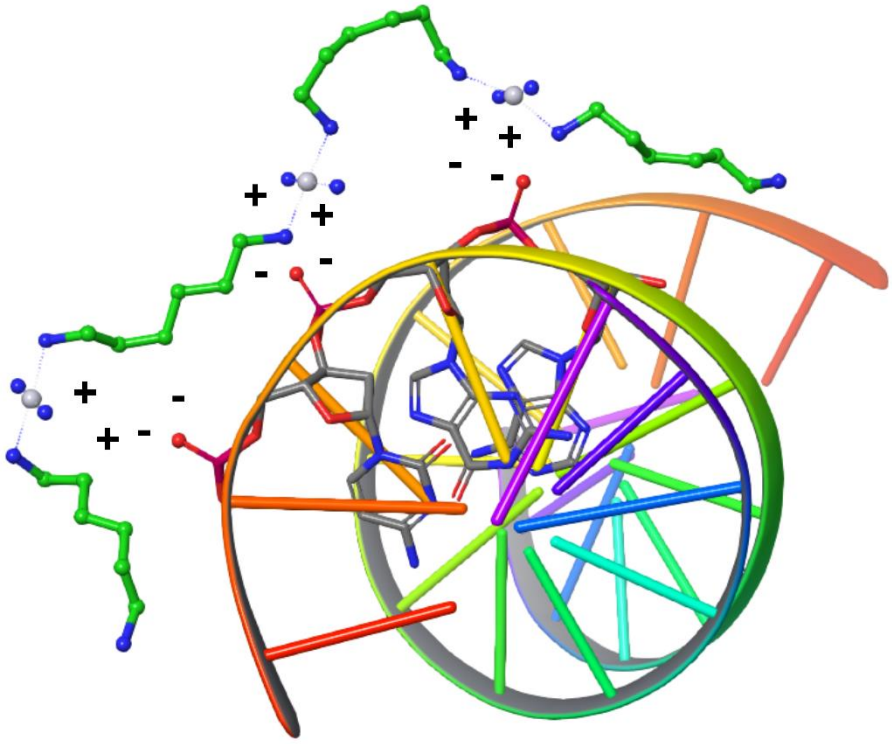


Figure 1.2: The X-ray crystal structure of TriplatinNC bound to dsDNA. The metallodrug binds the DNA phosphate backbone through electrostatic forces thereby disrupting replication and repair processes. Ligand carbons shown in green, nitrogen blue, and platinum grey.

Platinum-based drugs like TriplatinNC commonly target DNA, and the anticancer agent Satraplatin is no different. Satraplatin[9] is a third-generation platinum complex that provides efficacy against drug-resistant cancers and has unique pharmacological properties compared to the first-generation metallodrug-superstar, Cisplatin. Satraplatin is an octahedral Pt(IV) complex with lower reactivity than Pt(II) compounds which improves the therapeutic index by lessening toxic side effects.

Satraplatin acts as a prodrug that requires activation by reduction to the Pt(II) square planar complex. The reducing environment of hypoxic cancer cells activates the complex and releases the axially coordinated ligands; these released ligands may be bioactive which provides dual mechanistic therapeutic action. Upon reduction of Satraplatin to the square planar Pt(II) complex, nucleophilic attack of guanine on the metal centre can take place. The DNA base becomes covalently bonded to Pt(II) which results in intra- and inter-strand crosslinks that inhibit DNA replication and repair machinery. The mechanism of action for Satraplatin is shown in Figure 1.3.

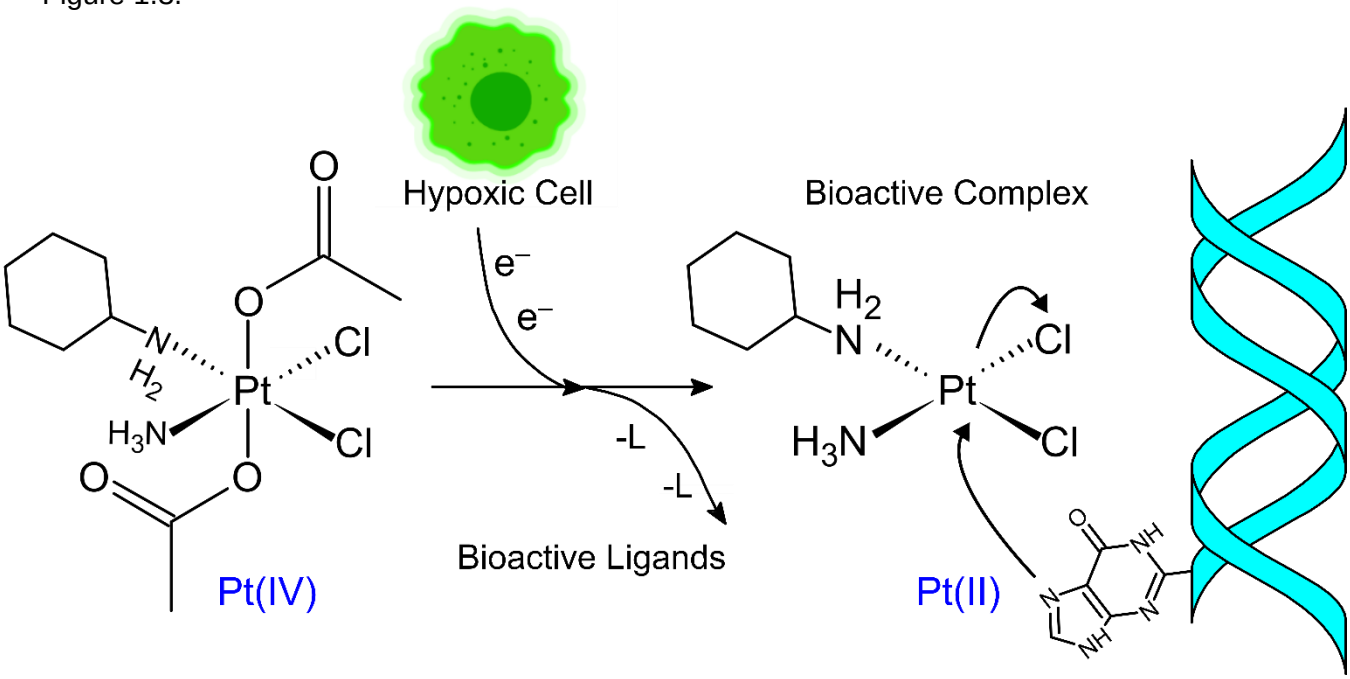


Figure 1.3: The octahedral Pt(IV) metallodrug Satraplatin. The complex is reduced to square planar Pt(II) in hypoxic environments, releasing potentially bioactive ligands for dual mechanistic action. The nucleobase guanine then attacks the metal centre, displacing chloride and becoming covalently linked to the metallodrug.

1.2.2 Gold

Auranofin is currently sold on the pharmaceutical market to treat arthritis.[10] The metallodrug contains the linear Au(I) ion which is instrumental to the drugs' mechanism of action. Au(I) has a high affinity for selenium and sulphur and this promotes substitution reactions with selenocysteine residues found in Thioredoxin Reductase (TrxR). This enzyme is overexpressed in inflamed joint tissues which causes pain due to redox stress in the cells. Auranofin inhibits ThxR by covalently binding a selenocysteine residue in the active site of the enzyme, thereby providing therapeutic relief. The gold-based metallodrug has since found other medicinal applications, such as the treatment of bilharzia.[11] The disease is caused by a parasitic worm called *Schistosoma mansoni* which relies on the cysteine-containing enzyme Thioredoxin-Glutathione Reductase (TGR) for detoxification of ROS. Auranofin serves as a delivery vehicle for the Au(I) ion, transporting the metal to the active site of TGR where cysteine residues bind the metal and displace the coordinated ligand. The enzyme becomes inhibited and ROS accumulate in the worm resulting in death of the parasite. The crystal structure[11] of Au(I) bound to the active site of TGR is presented in Figure 1.4.

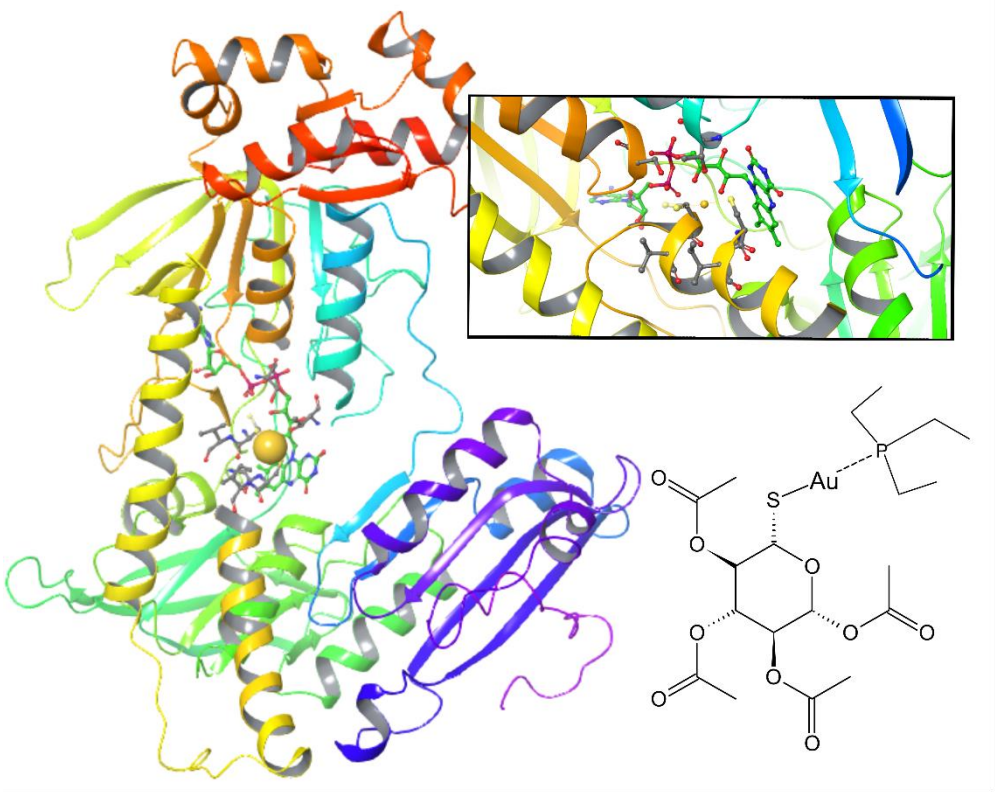


Figure 1.4: The chemical structure of Auranofin is shown, the metallodrug serves as a delivery vehicle for the Au(I) ion. The crystal structure of Au(I) bound to the active site of TGR is shown. The Au(I) ion inhibits the enzyme by preventing the reducing action of the flavin in the active site.

While gold-based metallodrugs typically target cysteine thiols to form metal-sulfur bonds, AuMesoIX[12] is unique because the gold ion activates the ligand for nucleophilic attack. AuMesoIX is a Au(III) mesoporphyrin IX that exhibits anticancer activity by targeting thiol-containing enzymes such as thioredoxin, peroxiredoxin, and deubiquitinases. The inhibition of these enzymes results in oxidative stress and accumulation of ubiquitinated proteins which ultimately results in death of the cancerous cells.

The Au(III) cation increases the electrophilicity of the porphyrin which allows nucleophilic attack of a thiol at the *meso* position on the macrocycle. Thiol-dependent enzymes are essential for cancerous cell survival, and inhibition of these enzymes results in an uncontrolled redox environment for the malignant cells. AuMesoIX highlights how the susceptibility of organic ligands can be fine-tuned for desirable reactivity in biological systems. AuMesoIX has a cationic charge under physiological conditions which may facilitate binding to the target protein by electrostatic forces and Lewis acid-base interactions. The reaction mechanism[12] of AuMesoIX has been shown in Figure 1.5.

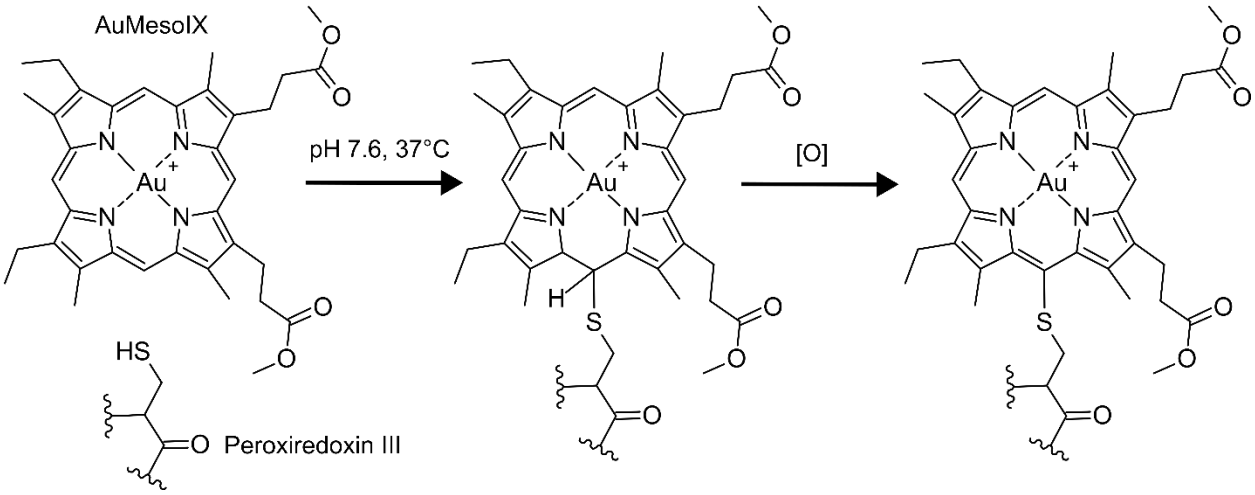


Figure 1.5: The chemical structure of AuMesoIX and its reaction with thiol-containing enzymes. The cysteine residue of Peroxiredoxin III found in the active site of the enzyme has been shown to covalently bind AuMesoIX under physiological conditions. The Au(III) ion increases the electrophilicity of the *meso* carbon, allowing nucleophilic attack by the thiol. The cysteine-porphyrin adduct is then easily oxidized to re-establish the electronic conjugation that extends throughout the macrocycle.

1.2.3 Ruthenium

Organic ligands that are known to be bioactive may be complexed with metals to modulate activity and overcome drug resistance. One such example is the indolocarbazole ruthenium complex[13] which will be referred to herein as Ru-Staurosporine. The complex was synthesized from the lead compound Staurosporine[14] which was already known to show anticancer activity by inhibition of protein kinases. The organic ligand is an ATP-mimetic that inhibits Glycogen Synthase Kinase 3 (GSK-3) and prevents cancer cell proliferation.

Upon complexation with Ru(II), the compound Ru-Staurosporine shows improved affinity, specificity, and activity in comparison to the free ligand. Ru-Staurosporine is a selective inhibitor of GSK-3 in the low-nanomolar range and inhibits cell proliferation in the pancreatic cancer model. It is suggested that the GSK-3 binding site is the same for Staurosporine and Ru-Staurosporine, and the improved activity of the metallodrug is due to modulated pharmacological properties. The crystal structure[14] of Staurosporine bound to the active site of GSK-3 is shown in Figure 1.6 and alongside is the Ru-Staurosporine metallodrug structure.

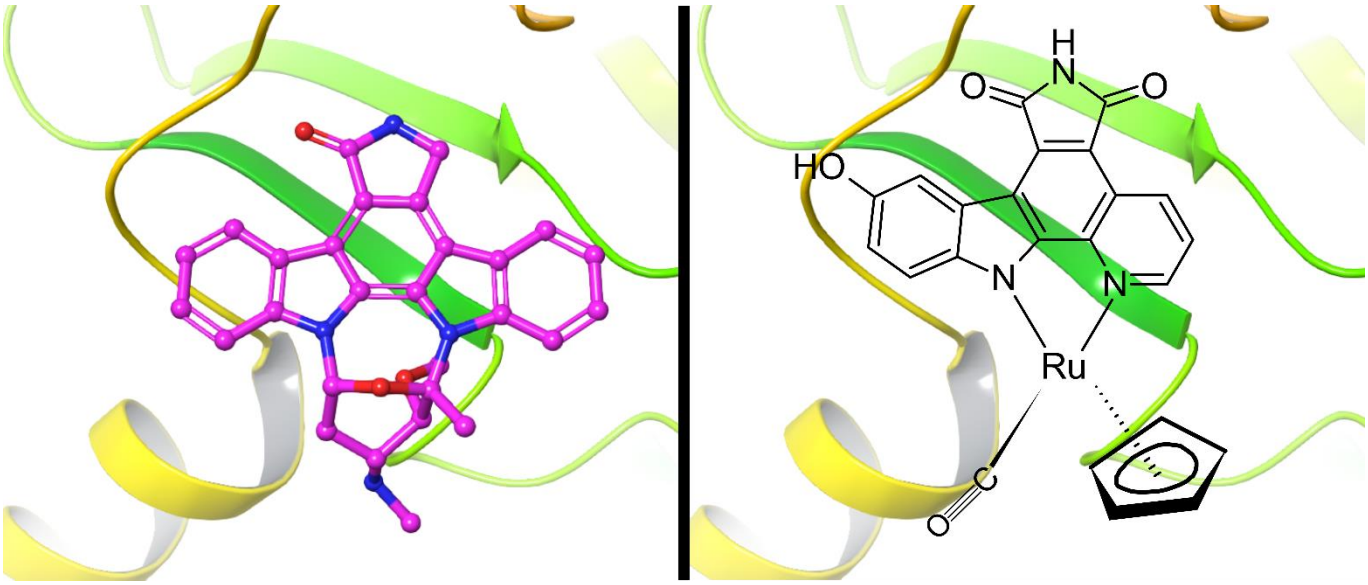


Figure 1.6: The X-ray structure of Staurosporine bound to the active site of GSK-3. The metallodrug Ru-Staurosporine targets the same protein kinase with improved specificity and activity. ATP-mimetics need to be highly specific for cancer proliferating proteins as off-target effects are common. While the indolocarbazole moiety is mostly the same between drugs, the Ru(II) ion can fill the 3D space of the active site to form a coordination sphere involving the protein residues.

While Ru-Staurosporine takes advantage of lead organic molecules that have proved to be effective anticancer agents, RM175[15] is a completely novel metallodrug candidate. RM175 is a half-sandwich Ru(II) complex that exhibits anticancer properties by binding DNA in drug-resistant cancer cells. The rate of hydrolysis for RM175 can be modulated by substituting the monodentate anionic ligand with the rate increasing in the order $N_3^- < I^- < Br^- \approx Cl^-$.[16] By fine-tuning the rate of hydrolysis and controlling the rate of ligand substitution, the metallodrug can more effectively target cancer cells thus improving the therapeutic index.

The monocationic RM175 complex enters the cytoplasm of cancerous cells where hydrolysis is activated by a lower concentration of chloride ions, resulting in the hydrated complex with a charge of 2+. The $RM175^{2+}$ complex is then reduced to $RM175^{+}$ by intracellular glutathione (GSH) where the tripeptide displaces the aqua ligand and becomes coordinated. The RM175-GSH complex is stable under physiological conditions which is important because GSH reduction is a cellular defence strategy against xenobiotics. The Ru(II) complex then permeates the nuclear membrane so that it may interact with DNA in the nucleus. Once RM175 has entered the nucleus, nucleophilic attack of guanine at the metal centre displaces GSH to form a covalent bond between Ru(II) and the nucleobase. The DNA-metal adduct is then unable to undergo transcription and replication, thereby resulting in apoptosis of the malignant cells. The structure of RM175 and the mechanism of action have been presented in Figure 1.7.

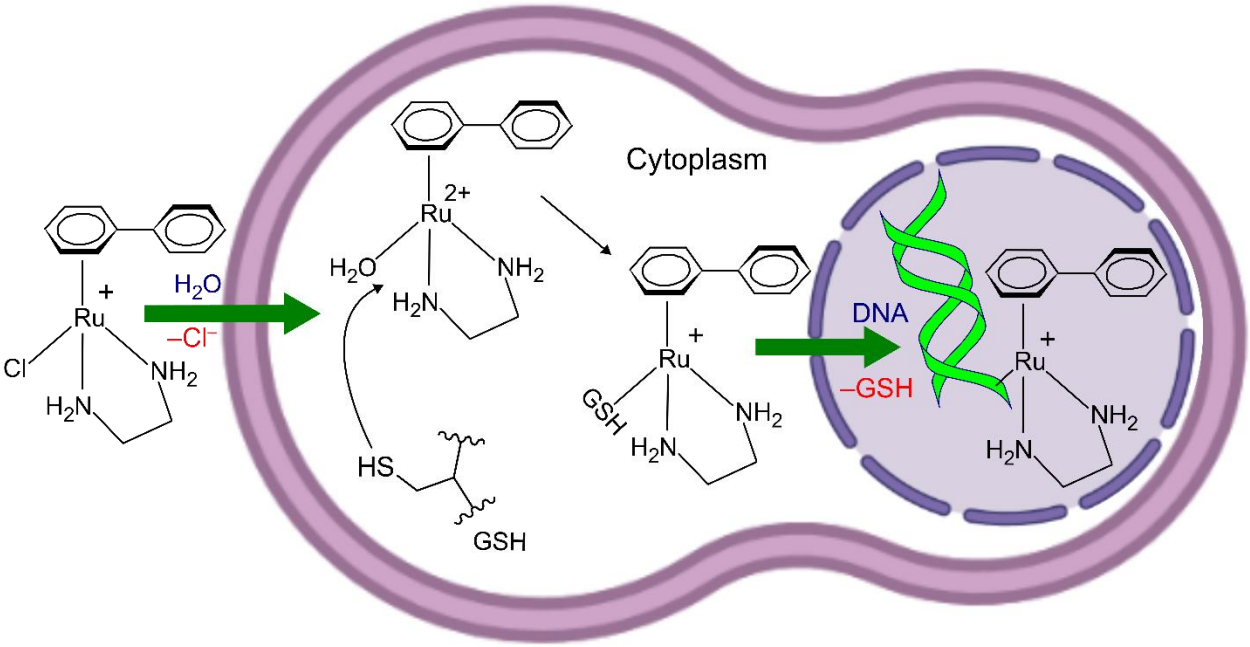


Figure 1.7: The chemical structure of RM175 and the metallodrug mechanism of action.

1.2.4 Iron

Sodium nitroprusside[17] (SNP) is an octahedral Fe(II) complex currently sold on the pharmaceutical market as a vasodilator used in cardiac surgery and in cases of hypertensive crisis. SNP is administered to the bloodstream where it interacts with thiol groups on erythrocytes and serum albumins resulting in the concomitant release of nitric oxide (NO) into the blood. NO is an endothelium relaxing factor that inhibits cellular contraction thereby reducing blood pressure. This has been presented in Figure 1.8.

The controlled release of bioactive ligands from metal complexes is an exciting strategy for drug development, and SNP is not the only iron-containing candidate to do so. Sanguinate[18] is a PEGylated carboxyhaemoglobin that is being used to treat sickle cell disease and during cardiopulmonary bypass surgery. The therapeutic action of Sanguinate is due to the release of carbon monoxide (CO) that is coordinated to the iron centre of the haemoglobin derivative. Sanguinate is also able to effectively deliver oxygen to hypoxic tissues during periods of hemodilution.

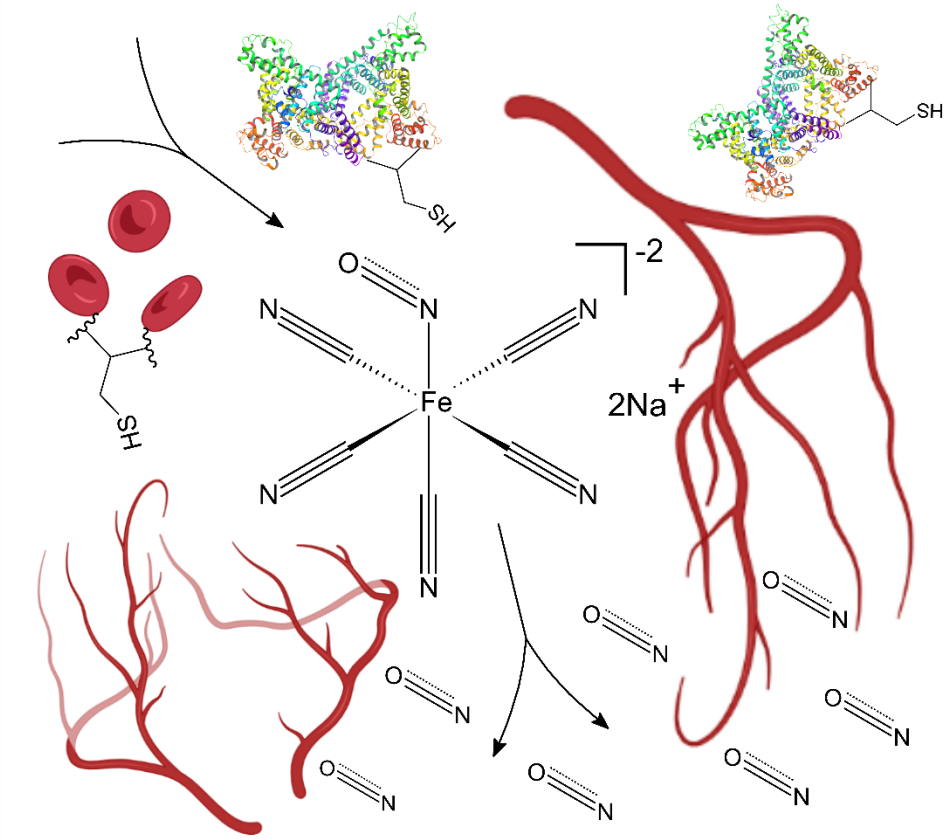


Figure 1.8: The structure of sodium nitroprusside and its interaction with thiol groups of erythrocytes and albumins in the bloodstream. The release of NO from SNP results in vasodilation and reduced blood pressure.

Finally, we present an iron-based metallodrug currently in clinical trials that takes advantage of a lead organic molecule and modules the activity through a dual mechanistic approach. Ferroquine[19] is an Fe(II) analogue of chloroquine which is being investigated due to its increased activity compared to the organic molecule. Chloroquine was previously used to treat malaria caused by the blood-feeding parasite *Plasmodium falciparum* which accumulates heme as a result of its nutrient source. Chloroquine interacts with Fe(II) heme and prevents the formation of Fe(III) hemozoin crystals.[20] The parasite is unable to regulate the concentration of toxic free Fe(II) heme when chloroquine prevents the formation of microcrystalline Fe(III) hematin, resulting in death of the hematophagous protozoa. However, chloroquine resistance has become prevalent and Ferroquine provides an effective new strategy as shown in Figure 1.9. In addition to the inhibition of hemozoin formation, Ferroquine produces ROS in acidic and oxidizing environments through the perturbation of the Fe^{III}/Fe^{II} redox couple. Ferroquine shows a reversible one-electron redox reaction in the digestive vacuole of the parasite, resulting in the generation of hydroxyl radicals that cause lipid peroxidation and death of the protozoa. Hence, Ferroquine affects its therapeutic actions through the dual action of inhibition of hemozoin formation and generation of ROS. Ultimately, the metallodrug is a better candidate because it is more selective, more active, and has better pharmacological properties such as lipophilicity.

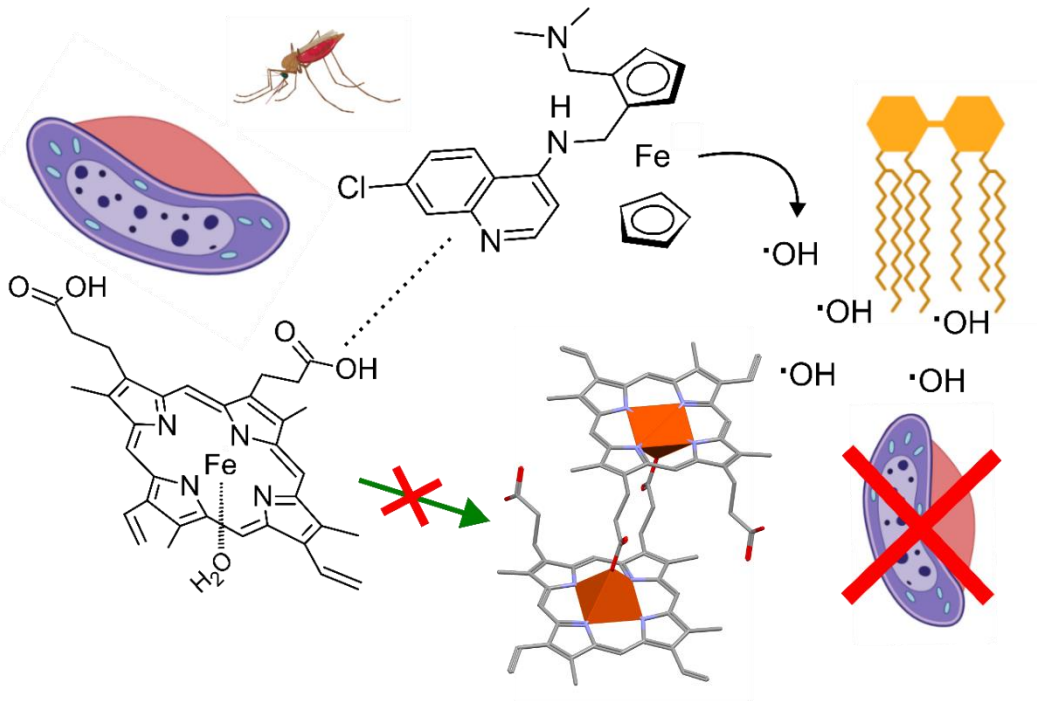


Figure 1.9: The dual mechanistic action of Ferroquine prevents the formation of Fe(III) hematin crystals and generates ROS causing lipid peroxidation in the digestive vacuole of *Plasmodium falciparum*.

1.3 Antiviral Metal Complexes

We now turn our attention to metal complexes as potential antiviral agents. This current work aims to prove the concept that bioavailable metal ion complexes may be used to specifically target certain protein residues and potentially function as antiviral membrane fusion inhibitors. Hence, we look at some metal complexes that have already shown therapeutic activity against various viruses.

$Au(bnpy)Cl_2$ is an organometallic Au(III) chelate that shows potential antiviral activity by inhibiting zinc finger (ZnF) proteins of the human immunodeficiency virus (HIV). The Au(III) complex inhibits the ZnF HIV nucleocapsid protein 7 (NCp7) as a result of a C–S aryl transfer reaction.[21] The HIV ZnF NCp7 is a metalloprotein that contains the Zn(II) ion which functions to stabilise the protein conformation as well as enhance RNA affinity. HIV NCp7 contains nucleic acid binding domains with metallocentres that are highly conserved among retroviruses and inhibition of NCp7 results in disruption of RNA- and membrane-binding processes as well as reverse transcription.[22] Hence, the HIV ZnFs are suitable therapeutic targets for metallodrugs such as $Au(bnpy)Cl_2$. The cyclometalated Au(III) compound inhibits NCp7 through a mechanism of ligand replacement and reductive elimination which results in Zn(II) ion displacement. The process of inhibition begins upon nucleophilic attack of Cys on the Au(III) centre and concomitant replacement of chloride. Then S-arylation occurs between Cys and Au(bnpy)Cl which results in reductive elimination of Au(I) and displacement of Zn(II). This results in a covalent linkage between NCp7 and the benzylpyridine ligand, leaving the metalloprotein inactive. The mechanism of NCp7 ZnF inhibition by $Au(bnpy)Cl_2$ is shown in Figure 1.10.

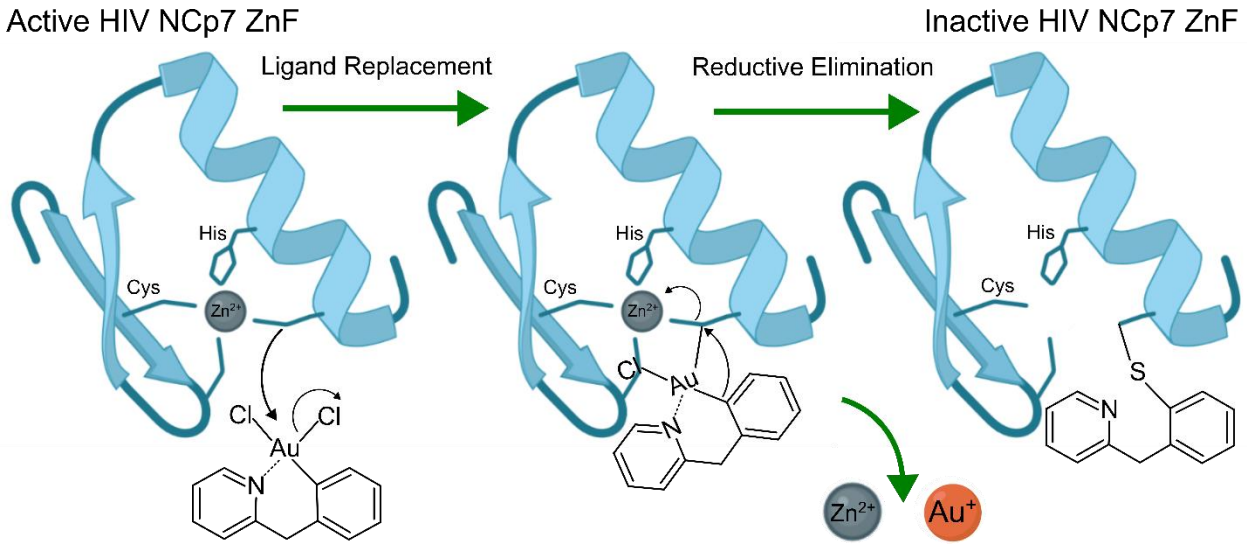


Figure 1.10: The mechanism of HIV NCp7 ZnF inhibition by $Au(bnpy)Cl_2$.

Another metallodrug shown to inhibit HIV NCp7 ZnF proteins by Zn(II) ion displacement is Doxovir. The octahedral Co(III) complex inhibits HIV NCp7 as the metallodrug targets histidine residues of the ZnF.[23] The histidine residues of the ZnF substitute axially coordinated 2-methylimidazole from Doxovir, and upon coordination, the native Zn(II) ion is displaced thereby inhibiting the viral protein. Although Doxovir has shown antiviral potential against HIV, it has been more recently explored for the treatment of herpes viruses.[24]

Herpes simplex virus 1 (HSV-1) was unable to enter human cells when treated with Doxovir and this effect was independent of the virion envelope glycoproteins (gC and gD) as well as surface cell receptors such as herpesvirus entry mediator receptors HveA and HveC.[24] The Co(III) complex was found not to affect the attachment of HSV-1 to host cells, but it does inhibit entry, suggesting that the inhibition takes effect after viral attachment but before protein synthesis.[22] Furthermore, Doxovir was able to non-specifically inhibit cell-entry of herpes viruses such as varicella-zoster virus, cytomegalovirus, and Epstein-Barr virus, suggesting that Doxovir targets a common cellular mechanism required for infection by these enveloped viruses.[24] Hence, Doxovir is a lead metallodrug candidate for a nonspecific broad-spectrum fusion inhibitor of enveloped viruses with a mechanism of action that prevents cell entry and is independent of host cellular receptors. The structure of Doxovir is presented in Figure 1.11.

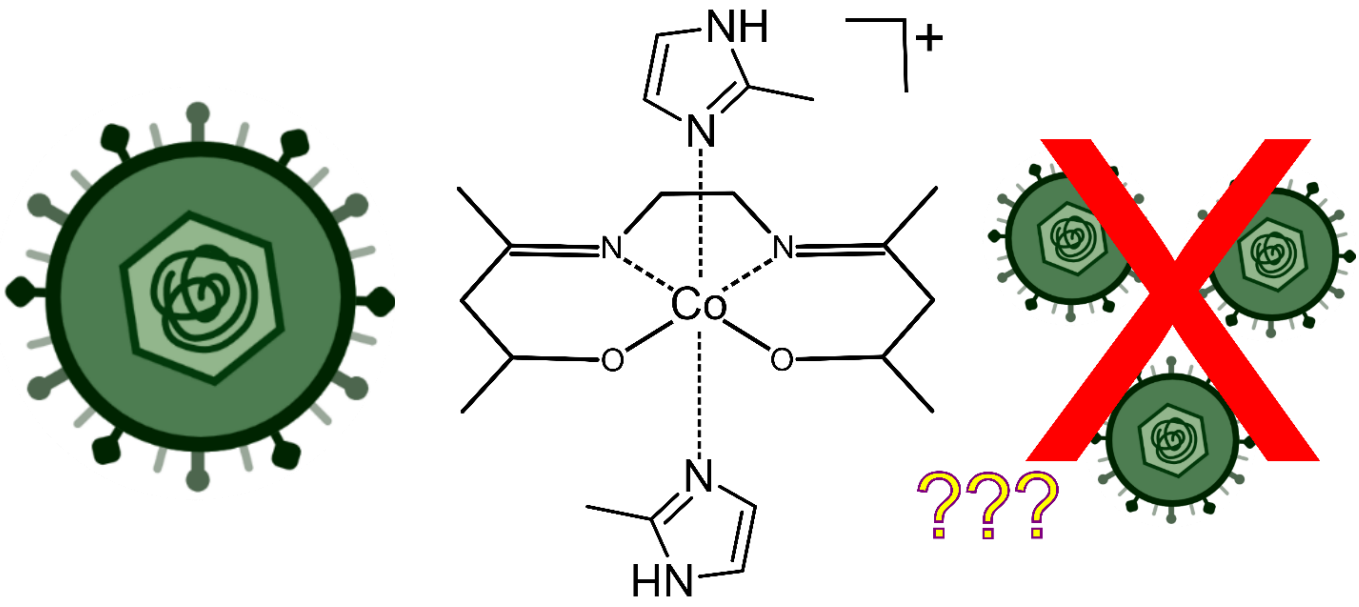


Figure 1.11: The structure of Doxovir, a lead antiviral metallodrug candidate. Doxovir shows broad-spectrum inhibition of enveloped viruses such as HSV and acts in a post-attachment phase of infection. The Co(III) complex prevents cell-to-cell infection of herpes viruses, but its exact mechanism of action has not yet been delineated.

The seasonal flu caused by influenza viruses results in between 300 000 and 600 000 deaths every year.[25] It is thus important to develop therapeutics that target influenza viruses and modifying lead organic molecules with metal ions has shown promise in the development of novel antivirals. Compounds such as amantadine (AMT) have shown antiviral activity against influenza by blocking the Matrix-2 (M2) proton channel at the viral membrane.[26] The disruption of proton equilibrium in the virus impedes membrane uncoating mechanisms which result in inhibition of viral replication.[22] However, mutations of the influenza M2 protein have decreased the efficacy of channel blockers such as amantadine.

The development of tripodal Cu(II) complexes such as copper adamantyl iminodiacetate, Cu(AMT-IDA), have shown efficacy in overcoming amantadine-resistant influenza.[27] The Cu(AMT-IDA) metallodrug candidate is effective against at least three influenza strains, more effective than AMT and less toxic than $CuCl_2$.[28] Importantly, the copper complex effectively blocks the M2 channel of amantadine-resistant influenza possessing the S31N mutation. Cu(AMT-IDA) does not block the influenza M2 channel possessing the site-directed H37A mutation, suggesting that His coordination to Cu(II) is required for effective blockage.[28] The H37 cluster of the M2 channel protein is highly conserved among influenza strains and hence represents a suitable therapeutic target for broad-spectrum antiviral activity. The M2 channel, H37 cluster, and Cu(AMT-IDA) have been shown in Figure 1.12.

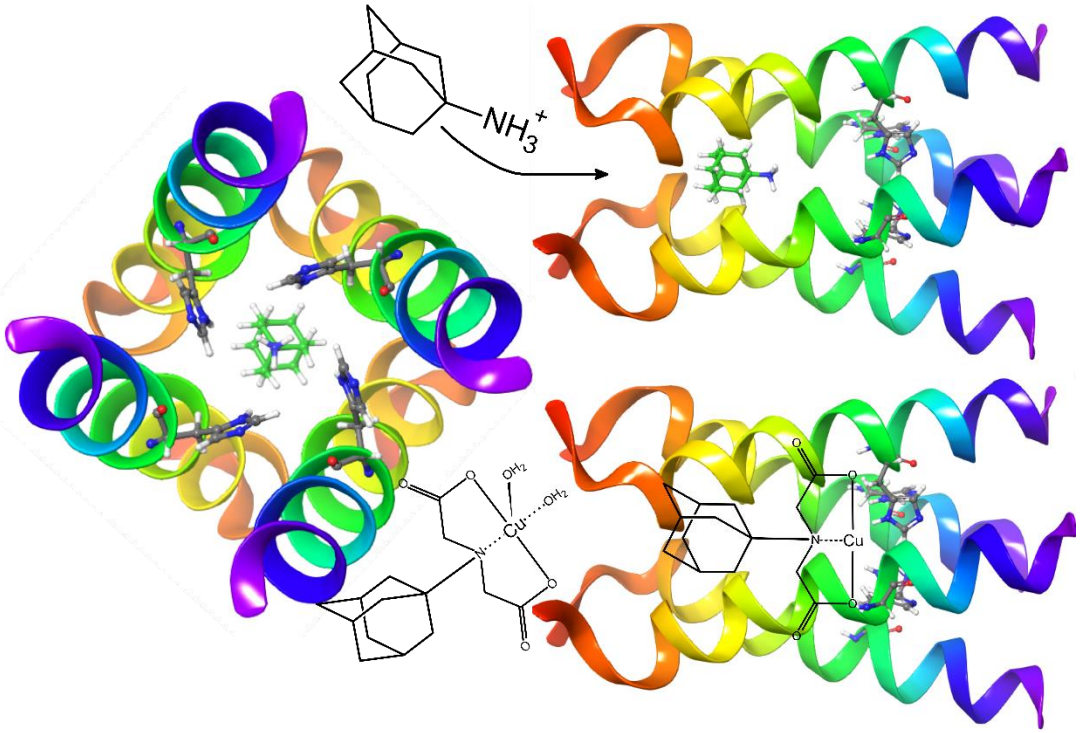


Figure 1.12: The crystal structure of the influenza M2 channel blocked by AMT. The Cu(II) derivative is shown to block the channel by coordinating at the H37 cluster.

Having looked at metal complexes that target HIV, herpes, and influenza viruses, we now turn our attention to the severe acute respiratory syndrome coronavirus 2, SARS-CoV-2. The focus of the current work is to develop metal chelates that inhibit SARS-CoV-2 replication by preventing membrane fusion events. Already, bioavailable metal ions such as Zn(II) have shown therapeutic potential by inhibiting the SARS-CoV-2 main protease, Mpro.[22] The Mpro is responsible for maturation of viral proteins as the enzyme cleaves peptide bonds of polyproteins, a process required for replication of the coronavirus. The active site of Mpro comprises of a catalytic dyad, where Cys145 acts as a nucleophile attacking the peptide bond of the polyprotein substrate, and H41 acts as a base to abstract the thiol proton thereby facilitating nucleophilic attack.[29]

It has recently been shown that various Zn(II) salts on the market, such as chloride, acetate, and glycinate zinc salts, inhibit SARS-CoV-2 Mpro with nanomolar affinity.[30] $ZnCl_2$ produced an IC_{50} value of 398 nM with complete inhibition of Mpro at 6.25 μM. The crystal structure of Zn(II) bound to the catalytic dyad of Mpro was solved and provides insight into the mechanism of inhibition.[30] The Zn(II) ion occupies the active site of Mpro, bound to Cys145 and His41 with two water molecules making up the tetrahedral coordination sphere. The catalytic dyad is inactivated upon metal ion coordination because the Zn(II) ion is tightly bound to the catalytic nucleophile. Zinc is readily transported into host cells by zinc importer proteins (ZIP)[31] and because the Mpro is highly conserved among coronaviruses, this serves as a viable option in the treatment of COVID-19.

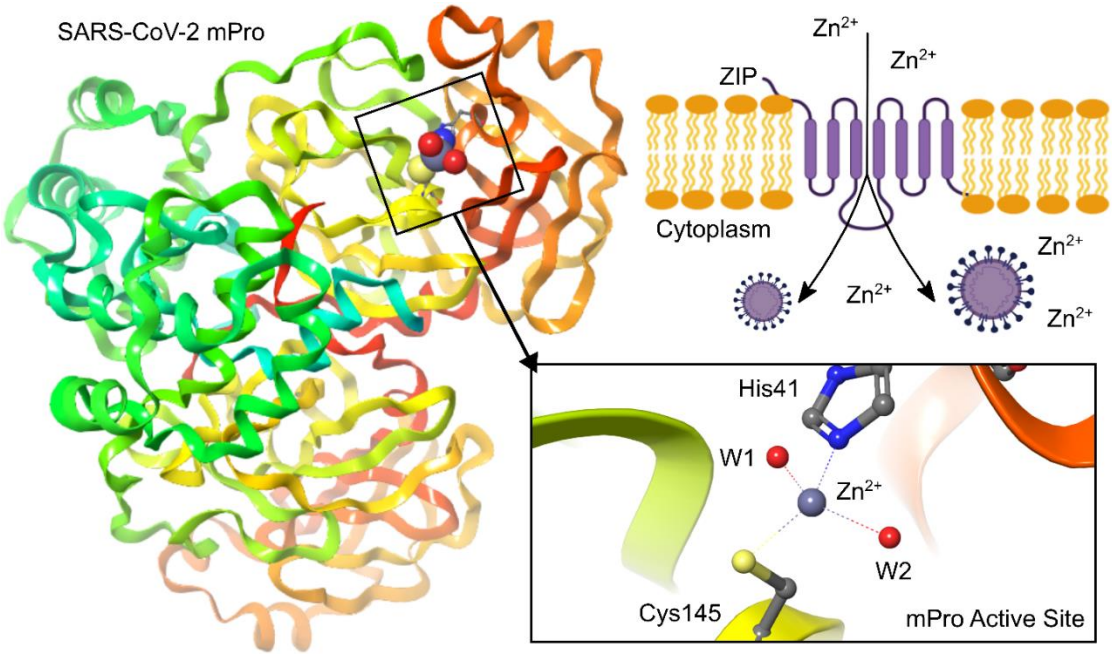


Figure 1.13: The crystal structure of Zn(II) bound to the catalytic dyad of SARS-CoV-2 Mpro.

2. Metal Pincers

The focus of this current work is to develop NNN amide metal pincers that target SARS-CoV-2 so that they may potentially act as antiviral fusion inhibitors. So, what is a pincer? A pincer is a tridentate ligand that chelates to three adjacent coplanar sites on the metal centre that results in two five-membered metallocyclic rings but sometimes a six-membered ring.[32] Metal pincers have mostly been used in homogenous catalysis because the versatility of the ligands allows fine-tuned modulation of the stereoelectronic properties of the complex. These complexes are diverse with types of ligands including NCN, CNC, PCP, PNP, SNS, PCN, and ONS and metal ions including Ti(IV), Fe(II), Co(III), Ni(II), Cu(II), Ru(III), Pd(II), and Ir(III).[32]

While NNN amide metal pincers have not yet been studied in the field of medicinal chemistry, pincers of Cu(II)[33] as well as Fe(III), Co(II), and Ni(II)[34] have recently been studied for their antimicrobial properties. There is also a lack of research focus on the antiviral efficacy of these compounds. However, extensive research has been carried out on the anticancer activity of these tridentate metal complexes.[35] We will look at some NNN pincers of Au(III), Pd(II), and Cu(II) and their anticancer efficacy. These compounds have been collated in Table 1.1.

Au(III) NNN pincer compounds **1** and **2** show relevant cytotoxicity against human ovarian A2780 cancer cell line with **2** effective against cisplatin-resistant A2780/R cells in the submicromolar range.[36] Compounds **1** and **2** both show a direct interaction between DNA and Au(III), with the ligand of **1** being completely inactive against the cancer cell lines. However, the ligand of **2** is as effective as the gold complex with an IC_{50} of 0.125 μM but **2** has a better selectivity index for resistant cells. Au(III) pincer **3** was shown to interact with DNA through H-bonding, van der Waals forces and π–π stacking and was active in the micromolar range against colon carcinoma LS-174, lung carcinoma A549 and skin melanoma A375.[37] Gold chelate **3** was more effective at inhibiting cancer growth than the ligand or cisplatin.

Au(III) pincers **4** to **9** are active in the low to moderate micromolar range against various cancer cell lines including cervical HeLa, liver HepG2, lung NCI-H460, breast MCF-7, neuronal SUNE1, and skin B16 cells.[38] The 2,6-bis(imidazol-2-yl)pyridine Au(III) series **4** to **7** are particularly effective against lung cancer cell lines and the efficacy of these compounds increases with increasing lipophilicity, exemplified in the poorer efficacy of **4**. The efficacy of **6** is dramatically improved for skin cancers upon introduction of lipophilic C_{16} chain compared to the methyl group of **4**. The 2,6-bis(benzimidazol-2-yl)pyridine Au(III) series **8** and **9** are not particularly more effective than the 2,6-bis(imidazol-2-yl)pyridine series but efficacy follows the same trend as

lipophilicity. These Au(III) NNN pincers accumulate in the cytoplasm and **6** was shown to inhibit the anticancer enzyme target TrxR with an IC_{50} value of 3.8 μM.[38]

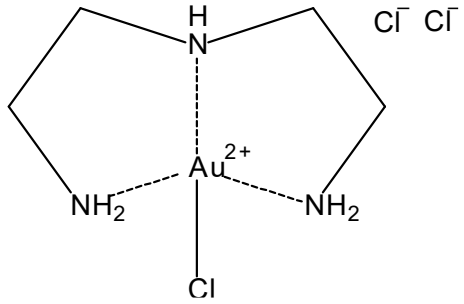
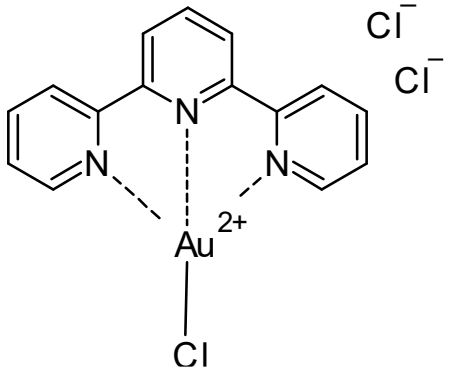
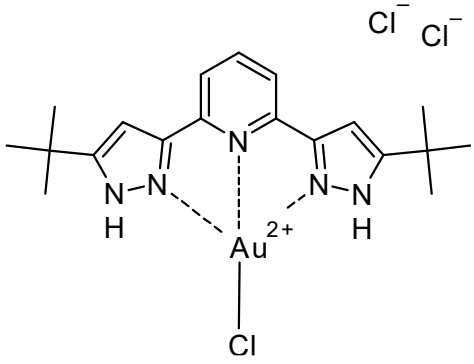
Pd(II) NNN pincers have also been investigated for their antitumor activity.[35] Palladium complexes **10** and **11** are particularly effective against breast cancer MCF-7 cell lines with IC_{50} values at about 4 μM.[39, 40, 41] Compound **10** inhibits normal Chinese hamster ovary (CHO) cells in the low micromolar range leading to unacceptable therapeutic indexes against lung A546 cancer and glioma C6 cancer. However, Pd(II) pincer **10** inhibits breast cancers MCF-7 and MDA-MB-231 below the inhibitory concentration of normal cells indicating that it may be used to treat mammary carcinomas.[39] Compound **11** shows impressive efficacy against numerous cell lines with particular inhibition of liver HepG2 and colorectal HT-29 cell lines. The Pd(II) pincer **11** readily binds serum albumin promising favourable pharmacokinetic properties and the chelate cleaves DNA by a hydrolytic mechanism suggesting this is the mode of cytotoxic action.[41]

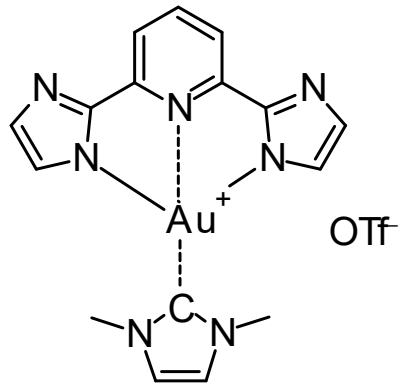
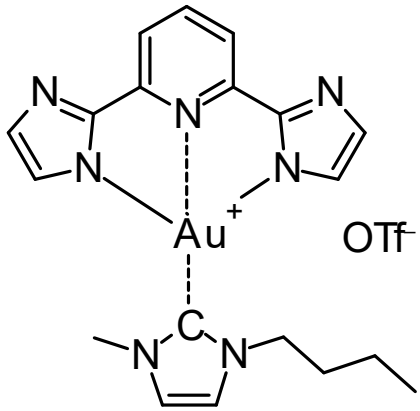
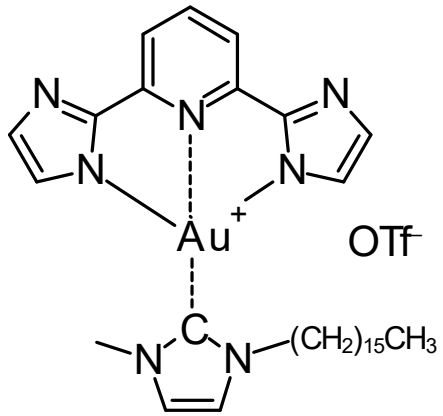
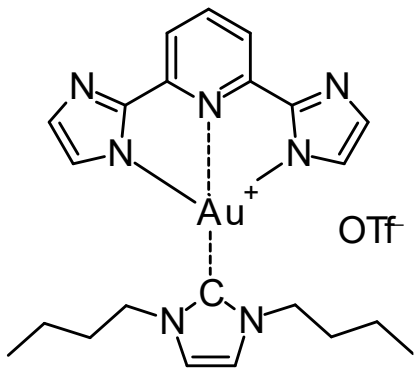
Cu(II) NNN pincers are also numerous and have been studied for their anticancer activity.[35] Compounds **12** to **14** were synthesised and analogues varied by the substitution of methoxy groups on the benzene ring. These Cu(II) NNN pincers showed good efficacy against cervical HeLa cells as well as liver cell lines HepG2 and BEL-7402 with compound **12** showing particular efficacy against HepG2 with an IC_{50} value of 2.72 μM.[42] The compounds were tested for DNA binding affinity and followed the order **13** > **12** > **14** which provided no correlation with HeLa cell inhibition. However, ROS generation of these compounds followed the order **14** > **12** > **13** which correlates with HeLa cell inhibition thus indicating that ROS generation is the cytotoxic mechanism of action against the malignant cells.

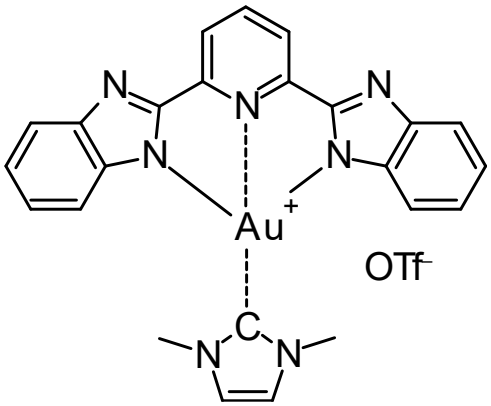
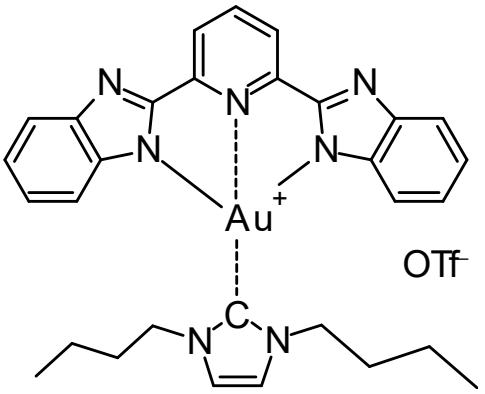
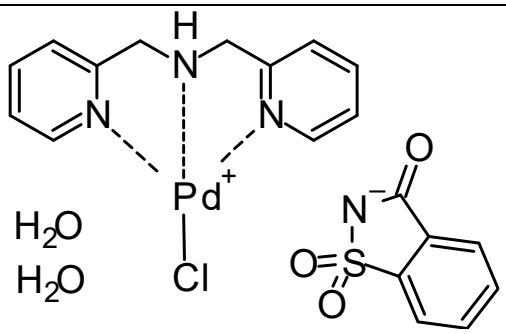
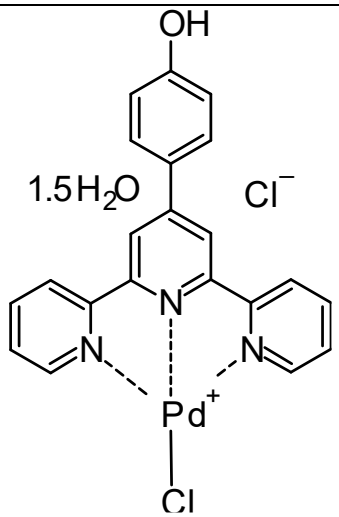
Cu(II) pincers **15** to **17** were synthesized and analogues varied by the substitution of furan, thiophene, and N-methylpyrrole groups. These functional group substitutions had drastic effects on the efficacy of the Cu(II) pincers against various cell lines.[43] The furan functionalized complex **15** was extremely potent against ovarian A2780 cells but analogues **16** and **17** produced no inhibitory effect. However, thiophene substituted **16** showed excellent activity against colorectal HCT116 cells with an IC_{50} value of 2.1 μM but produced no inhibitory effect on normal fibroblasts, indicating good selectivity and therapeutic index. Compound **16** was more effective against colorectal HCT116 and lung A549 cancer cell lines than **15** while compound **17** produced no inhibitory effect. This suggests that the molecular target donates a H-bond to the heteroatom of the five-membered substituent, as the sulfur atom of **16** is more basic than the oxygen atom of **15** and compound **17** cannot accept a H-bond because the heteroatom has been methylated. Hence, anticancer efficacy against A549 follows the order **16** > **15** > **17** and

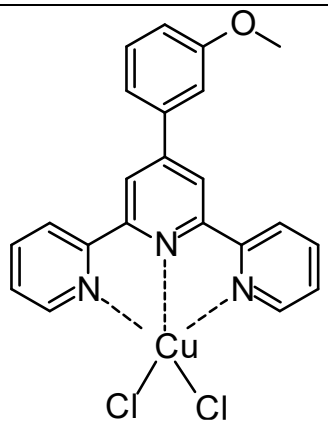
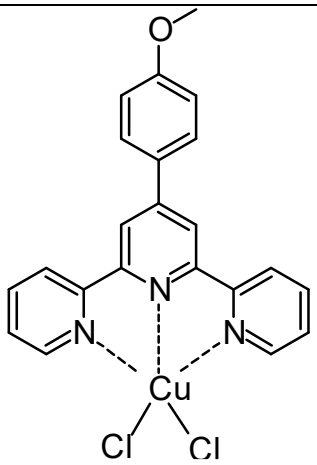
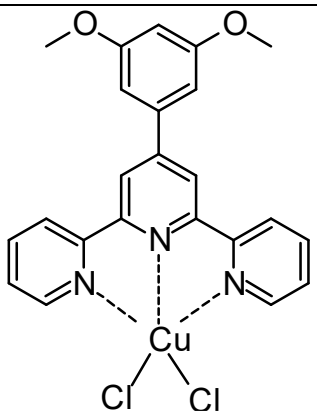
the basicity of the heteroatom follows the same order. Finally, trinuclear Cu(II) NNN pincer **18** was tested against several cancerous cell lines and was found to be more effective than cisplatin in all cases.[44] The Cu(II) pincer was found to completely cleave pUC19 plasmid DNA in 24 hours and the cleaving potency increased with an increasing number of metal centres. The planar terpyridine moiety of **18** was found to intercalate DNA while the Cu(II) bis-pyridyl arms interact with the groove and can produce superoxide ions that induce cleavage.[44] These NNN metal pincers have shown potential as therapeutic agents but interest is only recently gaining traction. There is a need to explore alternative antiviral, antimicrobial, and anticancer therapeutics and the metal pincer is a suitable candidate in the field of medicinal chemistry.

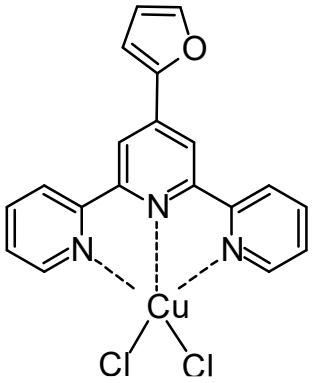
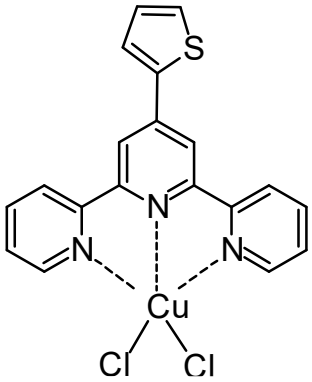
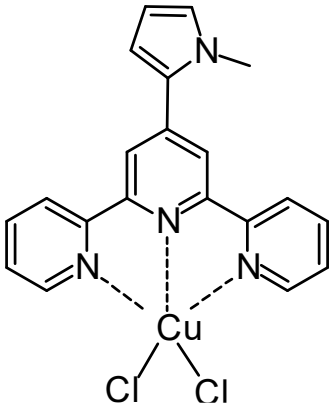
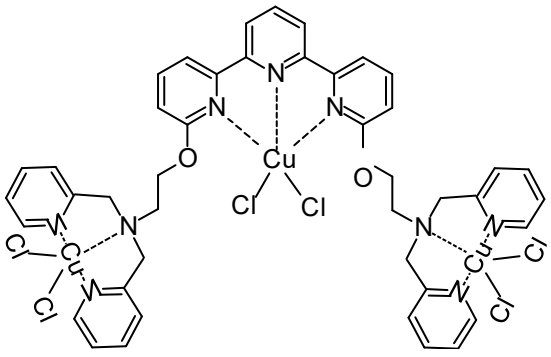
Table 1.1: NNN metal pincers and their inhibitory concentrations against various cancer cell lines. Cell cultures were incubated between 24 and 72 hours at 37°C with 5% CO_2.

NNN Metal Pincer	Entry	Cell Line	IC50
	**1**[36]	A2780/S A2780/R	8.2 ± 0.93 18.7 ± 2.16
	**2**[36]	A2780/S A2780/R	0.2 0.37 ± 0.032
	**3**[37]	LS-174 A549 A375	11.2 ± 1.6 20.1 ± 0.5 13.1 ± 2.0

	**4**[38]	HeLa HepG2 NCI-H460 MCF-7 SUNE1 B16	32.9 36.2 55.0 18.4 28.7 30.6
	**5**[38]	HeLa HepG2 NCI-H460 MCF-7 SUNE1 B16	16.5 33.2 11.0 17.2 9.9 5.0
	**6**[38]	HeLa HepG2 NCI-H460 MCF-7 SUNE1 B16	1.4 3.3 1.4 2.9 ND 2.2
	**7**[38]	HeLa HepG2 NCI-H460 MCF-7 SUNE1 B16	13.0 28.7 7.9 12.9 9.9 8.3

	**8**[38]	HeLa HepG2 NCI-H460 MCF-7 SUNE1 B16	14.4 18.0 11.2 11.9 11.2 12.4
	**9**[38]	HeLa HepG2 NCI-H460 MCF-7 SUNE1 B16	9.2 14.7 5.5 8.7 5.2 5.2
	**10**[39, 40]	A546[39] C6[39] CHO[39] MCF-7[40] MDA-MB-231[40]	23 43 12 3.9 4.2
	**11**[41]	HepG2 MCF-7 A549 HT-29 K562	3.20 ± 0.20 4.11 ± 0.50 6.84 ± 0.90 3.79 ± 0.12 9.47 ± 1.50

	**12**[42]	HeLa HepG2 BEL-7402	5.34 2.72 5.32
	**13**[42]	HeLa HepG2 BEL-7402	8.98 4.13 8.35
	**14**[42]	HeLa HepG2 BEL-7402	3.03 3.91 6.21

	**15**[43]	HCT116 A2780 A549 MCF-7 Fibroblast	17.3 ± 0.3 2.9 ± 0.1 20.5 ± 0.2 43 ± 0.2 59.5 ± 0.5
	**16**[43]	HCT116 A2780 A549 MCF-7 Fibroblast	2.1 ± 0.1 >100 4.2 ± 0.2 >100 >100
	**17**[43]	HCT116 A2780 A549 MCF-7 Fibroblast	>100 >100 >100 >100 >100
	**18**[44]	U2OS HEK298T GMO5757 SH-SY5Y MOLT-4	25 ± 6 26 ± 9 22 ± 9 23 ± 4 23 ± 3

3. SARS-CoV-2 & COVID-19

On the 31st of December 2019, intelligence operations at the World Health Organisation picked up a media statement from Wuhan, China, reporting cases of a novel “viral pneumonia”. Within 2 weeks, the first death was reported, and the genetic sequence of the RNA virus was made publicly available. Then by 11th March 2020, the WHO declared a Public Health Emergency of International Concern and stated that SARS-CoV-2 transmission had resulted in a global pandemic.[45] The world stopped breathing – global lockdown collapsed trade, crippled economies, and the rapid dissemination of the virus overwhelmed healthcare systems resulting in unprecedented deaths by suffocation. In the short space of 3 years, over 750 million people have been infected with SARS-CoV-2 and over 6.8 million people have died from COVID-19.[46] The rapid dying of so many elderly people resulted in a decrease of the global life expectancy with 28 million excess years of life lost in 2020.[47]

This massive death toll may have been reduced had broad-spectrum antiviral agents already been approved for medical use. It is important to develop a chemical arsenal that doctors may use in the front-line fight against novel and existing diseases. In addition to the humanitarian life-saving potential of such a universal antiviral drug, there is also incredible financial-earning potential of pharmaceuticals during a pandemic. Figure 1.14 shows how the stock prices at various biopharmaceutical companies increased over the worst period of the COVID-19 pandemic.[48] Companies such as Moderna that focused on COVID-19 and vaccine development showed the highest percentage increase in stock prices, while larger pharmaceutical manufacturers like Pfizer showed smaller increases in stock prices because production pipelines across the industry were affected by the global lockdown. This coronavirus crisis is not the last[49], and hence it is important to develop broad-spectrum therapeutics so that we are poised for the next pandemic. The life-saving and fiscal-earning potential of a universal antiviral agent during the next global pandemic can be realized if we begin development today.

Let us begin by looking at SARS-CoV-2 biology and pathology. Severe acute respiratory syndrome coronavirus 2 (SARS-CoV-2) is the infectious agent that causes coronavirus disease 19 (COVID-19). The cognate host cell receptor for SARS-CoV-2 is the human angiotensin-converting enzyme 2 (ACE2) which is expressed on the surface of epithelial cells in the respiratory and intestinal tracts. The virus is mainly transmitted through respiratory droplets that expose new hosts to the infectious agent. The human nasal and oral tissues expressing ACE2 are colonized by SARS-CoV-2 and COVID-19 symptoms begin to show in as little as two days after viral exposure.[50] The lung is the primary tropism of SARS-CoV-2 and infection may

progress to diseased states of severe pneumonia and eventually multiorgan dysfunction which ultimately results in death by COVID-19.

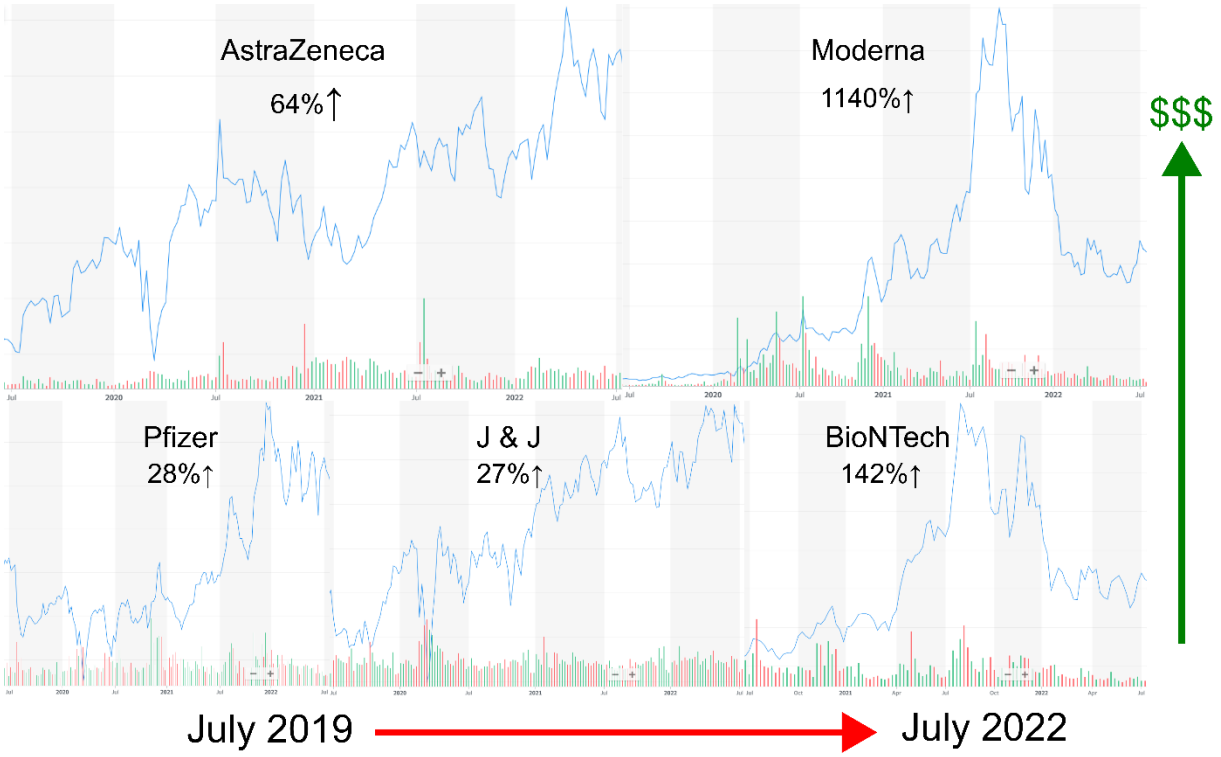


Figure 1.14: The stock price in US dollars of major biopharmaceutical companies over the worst period of the COVID-19 pandemic. Companies that focused on vaccine development saw the largest percentage increase in their stock prices with incredible investment during vaccine roll-out. Moderna showed an astonishing 1140% increase in stock value compared to the pre-pandemic market. The larger "Big Pharma" players such as Pfizer and Johnson & Johnson did not see such steep percentage increases because the relative investment has less impact on the evaluation of the company and demand for shares. In July 2022, Moderna and J&J were trading at $176.23 and $178.28 per share respectively.

SARS-CoV-2 is a +ssRNA envelope virus, the genome of which encodes four main structural proteins and 16 non-structural proteins (NSP), all of which represent molecular targets for drug design.[51] The most recognizable structural protein of CoV is the spike (S) which is an ectodomain homotrimeric glycoprotein where each S protein monomer consists of two subunits, S1 and S2. The S1 subunit makes up the "head" of the spike and contains the receptor binding domain (RBD) that recognizes human ACE2 as its cognate receptor. The S2 subunit makes up the "stalk" of the spike and contains the fusion peptide (FP) and heptad repeat (HR) domain that mediates the integration of viral and host cell membranes.[52]

There is a host-recognized furin cleavage site between S1 and S2 subunits that is processed by transmembrane serine protease 2 (TMPRSS2) expressed on the surface of host cells. This cleavage is crucial for membrane fusion events to occur and may be catalyzed by furin

expressed in the extracellular matrix resulting in rapid viral infection.[51] The S protein can evade the host immune response by displaying conformational heterogeneity as the RBD may be in either the “up” or “down” position. The RBD is the main epitope recognized by the host immune system and SARS-CoV-2 evades detection by keeping the RBD in the “down” position so that host immune systems cannot detect the epitope.[53] However, the RBD must be in the “up” position and solvent-exposed for binding ACE2.

The homodimeric membrane (M) protein is another structural protein encoded in the SARS-CoV-2 genome that is required for virion synthesis. The M protein is associated with other structural proteins, facilitating assembly of the virus and stabilizing the viral molecular architecture.[54] The envelope (E) protein is the smallest structural protein that consists of a homopentameric cation channel constructed from a five-helical bundle that surrounds a narrow pore. The E protein is involved with cation transport of ions such as calcium and the ion activity of the E protein contributes to virion assembly and maturation.[55] This E protein is homologous to the M2 channel protein of influenza and channel-blockers like AMT are potential chemotherapeutic agents against the novel CoV.

The fourth and final structural SARS-CoV-2 protein is the nucleocapsid (N) protein. The N protein is involved with structural organization of the viral RNA and packages the genetic material in a beads-on-a-string conformation.[51] The N protein organizes the viral genome, enhances viral transcription, and facilitates virion assembly. Nucleocapsid protein contains a U-shaped RNA-binding cleft that carries positive charge due to regularly distributed arginines and lysines which electrostatically attract the negatively charged phosphate backbone of the RNA.[56] Hence, the S, E, and N proteins represent suitable therapeutic targets and have been presented in Figure 1.15.

The life cycle of SARS-CoV-2 begins with the S protein-mediated viral attachment to host cells. ACE2 serves as the host cell receptor and is expressed on the surface of epithelial cells in the lung, intestine, heart, and kidney. The ubiquitous expression of ACE2 is an underlying contribution to the multi-organ pathogenesis observed upon viral infection.[57] Following the binding between the RBD and ACE2, the S protein undergoes cleavage at the S1/S2 furin cleavage site which is mediated by membrane-bound protease TMPRSS2.[51] Cleavage of the S protein subunits results in irreversible conformational changes which culminate in release of the S1 subunit and membrane fusion as the core of the spike penetrates the host membrane. Upon membrane fusion, viral uncoating occurs and the CoV genome is released into the cytosol

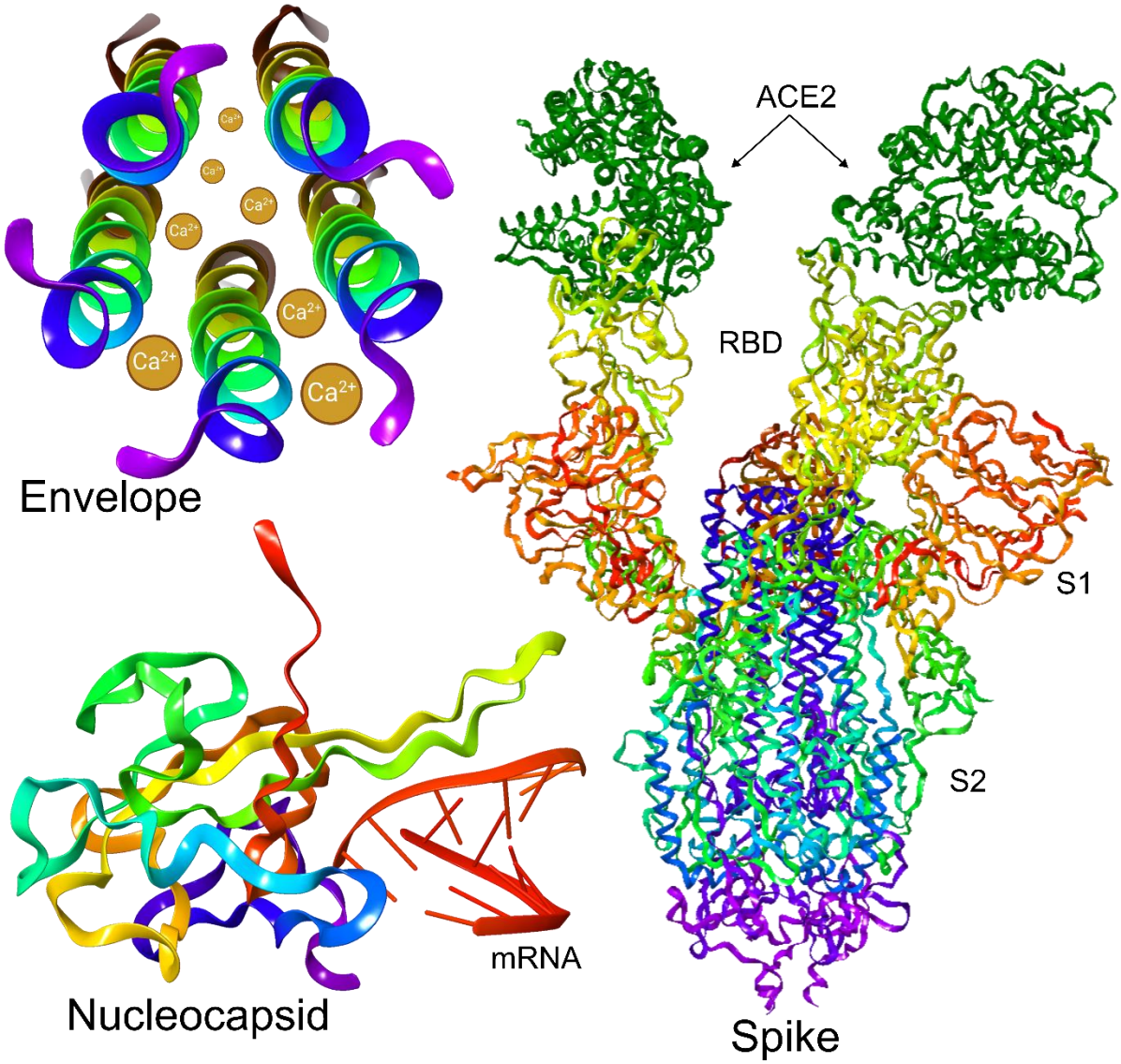


Figure 1.15: Some structural proteins of SARS-CoV-2 that represent suitable therapeutic targets. The E protein functions as an ion channel that may be inhibited by channel blockers such as AMT. The N protein is shown bound to mRNA and is instrumental to virion assembly, hence it serves as a suitable molecular target for vaccine and drug design. The S protein is shown with two RBDs in the "up" position and bound to the human ACE2 receptor.

where free host ribosomes recognize the +ssRNA and begin transcription of NSPs that arrange to form the replication-transcription complex (RTC) or simply, the replicase complex.[58] The RTC is required for expression of subgenomic RNA that codes for structural and accessory proteins which are translated by host ribosomes in the ER. After synthesis of S, E, and M proteins at the rough ER and the N protein by cytosolic ribosomes, the structural proteins undergo posttranslational modification.[51] The virion assembly then converges at the endoplasmic reticulum-Golgi intermediate compartment (ERGIC) where the M protein is instrumental to the construction of the viral architecture.

The M protein provides a scaffold by interaction with other structural proteins, such as S and E, thereby facilitating the molecular incorporation of these functional units. There are also M-N interactions which mediate nucleocapsid condensation and incorporation of the viral genome within the envelope.[51] The post-molecular assembly virions are then transported in smooth-walled vesicles to the plasma membrane via secretory pathways where the virus exits the host cell by exocytosis.[59] The viral progeny are then able to infect additional host cells, where the process begins again with S protein-mediated viral attachment as shown in Figure 1.16.

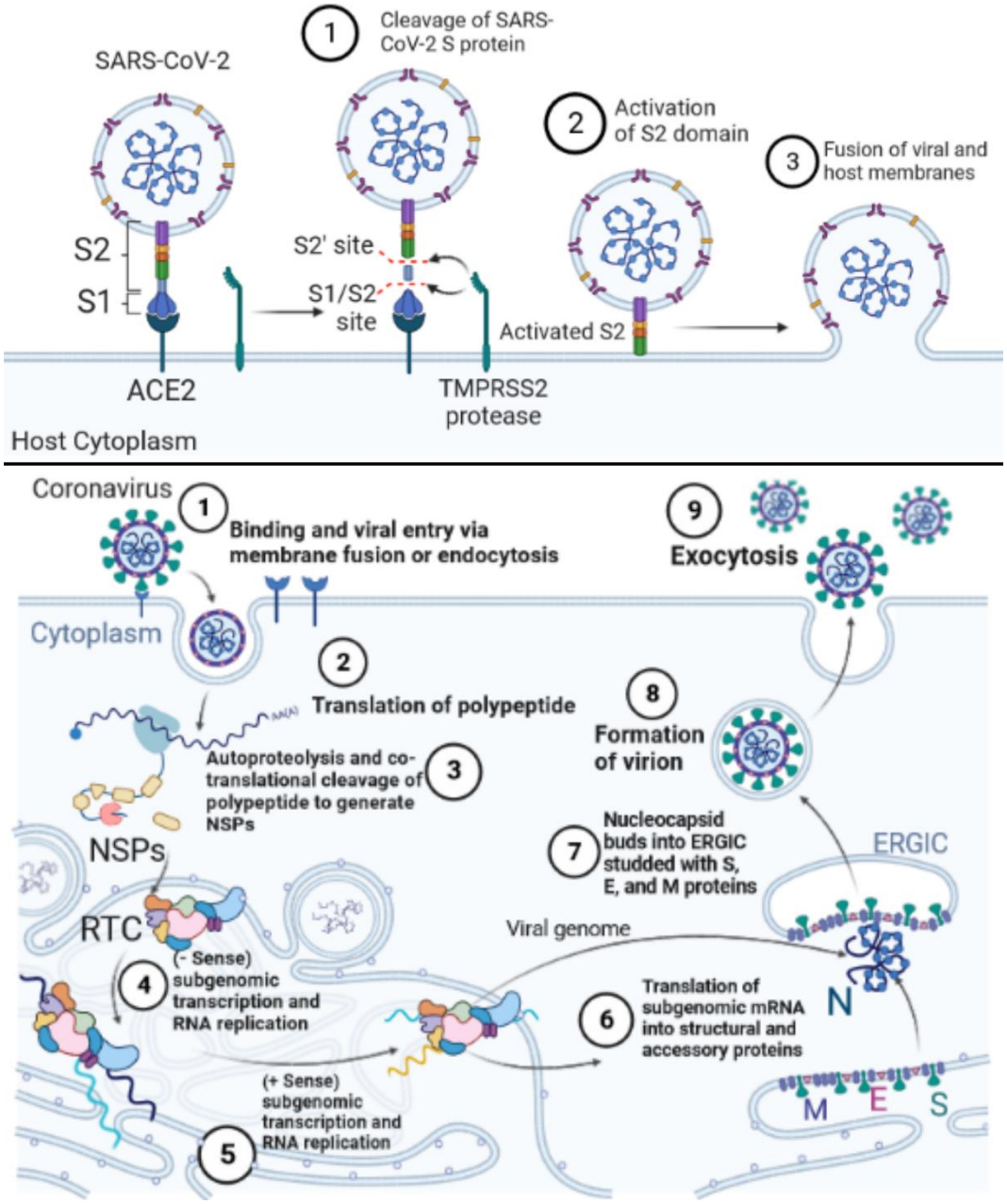


Figure 1.16: S protein-mediated viral attachment and the life cycle of SARS-CoV-2.

The S protein is instrumental to host infection and understanding the structural basis of ACE2 receptor recognition is crucial for the rational design of novel fusion inhibitors that target SARS-CoV-2.[60-61] The ACE2 receptor is bound at the peptidase domain which contains an α-helical coil that serves as a binding site when cradled within the concave receptor binding motif of the S protein. The bridge that forms when ACE2 is flanked against the RBD involves key interactions with 17 protein residues including four tyrosine residues.[61] These four tyrosine residues on SARS-CoV-2, Y449, Y453, Y489, and Y505, correspond to Y436, Y440, Y475, and Y491 on SARS-CoV, indicating that these residues are instrumental in orchestrating ACE2 binding as the CoVs show convergent evolution.[62, 61]

Additionally, evolution of new SARS-CoV-2 variants such as Delta[63] and Omicron[64] occurred over the course of the pandemic. These variants mostly harbour mutations in the S protein, bringing into question the suitability of this protein as a therapeutic target. However, because the tyrosine residues impart such favourable binding affinity between the RBD and ACE2, these residues are conserved among CoV variants. The crystal structures of wild-type (WT)[61], Delta[63], and Omicron[64] RBD bound to ACE2 are presented in Figure 1.17. The structural alignment of WT, Delta, and Omicron RBDs has 99% sequence identity and an RMSD of 0.72 Å. The tyrosine residues involved with ACE2 receptor recognition are identical for WT and Delta variants. The Omicron variant harbours the Y505H mutation as well as the N501Y mutation, the newly emerged Y501 is still involved with ACE2 recognition.

Hence, we propose the design of novel metal pincers that selectively target solvent-exposed tyrosine residues on the CoV RBD so that they may act as broad-spectrum fusion inhibitors. The disruption of key interactions between the RBD and ACE2 involving tyrosine is likely to thwart receptor recognition and prevent membrane fusion between host and virus. Already, fusion inhibitors involving therapeutic antibodies[65] and lipopeptides[66] have been shown to inhibit SARS-CoV-2 replication *in vitro*. We will design metal pincers with bioavailable metal ions such as copper, which has been shown to avidly bind tyrosine.[67,68] The copper-based metal pincer serves as a viable option for the development of a universal fusion inhibitor that targets solvent-exposed tyrosine residues on the CoV RBD.

The mechanism may involve disruption of RBD-ACE2 recognition, thereby preventing viral entry, or the RBD-bound metal pincer may prevent favourable ACE2 binding conformation and prevent cleavage and release of the S1 subunit. The metal pincer bound to the RBD may also prevent the “down” conformation, exposing the epitope to host immune response, or the Cu(II) pincer may generate radicals on the S protein surface via the Cu^{II}/Cu^{I} redox couple thereby

degrading the viral protein. Will the novel metal pincer be a suitable antiviral agent against SARS-CoV-2? The answer lies herein.

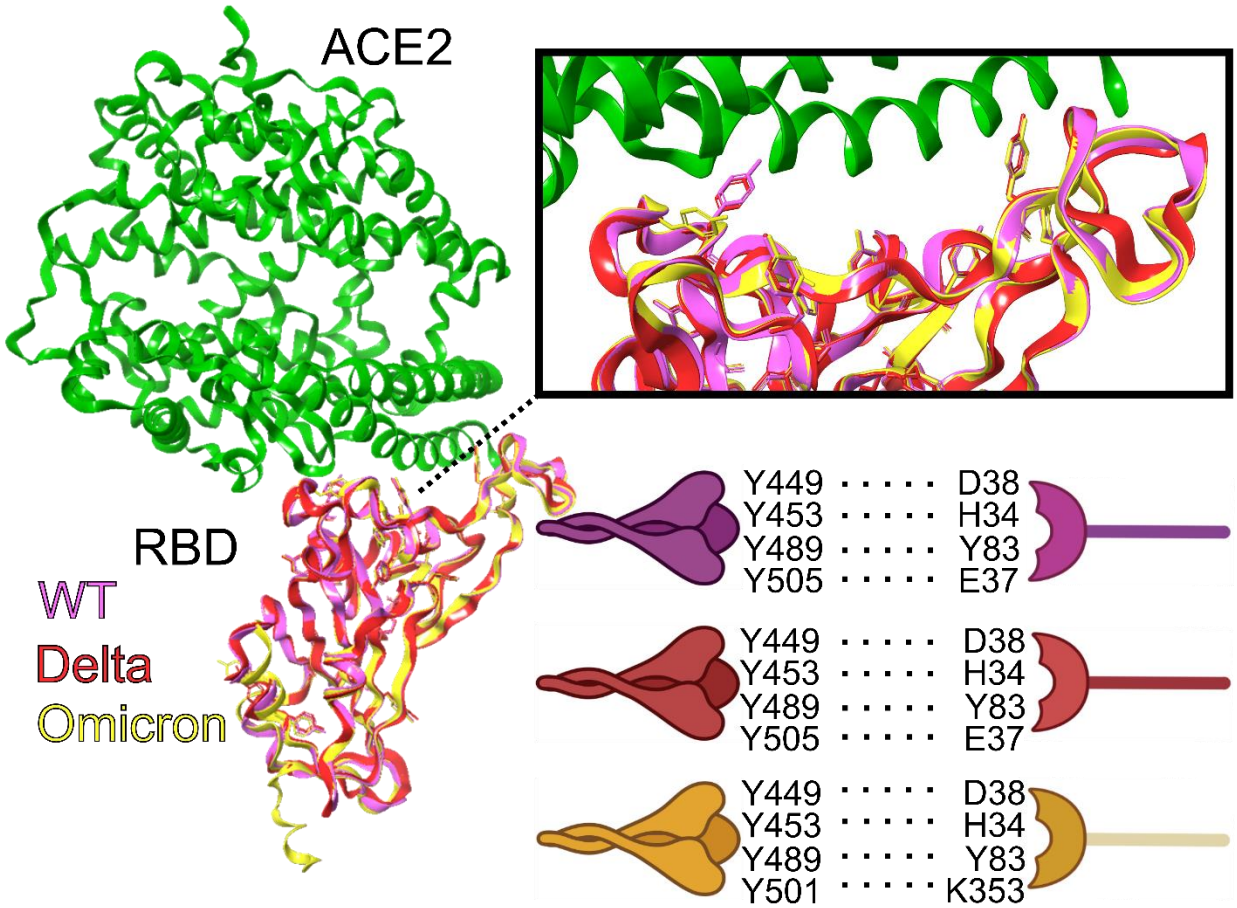


Figure 1.17: The structural alignment of WT, Delta, and Omicron RBDs bound to human ACE2. The tyrosine residues of the RBD have been conserved among CoVs indicating the importance of these contacts concerning ACE2 receptor recognition. The design of novel metallodrugs that specifically target the phenolic side chains of the RBD may result in the development of a universal fusion inhibitor that targets new and emerging CoVs.

4. Aims & Objectives

The core aims and objectives of the study are enumerated below:

1) Use computer-aided drug design simulations to develop novel metal chelates that specifically recognize tyrosine residues on the RBD involved with ACE2 receptor recognition. These residues are Y449, Y453, Y489, and Y505. The residues Y489 and Y505 are the most likely targets as these are more solvent-exposed and distal from the buried cleft of the RBD. The metal pincer ligand will have H-bond donors or acceptors that may facilitate additional interactions with the protein target. The *in silico* methods will be used to screen a large library of novel metal pincers to determine the optimal design of the pincer ligand. The library will then be scrutinized and synthetically feasible chelates chosen for development.
2) Chemically synthesize and fully characterize the novel NNN amide metal pincers by standard spectroscopic techniques.
3) Determine the binding affinity of the metal pincers for phenolic groups. We will use biomimetic models for the S protein, such as *p*-cresol which serves as a simple model for tyrosine. The binding affinity will also be determined for the hexapeptide epitope corresponding to Y505 on the RBD. We will then determine the binding affinity and residue targets between the metal pincers and the SARS-CoV-2 RBD Delta variant.
4) Collect high-resolution X-ray data for all novel chelates as well as attempt to grow crystals of the peptide and RBD in complex with the novel metallodrugs.
5) Determine *in vitro* efficacy of the fusion inhibitors against SARS-CoV-2 in a live virus cell culture.

5. References

(1) Morrison, C. N.; Prosser, K. E.; Stokes, R. W.; Cordes, A.; Metzler-Nolte, N.; Cohen, S. M. Expanding Medicinal Chemistry into 3D Space: Metallofragments as 3D Scaffolds for Fragment-Based Drug Discovery. *Chem. Sci.* **2020**, *11* (5), 1216–1225. https://doi.org/10.1039/C9SC05586J.

(2) Mjos, K. D.; Orvig, C. Metallodrugs in Medicinal Inorganic Chemistry. *Chem. Rev.* **2014**, *114* (8), 4540–4563. https://doi.org/10.1021/cr400460s.

(3) Alonso-de Castro, S.; Terenzi, A.; Gurruchaga-Pereda, J.; Salassa, L. Catalysis Concepts in Medicinal Inorganic Chemistry. *Chem. – Eur. J.* **2019**, *25* (27), 6651–6660. https://doi.org/10.1002/chem.201806341.

(4) Zhang, P.; Sadler, P. J. Redox-Active Metal Complexes for Anticancer Therapy. *Eur. J. Inorg. Chem.* **2017**, *2017* (12), 1541–1548. https://doi.org/10.1002/ejic.201600908.

(5) Anthony, E. J.; Bolitho, E. M.; Bridgewater, H. E.; Carter, O. W. L.; Donnelly, J. M.; Imberti, C.; Lant, E. C.; Lermyte, F.; Needham, R. J.; Palau, M.; Sadler, P. J.; Shi, H.; Wang, F.-X.; Zhang, W.-Y.; Zhang, Z. Metallodrugs Are Unique: Opportunities and Challenges of Discovery and Development. *Chem. Sci.* **2020**, *11* (48), 12888–12917. https://doi.org/10.1039/D0SC04082G.

(6) Miranda, V. M. Medicinal Inorganic Chemistry: An Updated Review on the Status of Metallodrugs and Prominent Metallodrug Candidates. *Rev. Inorg. Chem.* **2022**, *42* (1), 29–52. https://doi.org/10.1515/revic-2020-0030.

(7) Farrell, N. P. Multi-Platinum Anti-Cancer Agents. Substitution-Inert Compounds for Tumor Selectivity and New Targets. *Chem. Soc. Rev.* **2015**, *44* (24), 8773–8785. https://doi.org/10.1039/C5CS00201J.

(8) Komeda, S.; Moulaei, T.; Woods, K. K.; Chikuma, M.; Farrell, N. P.; Williams, L. D. A Third Mode of DNA Binding: Phosphate Clamps by a Polynuclear Platinum Complex. *J. Am. Chem. Soc.* **2006**, *128* (50), 16092–16103. https://doi.org/10.1021/ja062851y.

(9) Yoon, C. Y.; Gong, M. K.; Kang, D. H.; Kim, M. S.; Jung, W. S.; Kim, Y. S.; Cho, I. R.; Choi, Y. D. MP98-18 INHIBITION OF HSP90 SYNERGISTICALLY POTENTIATES ANTITUMOR EFFECT OF NVP-BEZ235 AND SATRAPLATIN COMBINATION THERAPY IN CISPLATIN-RESISTANT HUMAN BLADDER CANCER CELLS THROUGH THE DOWN-REGULATION OF AKT AND ERK SIGNALING. *J. Urol.* **2017**, *197* (4S). https://doi.org/10.1016/j.juro.2017.02.3083.

(10) Madeira, J. M.; Gibson, D. L.; Kean, W. F.; Klegeris, A. The Biological Activity of Auranofin: Implications for Novel Treatment of Diseases. *Inflammopharmacology* **2012**, *20* (6), 297–306. https://doi.org/10.1007/s10787-012-0149-1.

(11) Angelucci, F.; Sayed, A. A.; Williams, D. L.; Boumis, G.; Brunori, M.; Dimastrogiovanni, D.; Miele, A. E.; Pauly, F.; Bellelli, A. Inhibition of Schistosoma Mansoni Thioredoxin-Glutathione

Reductase by Auranofin. *J. Biol. Chem.* **2009**, *284* (42), 28977–28985. https://doi.org/10.1074/jbc.M109.020701.

(12) Tong, K.-C.; Lok, C.-N.; Wan, P.-K.; Hu, D.; Fung, Y. M. E.; Chang, X.-Y.; Huang, S.; Jiang, H.; Che, C.-M. An Anticancer Gold(III)-Activated Porphyrin Scaffold That Covalently Modifies Protein Cysteine Thiols. *Proc. Natl. Acad. Sci.* **2020**, *117* (3), 1321–1329. https://doi.org/10.1073/pnas.1915202117.

(13) Bergamo, A.; Sava, G. Ruthenium Complexes Can Target Determinants of Tumour Malignancy. *Dalton Trans.* **2007**, No. 13, 1267. https://doi.org/10.1039/b617769g.

(14) Bertrand, J. A.; Thieffine, S.; Vulpetti, A.; Cristiani, C.; Valsasina, B.; Knapp, S.; Kalisz, H. M.; Flocco, M. Structural Characterization of the GSK-3β Active Site Using Selective and Non-Selective ATP-Mimetic Inhibitors. *J. Mol. Biol.* **2003**, *333* (2), 393–407. https://doi.org/10.1016/j.jmb.2003.08.031.

(15) Wang, F.; Xu, J.; Habtemariam, A.; Bella, J.; Sadler, P. J. Competition between Glutathione and Guanine for a Ruthenium(II) Arene Anticancer Complex: Detection of a Sulfenato Intermediate. *J. Am. Chem. Soc.* **2005**, *127* (50), 17734–17743. https://doi.org/10.1021/ja053387k.

(16) Wang, F.; Habtemariam, A.; van der Geer, E. P. L.; Fernández, R.; Melchart, M.; Deeth, R. J.; Aird, R.; Guichard, S.; Fabbiani, F. P. A.; Lozano-Casal, P.; Oswald, I. D. H.; Jodrell, D. I.; Parsons, S.; Sadler, P. J. Controlling Ligand Substitution Reactions of Organometallic Complexes: Tuning Cancer Cell Cytotoxicity. *Proc. Natl. Acad. Sci.* **2005**, *102* (51), 18269–18274. https://doi.org/10.1073/pnas.0505798102.

(17) Hottinger, D.; Beebe, D.; Kozhimannil, T.; Prielipp, R.; Belani, K. Sodium Nitroprusside in 2014: A Clinical Concepts Review. *J. Anaesthesiol. Clin. Pharmacol.* **2014**, *30* (4), 462. https://doi.org/10.4103/0970-9185.142799.

(18) Romito, B. T.; McBroom, M. M.; Bryant, D.; Gamez, J.; Merchant, A.; Hill, S. E. The Effect of SANGUINATE ® (PEGylated Carboxyhemoglobin Bovine) on Cardiopulmonary Bypass Functionality Using a Bovine Whole Blood Model of Normovolemic Hemodilution. *Perfusion* **2020**, *35* (1), 19–25. https://doi.org/10.1177/0267659119850681.

(19) Dubar, F.; Khalife, J.; Brocard, J.; Dive, D.; Biot, C. Ferroquine, an Ingenious Antimalarial Drug –Thoughts on the Mechanism of Action. *Molecules* **2008**, *13* (11), 2900–2907. https://doi.org/10.3390/molecules13112900.

(20) Gildenhuys, J.; Roex, T. le; Egan, T. J.; de Villiers, K. A. The Single Crystal X-Ray Structure of β-Hematin DMSO Solvate Grown in the Presence of Chloroquine, a β-Hematin Growth-Rate Inhibitor. *J. Am. Chem. Soc.* **2013**, *135* (3), 1037–1047. https://doi.org/10.1021/ja308741e.

(21) de Paiva, R. E. F.; Du, Z.; Nakahata, D. H.; Lima, F. A.; Corbi, P. P.; Farrell, N. P. Gold-Catalyzed C–S Aryl-Group Transfer in Zinc Finger Proteins. *Angew. Chem. Int. Ed.* **2018**, *57* (30), 9305–9309. https://doi.org/10.1002/anie.201803082.

(22) de Paiva, R. E. F.; Marçal Neto, A.; Santos, I. A.; Jardim, A. C. G.; Corbi, P. P.; Bergamini, F. R. G. What Is Holding Back the Development of Antiviral Metallodrugs? A Literature Overview and Implications for SARS-CoV-2 Therapeutics and Future Viral Outbreaks. *Dalton Trans.* **2020**, *49* (45), 16004–16033. https://doi.org/10.1039/D0DT02478C.

(23) Louie, A. Y.; Meade, T. J. A Cobalt Complex That Selectively Disrupts the Structure and Function of Zinc Fingers. *Proc. Natl. Acad. Sci.* **1998**, *95* (12), 6663–6668. https://doi.org/10.1073/pnas.95.12.6663.

(24) Schwartz, J. A.; Lium, E. K.; Silverstein, S. J. Herpes Simplex Virus Type 1 Entry Is Inhibited by the Cobalt Chelate Complex CTC-96. *J. Virol.* **2001**, *75* (9), 4117–4128. https://doi.org/10.1128/JVI.75.9.4117-4128.2001.

(25) *Influenza (Seasonal)*. https://www.who.int/news-room/fact-sheets/detail/influenza-(seasonal) (accessed 2023-03-08).

(26) Thomaston, J. L.; Polizzi, N. F.; Konstantinidi, A.; Wang, J.; Kolocouris, A.; DeGrado, W. F. Inhibitors of the M2 Proton Channel Engage and Disrupt Transmembrane Networks of Hydrogen-Bonded Waters. *J. Am. Chem. Soc.* **2018**, *140* (45), 15219–15226. https://doi.org/10.1021/jacs.8b06741.

(27) McGuire, K. L.; Smit, P.; Ess, D. H.; Hill, J. T.; Harrison, R. G.; Busath, D. D. Mechanism and Kinetics of Copper Complexes Binding to the Influenza A M2 S31N and S31N/G34E Channels. *Biophys. J.* **2021**, *120* (1), 168–177. https://doi.org/10.1016/j.bpj.2020.11.016.

(28) Gordon, N. A.; McGuire, K. L.; Wallentine, S. K.; Mohl, G. A.; Lynch, J. D.; Harrison, R. G.; Busath, D. D. Divalent Copper Complexes as Influenza A M2 Inhibitors. *Antiviral Res.* **2017**, *147*, 100–106. https://doi.org/10.1016/j.antiviral.2017.10.009.

(29) Jin, Z.; Du, X.; Xu, Y.; Deng, Y.; Liu, M.; Zhao, Y.; Zhang, B.; Li, X.; Zhang, L.; Peng, C.; Duan, Y.; Yu, J.; Wang, L.; Yang, K.; Liu, F.; Jiang, R.; Yang, X.; You, T.; Liu, X.; Yang, X.; Bai, F.; Liu, H.; Liu, X.; Guddat, L. W.; Xu, W.; Xiao, G.; Qin, C.; Shi, Z.; Jiang, H.; Rao, Z.; Yang, H. Structure of Mpro from SARS-CoV-2 and Discovery of Its Inhibitors. *Nature* **2020**, *582* (7811), 289–293. https://doi.org/10.1038/s41586-020-2223-y.

(30) Panchariya, L.; Khan, W. A.; Kuila, S.; Sonkar, K.; Sahoo, S.; Ghoshal, A.; Kumar, A.; Verma, D. K.; Hasan, A.; Khan, M. A.; Jain, N.; Mohapatra, A. K.; Das, S.; Thakur, J. K.; Maiti, S.; Nanda, R. K.; Halder, R.; Sunil, S.; Arockiasamy, A. Zinc $^{2+}$ Ion Inhibits SARS-CoV-2 Main Protease and Viral Replication *in Vitro*. *Chem. Commun.* **2021**, *57* (78), 10083–10086. https://doi.org/10.1039/D1CC03563K.

(31) Bafaro, E.; Liu, Y.; Xu, Y.; Dempski, R. E. The Emerging Role of Zinc Transporters in Cellular Homeostasis and Cancer. *Signal Transduct. Target. Ther.* **2017**, *2* (1), 17029. https://doi.org/10.1038/sigtrans.2017.29.

(32) Lawrence, M. A. W.; Green, K.-A.; Nelson, P. N.; Lorraine, S. C. Review: Pincer Ligands—Tunable, Versatile and Applicable. *Polyhedron* **2018**, *143*, 11–27. https://doi.org/10.1016/j.poly.2017.08.017.

(33) Aragón-Muriel, A.; Reyes-Márquez, V.; Cañavera-Buelvas, F.; Parra-Unda, J. R.; Cuenú-Cabezas, F.; Polo-Cerón, D.; Colorado-Peralta, R.; Suárez-Moreno, G. V.; Aguilar-Castillo, B. A.; Morales-Morales, D. Pincer Complexes Derived from Tridentate Schiff Bases for Their Use as Antimicrobial Metallopharmaceuticals. *Inorganics* **2022**, *10* (9), 134. https://doi.org/10.3390/inorganics10090134.

(34) Shukla, S. N.; Gaur, P.; Raidas, M. L.; Chaurasia, B.; Bagri, S. S. Novel NNO Pincer Type Schiff Base Ligand and Its Complexes of Fe(III), Co(II) and Ni(II): Synthesis, Spectroscopic Characterization, DFT, Antibacterial and Anticorrosion Study. *J. Mol. Struct.* **2021**, *1240*, 130582. https://doi.org/10.1016/j.molstruc.2021.130582.

(35) Wu, S.; Wu, Z.; Ge, Q.; Zheng, X.; Yang, Z. Antitumor Activity of Tridentate Pincer and Related Metal Complexes. *Org. Biomol. Chem.* **2021**, *19* (24), 5254–5273. https://doi.org/10.1039/D1OB00577D.

(36) Messori, L.; Abbate, F.; Marcon, G.; Orioli, P.; Fontani, M.; Mini, E.; Mazzei, T.; Carotti, S.; O'Connell, T.; Zanello, P. Gold(III) Complexes as Potential Antitumor Agents: Solution Chemistry and Cytotoxic Properties of Some Selected Gold(III) Compounds. *J. Med. Chem.* **2000**, *43* (19), 3541–3548. https://doi.org/10.1021/jm990492u.

(37) Radisavljević, S.; Bratsos, I.; Scheurer, A.; Korzekwa, J.; Masnikosa, R.; Tot, A.; Gligorijević, N.; Radulović, S.; Simović, A. R. New Gold Pincer-Type Complexes: Synthesis, Characterization, DNA Binding Studies and Cytotoxicity. *Dalton Trans.* **2018**, *47* (38), 13696–13712. https://doi.org/10.1039/C8DT02903B.

(38) Zou, T.; Lum, C. T.; Chui, S. S.-Y.; Che, C.-M. Gold(III) Complexes Containing N-Heterocyclic Carbene Ligands: Thiol "Switch-on" Fluorescent Probes and Anti-Cancer Agents. *Angew. Chem. Int. Ed.* **2013**, *52* (10), 2930–2933. https://doi.org/10.1002/anie.201209787.

(39) Guney, E.; Yilmaz, V. T.; Ari, F.; Buyukgungor, O.; Ulukaya, E. Synthesis, Characterization, Structures and Cytotoxic Activity of Palladium(II) and Platinum(II) Complexes Containing Bis(2-Pyridylmethyl)Amine and Saccharinate. *Polyhedron* **2011**, *30* (1), 114–122. https://doi.org/10.1016/j.poly.2010.09.037.

(40) Ari, F.; Ulukaya, E.; Sarimahmut, M.; Yilmaz, V. T. Palladium(II) Saccharinate Complexes with Bis(2-Pyridylmethyl)Amine Induce Cell Death by Apoptosis in Human Breast Cancer Cells in Vitro. *Bioorg. Med. Chem.* **2013**, *21* (11), 3016–3021. https://doi.org/10.1016/j.bmc.2013.03.073.

(41) Darabi, F.; Hadadzadeh, H.; Simpson, J.; Shahpiri, A. A Water-Soluble Pd(II) Complex with a Terpyridine Ligand: Experimental and Molecular Modeling Studies of the Interaction with DNA and BSA; and in Vitro Cytotoxicity Investigations against Five Human Cancer Cell Lines. *New J. Chem.* **2016**, *40* (11), 9081–9097. https://doi.org/10.1039/C6NJ01880G.

(42) Liang, J.-W.; Wang, Y.; Du, K.-J.; Li, G.-Y.; Guan, R.-L.; Ji, L.-N.; Chao, H. Synthesis, DNA Interaction and Anticancer Activity of Copper(II) Complexes with 4′-Phenyl-2,2′:6′,2″-Terpyridine Derivatives. *J. Inorg. Biochem.* **2014**, *141*, 17–27. https://doi.org/10.1016/j.jinorgbio.2014.08.006.

(43) Czerwińska, K.; Machura, B.; Kula, S.; Krompiec, S.; Erfurt, K.; Roma-Rodrigues, C.; Fernandes, A. R.; Shul'pina, L. S.; Ikonnikov, N. S.; Shul'pin, G. B. Copper(II) Complexes of Functionalized 2,2′:6′,2″-Terpyridines and 2,6-Di(Thiazol-2-Yl)Pyridine: Structure, Spectroscopy, Cytotoxicity and Catalytic Activity. *Dalton Trans.* **2017**, *46* (29), 9591–9604. https://doi.org/10.1039/C7DT01244F.

(44) Suntharalingam, K.; Hunt, D. J.; Duarte, A. A.; White, A. J. P.; Mann, D. J.; Vilar, R. A Tri-Copper(II) Complex Displaying DNA-Cleaving Properties and Antiproliferative Activity against Cancer Cells. *Chem. - Eur. J.* **2012**, *18* (47), 15133–15141. https://doi.org/10.1002/chem.201202482.

(45) *Timeline: WHO's COVID-19 response*. https://www.who.int/emergencies/diseases/novel-coronavirus-2019/interactive-timeline (accessed 2023-03-15).

(46) *WHO Coronavirus (COVID-19) Dashboard*. https://covid19.who.int (accessed 2023-03-15).

(47) Islam, N.; Jdanov, D. A.; Shkolnikov, V. M.; Khunti, K.; Kawachi, I.; White, M.; Lewington, S.; Lacey, B. Effects of Covid-19 Pandemic on Life Expectancy and Premature Mortality in 2020: Time Series Analysis in 37 Countries. *BMJ* **2021**, e066768. https://doi.org/10.1136/bmj-2021-066768.

(48) *Yahoo Finance - Stock Market Live, Quotes, Business & Finance News*. https://finance.yahoo.com/ (accessed 2023-03-13).

(49) Perlman, S. Another Decade, Another Coronavirus. *N. Engl. J. Med.* **2020**, *382* (8), 760–762. https://doi.org/10.1056/NEJMe2001126.

(50) Harrison, A. G.; Lin, T.; Wang, P. Mechanisms of SARS-CoV-2 Transmission and Pathogenesis. *Trends Immunol.* **2020**, *41* (12), 1100–1115. https://doi.org/10.1016/j.it.2020.10.004.

(51) Yadav, R.; Chaudhary, J. K.; Jain, N.; Chaudhary, P. K.; Khanra, S.; Dhamija, P.; Sharma, A.; Kumar, A.; Handu, S. Role of Structural and Non-Structural Proteins and Therapeutic Targets of SARS-CoV-2 for COVID-19. *Cells* **2021**, *10* (4), 821. https://doi.org/10.3390/cells10040821.

(52) Walls, A. C.; Park, Y.-J.; Tortorici, M. A.; Wall, A.; McGuire, A. T.; Veesler, D. Structure, Function, and Antigenicity of the SARS-CoV-2 Spike Glycoprotein. *Cell* **2020**, *181* (2), 281-292.e6. https://doi.org/10.1016/j.cell.2020.02.058.

(53) Benton, D. J.; Wrobel, A. G.; Xu, P.; Roustan, C.; Martin, S. R.; Rosenthal, P. B.; Skehel, J. J.; Gamblin, S. J. Receptor Binding and Priming of the Spike Protein of SARS-CoV-2 for Membrane Fusion. *Nature* **2020**, *588* (7837), 327–330. https://doi.org/10.1038/s41586-020-2772-0.

(54) Dolan, K. A.; Dutta, M.; Kern, D. M.; Kotecha, A.; Voth, G. A.; Brohawn, S. G. Structure of SARS-CoV-2 M Protein in Lipid Nanodiscs. *eLife* **2022**, *11*, e81702. https://doi.org/10.7554/eLife.81702.

(55) Mandala, V. S.; McKay, M. J.; Shcherbakov, A. A.; Dregni, A. J.; Kolocouris, A.; Hong, M. Structure and Drug Binding of the SARS-CoV-2 Envelope Protein Transmembrane Domain in Lipid Bilayers. *Nat. Struct. Mol. Biol.* **2020**, *27* (12), 1202–1208. https://doi.org/10.1038/s41594-020-00536-8.

(56) Dinesh, D. C.; Chalupska, D.; Silhan, J.; Koutna, E.; Nencka, R.; Veverka, V.; Boura, E. Structural Basis of RNA Recognition by the SARS-CoV-2 Nucleocapsid Phosphoprotein.

(57) Hamming, I.; Timens, W.; Bulthuis, M.; Lely, A.; Navis, G.; van Goor, H. Tissue Distribution of ACE2 Protein, the Functional Receptor for SARS Coronavirus. A First Step in Understanding SARS Pathogenesis. *J. Pathol.* **2004**, *203* (2), 631–637. https://doi.org/10.1002/path.1570.

(58) V'kovski, P.; Kratzel, A.; Steiner, S.; Stalder, H.; Thiel, V. Coronavirus Biology and Replication: Implications for SARS-CoV-2. *Nat. Rev. Microbiol.* **2021**, *19* (3), 155–170. https://doi.org/10.1038/s41579-020-00468-6.

(59) Astuti, I.; Ysrafil. Severe Acute Respiratory Syndrome Coronavirus 2 (SARS-CoV-2): An Overview of Viral Structure and Host Response. *Diabetes Metab. Syndr. Clin. Res. Rev.* **2020**, *14* (4), 407–412. https://doi.org/10.1016/j.dsx.2020.04.020.

(60) Yuan, M.; Wu, N. C.; Zhu, X.; Lee, C.-C. D.; Mok, C. K. P.; Wilson, I. A. A Highly Conserved Cryptic Epitope in the Receptor Binding Domains of SARS-CoV-2 and SARS-CoV. **2020**, 5.

(61) Lan, J.; Ge, J.; Yu, J.; Shan, S.; Zhou, H.; Fan, S.; Zhang, Q.; Shi, X.; Wang, Q.; Zhang, L.; Wang, X. Structure of the SARS-CoV-2 Spike Receptor-Binding Domain Bound to the ACE2 Receptor. *Nature* **2020**, *581* (7807), 215–220. https://doi.org/10.1038/s41586-020-2180-5.

(62) Yan, R.; Zhang, Y.; Li, Y.; Xia, L.; Guo, Y.; Zhou, Q. Structural Basis for the Recognition of SARS-CoV-2 by Full-Length Human ACE2. *Science* **2020**, *367* (6485), 1444–1448. https://doi.org/10.1126/science.abb2762.

(63) Wang, Y.; Liu, C.; Zhang, C.; Wang, Y.; Hong, Q.; Xu, S.; Li, Z.; Yang, Y.; Huang, Z.; Cong, Y. Structural Basis for SARS-CoV-2 Delta Variant Recognition of ACE2 Receptor and Broadly Neutralizing Antibodies. *Nat. Commun.* **2022**, *13* (1), 871. https://doi.org/10.1038/s41467-022-28528-w.

(64) Huo, J.; Dijokaite-Guraliuc, A.; Liu, C.; Zhou, D.; Ginn, H. M.; Das, R.; Supasa, P.; Selvaraj, M.; Nutalai, R.; Tuekprakhon, A.; Duyvesteyn, H. M. E.; Mentzer, A. J.; Skelly, D.; Ritter, T. G.; Amini, A.; Bibi, S.; Adele, S.; Johnson, S. A.; Paterson, N. G.; Williams, M. A.; Hall, D. R.; Plowright, M.; Newman, T. A. H.; Hornsby, H.; de Silva, T. I.; Temperton, N.; Klenerman, P.; Barnes, E.; Dunachie, S. J.; Pollard, A. J.; Lambe, T.; Goulder, P.; Fry, E. E.; Mongkolsapaya, J.; Ren, J.; Stuart, D. I.; Screaton, G. R. A Delicate Balance between Antibody Evasion and ACE2 Affinity for Omicron BA.2.75. *Cell Rep.* **2023**, *42* (1), 111903. https://doi.org/10.1016/j.celrep.2022.111903.

(65) Jiang, S.; Zhang, X.; Du, L. Therapeutic Antibodies and Fusion Inhibitors Targeting the Spike Protein of SARS-CoV-2. *Expert Opin. Ther. Targets* **2021**, *25* (6), 415–421. https://doi.org/10.1080/14728222.2020.1820482.

(66) Zhu, Y.; Yu, D.; Yan, H.; Chong, H.; He, Y. Design of Potent Membrane Fusion Inhibitors against SARS-CoV-2, an Emerging Coronavirus with High Fusogenic Activity. *J. Virol.* **2020**, *94* (14), 12.

(67) Siu, C.-K.; Ke, Y.; Guo, Y.; Hopkinson, A. C.; Michael Siu, K. W. Dissociations of Copper(Ii)-Containing Complexes of Aromatic Amino Acids: Radical Cations of Tryptophan, Tyrosine, and Phenylalanine. *Phys. Chem. Chem. Phys.* **2008**, *10* (38), 5908. https://doi.org/10.1039/b807692h.

(68) Kiss, T. Copper(II) Complexes of Tyrosine-Containing Tripeptides. *J. Chem. Soc. Dalton Trans.* **1987**, No. 5, 1263–1265. https://doi.org/10.1039/DT9870001263.

Chapter 2
Synthesis & Spectroscopy

2.1 General Methods

All chemicals were purchased from Sigma-Aldrich and used without further purification. All solvents were purchased from Merck, and when necessary, freshly distilled or dried over 4 Å molecular sieves for at least 48 hours. The copper metalation reactions and syntheses using NaH were carried out using inhibitor-free THF.

2.2 Instrumentation

2.2.1 NMR Spectrometer

NMR data were acquired on Bruker Avance III 400 or Avance III 300 NMR spectrometers at frequencies of 400 MHz or 300 MHz (^{1}H), respectively, and 100 MHz or 75 MHz (^{13}C), respectively, using either a 5 mm BBOZ probe or a 5 mm TBIZ probe. All proton and carbon chemical shifts are quoted relative to the relevant solvent reference signal. Spectra were analysed with MestReNova (Version 12.0.0-20080). Data were acquired at a temperature of 300 K.

2.2.2 Mass Spectrometer

Mass spectra were recorded with a Bruker compact Q-TOF high resolution mass spectrometer with Bruker Daltronics HyStar 3.2 SR4 software. Chromatograms were analysed with Bruker Compass DataAnalysis software (Version 4.3) or with MestReNova Software (Version 12.0.0-20080). Samples were prepared to less than 10 µg/mL to prevent damaging of the spectrometer capillary. Samples were prepared by weighing out less than 1 mg of pure product or single crystals and dissolving this in 100 µL of HPLC grade DMSO before making up a final volume of 1 mL with HPLC grade MeOH and subsequent 100-fold dilution with MeOH.

2.2.3 FTIR Spectrometer

Infrared spectra of pure powder or crystalline samples were recorded using a Bruker Alpha FTIR spectrometer using a Bruker Platinum diamond Attenuated Total Reflectance sampling accessory. OPUS software (Version 7.5) was used to analyse spectra. The spectra were acquired over 32 scans between 19 and 24 °C with a spectral resolution of 4 cm^{-1}.

2.2.4 X-ray Diffractometer

See Chapter Five: Crystallography.

2.2.5 UV-Vis Spectrometer

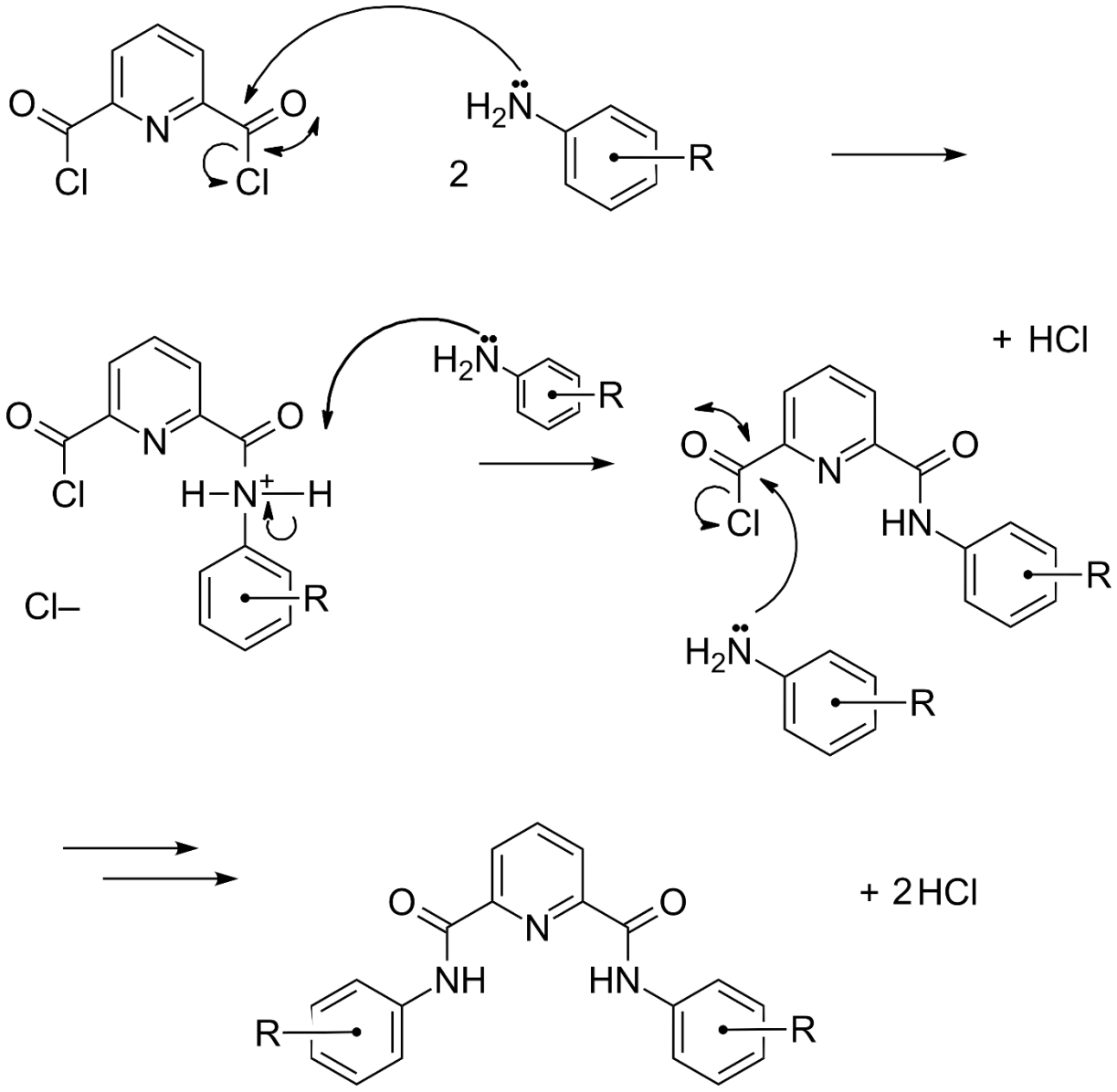
Absorbance spectra were recorded at 20 °C using a Specord 210® Plus (Analytik Jena) using WinASPECT Plus version 4.2.0.0. The temperature was controlled by an external thermostatted circulating water bath and water-circulating cell holders.

2.3 Ligand Synthesis

The ligand syntheses involved a simple nucleophilic acyl substitution between an arylamine and pyridine-2,6-dicarbonyl dichloride. The acid chloride used is highly reactive and the reactions were generally high yielding and robust. The variety of arylamines available for purchase allowed a modest library of ligands to be easily synthesized. The ligands typically precipitate out of reactions performed in acetonitrile thus facilitating facile purification and recovery. The reactions are irreversible and run to completion within an hour or two. Overall, the pincer ligand synthesis performed in this way is quick and simple. Shown below is the general reaction mechanism and table of yields for the 11 ligands successfully synthesized and characterized in this work.

Table 2.1: List of yields for synthesized ligands.

Aryl Amine	Ligand	Yield (%)
5-aminopyridine-3-carboxylic acid	H_4L1	42
3-aminobenzoic acid	H_4L2	66
4-aminobenzoic acid	H_4L3	95
4-aminophenylacetic acid	H_4L4	67
3-amino-*N*,*N*-dimethylbenzamide	H_2L5	81
3-amino-*N*-isopropylbenzamide	H_4L6	98
5-amino-1*H*-isoindole-1,3(2*H*)-dione	H_4L7	54
3-amino-N-ethylbenzamide	H_4L8	96
N-(3-aminophenyl)acetamide	H_4L9	97
3-aminobenzonitrile	H_2L10	95
3-amino-*N*-phenylbenzamide	H_4L11	98



Scheme 2-1: General reaction mechanism for nucleophilic acyl substitution.

2.3.1 Synthesis of 5,5'-[(pyridine-2,6-dicarbonyl)bis(azanediyl)]dinicotinic acid, H_4L1

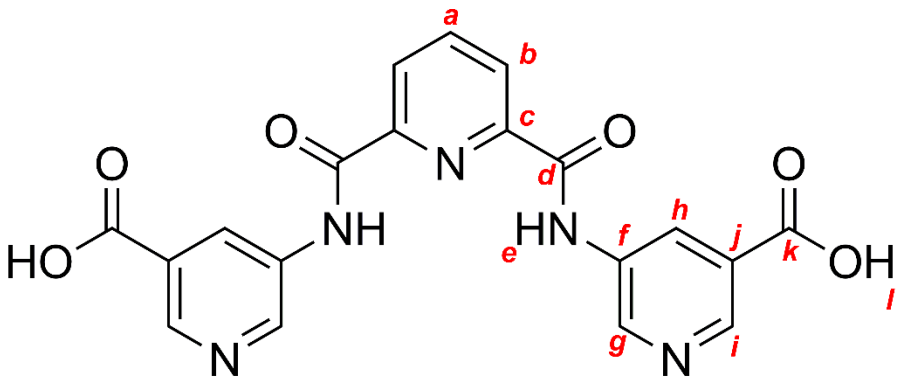


Figure 2.1: Structure and atom labelling of 5,5'-[(pyridine-2,6-dicarbonyl)bis(azanediyl)]dinicotinic acid.

This compound was prepared by novel synthetic methods and will be referred to as H_4L1. The amine, 5-aminopyridine-3-carboxylic acid (51.5 mg, 0.373 mmol), was dissolved in 50 mL of dry THF before adding pyridine-2,6-dicarbonyl dichloride (33.7 mg, 0.165 mmol) which had been dissolved in 10 mL of dry MeCN. A white precipitate immediately formed. The reaction was refluxed at 60 °C open to the atmosphere while being gently stirred for 2 hours. The mixture was then filtered under vacuum while still hot and the collected precipitate was washed with 10 mL of THF. The remaining white powder is H_4L1 (28 mg, 42% yield). Supporting Information S1.1.

^{1}H NMR: (400 MHz, DMSO-d_6, 293K) [δ, ppm]: 11.64 (s, 2H, ***e***), 9.47 (d, J = 2.5 Hz, 2H, ***g***), 9.03 (t, J = 2.2 Hz, 2H, ***i***), 8.95 – 8.83 (m, 2H, ***h***), 8.47 (d, J = 7.7 Hz, 2H, ***b***), 8.37 (dd, J = 8.6, 6.9 Hz, 1H, ***a***). ^{13}C NMR: (100 MHz, DMSO-d_6, 293K) [δ, ppm]: 166.35 (***k***), 162.99 (***d***), 148.73 (***c***), 145.48 (***g***), 145.22 (***h***), 140.79 (***a***), 135.76 (***f***), 129.48 (***i***), 127.40 (***j***), 126.49 (***b***). FTIR (cm^{-1}): 3414.54 (w, asymmetric N-H stretch), 3099.19 (w, aromatic C-H stretch), 1686.79 (s, C=O stretch), 1536.23 (s, symmetric N-H wag). HRMS (m/z) $C_{19}H_{13}N_5O_6$ [M + H]$^+$: calc 408.09386; found 408.08978.

2.3.2 Synthesis of 3,3'-[(pyridine-2,6-dicarbonyl)bis(azanediyl)]dibenzoic acid, H_4L2

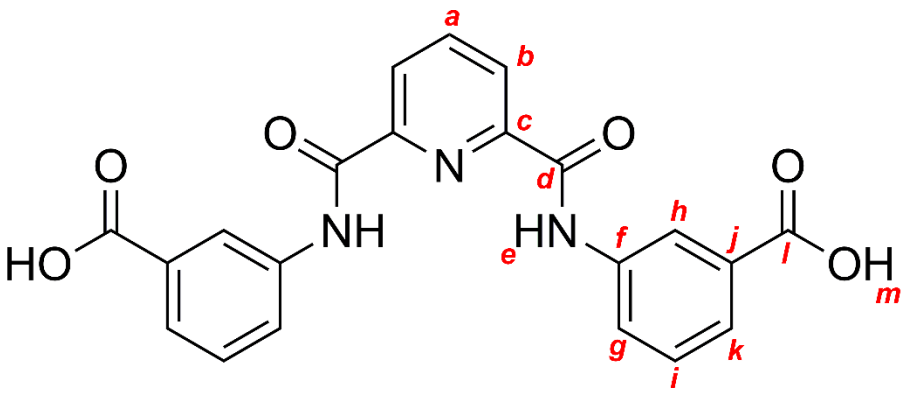


Figure 2.2: Structure and atom labelling of 3,3'-[(pyridine-2,6-dicarbonyl)bis(azanediyl)]dibenzoic acid.

This compound was prepared by modified synthetic methods[1] and will be referred to as H_4L2. The aryl amine, 3-aminobenzoic acid, (375 mg, 2.73 mmol) was dissolved in 50 mL of dry THF before adding pyridine-2,6-dicarbonyl dichloride (256 mg, 1.26 mmol) which had been dissolved in 10 mL of dry MeCN. A white precipitate immediately formed. The reaction mixture was refluxed at 60 °C open to the atmosphere while being gently stirred for 2 hours. The reaction mixture was then filtered while hot and the collected precipitate was washed with 10 mL of THF. The remaining white powder is H_4L2 (338 mg, 66% yield). Supporting Information S1.2.

^{1}H NMR: (400 MHz, DMSO-d_6, 293K) [δ, ppm]: 11.23 (s, 2H, ***e***), 8.58 (s, 2H, ***h***), 8.44 (dd, J = 7.6, 2.2 Hz, 2H, ***b***), 8.38 – 8.29 (m, 1H, ***a***), 8.21 (d, J = 8.1 Hz, 2H, ***g***), 7.78 (d, J = 7.7 Hz, 2H, ***k***), 7.59 (td, J = 7.9, 2.2 Hz, 2H, ***i***). ^{13}C NMR: (100 MHz, DMSO-d_6, 293K) [δ, ppm]: 167.61 (***l***), 162.44 (***d***), 149.21 (***c***), 140.50 (***a***), 138.84 (***f***), 131.86 (***j***), 129.55 (***i***), 126.06 (***b***), 125.83 (***g***), 125.66 (***k***), 122.31 (***h***). FTIR (cm^{-1}): 3606.18 (w, symmetric O-H stretch), 3479.86 (w, asymmetric N-H stretch), 3233.36 (w, aromatic C-H stretch), 1688.08 (s, C=O stretch), 1589.45 (s, symmetric N-H wag). HRMS (m/z) $C_{21}H_{15}N_3O_6$ [M + Na]$^+$: calc 428.08530; found 428.08112.

2.3.3 Synthesis of 4,4'-[(pyridine-2,6-dicarbonyl)bis(azanediyl)]dibenzoic acid, H_4L3

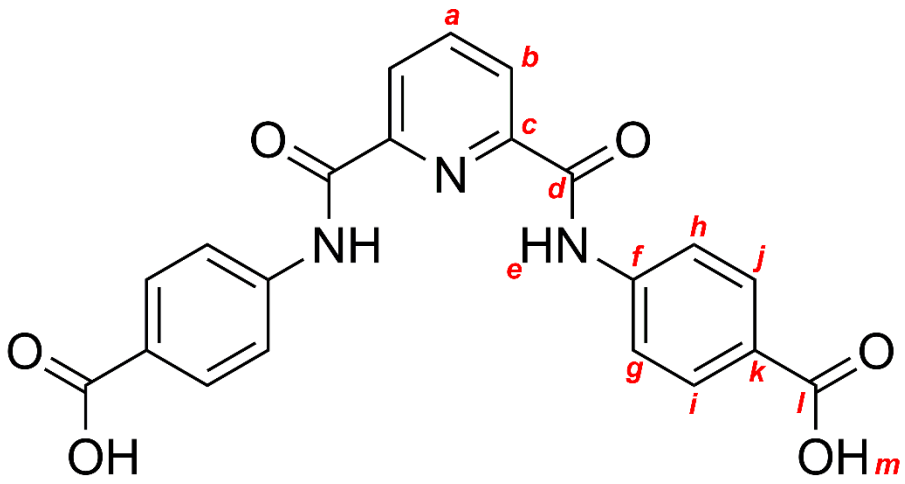


Figure 2.3: Structure and atom labelling of 4,4'-[(pyridine-2,6-dicarbonyl)bis(azanediyl)]dibenzoic acid.

This compound was synthesized by modified literature methods[1,2] and will be referred to as H_4L3. The reagents, 4-aminobenzoic acid (51.2 mg, 0.373 mmol) and pyridine-2,6-dicarbonyl dichloride (33.6 mg, 0.165 mmol), were dissolved in 10 mL of dry MeCN. A white precipitate immediately formed. The reaction mixture was refluxed at 80 °C open to the air while being vigorously stirred for 2 hours. The mixture was filtered while hot and the precipitate was washed with 2 mL of MeCN to afford a clean white powder of H_4L3 (63.3 mg, 95% yield). This is in accordance with literature. Supporting Information S1.3.

^{1}H NMR: (400 MHz, DMSO-d_6, 293K) [δ, ppm]: 11.28 (s, 2H, ***e***), 8.49 – 8.43 (m, 2H, ***b***), 8.39 – 8.32 (m, 1H, ***a***), 8.15 – 8.08 (m, 4H, ***g*****/*****h***), 8.08 – 8.01 (m, 4H, ***i*****/*****j***). ^{13}C NMR: (100 MHz, DMSO-d_6, 293K) [δ, ppm]: 167.39 (***l***), 162.48 (***d***), 153.51 (***f***), 149.04 (***c***), 142.58 (***k***), 140.68 (***a***), 130.84 (***i*****/*****j***), 126.68 (***b***), 120.62 (***g*****/*****h***). FTIR (cm^{-1}): 3749.55 (w, symmetric O-H stretch), 3302.05 (m, asymmetric N-H stretch), 2972.09 (w, aromatic C-H stretch), 1674.00 (s, symmetric C=O stretch), 1520.87 (s, symmetric N-H wag). HRMS (m/z) $C_{21}H_{15}N_3O_6$ [M + Na]$^+$: calc 428.08530; found 428.08066.

2.3.4 Synthesis of 2,2'-[((pyridine-2,6-dicarbonyl)bis(azanediyl))bis(4,1-phenylene)]diacetic acid, H_4L4

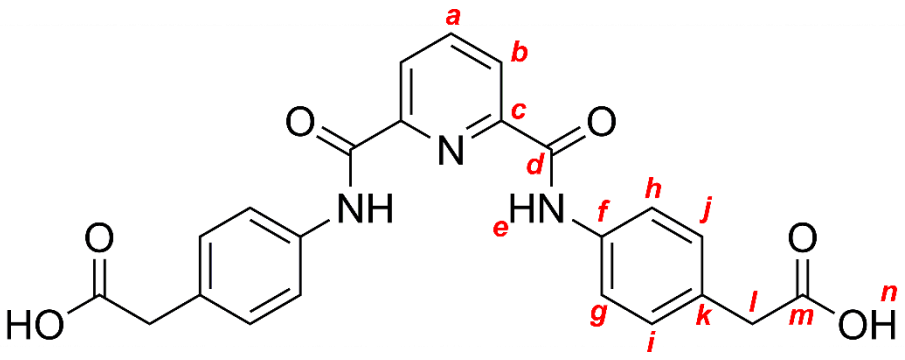


Figure 2.4: Structure and atom labelling of 2,2'-[((pyridine-2,6-dicarbonyl)bis(azanediyl))bis(4,1-phenylene)]diacetic acid.

This compound was prepared by novel synthetic methods and will be referred to as H_4L4. The aryl amine, 4-aminophenylacetic acid, (186 mg, 1.23 mmol) was dissolved in 25 mL of dry THF before being added to a 25 mL dry MeCN solution containing pyridine-2,6-dicarbonyl dichloride (116 mg, 0.570 mmol). The reaction mixture was refluxed at 80 °C open to the atmosphere while being gently stirred for 2 hours. The mixture turned a golden brown as the newly formed product stayed in solution. The solvent was then removed under reduced pressure at 50 °C. The resulting brown-white powder was collected from the 100 mL round-bottom flask using 30 mL of hexane and then filtered. The powder was then washed with 5 mL of cold EtOH to remove the remaining starting material. The light brown powder that remained was H_4L4 (166 mg, 67% yield). Supporting Information S1.4.

^{1}H NMR: (400 MHz, DMSO-d_6, 293K) [δ, ppm]: 12.35 (s, 2H, ***n***), 11.03 (s, 2H, ***e***), 8.44 – 8.38 (m, 2H, ***b***), 8.31 (dd, J = 8.6, 6.9 Hz,1H, ***a***), 7.90 – 7.82 (m, 4H, ***g***/***h***), 7.38 – 7.30 (m, 4H, ***i***/***j***), 3.59 (s, 4H, ***l***). ^{13}C NMR: (100 MHz, DMSO-d_6, 293K) [δ, ppm]: 173.22 (***m***), 162.08 (***d***), 149.34 (***c***), 140.47 (***a***), 137.02 (***k***), 131.57 (***f***), 130.19 (***i***/***j***), 125.78 (***b***), 121.52 (***g***/***h***), 40.65 (***l***). FTIR (cm^{-1}): 3688.96 (w, asymmetric O-H stretch), 3291.12 (m, symmetric N-H stretch), 2907.48 (w, symmetric CH_2 stretch), 1686.05 (s, symmetric C=O stretch), 1519.24 (s, asymmetric N-H wag). HRMS (m/z) $C_{23}H_{19}N_3O_6$ $[M + Na]^+$: calc 456.11660; found 456.11148.

2.3.5 Synthesis of N^2,N^6-bis[3-(dimethylcarbamoyl)phenyl]pyridine-2,6-dicarboxamide, H_2L5

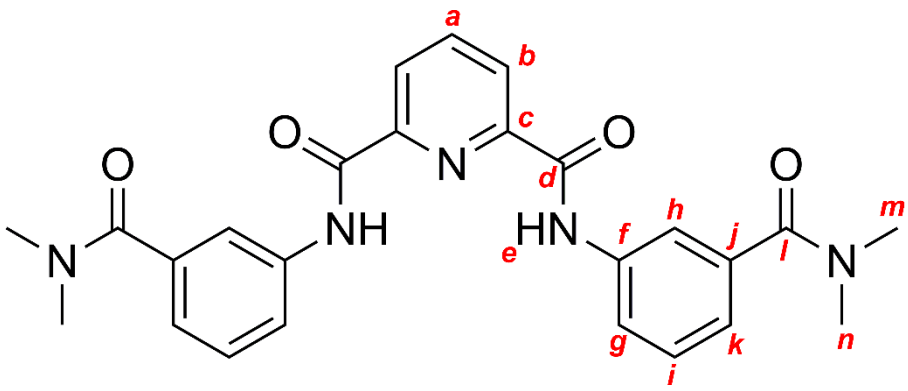


Figure 2.5: Structure and atom labelling of N^2,N^6-bis[3-(dimethylcarbamoyl)phenyl]pyridine-2,6-dicarboxamide.

This compound was prepared by novel synthetic methods and henceforth will be referred to as H_2L5. The reagents, 3-amino-*N*,*N*-dimethylbenzamide (250 mg, 1.52 mmol) and pyridine-2,6-dicarbonyl dichloride (149 mg, 0.729 mmol), were dissolved in 25 mL of dry MeCN. The reaction mixture was refluxed at 88 °C open to the atmosphere while being gently stirred for 2 hours. The mixture turned a deep golden brown as the product formed stayed in solution. The solvent was then removed under reduced pressure at 50 °C which left a sticky honey-like oil coated on the 50 mL round-bottom flask. The oil was then triturated against the glass in 30 mL of hexane until a fine brown powder formed. The mixture was filtered, and the collected powder was washed with an additional 20 mL of hexane to yield H_2L5 (270 mg, 81% yield). Supporting Information S1.5.

^{1}H NMR: (400 MHz, DMSO-d_6, 293K) [δ, ppm] 11.14 (s, 2H, ***e***), 8.43 (dd, *J* = 7.8, 2.5 Hz, 2H, ***b***), 8.37 – 8.29 (m, 1H, ***a***), 8.01 (d, *J* = 10.6 Hz, 4H, ***g***/***h***), 7.52 (td, *J* = 8.0, 2.4 Hz, 2H, ***i***), 7.23 (d, *J* = 7.6 Hz, 2H, ***k***), 3.03 (s, 6H, ***m*** or ***n***), 2.98 (s, 6H, ***m*** or ***n***). ^{13}C NMR: (100 MHz, DMSO-d_6, 293K) [δ, ppm] 170.31 (***l***), 162.31 (***d***), 149.19 (***c***), 140.55 (***a***), 138.56 (***f***), 137.51 (***j***), 129.25 (***i***), 125.99 (***b***), 123.16 (***k***), 122.28 (***g***), 120.05 (***h***), 40.70 (***m*** or ***n***), 35.25 (***m*** or ***n***). FTIR (cm^{-1}): 3270.66 (m, asymmetric N-H stretch), 2929.91 (m, symmetric CH_3 stretch), 1679.08 (s, symmetric C=O stretch), 1608.23 (s, asymmetric C=O stretch), 1536.54 (s, symmetric N-H wag). HRMS (m/z) $C_{25}H_{25}N_5O_4$ $[M + Na]^+$: calc 482.17987; found 482.17490.

2.3.6 Synthesis of N^2,N^6-bis[3-(isopropylcarbamoyl)phenyl]pyridine-2,6-dicarboxamide, H_4L6

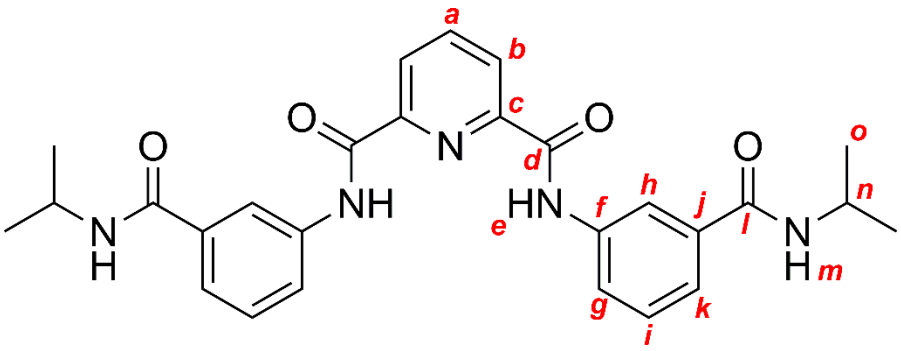


Figure 2.6: Structure and atom labelling of N^2,N^6-bis[3-(isopropylcarbamoyl)phenyl]pyridine-2,6-dicarboxamide.

This compound was prepared by novel synthetic methods and will be referred to as H_4L6. The reagents, 3-amino-*N*-isopropylbenzamide (203 mg, 1.14 mmol) and pyridine-2,6-dicarbonyl dichloride (109 mg, 0.534 mmol), were dissolved in 50 mL of dry MeCN. The product immediately formed as a snowy precipitate. The reaction mixture was refluxed at 88 °C open to the atmosphere while being vigorously stirred for 2 hours. The mixture was allowed to cool before filtering under vacuum, after which, the collected precipitate was washed with 5 mL of MeCN. The white powder is clean H_4L6 (256 mg, 98% yield). Supporting Information S1.6.

^{1}H NMR: (400 MHz, DMSO-d_6, 293K) [δ, ppm] 11.21 (s, 2H, ***e***), 8.44 (d, *J* = 7.8 Hz, 2H, ***b***), 8.32 (q, *J* = 8.1, 7.7 Hz, 5H, ***a***/***h***/***m***), 8.12 (d, *J* = 8.0 Hz, 2H, ***g***), 7.68 (d, *J* = 7.8 Hz, 2H, ***k***), 7.55 (q, *J* = 10.5, 7.9 Hz, 2H, ***i***), 4.14 (dt, *J* = 13.7, 6.7 Hz, 2H, ***n***), 1.20 (d, *J* = 6.6 Hz, 12H, ***o***). ^{13}C NMR: (100 MHz, DMSO-d_6, 293K) [δ, ppm] 165.72 (***l***), 162.35 (***d***), 149.27 (***c***), 140.51 (***a***), 138.53 (***f***), 136.15 (***j***), 129.02 (***i***), 125.98 (***b***), 124.25 (***g***), 123.46 (***k***), 121.21 (***h***), 41.55 (***n***), 22.79 (***o***). FTIR (cm^{-1}): 3248.85 (s, asymmetric N-H stretch), 2973.69 (s, isopropyl stretch), 1672.76 (s, symmetric C=O stretch; N-H wag), 1658.98, (s, asymmetric C=O stretch), 1628.90 (s, symmetric C=O stretch; N-H wag), 1584.54 (s, symmetric N-H wag). HRMS (m/z) $C_{27}H_{29}N_5O_4$ $[M + H]^+$: calc 488.22923; found 488.22424.

2.3.7 Synthesis of N^2,N^6-bis(1,3-dioxoisoindolin-6-yl)pyridine-2,6-dicarboxamide, H_4L7

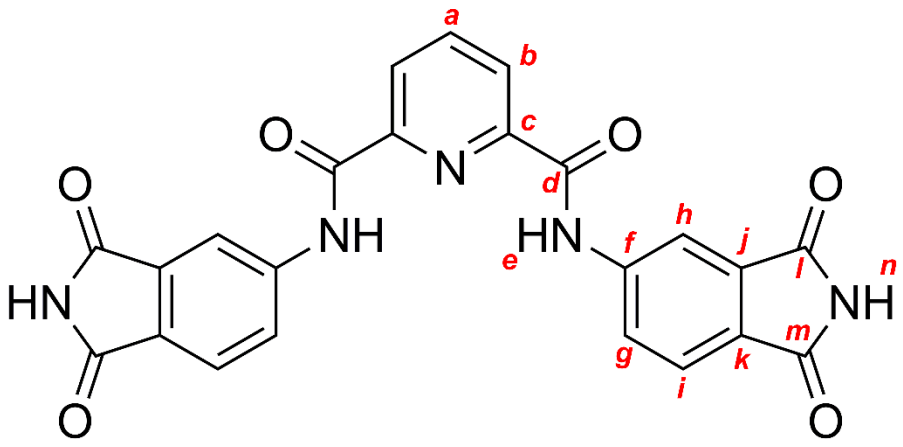


Figure 2.7: Structure and atom labelling of N^2,N^6-bis(1,3-dioxoisoindolin-6-yl)pyridine-2,6-dicarboxamide.

This compound was prepared by novel synthetic methods and will be referred to as H_4L7. The aryl amine, 5-amino-1*H*-isoindole-1,3(2*H*)-dione (100 mg, 0.617 mmol), was dissolved in 50 mL of dry THF before pyridine-2,6-dicarbonyl dichloride (58.2 mg, 0.285 mmol) dissolved in 10 mL of dry MeCN was added to the mixture. The reaction was refluxed at 60 °C open to the atmosphere while being vigorously stirred for 18 hours. In the first hour of reflux, the reaction mixture became a gelatinous jelly with white, fibrous material suspended in a pale-yellow matrix. After intense stirring, the mixture returned to its liquid state and became a deep yellow-brown. After the reaction time had elapsed, there was a yellow precipitate that had formed. The mixture was allowed to cool before filtering off the precipitate and then washing with 5 mL of THF. The yellow powder was H_4L7 (69.7 mg, 54% yield). Supporting Information S1.7.

^{1}H NMR: (400 MHz, DMSO-d_6, 293K) [δ, ppm] 11.45 (s, 2H, ***n***), 11.36 (s, 2H, ***e***), 8.54 (d, *J* = 1.8 Hz, 2H, ***b***), 8.51 – 8.47 (m, 2H, ***h***), 8.35 (ddd, *J* = 10.2, 8.3, 1.7 Hz, 3H, ***a***/***i***), 7.96 (d, *J* = 8.2 Hz, 2H, ***g***). ^{13}C NMR: (100 MHz, DMSO-d_6, 293K) [δ, ppm] 169.51 (***l***), 169.33 (***m***), 162.69 (***d***), 148.72 (***j***), 143.96 (***k***), 140.87 (***a***), 134.53 (***f***), 128.02 (***c***), 126.60 (***h***), 125.70 (***i***), 124.63 (***g***), 114.71 (***b***). FTIR (cm^{-1}): 3317.37 (m, isoindole N-H stretch), 3172.02 (m, symmetric amide N-H stretch), 3068.12 (m, asymmetric amide N-H stretch), 1768.58 (s, symmetric isoindoledione C=O stretch), 1706.99 (s, asymmetric isoindoledione C=O stretch), 1687.46 (s, symmetric amide C=O stretch; N-H wag), 1533.78 (s, symmetric amide N-H wag). HRMS (m/z) $C_{23}H_{13}N_5O_6$ [M + Na]$^+$: calc 478.07580; found 478.06940.

2.3.8 Synthesis of N^2,N^6-bis(3-(ethylcarbamoyl)phenyl)pyridine-2,6-dicarboxamide, H_4L8

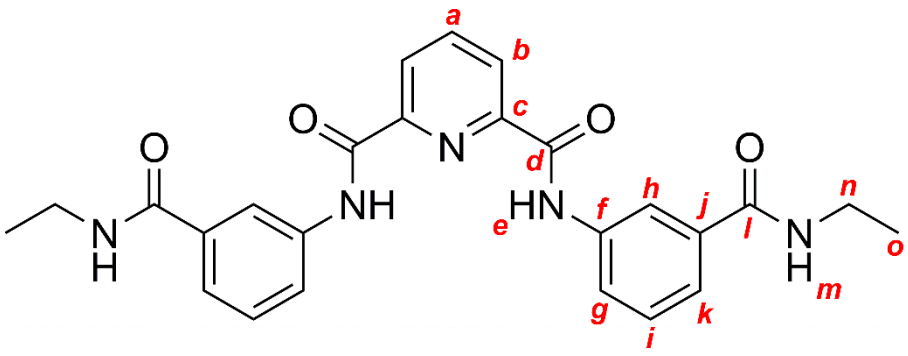


Figure 2.8: Structure and atom labelling of N^2,N^6-bis(3-(ethylcarbamoyl)phenyl)pyridine-2,6-dicarboxamide.

This compound was prepared by novel synthetic methods and will be referred to as H_4L8. The reagents, 3-amino-*N*-ethylbenzamide (95.7 mg, 0.583 mmol) and pyridine-2,6-dicarbonyl dichloride (56.6 mg, 0.277 mmol), were dissolved in 50 mL of dry MeCN. The product instantly precipitated as a white powder. The reaction mixture was refluxed at 88 °C open to the atmosphere while being vigorously stirred for 2 hours. The reaction mixture was then filtered while hot and the collected precipitate was washed with 5 mL of MeCN. The flaky white powder is clean H_4L8 (123 mg, 96% yield). Supporting Information S1.8.

^{1}H NMR: (400 MHz, DMSO-d_6, 300K) [δ, ppm] 11.19 (s, 2H, ***e***), 8.53 (t, *J* = 5.7 Hz, 2H, ***m***), 8.44 (d, *J* = 7.7 Hz, 2H, ***b***), 8.34 (d, *J* = 7.4 Hz, 3H, ***a***/***h***), 8.15 – 8.08 (m, 2H, ***g***), 7.67 (d, *J* = 7.8 Hz, 2H, ***k***), 7.54 (t, *J* = 7.9 Hz, 2H, ***i***), 3.33 – 3.29 (m, 4H, ***n***), 1.15 (t, *J* = 7.2 Hz, 6H, ***o***). ^{13}C NMR: (100 MHz, DMSO-d_6, 300K) [δ, ppm] 166.24 (***l***), 162.34 (***d***), 149.24 (***c***), 140.53 (***a***), 138.60 (***f***), 135.95 (***j***), 129.14 (***i***), 125.99 (***b***), 124.26 (***g***), 123.25 (***k***), 121.07 (***h***), 34.59 (***n***), 15.26 (***o***). FTIR (cm^{-1}): 3249.56 (s, asymmetric N-H stretch), 2971.97 (m, symmetric CH_2 stretch), 2882.99 (m, symmetric CH_3 stretch), 1672.48 (s, asymmetric C=O stretch), 1659.89 (s, symmetric C=O stretch), 1583.30 (s, symmetric N-H wag). HRMS (m/z) $C_{25}H_{25}N_5O_4$ $[M + H]^+$: calc 460.19793; found 460.19263.

2.3.9 Synthesis of N^2,N^6-bis(3-acetamidophenyl)pyridine-2,6-dicarboxamide, H_4L9

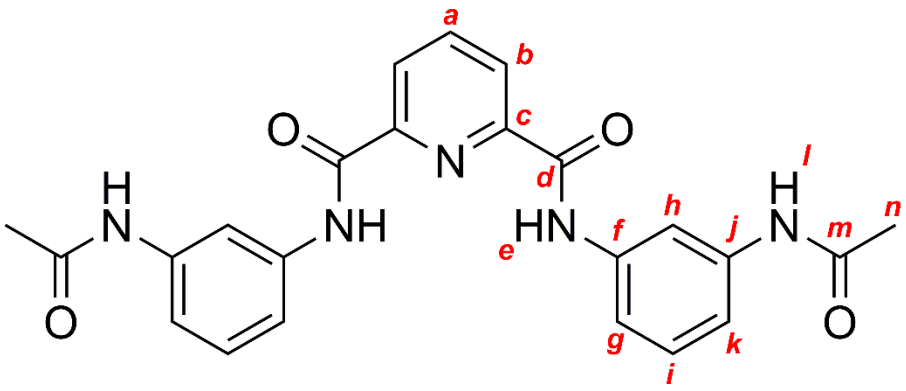


Figure 2.9: Structure and atom labelling of N^2,N^6-bis(3-acetamidophenyl)pyridine-2,6-dicarboxamide.

This compound was prepared by novel synthetic methods and will henceforth be referred to as H_4L9. The reagents, *N*-(3-aminophenyl)acetamide (250 mg, 1.67 mmol) and pyridine-2,6-dicarbonyl dichloride (156 mg, 0.765 mmol), were dissolved in 50 mL of dry MeCN. The product instantly precipitated as a white powder. The reaction was refluxed at 88 °C open to the atmosphere while being vigorously stirred for 2 hours. The mixture was then filtered while hot and the collected precipitate was washed with 5 mL of MeCN. The white powder is H_4L9 (320 mg, 97% yield). Supporting Information S1.9.

^{1}H NMR: (400 MHz, DMSO-d_6, 293K) [δ, ppm] 11.06 (s, 2H, ***e***), 10.09 (s, 2H, ***l***), 8.41 (d, J = 7.8 Hz, 2H, ***b***), 8.31 (t, J = 7.9 Hz, 1H, ***a***), 8.21 (s, 2H, ***h***), 7.49 (dd, J = 14.5, 8.2 Hz, 4H, ***g***/***k***), 7.35 (t, J = 8.2 Hz, 2H, ***i***), 2.08 (s, 6H, ***n***). ^{13}C NMR: (100 MHz, DMSO-d_6, 293K) [δ, ppm] 168.87 (***m***), 162.22 (***d***), 149.40 (***c***), 140.40 (***a***), 140.17 (***j***), 138.71 (***f***), 129.31 (***i***), 125.85 (***b***), 116.75 (***g***), 115.78 (***k***), 112.58 (***h***), 24.52 (***n***). FTIR (cm^{-1}): 3327.54 (m, asymmetric acetamide N-H stretch), 3270.59 (m, asymmetric carboxamide N-H stretch), 2860.95 (w, asymmetric CH_3 stretch), 1669.91 (s, asymmetric C=O stretch; N-H wag), 1557.48 (s, symmetric N-H wag). HRMS (m/z) $C_{23}H_{21}N_5O_4$ $[M + H]^+$: calc 432.16663; found 432.16208.

2.3.10 Synthesis of N^2,N^6-bis(3-cyanophenyl)pyridine-2,6-dicarboxamide, H_2L10

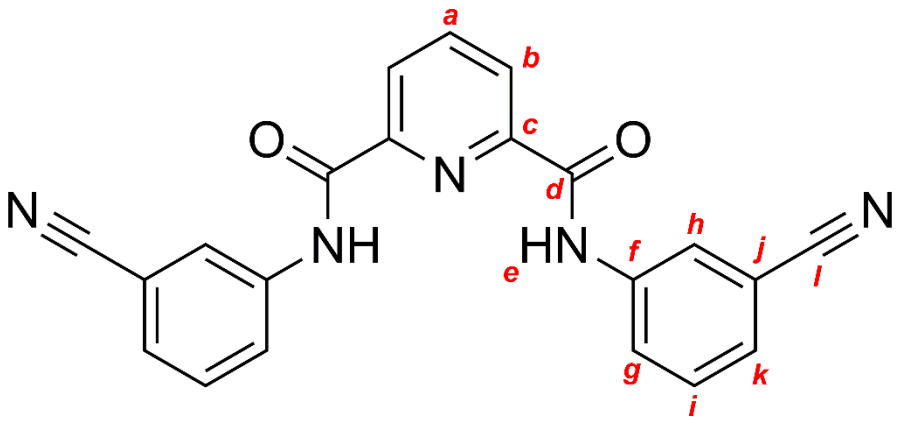


Figure 2. 10: Structure and atom labelling of N^2,N^6-bis(3-cyanophenyl)pyridine-2,6-dicarboxamide.

This compound was prepared by modified synthetic methods[3] and will be referred to as H_2L10. The reagents, 3-aminobenzonitrile (254 mg, 2.15 mmol) and pyridine-2,6-dicarbonyl dichloride (198 mg, 0.973 mmol), were dissolved in 50 mL of dry MeCN. The product instantly precipitated as a white powder. The reaction mixture was refluxed at 88 °C open to the atmosphere while being vigorously stirred for 2 hours. The product is soluble in hot MeCN and a clear yellowish solution was obtained during reflux. The reaction mixture was then cooled to 4 °C before filtering off the snow-white H_2L10 (340 mg, 95% yield). This is an improved 13% yield compared to literature methods.[3] Supporting Information S1.10.

^{1}H NMR: (400 MHz, DMSO-d_6, 293K) [δ, ppm] 11.27 (s, 2H, ***e***), 8.48 – 8.42 (m, 4H, ***b***/***h***), 8.36 (dd, J = 8.6, 6.9 Hz, 1H, ***a***), 8.24 (dq, J = 7.8, 2.7 Hz, 2H, ***i***), 7.75 – 7.65 (m, 4H, ***g***/***k***). ^{13}C NMR: (100 MHz, DMSO-d_6, 293K) [δ, ppm] 162.53 (***d***), 148.78(***c***), 140.80 (***a***), 139.35 (***f***), 130.80 (***k***), 128.40 (***g***), 126.32 (***h***), 126.15 (***i***), 124.12 (***b***), 119.15 (***j***), 112.10 (***l***). FTIR (cm^{-1}): 3288.66 (m, asymmetric N-H stretch), 3086.81 (w, aromatic C-H stretch), 2230.18 (m, symmetric C≡N stretch), 1667.75 (s, asymmetric C=O stretch; N-H wag), 1534.30 (s, asymmetric N-H wag). HRMS (m/z) $C_{21}H_{13}N_5O_2$ $[M + Na]^+$: calc 390.09614; found 390.09229.

2.3.11 Synthesis of N^2,N^6-bis(3-(phenylcarbamoyl)phenyl)pyridine-2,6-dicarboxamide, H_4L11

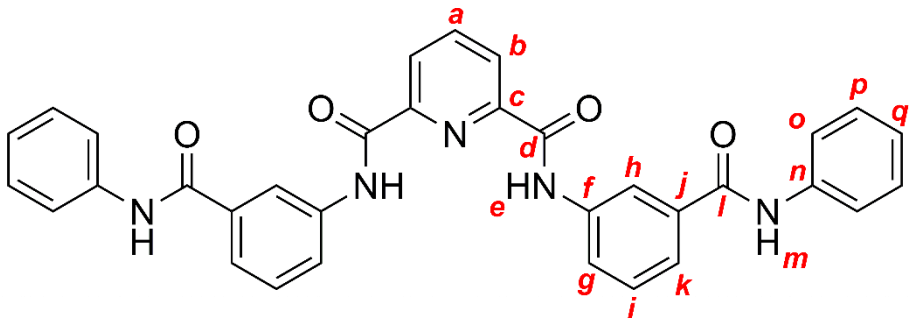


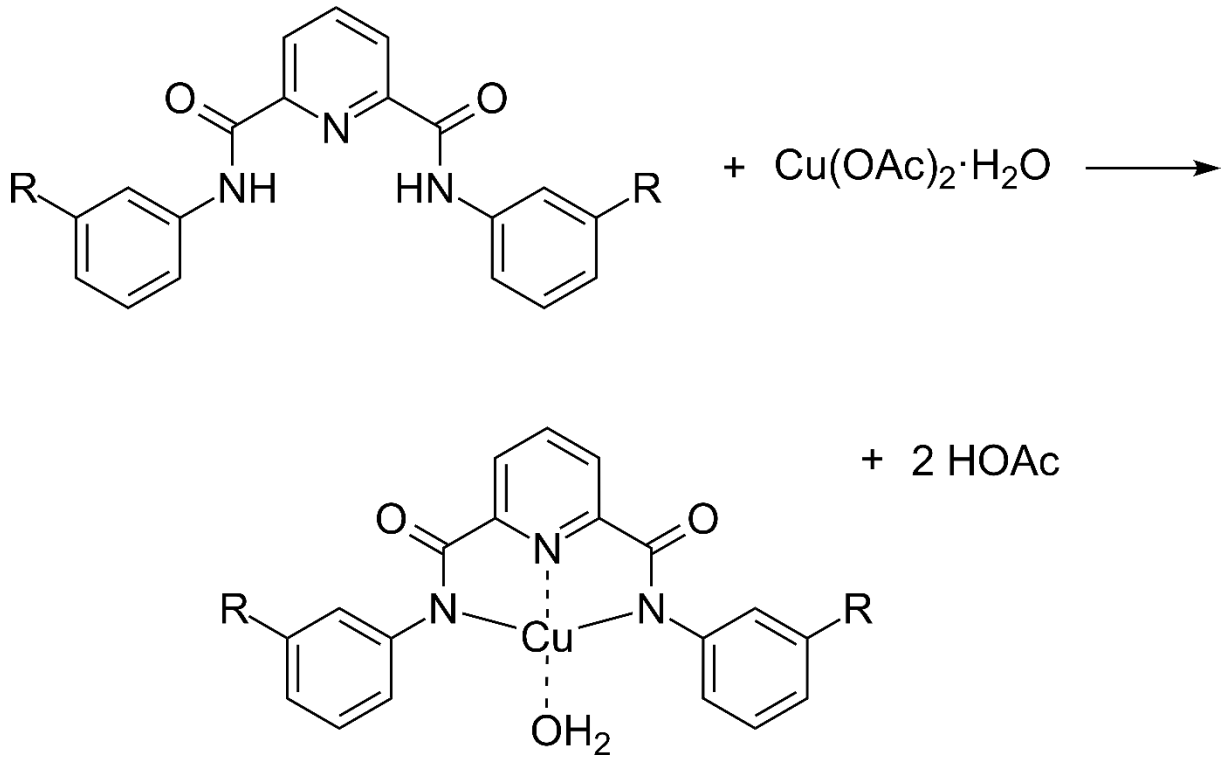
Figure 2.11: Structure and atom labelling of N^2,N^6-bis(3-(phenylcarbamoyl)phenyl)pyridine-2,6-dicarboxamide.

This compound was prepared by modified synthetic methods[4] and will be referred to as H_4L11. The reagents, 3-amino-*N*-phenylbenzamide (250 mg, 1.18 mmol) and pyridine-2,6-dicarbonyl dichloride (114 mg, 0.557 mmol), were dissolved in 50 mL of dry MeCN. The product instantly precipitated as a white powder. The reaction mixture was refluxed at 88 °C open to the atmosphere while being vigorously stirred for 2 hours. The mixture was then filtered while hot to isolate the white powder which was clean H_4L11 (305 mg, 98% yield). This is an excellent 46% improvement on yield compared to literature.[4] Supporting Information S1.11.

^{1}H NMR: (400 MHz, DMSO-d_6, 293K) [δ, ppm] 11.27 (s, 2H, ***e***), 10.38 (s, 2H, ***m***), 8.52 – 8.44 (m, 4H, ***b***/***h***), 8.36 (dd, *J* = 8.4, 7.0 Hz, 1H, ***a***), 8.19 (ddd, *J* = 8.1, 2.2, 1.0 Hz, 2H, ***g***), 7.81 (ddt, *J* = 6.8, 2.0, 1.1 Hz, 6H, ***o***/***k***), 7.64 (t, *J* = 7.9 Hz, 2H, ***i***), 7.42 – 7.33 (m, 4H, ***p***), 7.17 – 7.08 (m, 2H, ***q***). ^{13}C NMR: (100 MHz, DMSO-d_6, 293K) [δ, ppm] 165.88 (***l***), 162.41 (***d***), 149.20 (***c***), 140.62 (***a***), 138.75 (***f***), 136.22 (***j***), 129.34 (***i***), 129.12 (***p***), 126.09 (***h***), 124.66 (***g***), 124.22 (***n***), 123.86 (***k***/***q***), 121.17 (***b***), 120.90(***o***). FTIR (cm^{-1}): 3240.25 (m, asymmetric N-H stretch), 3059.93 (w, aromatic C-H stretch), 1648.44 (s, asymmetric C=O stretch; N-H wag), 1586.71 (s, symmetric N-H wag), 1556.77 (s, asymmetric N-H wag). HRMS (m/z) $C_{33}H_{25}N_5O_4$ [M + Na]$^+$: calc 578.17987; found 578.17328.

2.4 Metal Chelate Synthesis

The project aimed to synthesize metal pincers with bioavailable ions like zinc(II) and copper(II). The synthetic attempts were guided by molecular docking which showed that carboxylic acid substituted aryl rings were best suited for protein binding. However, the ligand frameworks containing these carboxylates produced off-target chelates. The ligands were then reconsidered and successful metalation at the amide pincer cleft was achieved. The zinc pincers were shown to be unstable in water and would thus be unsuitable for the desired biological application. In general, the zinc pincers formed in lower yields and required longer reaction times than metalation with copper. The copper pincers form instantly in solution and the general synthetic scheme is shown below. The synthesis is highly atom economical and unreacted ligand and metal salt may be recovered and reused. There were no side reactions detected from the successful copper chelate syntheses and the only by-product is acetic acid. The reactions were designed such that the metal pincer would precipitate out of solution, when possible, thereby allowing facile purification and recovery. The total synthesis of the copper complexes characterized in this work is smooth and straightforward and clean product can be obtained in 48 hours for most cases.



Scheme 2-2: The general metalation reaction between ligand and copper acetate.

2.4.1 Zinc and the Carboxylic Catastrophe

The ligand scaffolds were designed to be tridentate NNN donors with suitably functionalized aryl groups for binding protein surfaces. Molecular docking showed that carboxylic acid substituted aryl rings gave the best docking scores when bound to the target protein. Thus, attempts to metalate the pincer ligand framework containing carboxylic acid functional groups were made but proved unsuccessful.

2.4.1.1 Zn(H_2L1)

H_4L1 (106 mg, 0.206 mmol) was suspended in 50 mL of dry THF before adding $Zn(OAc)_2$ (48.5 mg, 0.264 mmol) which had been dissolved in 10 mL of dry MeCN. Then 3 drops of NEt_3 were added to mixture, deprotonating the ligand and effecting dissolution. The reaction was gently stirred at room temperature while open to the atmosphere for 18 hours. No product was detected by TLC or NMR. It is suspected that water from the air either reversed the metalation reaction or prevented it from occurring in measurable yields. The reaction was repeated but instead of stirring the mixture overnight, the solution was refluxed at 66 °C for 2 hours open to the air. A yellow-white precipitate was isolated from the mixture. The ^{1}H NMR spectrum of the precipitate was recorded but due to poor solubility of the compound in DMSO-d_6 it was difficult to get a decent spectrum. However, there is an NMR signal for proton ***e*** (Fig. 2.1) indicating that metalation at the NNN pincer cleft did not occur. The broad ^{1}H NMR signals (S2.1) suggest that coordination polymers of variable molecular weight were synthesized.[5] Supporting Information S2.1.

2.4.1.2 $Zn(H_2L2)$

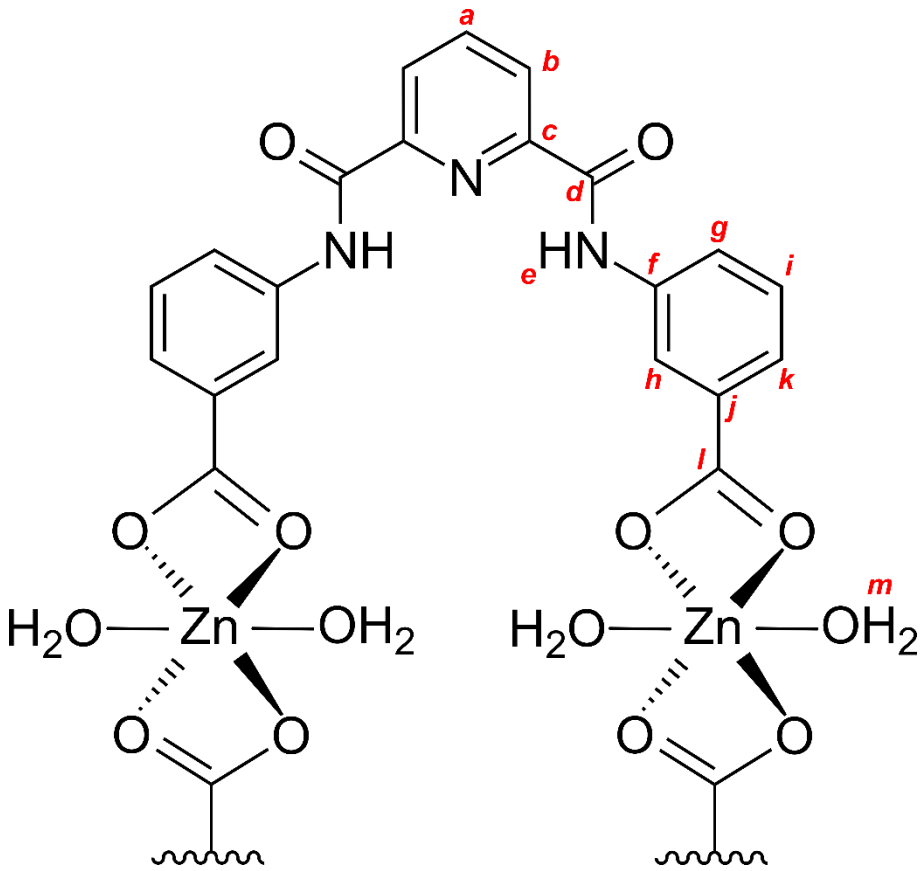


Figure 2.12: Structure and atom labelling of $Zn_2(H_2L2)_2(H_2O)_4$.

H_4L2 (103 mg, 0.253 mmol) was suspended in 50 mL of dry THF before adding $Zn(OAc)_2$ (49.8 mg, 0.272 mmol) which had been dissolved in 10 mL of dry MeCN. Then 3 drops of NEt_3 were added to the mixture, deprotonating the ligand and effecting dissolution. The reaction mixture was refluxed at 66 °C for 2 hours open to the atmosphere. No product was detected by TLC or NMR. It is suspected that metalation of the pincer by zinc(II) is prevented in the presence of water. Hence, a solid-state reaction was attempted as follows: H_4L2 (102 mg, 0.250 mmol) and NaH 60% dispersion in mineral oil (55.0 mg, 1.38 mmol NaH) were placed in a mortar and ground with a pestle until the white ligand turned yellow. Then $Zn(OTf)_2$ (88.8 mg, 0.244 mmol) was added to the yellow reaction mixture and vigorously ground for 10 minutes. The resulting powder was washed with 10 mL of MeCN and 5 mL of hexane to remove the excess NaH, $Zn(OTf)_2$ and mineral oil. The remaining yellow-white powder was recrystallized by evaporation from wet MeOH to afford $Zn(H_2L2)$. ^1H NMR was run on the clear crystals and showed no

substantial chemical shift difference for protons ***a*** or ***b*** (Fig. 2.2 and Fig. 2.12) between H_4L2 and the Zn(II) product. However, significant upfield shifts were observed for aryl protons ***h*** and ***k*** (Fig. 2.2 and Fig. 2.12) on the Zn(II) complex suggesting that metalation occurred at the carboxylic acid and the NNN metal pincer was not formed. This was confirmed by XRD. Supporting Information S2.2.

Zn(H_2L2) ^{1}H NMR: (400 MHz, Methanol-d_4, 293K) [δ, ppm] 8.51 – 8.44 (m, 2H, ***b***), 8.29 (s, 3H, ***a***/***h***), 7.97 (d, J = 8.1 Hz, 2H, ***g***), 7.80 (d, J = 7.8 Hz, 2H, ***k***), 7.43 (t, J = 7.9 Hz, 2H, ***i***) 4.66 (s, 4H, ***m***). FTIR (cm^{-1}): 3498.36 (m, aqua O-H stretch), 3280.65 (s, N-H stretch), 1638.22 (s, C=O stretch), 1535.80 (s, N-H wag). Crystal Data: $C_{22}H_{34}N_3O_{16}Zn$ (M = 661.89 g/mol): triclinic, space group P-1 (no. 2), a = 9.0904(4) Å, b = 11.3150(5) Å, c = 15.5045(7) Å, α = 105.9440(10)°, β = 95.497(2)°, γ = 111.525(2)°, V = 1391.59(11) $Å^3$, Z = 2, T = 173.0 K, μ(MoKα) = 0.965 mm^{-1}, D_{calc} = 1.580 g/cm^3, 11341 reflections measured (5.602° ≤ 2Θ ≤ 56.598°), 6200 unique (R_{int} = 0.0458, R_{sigma} = 0.0726) which were used in all calculations. The final R_1 was 0.0517 (I > 2σ(I)) and wR_2 was 0.1657 (all data).

2.4.1.3 Zn(H_2L3)

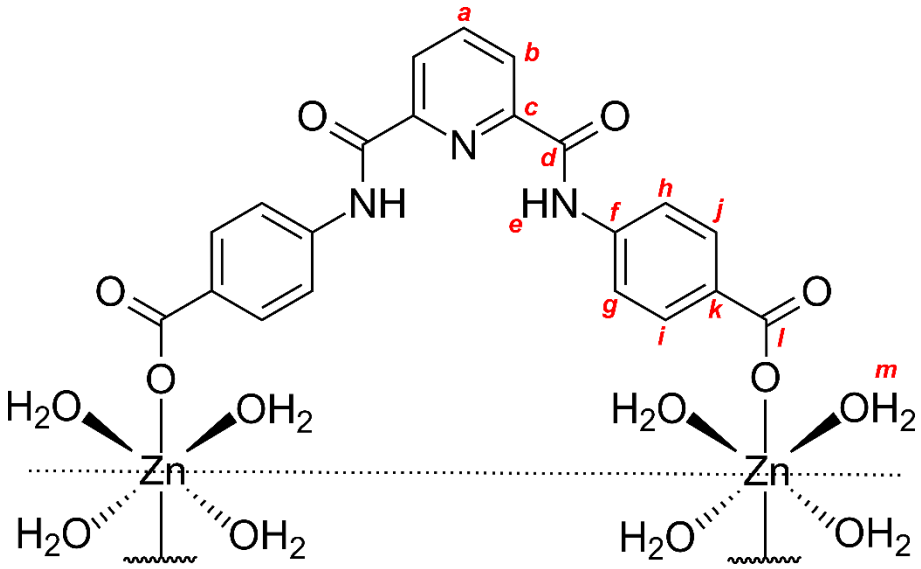


Figure 2.13: Structure and atom labelling of $Zn_2(H_2L3)_2(H_2O)_8$.

$ZnCl_2$ (41.4 mg, 0.304 mmol) was dissolved in 20 mL of dry DCM before adding H_4L3 (102 mg, 0.251 mmol) which had been dissolved in 30 mL of dry THF. The reaction mixture was refluxed at 50 °C for 18 hours open to the atmosphere. A yellow precipitate formed, and this was filtered from the reaction mixture after cooling to room temperature. The isolated product was washed with 5 mL of DCM and 10 mL of THF to yield clean Zn(H_2L3). ^{1}H NMR was run on the pale-yellow powder and confirmed unambiguously that the target pincer was not formed. The changes in chemical shift of the aryl protons between H_4L3 and Zn(H_2L3) and the presence of the amide proton signal ***e*** show that the Zn(II) ion preferentially targets the carboxylic acid functional groups over the amide pincer cleft. Similar attempts at metalation using $Zn(OAc)_2$ proved futile due to the poor solubility of the metal salt in dry organic solvents. Solid-state reactions were also performed as follows: H_4L3 (35 mg, 0.0863 mmol) and NaH 60% dispersion in mineral oil (20.7 mg, 0.518 mmol NaH) were placed in a mortar and ground with a pestle until the white ligand turned yellow. Then $Zn(OTf)_2$ (32.0 mg, 0.0880 mmol) was added to the yellow reaction mixture and vigorously ground for 10 minutes. The resulting powder was washed with 20 mL of THF, 5 mL of MeCN and 5 mL of hexane to remove the mineral oil. The remaining yellow powder is clean Zn(H_2L3). ^{1}H NMR was run on the reaction product and confirmed unambiguously that the target pincer was not formed, and the zinc(II) ion preferentially binds

carboxylates on the ligand. This is in accordance with similar attempts at metalating H_4L3 with Zn(II).[6] Supporting Information S2.3.

^{1}H NMR: (400 MHz, DMSO-d_6, 293K) [δ, ppm] 11.06 (s, 2H, ***e***), 8.44 – 8.38 (m, 2H, ***b***), 8.31 (t, *J* = 7.6 Hz, 1H, ***a***), 7.91 (d, *J* = 7.8 Hz, 4H, ***g***/***h***), 7.80 (d, *J* = 8.1 Hz, 4H, ***i***/***j***), 4.64 (s, 8H, ***m***). FTIR (cm^{-1}): 3360.14 (s, N-H stretch), 1668.64 (s, C=O stretch), 1536.25 (s, N-H wag).

2.4.1.4 Zn(H_2L4)

Metalation of H_4L4 was not attempted as it had become obvious that esterification of the carboxylic acids was necessary for the Zn(II) ion to target to the amide pincer cleft of the ligand. The ligand was made preemptively as it had one of the best docking scores out of the 11 synthetically feasible ligands characterized in this work.

2.4.2 Copper and the Carboxylic Catastrophe

Synthetic attempts were made to metalate carboxylic acid functionalized ligands at the NNN amide pincer site but proved unsuccessful. The Cu(II) ion preferentially binds carboxylates and thus esterification is absolutely necessary if the desired mononuclear metal pincer is to be formed.

2.4.2.1 Cu(H_2L1)

H_4L1 (30.7 mg, 0.0754 mmol) and $Cu(OAc)_2 \cdot H_2O$ (17.5 mg, 0.0877) were dissolved in 25 mL of MeOH and refluxed at 65 °C for 2 hours. Over the course of the reaction, a fine forest green powder was precipitated. The reaction mixture was then centrifuged at 4000 rpm to collect the powder as a pellet before discarding the solvent containing unreacted ligand and metal salt. The powder was then washed with 10 mL of MeOH to afford 17.3 mg of Cu(H_2L1). The reaction was repeated with stoichiometry H_4L1 (30.0 mg, 0.0735 mmol) and $Cu(OAc)_2 \cdot H_2O$ (44.5 mg, 0.223 mmol) to afford 35.4 mg of product. The metal complex isolated from both reactions is practically insoluble making characterization difficult. It is unclear if the increased yield from the 1:3 reaction is due to Le Chatelier's principle and the same product is obtained as the 1:1 reaction, or if the excess Cu(II) is targeting both the carboxylates and the amide cleft of the ligand thus forming a dinuclear complex. The FTIR spectra obtained for both are virtually identical and it is difficult to make concluding remarks as the tell-tale amide stretches are overshadowed by broad aqua ligand absorption. Supporting Information S2.4.

FTIR (cm^{-1}): 3572.87 (s, aqua O-H stretch), 3092.75 (m, aromatic C-H stretch), 1557.12 (s, C=O stretch).

2.4.2.2 $Cu_2(H_2L2)_2$

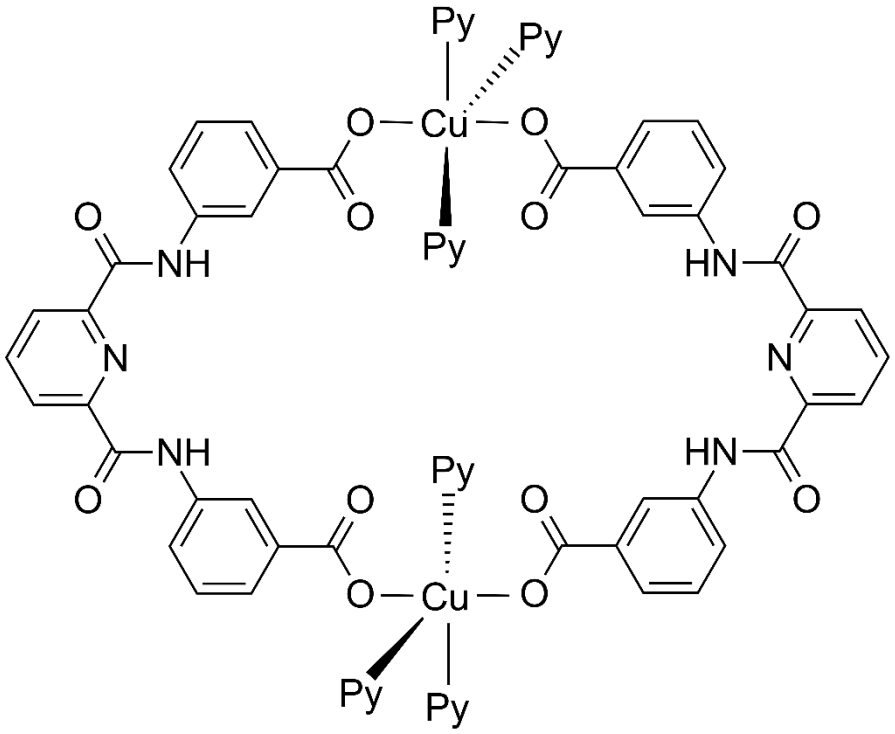


Figure 2. 14: The structure of $Cu_2(H_2L2)_2$ when crystallized from pyridine.

H_4L2 (101 mg, 0.249 mmol) was suspended in 40 mL of THF before adding 3 drops of NEt_3 to effect dissolution. Then $Cu(OTf)_2$ (91.1 mg, 0.252 mmol) which had been dissolved in 10 mL of MeCN was added to the mixture. The purple $Cu(OTf)_2$ solution changes to a brown colour after addition to the mixture before eventually turning green. The reaction was briefly heated before stirring at room temperature for 2 hours, after which a deep green precipitate had formed. The solvent was removed under reduced pressure and the solid material was collected, before being washed with 5 mL of MeCN and 100 mL of THF. An IR spectrum was obtained for the green powder. The reaction was also attempted in the solid state: H_4L2 (50.0 mg, 0.123 mmol) was placed into a mortar with NaH 60% dispersion in mineral oil (19.7 mg, 0.493 mmol NaH). The components were then ground with a pestle until the white ligand turned yellow. Then $Cu(OTf)_2$ (44.8 mg, 0.124 mmol) was added to the reaction mixture and vigorously ground until the yellow powder turned a dark green. This was then washed with 50 mL of THF, 10 mL MeCN and 5 mL of hexane. The green powder was then dissolved in pyridine and allowed to evaporate over 4 weeks to afford deep blue and green solvatochromic crystals. XRD data confirmed that the target pincer was not formed, and Cu(II) preferentially binds carboxylates on the ligand to form a

dinuclear cage complex (Fig. 2.14). Similar tetranuclear Cu(II) complexes have been synthesized previously.[7] An IR spectrum was obtained for the deep blue crystals and compared to the green powder obtained from the solvent reaction. The two spectra are very similar, suggesting the same product is formed in solution and the solid state. The small differences may be ascribed to the solvent molecules that form part of the lattice when crystalized from pyridine. Supporting Information S2.5.

FTIR (cm^{-1}): 3462.68 (w, N-H stretch), 1680.23 (s, C=O stretch), 1544.65 (s, N-H wag). Blue Crystal Data: $C_{92}H_{88.04}Cu_2N_{16}O_{18.02}$ (M = 1833.22 g/mol): triclinic, space group P-1 (no. 2), a = 15.3159(6) Å, b = 16.8888(7) Å, c = 18.9152(7) Å, α = 97.9570(10)°, β = 113.0810(10)°, γ = 96.638(2)°, V = 4379.6(3) $Å^3$, Z = 2, T = 153.0 K, μ(MoKα) = 0.565 mm^{-1}, D_{calc} = 1.390 g/cm^3, 437150 reflections measured (5.052° ≤ 2Θ ≤ 61.482°), 26824 unique (R_{int} = 0.1246, R_{sigma} = 0.0634) which were used in all calculations. The final R_1 was 0.0487 (I > 2σ(I)) and wR_2 was 0.1302 (all data). Green Crystal Data: $C_{72}H_{68}Cu_2N_{12}O_{18}$ (M = 1516.46 g/mol): monoclinic, space group $P2_1/c$ (no. 14), a = 8.6922(5) Å, b = 27.6985(15) Å, c = 15.2690(8) Å, β = 105.377(2)°, V = 3544.6(3) $Å^3$, Z = 2, T = 153.0 K, μ(MoKα) = 0.680 mm^{-1}, D_{calc} = 1.421 g/cm^3, 143320 reflections measured (4.86° ≤ 2Θ ≤ 61.332°), 10934 unique (R_{int} = 0.1169, R_{sigma} = 0.0698) which were used in all calculations. The final R_1 was 0.0557 (I > 2σ(I)) and wR_2 was 0.1430 (all data).

2.4.2.3 Cu_2(L3)

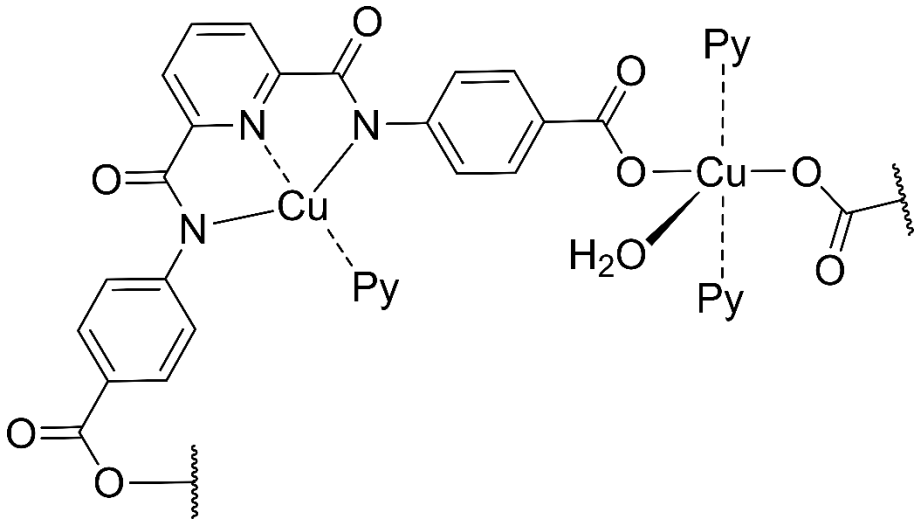


Figure 2. 15: The structure of Cu_2(L3) when crystallized from pyridine.

H_4L3 (72.0 mg, 0.178 mmol) was dissolved in 50 mL of THF before adding $Cu(OAc)_2 \cdot H_2O$ (102 mg, 0.512 mmol). The mixture was refluxed open to the atmosphere at 60 °C with gentle stirring for 18 hours. A fine lime-green precipitate formed over the reaction time which was isolated by centrifugation at 4000 rpm. The powder was then washed with 50 mL of THF to yield 95.5 mg of Cu_2(L3). The product was crystallized over two days by evaporating a mixture of pyridine and MeOH which had been saturated with the complex. This afforded small dark-green needles which were barely suitable for X-ray diffraction. The structure is a 2D MOF (metal-organic framework) and is presented in Fig. 2.15. The ligand scaffold has been metallated previously with Zn(II) and Cd(II) to form 2D MOF's.[8] Supporting information S2.6.

FTIR (cm^{-1}): 3339.84 (m, aqua O-H stretch), 1670.11 (s, C=O stretch), 1602.97 (s, C=O stretch). Crystal Data: $C_{72}H_{56}Cu_4N_{12}O_{14}$ (M = 1567.44 g/mol): monoclinic, space group *C*2 (no. 5), a = 36.605(5) Å, b = 16.354(2) Å, c = 16.399(2) Å, β = 111.797(4)°, V = 9116(2) Å3, Z = 4, T = 173.00 K, μ(MoKα) = 0.977 mm^{-1}, D_{calc} = 1.142 g/cm^3, 79338 reflections measured (2.764° ≤ 2Θ ≤ 50°), 15612 unique (Rint = 0.1950, Rsigma = 0.1385) which were used in all calculations. The final R1 was 0.0743 (I > 2σ(I)) and wR2 was 0.2289 (all data).

2.4.2.4 Cu(H_2L4)

Metalation of H_4L4 was not attempted as it had become obvious that esterification of the carboxylic acids was necessary for the Cu(II) ion to target to the amide pincer cleft of the ligand. The ligand was synthesized preemptively as it had one of the best docking scores out of the 11 ligands successfully characterized in this work.

2.4.3 Zinc Pincers

2.4.3.1 $Zn(L5)(H_2O)_2$

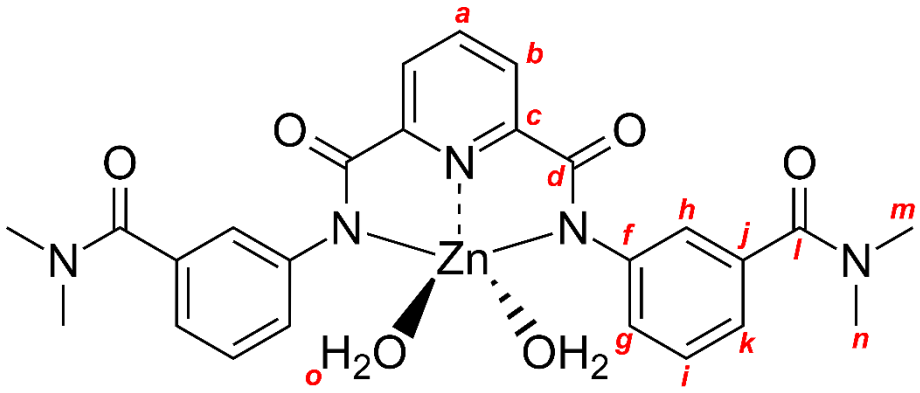


Figure 2.16: Structure and atom labelling of $Zn(L5)(H_2O)_2$.

H_2L5 (52.7 mg, 0.115 mmol) was dissolved in 25 mL of freshly distilled MeCN before adding NaH 60% dispersion in mineral oil (18.6 mg, 0.465 mmol NaH). The golden-brown solution containing H_2L5 started bubbling and the sodium salt of the ligand precipitated out as a white powder leaving the solution a pale yellow. The mixture was gently stirred at room temperature for 30 minutes before adding $Zn(OTf)_2$ (44.5 mg, 0.122 mmol). The reaction mixture was then refluxed at 85 °C open to the atmosphere for 24 hours. After the reaction time, the white precipitate had been replaced with a pale-yellow powder. The mixture was allowed to cool to room temperature before filtering the solution and isolating the pale-yellow product, $Zn(L5)(H_2O)_2$ (12.6 mg, 20% yield). Supporting information S3.1.

^{1}H NMR: (400 MHz, DMSO-d_6, 293K) [δ, ppm] 7.83 (q, J = 7.5, 7.1 Hz, 3H, ***a***/***b***), 6.97 – 6.88 (m, 4H, ***g***/***h***), 6.74 (t, J = 7.8 Hz, 2H, ***i***), 6.51 (d, J = 7.4 Hz, 2H, ***k***), 3.39 (s, 4H, ***o***), 2.84 (s, 6H, ***m*** or ***n***), 2.66 (s, 6H, ***m*** or ***n***). ^{13}C NMR: (100 MHz, DMSO-d_6, 293K) [δ, ppm] 171.45 (***l***), 162.57 (***d***), 151.60 (***c***), 151.38 (***f***), 139.70 (***a***), 135.34 (***j***), 126.95 (***i***), 125.65 (***g***), 123.47 (***h***), 121.17 (***b***), 118.49 (***k***), 35.00 (***m*** and ***n***). FTIR (cm^{-1}): 3380 (s, O-H stretch), 2931 (m, methyl stretch), 1599 (s, C=O stretch).

The aqua ligand was easily identified in the FTIR spectrum, but an assumption was made about the number of coordinated water molecules. A CSD analysis of the coordination geometries for divalent zinc show that the metal cation may be 4, 5 or 6 coordinate but there is a preference for

zinc(II) to adopt four-coordinate geometry.[9,10] However, a CSD search of similar Zn(II) pincers shows that the NNN coordination environment favours a 5-coordinate metal centre.[11,12,13] Hence, it is assumed that Zn(L5) was synthesized with two aqua ligands and the isolated product is $Zn(L5)(H_2O)_2$. This is supported by NMR data which shows a water peak at 3.39 ppm that integrates for four protons.

The pale-yellow powder $Zn(L5)(H_2O)_2$ was left exposed to the atmosphere and after a few days the powder became white. ^1H NMR was run on the white powder and showed that the metalation reaction had been reversed and the ligand amide signal had returned. The stability of the Zn(II) complex had come into question and water was suspected to be responsible for demetallation of the NNN pincer ligand. This was easily confirmed with NMR. $Zn(L5)(H_2O)_2$ was dissolved in DMSO-d_6 and ^1H NMR confirmed that the desired metal pincer had formed and was pure. The sample was then lyophilized to remove the DMSO-d_6 and the yellow powder remained. Then the powder was suspended in distilled water, at which point the powder turned from pale-yellow to white. The water was then removed by lyophilization and the remaining solid was redissolved in DMSO-d_6 before running ^1H NMR. This confirmed unambiguously that demetallation of the ligand occurred in the presence of water and the compound would not be suitable for biological applications.

Attempts to crystalize Zn(L5) by vapour diffusion of hexane into EtOH resulted in a white powder crashing out of solution. This precipitate was analyzed by ^1H NMR and showed that demetallation had occurred and the sample contained ligand with none of the desired product. A broad signal was also observed at 4.36 ppm which is tentatively assigned $Zn(OH)_2$ based on literature references.[14,15] Thus the proposed demetallation reaction is presented:

$$Zn(L5)(H_2O)_2 + 2H_2O \rightarrow H_2L5 + Zn(OH)_2(H_2O)_2$$

2.4.3.2 Zn(H_2L6)

H_4L6 (57.7 mg, 0.118 mmol) was dissolved in 15 mL of dry DMF before adding NaH 60% dispersion in mineral oil (22.2 mg, 0.555 mmol NaH). The mixture was then gently stirred for 30 minutes or until the bubbling stopped, after which the solution became yellow. Then $ZnCl_2$ (16.7 mg, 0.123 mmol) was added, and the mixture refluxed at 95 °C open to the atmosphere for 24 hours. After the reaction time, the solvent was removed under reduced pressure at 80 °C to leave a white and yellow powder. It was suspected that the white powder was unreacted H_4L6 while the yellow powder was the target complex. A ^{1}H NMR spectrum was recorded for the mixture to confirm that the product had been synthesized and if purification was worth pursuing. The NMR showed that there was some unreacted ligand but the majority of signals had become more shielded suggesting that the d^{10} Zn(II) ion had successfully occupied the NNN coordination site. The aryl protons ***k*** (Fig. 2.6) had become more shielded in the complex and the integration of these was used to determine the purity of the powder isolated from the reaction. It was found that the ratio of H_4L6 to Zn(H_2L6) was roughly 1:2.7. It had been shown that the Zn(II) NNN pincer was susceptible to demetallation in water and so this was explored before any further purification was attempted. The NMR sample was freeze dried to remove DMSO-d_6 and the remaining powder containing Zn(H_2L6) was suspended in distilled water. The water was then removed by freeze drying before redissolving the sample in DMSO-d_6 and running the ^{1}H NMR experiment. The spectra showed that demetallation had occurred and the sample contained only H_4L6. Hence, due to the Zn(II) pincer's instability in water the compound would not be suitable for biological application and further clean up would be futile. Supporting information S3.2.

2.4.3.3 Zn(H_2L7), Zn(H_2L8), Zn(H_2L9) and Zn(L10)

Attempts to metalate ligands H_4L7, H_4L8, H_4L9 and H_2L10 were made but yielded no results. The synthetic methods employed were similar to Zn(L5)(H_2O)$_2$ and Zn(H_2L6), where NaH was used to deprotonate the ligand and either $ZnCl_2$ or Zn(OTf)$_2$ was used as a source of metal ions. Often no product was identified from the reaction. In cases where a yellow powder was observed this served as visual evidence that the Zn(II) complex may have formed. However, these yellow powders quickly turned white in air or when exposed to wet solvents like MeOH. It was thus assumed that any product that may have formed was not water stable as was shown for Zn(L5)(H_2O)$_2$ and Zn(H_2L6). Hence, at this point, the Zn(II) pincers were abandoned and no further synthetic attempts were made.

2.4.4 Copper Pincers

2.4.4.1 Cu(L5)(H_2O)

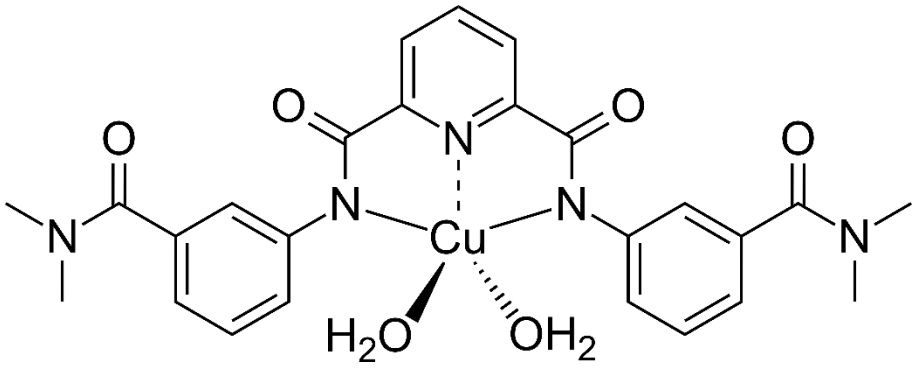


Figure 2.17: The structure of Cu(L5) in aqueous solution.

H_2L5 (98.9 mg, 0.215 mmol) was dissolved in 25 mL of dry THF to afford a honey-colored solution. Then NaH 60% dispersion in mineral oil (21.4 mg, 0.535 mmol NaH) was added to the mixture and gently stirred for 10 minutes or until the bubbling stopped. The sodium salt of the ligand precipitated out as a white powder leaving the solution pale-yellow. Then $Cu(OTf)_2$ (102 mg, 0.282 mmol) was added to the mixture and the solution allowed to reflux at 66 °C open to the atmosphere for 18 hours. Immediately after the addition of $Cu(OTf)_2$ the solution began to turn green, and a powder started to precipitate. After the reaction time, the white precipitate had been completely replaced with a dark green powder. This was filtered after cooling to room temperature and then washed with 5 mL of THF and 5 mL of hexane to afford 95.0 mg of product. This was crystalized by vapour diffusion of Et_2O into a saturated MeOH solution over 3 weeks at ambient temperature. The crystals obtained were small, green plates and the X-ray structure was solved. The structure contains NaOTf, hence the powder obtained from the reaction was not pure. The synthetic methods were thus revised to obtain clean Cu(L5).

H_2L5 (108.5 mg, 0.236 mmol) was dissolved in 25 mL of THF before adding $Cu(OAc)_2{\cdot}H_2O$ (154.6 mg, 0.774 mmol) to the mixture. The solution immediately began to turn green before a fine powder was precipitated. The mixture was refluxed at 70 °C open to the atmosphere for 6 hours. After the reaction time, the solution was allowed to cool to room temperature before filtering the mixture and isolating a dark green powder. This was washed with 2 mL of THF to yield clean Cu(L5)(H_2O) (19.4 mg, 15%). Attempts to improve the yield were made by increasing the reaction time.

H_2L5 (105.9 mg, 0.230 mmol) was dissolved in 25 mL of THF before adding $Cu(OAc)_2 \cdot H_2O$ (156.8 mg, 0.785 mmol) to the mixture. The reaction was refluxed at 55 °C open to the atmosphere while being gently stirred for 18 hours. After the reaction time, the mixture was allowed to cool to room temperature before being filtered and isolating a dark green powder. This was washed with 2 mL of THF to yield clean Cu(L5)(H_2O) (24.3 mg, 19.5%). This was a marginal improvement, so the reaction time was increased further. H_2L5 (105.8mg, 0.230 mmol) was dissolved in 25 mL of THF before adding $Cu(OAc)_2 \cdot H_2O$ (158.2 mg, 0.792 mmol) to the mixture. The reaction was then stirred at room temperature open to the air for 48 hours. After this, the solution was filtered, and the collected precipitate was washed with 2 mL of THF. The remaining green powder was clean Cu(L5)(H_2O) (42.2 mg, 34%). At this point it became clear that the yields were being affected by recovery. The copper complex has partial solubility in THF, and a substantial amount of the product remains in solution after it has formed in the reaction. This may be mitigated by allowing the reaction mixture to stand for some time at low temperatures or removing the solvent under reduced pressure and then replacing with 25 mL of THF before filtering. Nevertheless, the powder that forms is fine enough to pass through filter paper and the recovery is diminished.

Hence, the following method was developed: H_2L5 (107.2 mg, 0.233 mmol) was dissolved in 25 mL of THF to afford a honey-colored solution. Then $Cu(OAc)_2 \cdot H_2O$ (152.9 mg, 0.766 mmol) was added to the mixture at which point the solution begins to turn a deep green. The reaction was refluxed at 60 °C open to the air for 18 hours. After this time, the mixture is allowed to stand at -20 °C for at least one hour before centrifugation at 4000 rpm for 5 minutes. This allowed a dark green pellet of Cu(L5)(H_2O) to be collected; the solvent containing unreacted metal salt and ligand was discarded. The powder was then resuspended in 25 mL of THF and briefly sonicated to ensure any co-precipitated starting material was removed from the solid state. The mixture was again centrifuged at 4000 rpm for 5 minutes, after which the pellet was kept, and the solvent discarded. Finally, 5 mL of THF was used to gather the green pellet which was then filtered under vacuum. The forest green powder that remains in clean Cu(L5)(H_2O), (54.3 mg, 43%). The copper complex was crystalized by vapour diffusion of Et_2O into a saturated MeOH solution over 5 weeks at 4 °C. The X-ray quality crystals obtained were clear, dark green plates and the solution-state structure is presented in Fig. 2.17. Supporting Information S4.1.

FTIR (cm^{-1}): 3402.91 (m, O-H stretch), 2930.57 (m, CH_3 stretch), 1689.14 (w, O-H wag), 1597.23 (s, C=O stretch). HRMS (m/z) $C_{25}H_{23}CuN_5O_4$ $[M + H_2O + Na^+]^+$: calc 561.104388; found 561.31549. Error -376.22 ppm or -0.037622%. UV-Vis (H_2O) λ [nm] ($\varepsilon/M^{-1}cm^{-1}$): 230 (26 100),

310 (7080), 640 (208). Crystal Data: $C_{156}H_{162}Cu_6N_{30}O_{30}$ (M = 3318.39 g/mol): monoclinic, space group $C2/c$ (no. 15), a = 33.5199(11) Å, b = 19.1604(6) Å, c = 28.5691(10) Å, β = 105.9930(10)°, V = 17638.5(10) Å^3, Z = 4, T = 153.0 K, μ(MoKα) = 0.783 mm^{-1}, D_{calc} = 1.250 g/cm^3, 515044 reflections measured (2.472° ≤ 2Θ ≤ 61.124°), 26998 unique (R_{int} = 0.0696, R_{sigma} = 0.0274) which were used in all calculations. The final R_1 was 0.0484 (I > 2σ(I)) and wR_2 was 0.1369 (all data).

2.4.4.2 Cu(H_2L6)(MeOH)

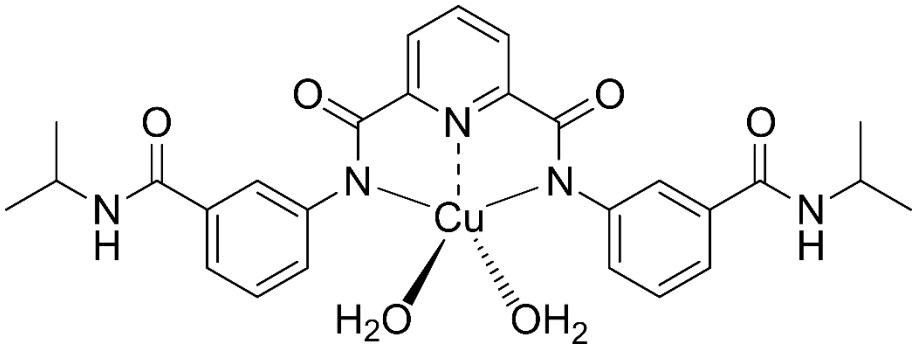


Figure 2.18: The structure of Cu(H_2L6) in aqueous solution.

H_4L6 (151 mg, 0.310 mmol) was dissolved in 12 mL of DMF before adding $Cu(OAc)_2 \cdot H_2O$ (216 mg, 1.08 mmol). The solution immediately begins to turn a dark green after addition of the metal salt. The mixture was gently stirred at 80 °C open to the atmosphere for 18 hours. The solvent was then removed under reduced pressure at 80 °C to leave a mixture of green, white, and blue powder in the round bottom flask. Then 15 mL of cold MeOH which had been stored at -20 °C was added to the flask to dissolve the copper complex and afford a deep green solution while most of the ligand and $Cu(OAc)_2 \cdot H_2O$ remained as a precipitate. This mixture was then filtered under vacuum close to the freezing point of MeOH with the use of liquid nitrogen. The filtrate was dark green while the collected precipitate contained most of the unreacted ligand and $Cu(OAc)_2 \cdot H_2O$. The filtrate was collected and then stored at -20 °C overnight after which more H_4L6 and $Cu(OAc)_2 \cdot H_2O$ had precipitated out of the green solution. The mixture was brought close to the freezing point of MeOH using liquid nitrogen before being passed through a 0.45μm PVDF or PTFE hydrophobic syringe filter. The filtrate at this point contains only small amounts of ligand and metal salt. The MeOH was removed under reduced pressure at 50 °C to leave a green powder in the 50 mL round bottom flask. Then 30 mL of EtOAc was added to the flask and vigorously stirred at 75 °C for 30 minutes. After this, the EtOAc solution had taken on a faint blue colour while the copper complex remained as a dark green powder. The mixture was filtered while hot and the filtrate was found to contain the last traces of unreacted ligand. The powder now contains only traces of $Cu(OAc)_2 \cdot H_2O$, which is removed by stirring the solid in 30 mL of a 1:3 THF:EtOAc mixture for 30 minutes at room temperature. The mixture was then centrifuged at 4000 rpm for 3 minutes before discarding the solvent containing the last of the unreacted metal salt. The deep green pellet was then collected using 10 mL of the 1:3

THF:EtOAc mixture before filtering under vacuum. The powder that remains is Cu(H_2L6)(MeOH), (50.1 mg, 28%). The copper chelate was crystallized by vapour diffusion of Et_2O into a saturated MeOH solution over 5-10 weeks at 4 °C and -20 °C. The crystals were poor quality, fragile, clear-green plates but the X-ray structure was obtained. However, better quality crystals were obtained by evaporating a saturated mixture of MeOH and Et_2O at 4 °C over 6 months. The solution-state structure is presented in Fig. 2.18. Supporting Information S4.2.

FTIR (cm^{-1}): 3478.06 (m, O-H stretch), 2970.68 (m, isopropyl stretch), 1633.63 (s, C=O stretch). HRMS $C_{27}H_{27}CuN_5O_4$ $[M + H_2O + Na^+]^+$: calc 589.135688; found 589.34698. Error -358.64 ppm or -0.035864%. UV-Vis (H_2O) λ [nm] (ε/$M^{-1}cm^{-1}$): 205 (57 000), 250 (20 700), 310 (7220), 620 (269). Crystal Data: $C_{163.27}H_{169.64}Cu_6N_{30}O_{26.55}$ (M = 3358.20 g/mol): triclinic, space group P-1 (no. 2), a = 16.5532(8) Å, b = 17.7078(8) Å, c = 17.8111(8) Å, α = 61.632(2)°, β = 74.172(2)°, γ = 83.485(2)°, V = 4418.9(4) $Å^3$, Z = 1, T = 173.00 K, μ(MoKα) = 0.781 mm^{-1}, D_{calc} = 1.262 g/cm^3, 227279 reflections measured (3.622° ≤ 2Θ ≤ 53.448°), 18564 unique (R_{int} = 0.1730, R_{sigma} = 0.0732) which were used in all calculations. The final R_1 was 0.0661 (I > 2σ(I)) and wR_2 was 0.2152 (all data).

2.4.4.3 Cu(H_2L7)

Attempts at metalating H_4L7 were not made as it was suspected that the isoindoledione may produce off-target chelates. However, in retrospect, it seems likely that the Cu(II) ion would preferentially bind the NNN pincer cleft of the ligand. It seems feasible to produce Cu(H_2L7) using similar synthetic methods already employed for the Cu(II) pincers successfully characterized in this work.

2.4.4.4 Cu(H$_2$L8)(H$_2$O)

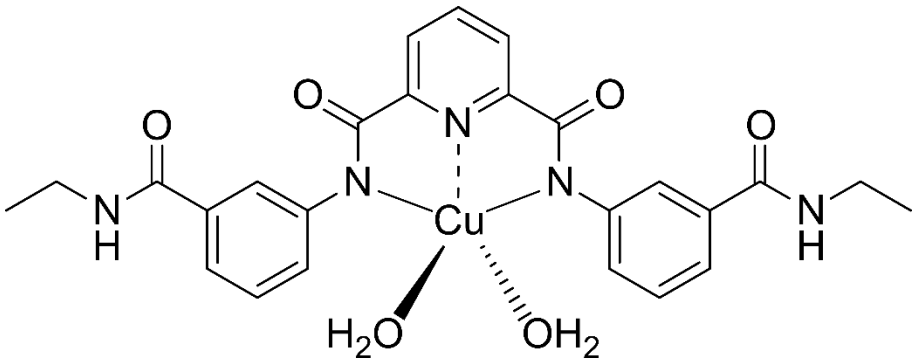


Figure 2.19: The structure of Cu(H$_2$L8) in aqueous solution.

H$_4$L8 (102 mg, 0.223 mmol) was mostly dissolved in 100 mL of THF before adding Cu(OAc)$_2$·H$_2$O (154.0 mg, 0.771 mmol) to the mixture. Soon after addition of the metal salt, the solution began to turn green, and a precipitate started to form. The reaction was gently stirred at room temperature open to the air for 3 days. After this, the mixture was centrifuged at 4000 rpm for 3 minutes to isolate a light green pellet and the solvent containing unreacted material was discarded. The powder was resuspended in 50 mL of THF and briefly sonicated before centrifugation at 4000 rpm for 3 minutes. The solvent was then discarded and 5 mL of fresh THF was used to gather the lime-coloured pellet for vacuum filtration. The remaining green powder is Cu(H$_2$L8)(H$_2$O) (80.0 mg, 67%). Due to the poor solubility of the ligand, the reaction was repeated under slightly different conditions as follows: H$_4$L8 (106.7 mg, 0.232 mmol) was dissolved in 250 mL of THF to afford a clear, colourless solution. Then Cu(OAc)$_2$·H$_2$O (153.0 mg, 0.766 mmol) was added to the mixture at which point the reaction began to turn a deep Sparletta™ green. After a short while, the copper chelate concentration becomes high enough that the product precipitates out leaving the solution a pale yellow-green. The reaction was vigorously stirred under reflux at 60 °C open to the air for 18 hours. The mixture was then centrifuged at 4000 rpm while still warm to isolate a light lime-green pellet. The solvent was discarded and then replaced with 60 mL of fresh THF before brief sonication and then centrifugation at 4000 rpm for 5 minutes. The solvent was discarded and then 5 mL of THF was used to gather the pellet before filtering under vacuum. The light green powder that remains is Cu(H$_2$L8)(H$_2$O) (88.3 mg, 71%). The reaction was repeated with 250 mL of THF but was allowed to reflux at 64 °C for 12 days. This yielded 102.7 mg (82%) of a dark green powder. Vapour diffusion of Et$_2$O into a saturated MeOH solution containing the lime-green product produced crystals overnight at ambient temperature. The needles that grow are flimsy and

poorly diffracting, but the X-ray structure was obtained. Crystals may also be obtained by vapour diffusion of Et_2O into a saturated mixture of EtOH and MeOH. This produced block-like crystals over 5 weeks at ambient temperature. The X-ray structure was obtained, and the solution-state structure is presented in Fig 2.19. Supporting Information S4.3.

FTIR (cm^{-1}): 3566.70 (m, O-H stretch), 2935.99 (w, CH_3 stretch), 1682.74 (w, O-H wag), 1625.84 (s, C=O stretch). HRMS (m/z) $C_{25}H_{23}CuN_5O_4$ $[M + DMSO + H]^+$: calc 599.12583; found 599.12445. Error -2.2950 ppm or 0.002%. UV-Vis (H_2O) λ [nm] ($\varepsilon/M^{-1}cm^{-1}$): 220 (36 500), 300 (7530), 610 (228). Crystal Data: $C_{180}H_{212.94}Cu_6N_{30}O_{40}$ (M = 3817.97 g/mol): triclinic, space group P-1 (no. 2), a = 16.1679(16) Å, b = 18.1100(14) Å, c = 18.7602(17) Å, α = 77.450(3)°, β = 78.909(4)°, γ = 71.509(4)°, V = 5039.5(8) $Å^3$, Z = 1, T = 150.00 K, μ(MoKα) = 0.698 mm^{-1}, D_{calc} = 1.258 g/cm^3, 165694 reflections measured (3.554° ≤ 2Θ ≤ 51.998°), 19808 unique (R_{int} = 0.0809, R_{sigma} = 0.0470) which were used in all calculations. The final R_1 was 0.1092 (I > 2σ(I)) and wR_2 was 0.2834 (all data).

2.4.4.5 Cu(H_2L9)(H_2O)

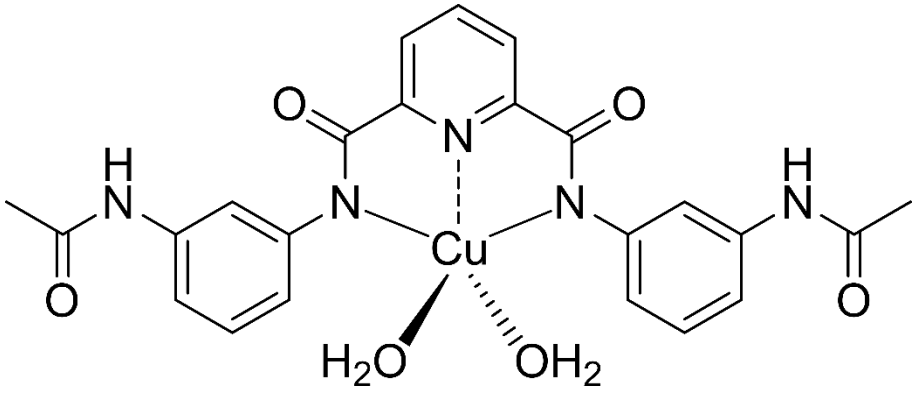


Figure 2.20: The structure of Cu(H_2L9) in aqueous solution.

H_4L9 (105 mg, 0.244 mmol) was mostly dissolved in 150 mL of THF before adding $Cu(OAc)_2{\cdot}H_2O$ (168.1 mg, 0.842 mmol) to the mixture. The resulting solution was vigorously stirred for 18 hours open to the air while under reflux at 66 °C. As the reaction proceeded, the solution turned a deep green before precipitating out the product and as this happened the remaining undissolved ligand went into solution. After the 18 hours, the mixture was allowed to cool to room temperature before being filtered under vacuum. The isolated lime-green powder was then washed with 20 mL of THF to afford Cu(H_2L9)(H_2O) (94.1 mg, 76%). Attempts to improve the yield were made by ensuring that the ligand was completely dissolved before addition of the metal salt. H_4L9 (152 mg, 0.352 mmol) was dissolved in 250 mL of THF before adding $Cu(OAc)_2{\cdot}H_2O$ (240.0 mg, 1.20 mmol) to the mixture. The reaction was then vigorously stirred for 24 hours open to the atmosphere while under reflux at 66 °C. The mixture was then centrifuged at 4000 rpm for 3 minutes to isolate a light-green pellet while the solvent containing unreacted material was discarded. Then 60 mL of fresh THF was used to resuspend the powder before centrifugation at 4000 rpm for 3 minutes. The solvent was discarded, and the pellet was collected using 5 mL of THF before being filtered under vacuum. The lime-green powder that remains is Cu(H_2L9)(H_2O) (103 mg, 57%). Hence, it is better to have a higher concentration of reactants and allow the ligand to fully dissolve over time as the equilibrium shifts upon chelate precipitation. The complex was crystalized by vapour diffusion of DCM into a saturated MeOH solution over 6 months at ambient temperature. The crystals that grow are green hexagonal prisms. The X-ray structure was obtained, and the solution-state structure is presented in Fig 2.20. Supporting Information S4.4.

FTIR (cm^{-1}): 3488.42 (m, O-H stretch), 3259.70 (m, acetamide N-H stretch), 1666.53 (s, C=O stretch). HRMS (m/z) $C_{23}H_{19}CuN_5O_4$ $[M + H]^+$: calc 493.08058; found 493.07983. Error -1.5 ppm or -0.0001 %. UV-Vis (DMSO) λ [nm] ($\varepsilon/M^{-1}cm^{-1}$): 270 (16 800), 330 (7230), 655 (287). Crystal Data: $C_{138}H_{165.666667}Cu_6N_{30}O_{49.833333}$ (M = 3423.30 g/mol): trigonal, space group R-3 (no. 148), a = 18.3593(9) Å, c = 39.415(3) Å, V = 11505.5(14) $Å^3$, Z = 3, T = 173.00 K, μ(MoKα) = 0.912 mm^{-1}, D_{calc} = 1.482 g/cm^3, 237319 reflections measured (4.438° ≤ 2Θ ≤ 56.726°), 6397 unique (R_{int} = 0.0756, R_{sigma} = 0.0208) which were used in all calculations. The final R_1 was 0.0375 (I > 2σ(I)) and wR_2 was 0.1063 (all data).

2.4.4.6 Cu(L10)(H_2O)

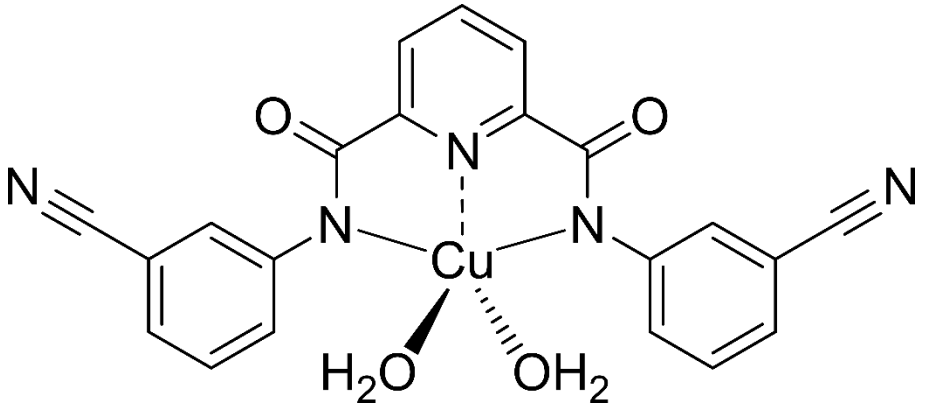


Figure 2.21: The structure of Cu(L10) in aqueous solution.

H_2L10 (105 mg, 0.287 mmol) was dissolved in 50 mL of THF before adding $Cu(OAc)_2 \cdot H_2O$ (100.6 mg, 0.504 mmol) to the mixture. Instantly, a light-green precipitate began to form. The reaction was refluxed at 50 °C open to the air for 24 hours. The mixture was then allowed to cool to room temperature before filtering under vacuum. The isolated green powder was then washed with 10 mL of THF to yield Cu(L10)(H_2O), (22.0 mg, 17%). The stoichiometry was adjusted to improve the yield as follows: H_2L10 (101 mg, 0.275 mmol) was dissolved in 50 mL of THF before adding $Cu(OAc)_2 \cdot H_2O$ (185.5 mg, 0.929 mmol) to the mixture. The reaction was refluxed at 50 °C open to the air for 24 hours. The mixture was then allowed to cool to room temperature before filtering under vacuum. The isolated lime-green powder was then washed with 10 mL of THF to yield Cu(L10)(H_2O), (59.8 mg, 49%). The synthesis was attempted using NaH and $Cu(OTf)_2$ with a yield of 35%, however these isolated powders contain some NaOTf. In any case, the $Cu(OAc)_2 \cdot H_2O$ reactions are more atom economical. The copper chelate may be crystalized by evaporation from a mixture of MeOH and EtOAc over 3 weeks at ambient temperatures. Similar crystals can be grown by vapour diffusion of Et_2O into a saturated MeOH solution containing Cu(L10) over 2-4 weeks at ambient temperature, 4 °C and -20 °C. The forest-green crystals are generally poor quality, but X-ray suitable single-crystals were found, and the structure is presented in Fig. 2.20. Supporting Information S4.5.

FTIR (cm^{-1}): 3626.76 (w, O-H stretch), 3066.06 (w, aromatic C-H stretch), 2226.17 (s, nitrile stretch), 1626.57 (s, C=O stretch). HRMS (m/z) $C_{21}H_{11}CuN_5O_2$ $[M + DMSO + H]^+$: calc 507.04209; found 507.04175. Error -0.6 ppm or -0.00001 %. UV-Vis (H_2O:DMSO {9:1}) λ [nm] ($\varepsilon/M^{-1}cm^{-1}$): 250 (14 100), 290 (11 200), 635 (203). Crystal Data: $C_{128}H_{78}Cu_6N_{30}O_{16}$ (*M* =

2673.44 g/mol): triclinic, space group *P*-1 (no. 2), *a* = 12.8621(7) Å, *b* = 14.6778(8) Å, *c* = 17.1404(9) Å, *α* = 76.085(2)°, *β* = 70.053(2)°, *γ* = 81.249(2)°, *V* = 2943.8(3) Å^3, *Z* = 1, *T* = 173.0 K, μ(MoKα) = 1.145 mm^{-1}, D_{calc} = 1.508 g/cm^3, 427398 reflections measured (4.23° ≤ 2Θ ≤ 56.834°), 14733 unique (R_{int} = 0.1383, R_{sigma} = 0.0338) which were used in all calculations. The final R_1 was 0.0430 (I > 2σ(I)) and wR_2 was 0.1228 (all data).

2.4.4.7 Cu(L11)(MeOH)

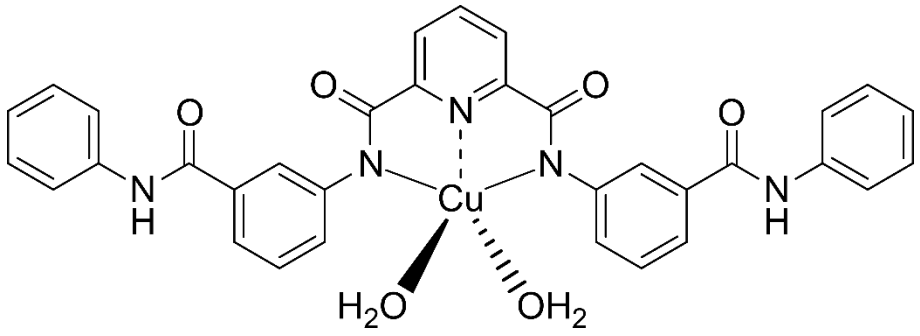


Figure 2.22: The structure of Cu(H_2L11) in aqueous solution.

H_4L11 (104.1 mg, 0.187 mmol) was dissolved in 15 mL of DMF before adding $Cu(OAc)_2{\cdot}H_2O$ (124.5 mg, 0.624 mmol) to the mixture. Immediately after addition of the metal salt, the solution began to turn a dark green. The reaction was gently stirred at 40 °C open to the air for 18 hours. After the reaction, the solvent was removed under reduced pressure at 80 °C to leave a mixture of green, white, and blue powders in the round bottom flask. Then 20 mL of cold MeOH, which had been stored at –20 °C, was added to the flask. The solution turns a deep green while most of the ligand and $Cu(OAc)_2{\cdot}H_2O$ remain as a precipitate. The mixture was then filtered under vacuum close to the freezing point of MeOH with the use of liquid nitrogen. The filtrate contains the copper chelate while most of the ligand and metal salt remain as precipitate. If the powder still has a faint green hue, it can be washed with a minimal amount of cold MeOH. The filtrate was collected and then stored at –20 °C for 3 days after which more H_4L11 and $Cu(OAc)_2{\cdot}H_2O$ had precipitated out of the green solution. The mixture was brought close to the freezing point of MeOH using liquid nitrogen before being passed through a 0.45 µm PVDF or PTFE hydrophobic syringe filter. The filtrate at this point contains only small amounts of ligand and metal salt. The MeOH was removed under reduced pressure at 50 °C to leave a green powder in the round bottom flask. Then 30 mL of EtOAc was added to the flask and vigorously stirred at 75 °C for 30 minutes. After this, the EtOAc solution had taken on a faint blue colour while the copper complex remained as a dark green powder. The mixture was filtered while hot and the filtrate was found to contain the last traces of unreacted ligand. The powder now contained only traces of $Cu(OAc)_2{\cdot}H_2O$, which was removed by stirring the solid in 30 mL of a 1:3 THF:EtOAc mixture for 30 minutes at room temperature. The mixture was then centrifuged at 4000 rpm for 3 minutes before discarding the solvent containing the last of the unreacted metal salt. The deep

green pellet was then collected using 10 mL of the 1:3 THF:EtOAc mixture before filtering under vacuum. The powder that remained was dark-green Cu(H_2L11)(MeOH) (57.4 mg, 47%). Numerous attempts at crystallization were made but proved unsuccessful. Supporting Information S4.6.

FTIR (cm^{-1}): 3498.74 (m, O-H stretch), 3284.16 (m, N-H stretch), 1722.06 (w, O-H wag), 1649.23 (s, C=O stretch). HRMS (m/z) $C_{33}H_{23}CuN_5O_4$ $[M + DMSO + H]^+$: calc 695.12582; found 695.12408. UV-Vis (H_2O:DMSO {1:1}) λ [nm] (ε/$M^{-1}cm^{-1}$): 300 (15 800), 400 (927), 650 (221).

References

(1) Park, J.; Chen, Y.-P.; Perry, Z.; Li, J.-R.; Zhou, H.-C. Preparation of Core–Shell Coordination Molecular Assemblies via the Enrichment of Structure-Directing “Codes” of Bridging Ligands and Metathesis of Metal Units. *J. Am. Chem. Soc.* **2014**, *136* (48), 16895–16901. https://doi.org/10.1021/ja508822r.

(2) Lee, H. J.; Cho, W.; Jung, S.; Oh, M. Morphology-Selective Formation and Morphology-Dependent Gas-Adsorption Properties of Coordination Polymer Particles. *Adv. Mater.* **2009**, *21* (6), 674–677. https://doi.org/10.1002/adma.200802485.

(3) Achar, T. K.; Ramakrishna, K.; Pal, T.; Porey, S.; Dolui, P.; Biswas, J. P.; Maiti, D. Regiocontrolled Remote C−H Olefination of Small Heterocycles. *Chem. – Eur. J.* **2018**, *24* (68), 17906–17910. https://doi.org/10.1002/chem.201804351.

(4) Brooks, S. J.; García-Garrido, S. E.; Light, M. E.; Cole, P. A.; Gale, P. A. Conformational Control of Selectivity and Stability in Hybrid Amide/Urea Macrocycles. *Chem. - Eur. J.* **2007**, *13* (12), 3320–3329. https://doi.org/10.1002/chem.200601647.

(5) Fleischer, E. B.; Shachter, A. M. Coordination Oligomers and a Coordination Polymer of Zinc Tetraarylporphyrins. *Inorg. Chem.* **1991**, *30* (19), 3763–3769. https://doi.org/10.1021/ic00019a038.

(6) Karmakar, A.; Soliman, M. M. A.; Rúbio, G. M. D. M.; Guedes da Silva, M. F. C.; Pombeiro, A. J. L. Synthesis and Catalytic Activities of a Zn(II) Based Metallomacrocycle and a Metal–Organic Framework towards One-Pot Deacetalization-Knoevenagel Tandem Reactions under Different Strategies: A Comparative Study. *Dalton Trans.* **2020**, *49* (24), 8075–8085. https://doi.org/10.1039/D0DT01312A.

(7) Karmakar, A.; Soliman, M. M. A.; Alegria, E. C. B. A.; Rúbio, G. M. D. M.; Guedes da Silva, M. F. C.; Pombeiro, A. J. L. A Copper-Amidocarboxylate Based Metal Organic Macrocycle and Framework: Synthesis, Structure and Catalytic Activities towards Microwave Assisted Alcohol Oxidation and Knoevenagel Reactions. *New J. Chem.* **2019**, *43* (25), 9843–9854. https://doi.org/10.1039/C9NJ02064K.

(8) Kumar, G.; Pachisia, S.; Kumar, P.; Kumar, V.; Gupta, R. Zn- and Cd-based Coordination Polymers Offering H-Bonding Cavities: Highly Selective Sensing of $S_2O_7^{2-}$ and Fe^{3+} Ions. *Chem. – Asian J.* **2019**, *14* (24), 4594–4600. https://doi.org/10.1002/asia.201901142.

(9) Kuppuraj, G.; Dudev, M.; Lim, C. Factors Governing Metal−Ligand Distances and Coordination Geometries of Metal Complexes. *J. Phys. Chem. B* **2009**, *113* (9), 2952–2960. https://doi.org/10.1021/jp807972e.

(10) Dudev, M.; Wang, J.; Dudev, T.; Lim, C. Factors Governing the Metal Coordination Number in Metal Complexes from Cambridge Structural Database Analyses. *J. Phys. Chem. B* **2006**, *110* (4), 1889–1895. https://doi.org/10.1021/jp054975n.

(11) Preston, A. J.; Gallucci, J. C.; Parquette, J. R. Folded Metallodendrons: Shell-Selective Metal Coordination and Conformational Properties. *Org. Lett.* **2006**, *8* (25), 5885–5888. https://doi.org/10.1021/ol062544x.

(12) Ballesteros, M.; Tsui, E. Y. Reactivity of Zinc Thiolate Bonds: Oxidative Organopolysulfide Formation and S 3 Insertion. *Inorg. Chem.* **2019**, *58* (16), 10501–10507. https://doi.org/10.1021/acs.inorgchem.9b01074.

(13) Preston, A. J.; Gallucci, J. C.; Parquette, J. R. Structural Impact of Coordinating a Helical 2,6-Pyridyl Diamide with Divalent Metals. *Org. Lett.* **2006**, *8* (23), 5259–5262. https://doi.org/10.1021/ol062086s.

(14) Wang, M.; Yu, G.; Ji, W.; Li, L.; Ding, W.; Peng, L. Identification of Intrinsic Hydrogen Impurities in ZnO with 1H Solid-State Nuclear Magnetic Resonance Spectroscopy. *Chem. Phys. Lett.* **2015**, *627*, 7–12. https://doi.org/10.1016/j.cplett.2015.03.024.

(15) Park, S. Y.; Kim, S.; Yoo, J.; Lim, K.-H.; Lee, E.; Kim, K.; Kim, J.; Kim, Y. S. Aqueous Zinc Ammine Complex for Solution-Processed ZnO Semiconductors in Thin Film Transistors. *RSC Adv.* **2014**, *4* (22), 11295. https://doi.org/10.1039/c3ra47437b.

Chapter 3
Molecular Docking & Dynamics

1. Introduction

In the short space of three years since the start of the Covid-19 pandemic, 760 million people have been infected by SARS-CoV-2 and over 6.8 million people have died from the resulting disease.[1] The spike (S) protein of the virus is an ectodomain trimer that mediates membrane fusion and entry into host cells through receptor recognition of human angiotensin-converting enzyme 2 (ACE2).[2,3] The S protein displays conformational heterogeneity as the receptor-binding domain (RBD) may fold “down” to evade immune system recognition of the epitope or fold “up” to become solvent-exposed for binding ACE2.[4] The RBD is a conserved epitope among coronaviruses and its binding to ACE2 is highly specific. The interaction between the RBD and ACE2 involves hydrogen bonding between multiple tyrosine residues on the surface of the RBD.[5,6,7] The mechanism by which SARS-CoV-2 invades host cells is well known and hence, novel fusion inhibitors may be rationally designed that prevent infection and viral replication in humans. We propose the design of metallodrugs that specifically target solvent-exposed tyrosine residues on the RBD with the potential to prevent viral infection by disrupting receptor recognition and host cell entry.

The design process was performed with Schrödinger Release 2021-1 (Maestro, Schrödinger, LLC, New York, NY, 2021). A modest library of synthetically feasible metal chelates was docked against the RBD of SARS-CoV-2 and their scores compared to the results of high-throughput virtual screening (HTVS). The docked ligands were then analyzed by molecular dynamics (MD) simulations to assess time-dependent phenomena. The docking grids were centred on various tyrosine residues involved with receptor recognition of ACE2 and it will be shown in Chapter 4 that the synthesized chelates specifically bind tyrosine on the S protein epitope. The development of novel metal-based fusion inhibitors is feasible as the bioavailable metal ion has selectivity for specific amino acids, and by masking these solvent-exposed residues on the RBD, its interaction with ACE2 will surely be disrupted. The tyrosine residues involved with ACE2 binding are conserved among coronaviruses and hence the development of such a therapeutic has the potential to become a universal fusion inhibitor, poised for the next pandemic.[8]

2. Methods

2.1 Protein Preparation

Three separate structures were retrieved from the Protein Data Bank (PDB) and prepared for docking in Glide.[9] The X-ray structure of the SARS-CoV-2 RBD in complex with the human ACE2 receptor was solved to a final resolution of 2.45 Å and retrieved (PDB: 6M0J) for protein preparation and docking.[6] The structure contains the ACE2 receptor (602 residues) which was deleted along with all solvent molecules before protein preparation using the Protein Preparation Wizard.[10] The RBD was then pre-processed using standard parameters: assign bond orders, add hydrogens, create zero-order bonds to metals, create disulfide bonds, and generate heteroatom ionization (HI) states using Epik[11] between pH 6 and 8. The residue E493 was committed to one position with 0.5 average occupancy. The workspace was then analysed using standard parameters and HI states generated for a single chloride ion (atom number 902) and a co-crystallized N-acetylglucosamine (NAG, atom number 601). The hydrogen-bond assignment was then optimized at pH 7 and restrained minimization was performed using the OPLS_2005[12] force field converging heavy atoms to a root-mean-square deviation (RMSD) of 0.30 Å.

The second cryo-EM structure retrieved (PDB: 7DK5) contained the S protein trimer with two RBDs in the “down” position and one RBD in the “up” position bound to monoclonal antibodies.[13] The RBD in the “up” conformation was selected, the selection inverted in Maestro and all other atoms deleted before protein preparation. The RBD that remains in the workspace contains 402 residues. The structure was then processed by the Protein Preparation Wizard as before, although there were no alternate positions or generated HI states.

The final cryo-EM structure retrieved for docking (PDB: 7KJ5) was solved to a resolution of 3.6 Å and contained the S protein trimer in pre-fusion conformation with one RBD solvent-exposed in the “up” position.[14] The solvent-exposed RBD was selected in Maestro, the selection inverted and all other atoms deleted. The RBD that remains in the workspace contains 392 residues. The structure was then prepared as previously, with HI states generated for four NAG molecules distal from the RBD.

2.2 Ligand Preparation

The metal chelates used for docking were first optimized with DFT at the B3LYP/LanL2DZ level of theory to determine the likely coordination geometry at the metal centre. The DFT-optimized structures were then subjected to optimization using the OPLS_2005 force field with standard parameters for LigPrep (LigPrep, Schrödinger, LLC, New York, NY, 2021). This was done to generate files associated with Schrödinger. The force field was not parameterized for the metal chelates under study and it was thus necessary to apply zero-order bonds between the metal ion and the organic framework. However, ionization states cannot be generated for the metal chelates and thus represents a limitation in the accuracy of the current force fields employed in Schrödinger. This was deemed acceptable because the purpose of docking was to determine ideal substitution patterns on the ligand framework. While ionization states on the ligand will affect the final docking score, the binding mode of the chelate is still accurately described because altering substitution patterns will change which residues on the protein target interact with the chelate.

A large library of metal chelates was prepared for HTVS in Glide XP[15] using R-Group Enumeration in Maestro. The R-groups were selected with functional groups comprising of amides, amines, alcohols, carboxylic acids, ethers, and esters. The R-groups were substituted on the 2-, 3- and 4-positions on the aryl rings of the metal chelate and the final library contained 164 000 ligands prepared for docking.

2.3 Molecular Docking

2.3.1 HTVS

HTVS using Glide XP was performed for a library of 164 000 copper chelates. The docking was carried out on the pre-processed crystal structure 6M0J, and Y453 on the RBD was selected as the centroid of the 30 × 30 × 30 Å grid box. The chelate binding was directed using parametrized electrostatic forces. This was achieved by removing the acidic proton on tyrosine and giving the oxygen atom a formal negative charge, while the metal centre had a charge of 2+. The HTVS utilized Virtual Screening Workflow (VSW) in Maestro with standard parameters. All docking was done flexibly and 10% of the best chelate poses were kept after Glide HTVS. These 16400 best-docked chelates were then subjected to SP docking where the best 10% (1640) were carried through to XP docking. After XP docking, the best 20 copper chelates were retained and reported with only one pose.

2.3.2 SP Docking

Standard Precision (SP) docking using Glide SP was performed for a library of 37 synthetically feasible metal chelates. The docking was carried out on three separate pre-processed PDB structures: 6M0J, 7DK5 and 7KJ5. The solvent-exposed tyrosine residues on the RBD selected for docking were Y449, Y453, Y489 and Y505, and four separate grids were generated for each residue. The residues were selected as the centroid of the grid box which was orthorhombic with a grid size of 30 × 30 × 30 Å. The selected tyrosines were allowed free rotation during grid generation and docking. The force field used for docking was not parameterized for the metal chelates and so electrostatic forces, which are parameterized, were used to direct the binding mode of the metal chelate to tyrosine. This was achieved by removing the acidic proton on tyrosine and giving the oxygen atom a formal negative charge, while the metal centre had a charge of 2+. This was done for all tyrosines before grid generation and docking. The SP docking was then performed using standard parameters and writing at most five poses per ligand.

2.3.3 XP Docking

Extra Precision (XP) docking using Glide XP was then performed for a library of 56 synthetically feasible metal chelates. The docking was carried out on three separate pre-processed PDB structures: 6M0J, 7DK5 and 7KJ5. The solvent-exposed tyrosine residues on the RBD selected for docking were Y453 and Y505, and two separate grids were generated for each residue. Again, electrostatic forces parameterized in the OPLS_2005 force field were used to direct the binding mode of the metal chelate to tyrosine. An anionic charge was given to the oxygen of Y453 and Y505 before grid generation and docking. An anionic charge was also given to Y449 and Y489 so that these residues may serve as “decoy” targets, allowing electrostatic forces to direct docking to the most favourable binding site. The residues Y453 and Y505 were selected as the centroid of the orthorhombic grid boxes with a box size of 30 × 30 × 30 Å. The XP docking was then performed using standard parameters and writing at most five poses per ligand.

2.3.4 Synthesized Chelate Docking: RBD

SP docking was also performed for the five synthesized copper chelates (Chapter 2) on pre-processed structures 6M0J, 7DK5 and 7KJ5. The RBD residues Y453, Y489 and Y505 were selected as the centroids of the grid boxes with a grid size of 20 × 20 × 20 Å. Now the binding of the chelates was directed to tyrosine by imposing positional constraints during grid generation. The oxygen atom of the phenol was selected to define the constraint position and

the NOE distance was restricted to between 1.8 and 3.3 Å. The SP docking was then performed with free rotation allowed for the selected residues (Y453, Y489 and Y505) and the grid-based constraint was applied. The feature definition for the constraint was applied as the SMARTS pattern for Cu(II), [Cu+2]. This constrained docking restricts the copper centre of the chelate to within 1.8 and 3.3 Å of the tyrosine residue and it will be shown by NMR in Chapter 4 that this constraint is valid.

2.3.5 Synthesized Chelate Docking: Epitope

Finally, SP docking was performed for the five synthesized copper chelates on the peptide epitope used to model Y505 on the RBD. The novel peptide Ac-GVGYQP-NH_2 was built in Maestro from the biopolymer sequence and alpha helix secondary structure chosen for the entry. The validity of imposing an alpha helix structure was confirmed with circular dichroism (CD) spectroscopy. The peptide was pre-processed using OPLS_2005 and standard parameters in the Protein Preparation Wizard. The single tyrosine residue was selected as the centroid of the grid box with a grid size of 20 × 20 × 20 Å. The grid was generated with a positional constraint where NOE distances were restricted to between 1.8 and 3.3 Å and the constraint position was defined as the oxygen atom of the phenol on tyrosine. The feature definition for the constraint was applied as the SMARTS pattern for Cu(II), [Cu+2], and SP docking performed with standard parameters and reporting at most five poses per ligand.

2.4 Molecular Dynamics

The MD simulations were performed on the best-docked protein-ligand complexes using Desmond[16] and the OPLS_2005 force field. The protein-ligand complexes were already pre-processed before the System Builder in Desmond was used to solvate the system with TIP3P[17] water molecules. The biomolecular system was placed in an orthorhombic box with a buffer region of 10 Å between the box boundary and the protein-ligand complex and neutralized with Na^+ or Cl^- ions as necessary. The simulation times varied between 30 and 100 ns and the approximate number of frames was kept constant at 1000 so that the recording interval varied between 30 and 100 ps. The model system was relaxed before simulation, and equilibration was done using the NPT[18] ensemble at 310 K and 1.01 bar. The trajectories were then analyzed in Maestro.

3. Results and Discussion

3.1 MD Analysis of RBD-ACE2 Complex

The crystal structure (6M0J) of the SARS-CoV-2 RBD and human ACE2 receptor in complex was subjected to a 50 ns MD simulation. The results indicate that Y449, Y453, Y489 and Y505 of the RBD maintain contact with ACE2 over the simulation period. Hence, targeting these residues should surely disrupt the specific recognition between the viral protein and human receptor. The RBD-ACE2 complex is highly stable in solution as illustrated in the RMSD plot in Figure 3.1.

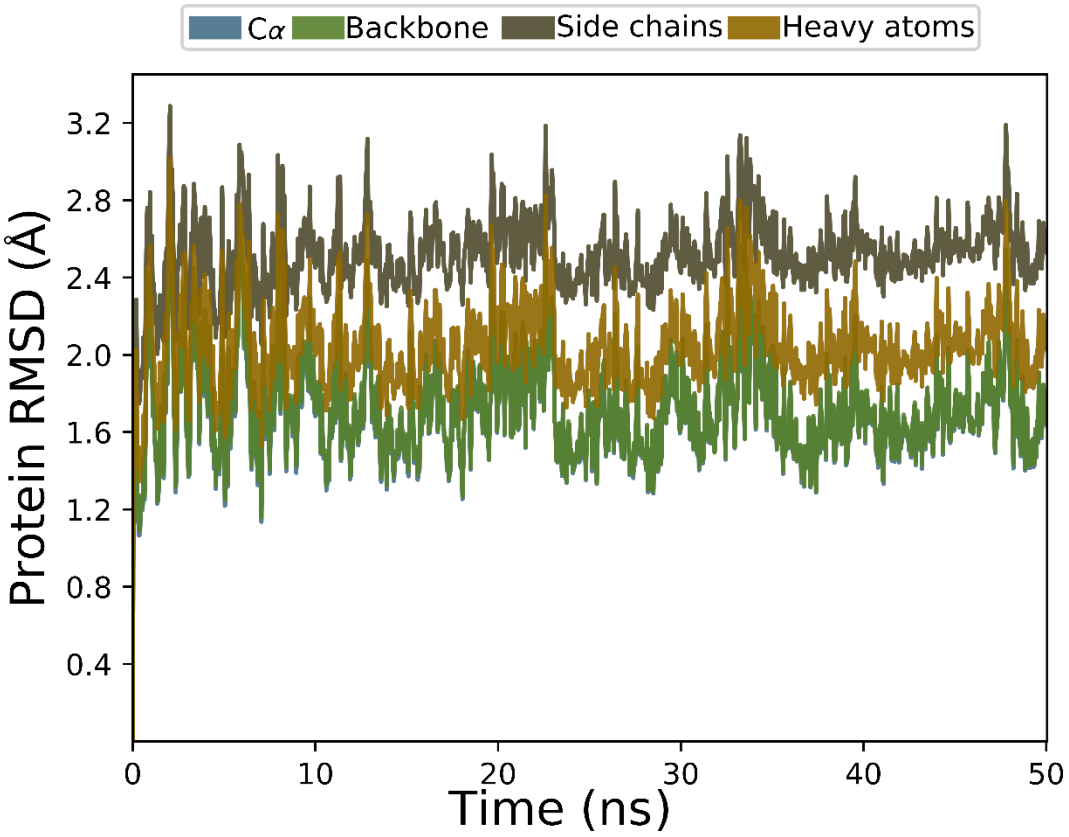


Figure 3.1: The Root Mean Square Deviation plot of the RBD-ACE2 complex over 50 ns. The RMSD measures the average change in displacement of atoms in each frame with respect to a reference frame. The RMSD analysis identifies structural conformational changes and RMSD values between 1 and 3 Å are normal for proteins. The C_α trace follows the backbone trajectory exactly and hence is not visible on the plot.

The protein-protein complex RMSD shows that the system easily equilibrates and maintains a stable thermal average structure with no major structural changes over 50 ns. This indicates that the RBD favourably binds ACE2, and the stability of the complex is further exemplified by the RMSF plot shown in Figure 3.2.

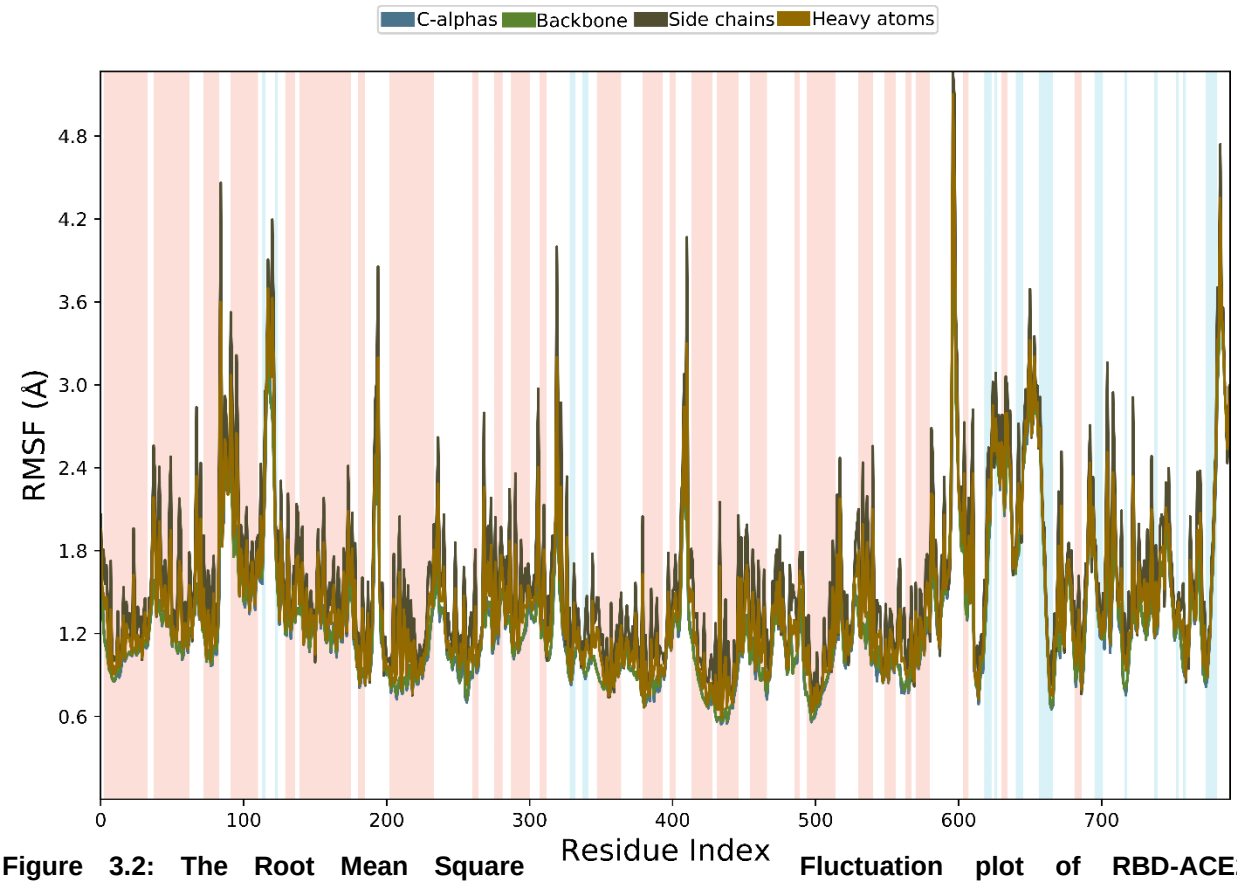


Figure 3.2: The Root Mean Square Fluctuation plot of RBD-ACE2 complex over 50 ns. The regions highlighted in red show that the α-helical secondary structure is maintained over 70% of the simulation time, and those regions highlighted in blue indicate β-strand secondary structure. The RMSF is used to indicate local changes in the protein chain and the peaks represent areas of high fluctuation. Secondary structure elements like α-helices are typically more rigid than loop, C-, and N-terminal regions of the protein. The C_α and backbone trajectory are exactly overlapped.

The RMSF plot shows that the β-strands of the RBD maintain their structure when in complex with ACE2 and the residues involved with receptor recognition undergo minimal local fluctuations. These residues include Y449, Y453, Y489 and Y505 as shown in the MD trajectory analysis in Figure 3.3.

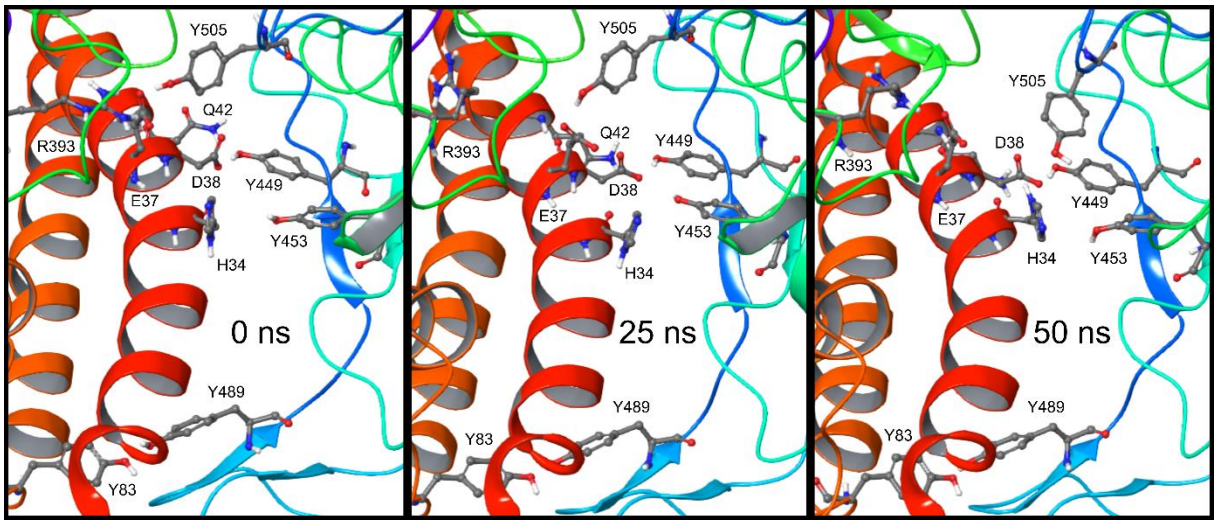


Figure 3.3: The MD trajectory analysis snapshots of the interfacial region of the SARS-CoV-2 spike protein RBD-ACE2 complex at 0, 25 and 50 ns. ACE2 is coloured red-orange and the RBD is coloured blue-green.

The MD trajectory snapshot in Figure 3.3 at 0 ns shows Y505 of the RBD interacting with E37 and R393 of ACE2; Y449 forms a hydrogen-bonded trimer between D38 and Q42 on ACE2; Y453 interacts with H34 and Y489 of the RBD hydrogen-bonds to Y83 of ACE2. The trajectory snapshot at 25 ns shows Y505 strongly H-bonded to E37 such that R393 is displaced from the anion; Y449 remains hydrogen-bonded to D38 and Q42; Y453 is slightly displaced from H34 while Y489 maintains its interaction with Y83. The trajectory at 50 ns shows that Y505 and Y453 now form a trimer including H34 with Y505 acting as the H-bond acceptor from H34 and Y453 donating an H-bond to H34. Y449 is now only bonded to D38 with a bond distance of 1.80 Å while Y489 has maintained its contact with Y83 over the entire trajectory period. The MD results indicate that these tyrosine residues are required for ACE2 receptor recognition and would be a suitable target for designing novel metal-based fusion inhibitors.

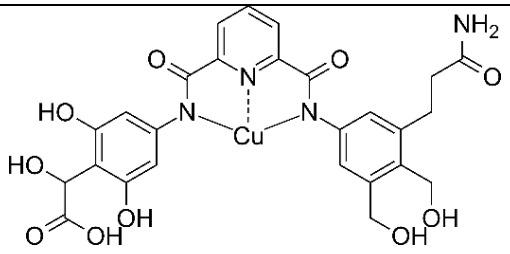
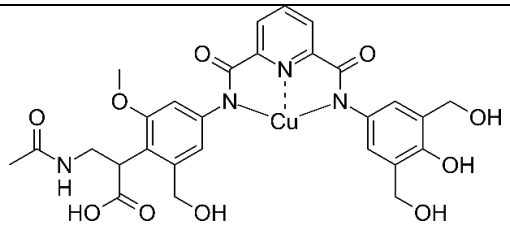
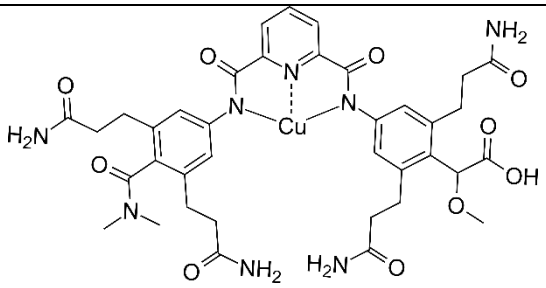
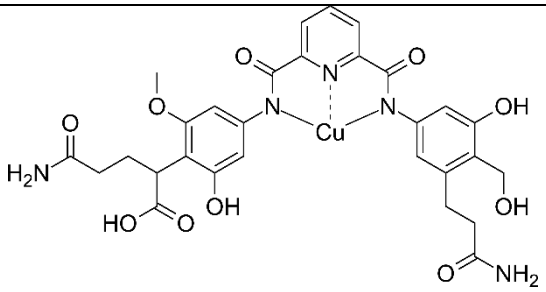
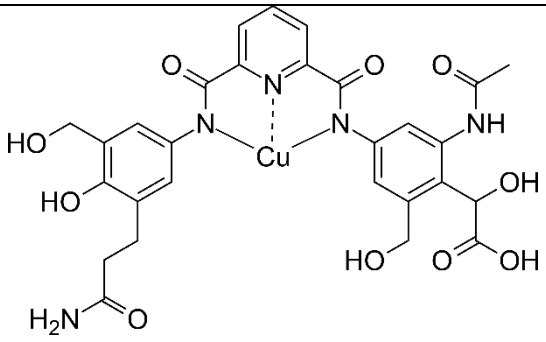
3.2 HTVS Molecular Docking & Dynamics

The HTVS process docked 164 000 copper chelates against Y453 of the RBD (6M0J) and filtered the entries down to the best-scoring 20 compounds. The top five entries are listed in Table 3.1 with their G-score and amino acid interactions. The top five structures and druglikeness[19, 20] parameters are listed in Table 3.2. Residues highlighted in yellow are targeted by all five of the HTVS top hits.

Table 3.1: The G-score and interaction profile of the top five hits obtained from HTVS.

Entry	Rank	G-score (kcal mol^{-1})	Amino Acid Interactions
HTVS1	1	–9.057	R403, E406, Q409, G416, K417, I418, Y453, L455, Q493, S494, Y495, G496, F497, Q498, N501, Y505
HTVS2	2	–8.442	R403, D405, E406, R408, G409, K417, I418, Y453, L455, Q493, S494, Y495, G496, Y505
HTVS3	3	–8.428	R403, Y449, L452, Y453, E484, Y489, F490, L492, Q493, S494, Y495, G496, F497, Q498, N501, Y505
HTVS4	4	–8.403	R403, K417, Y449, L452, Y453, L455, F490, Q493, S494, Y495, G496, Q498, N501, Y505
HTVS5	5	–8.365	R403, E406, Q409, G416, K417, I418, Y449, Y453, L455, F456, Q493, S494, Y495, G496, F497, Q498, N501, Y505

Table 3.2: The structures and druglikeness parameters for the top five HTVS hits.

Structure	Entry	MW[a]	#HBA[b]	#HBD[c]	#RB[d]
	HTVS1	554.51	11	7	6
	HTVS2	582.56	11	6	7
	HTVS3	760.79	15	5	8
	HTVS4	609.58	12	6	6
	HTVS5	594.57	12	7	7

[a] Molecular weight (MW) in g mol^{-1} of the organic framework only.
[b] Number of hydrogen-bond acceptors (HBA).
[c] Number of hydrogen-bond donors (HBD).
[d] Number of rotatable bonds (RB).

The amino acid interactions listed in Table 3.1 show that the five best-docked chelates interact with the same residues in the RBD, namely R403, K417, Y453, L455, Q493, S494, Y495, G496 and Y505. The compound **HTVS1** binds the RBD through π-cation and H-bonding interactions with R403. **HTVS1** interacts with K417 through H-bonding and electrostatic forces, while the interactions with Y453 and L455 are hydrophobic. The hit compound interacts with Q493 and S494 of the RBD through polar forces while interactions with Y495, G496 and Y505 are hydrophobic with H-bonding to G496 and Y505. These interactions between **HTVS1** and the RBD are shown in Figure 3.4.

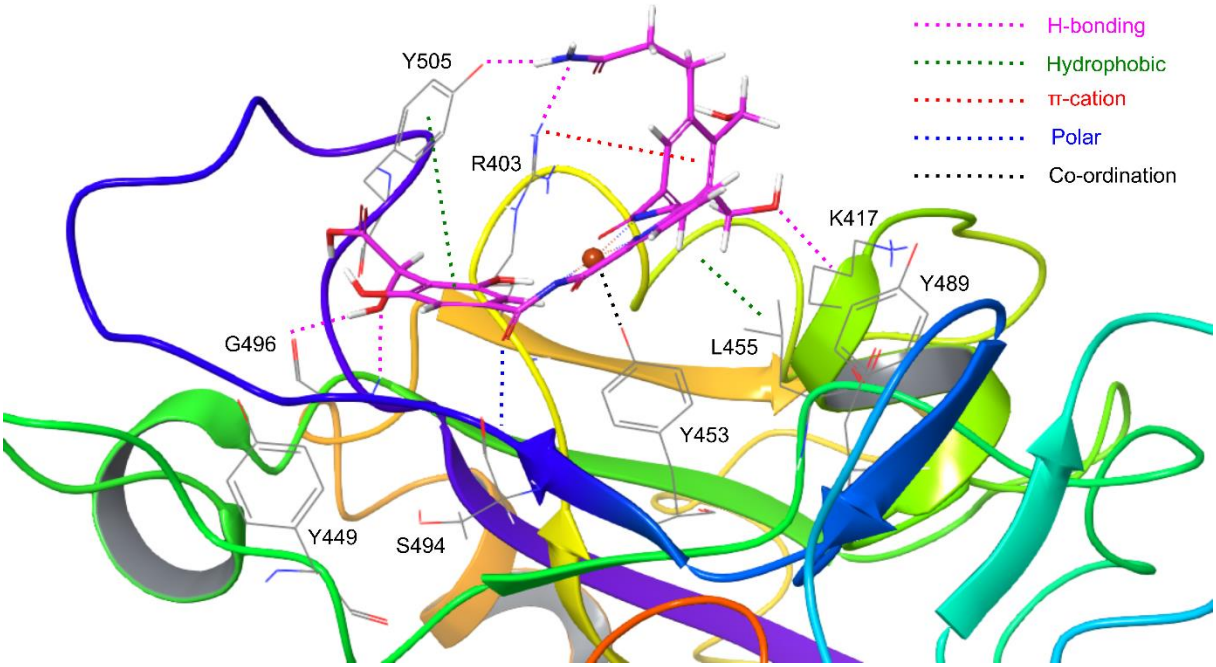


Figure 3.4: The top-scoring compound from HTVS docked against the RBD of SARS-CoV-2. The ligand is coloured magenta and the geometry around the copper centre is square-pyramidal with Y453 forming part of the inner coordination sphere. There are some residues omitted for clarity.

The best-docked chelate was then subjected to a 100 ns MD simulation to assess time-dependent dynamic interactions between the RBD and **HTVS1**. The RMSD plot presented in Figure 3.5 shows that the RBD-HTVS1 complex equilibrates after 20 ns and maintains a stable structure over the remaining 80 ns. A timeline of the protein-ligand contacts is presented in Figure 3.6 which highlights significant interactions between the chelate and the residues R403, K417, Y453, L455, S494 and G496 of the RBD. These key interactions are maintained over the trajectory period and thus designing ligands that target these residues may produce fusion inhibitors with a high affinity and specificity for the RBD of SARS-CoV-2.

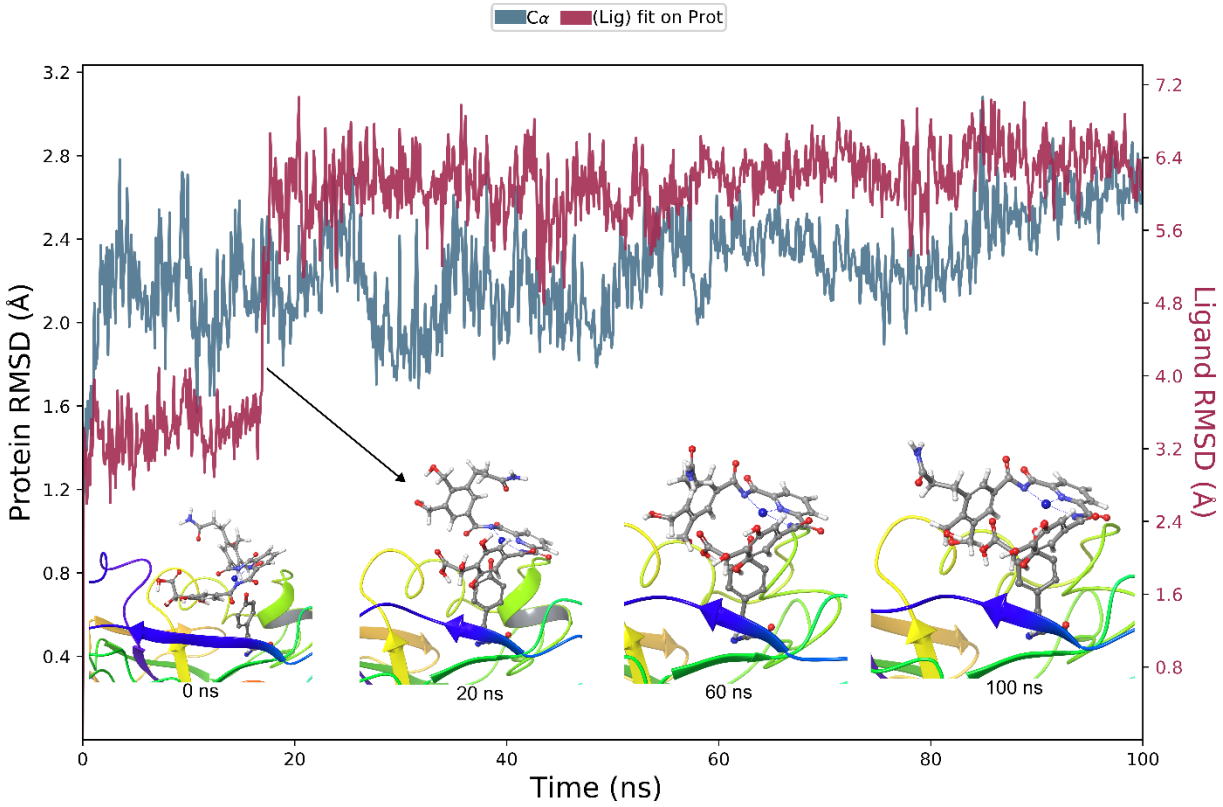


Figure 3.5: The RMSD plot of RBD-HTVS1 complex over 100 ns. The plot indicates that the dynamic system is stable in solution. The docked chelate undergoes conformational changes at 20 ns where the organic framework rearranges and binds more favourable residues at 60 ns. This binding pocket is maintained until 100 ns where the MD simulation has equilibrated. Despite rearrangement of the organic framework in solution, the Cu(II) centre remains coordinated to Y453 over the full trajectory period.

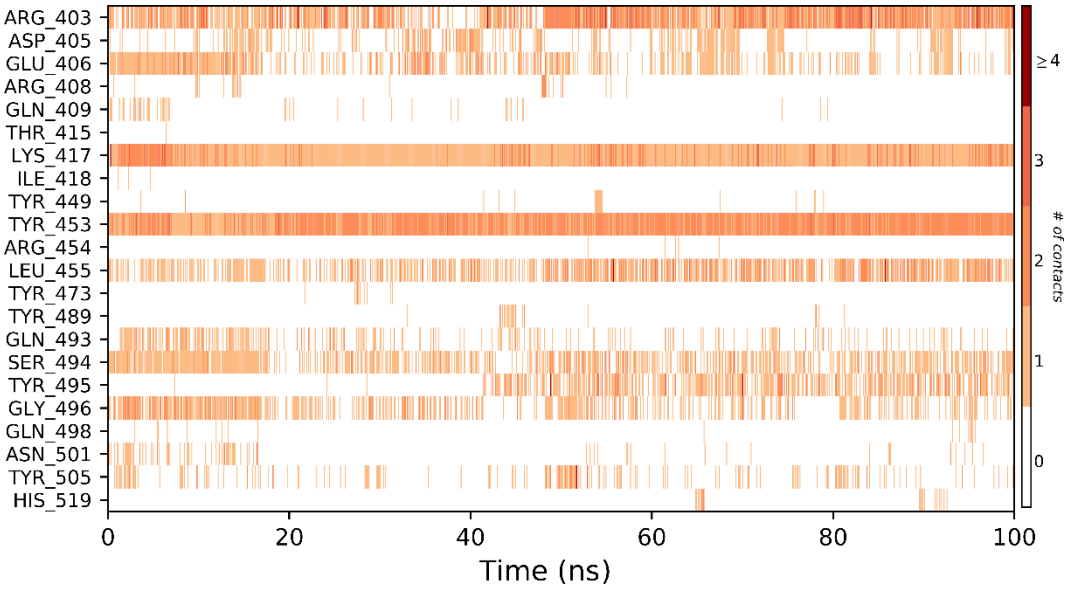


Figure 3.6: The protein-ligand interaction timeline of the RBD-HTVS1 complex showing the number of contacts per residue over 100 ns.

The G-scores listed in Table 3.1 are comparable to HTVS hits obtained from screening phytochemical libraries against the RBD.[21, 22, 23] Although these docking scores are impressive for molecules binding solvent-exposed protein surfaces, the molecules themselves violate Lipinski's rules for druglikeness. The parameters listed in Table 3.2 for the top five hits indicate that these compounds are unlikely to be good drug candidates and the high docking scores are an artefact of how the binding energy is calculated in Glide. The greater the number of functional groups interacting with the protein target, the more energy terms are summed into the final G-score. Although this certainly would improve the experimental binding affinity, the molecules become un-druglike when the molecular weight exceeds 500 g mol^{-1} and there are too many hydrogen-bond donors or acceptors. Hence, despite the remarkable docking scores, these compounds would not be suitable for synthesis and experimental testing.

3.3 SP Molecular Docking & Dynamics

The HTVS process showed that the best possible chelate structures produce G-scores between –9 and –8 kcal mol^{-1} when docked against the SARS-CoV-2 RBD. These chelates are not synthetically feasible and so SP docking was performed for a library of 37 viable metal chelates. The library was docked against three separate PDB structures and each of the four tyrosine residues were identified as necessary for ACE2 binding from the MD analysis of the RBD-ACE2 complex. The G-scores for each residue on each PDB structure are presented in Figure 3.7 and Figure 3.8. To determine the best-docked molecule across the four residues and three protein structures, an exponential consensus ranking[24] (ECR) strategy was employed. The strategy is based on the summation of exponential distributions as a function of molecule rank for each residue and protein structure. The exponential score for each docked molecule is calculated from equations **(1)** and **(2)** below. The original equation assigns the exponential score, $p(r_i^j)$, for each molecule, i, for each scoring function, j, using the rank of the molecule, r_i^j, given by different docking programs. Herein, j, represents each residue on each PDB structure as the force-field based scoring function is constant and the rank of the molecule, r_i^j, is given by different protein structures and residues rather than different programs.

$$p(r_i^j) = \frac{1}{\sigma}\exp\left(\frac{-r_i^j}{\sigma}\right) \quad \textbf{(1)}$$

The expected value of the exponential distribution, σ, was approximated as the average of the possible rankings, i.e., the average of rankings 1 to 37 is 18.97. However, it was shown by the

original authors of the strategy that the ECR results are almost independent of the value of σ. The final score for each molecule is defined in equation **(2)** below.

$$P(i) = \sum_j p\left(r_i^j\right) \quad \textbf{(2)}$$

The ECR approach is based on rank rather than score which overcomes the fact that scoring functions are weakly correlated with binding free energies.[25] The ECR approach assigns a higher score for molecules that are well docked against several residues or PDB structures but not necessarily all residues or protein structures. The ECR results thus eliminate bias toward a bad choice of a target structure. Furthermore, the ECR overcomes bias faced when a simple summation or average of docking scores is used because the average docking score may be skewed when a single docked molecule has an exceptionally high G-score. The docking scores presented in Figure 3.7 and Figure 3.8 were ranked for each residue and PDB structure and then the ECR strategy was employed. The top 10 entries ranked by ECR are presented in Table 3.3 along with the entry ranking as determined by a summation of docking scores across the protein structures and residues.

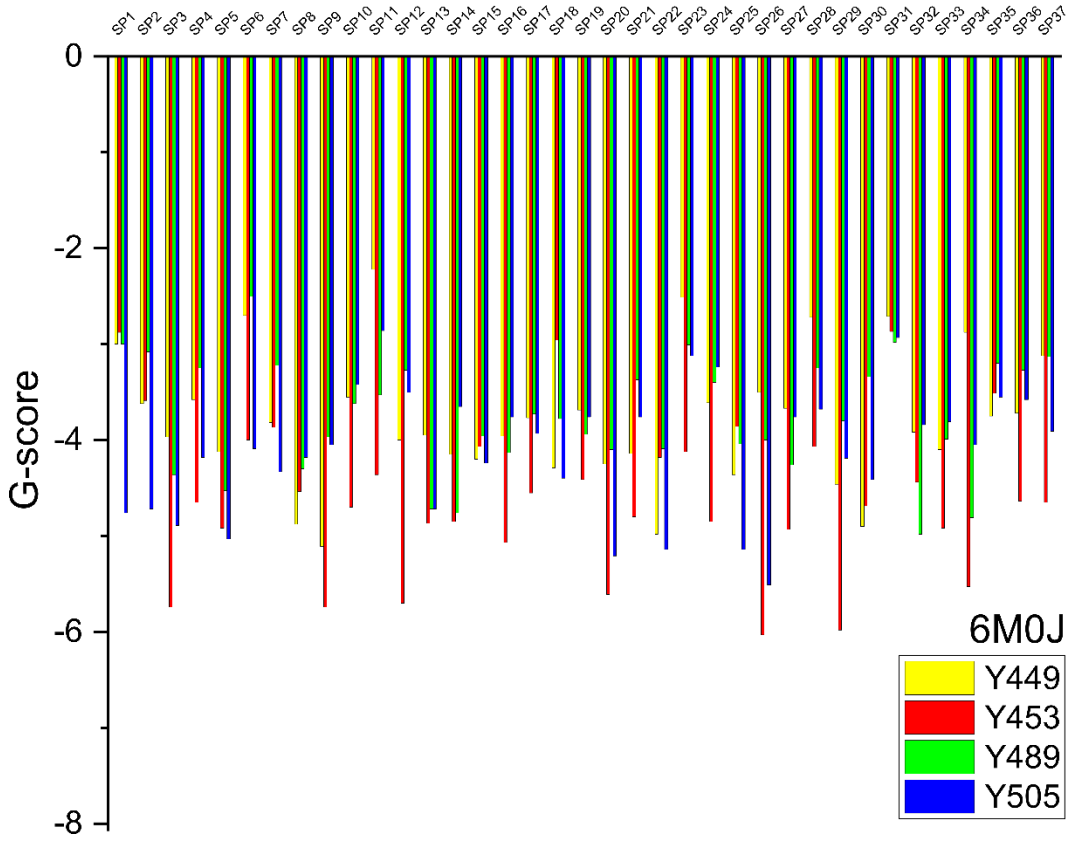


Figure 3.7: The G-scores obtained from docking entries *SP1* through *SP37* against 6M0J.

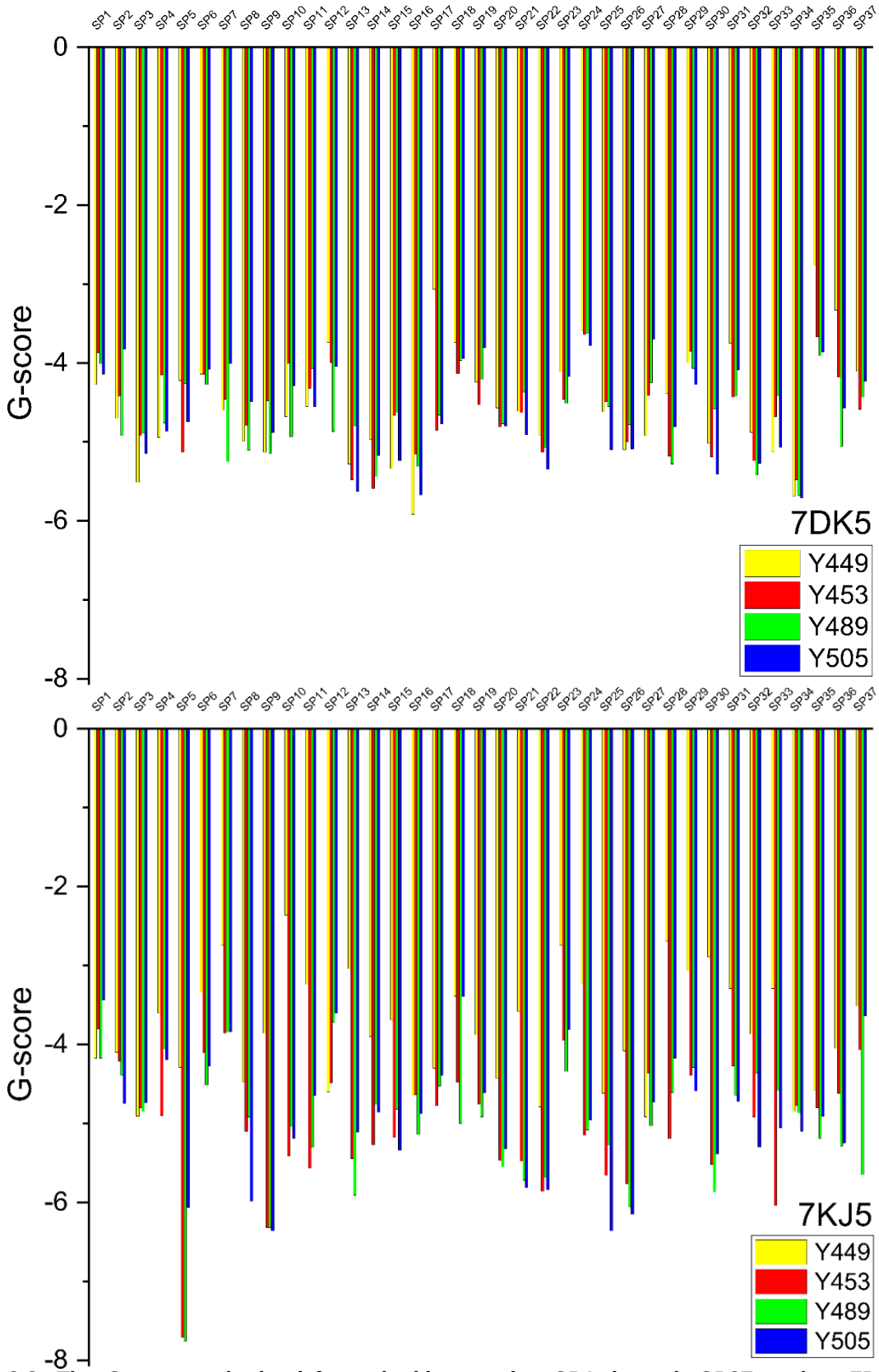


Figure 3.8: The G-scores obtained from docking entries *SP1* through *SP37* against 7DK5 and 7KJ5.

Table 3.3: The best-ranked entries from SP docking as determined by ECR and summation.

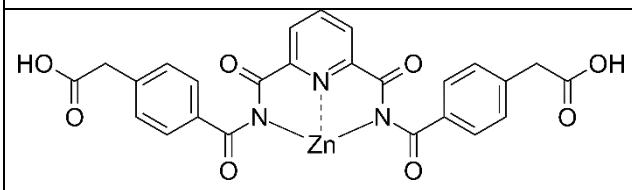
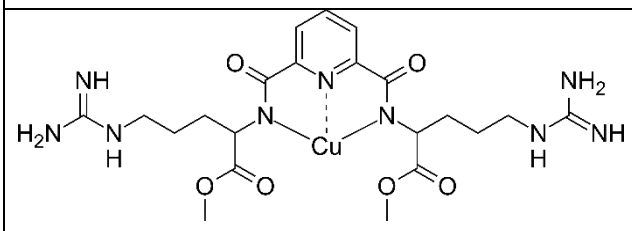
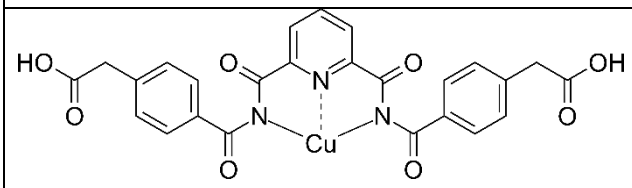
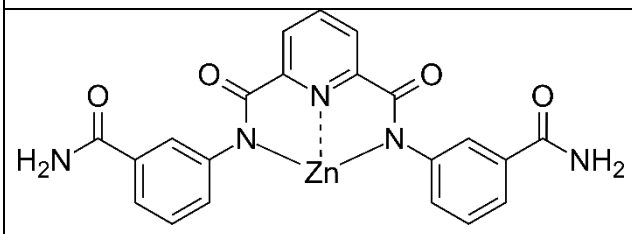
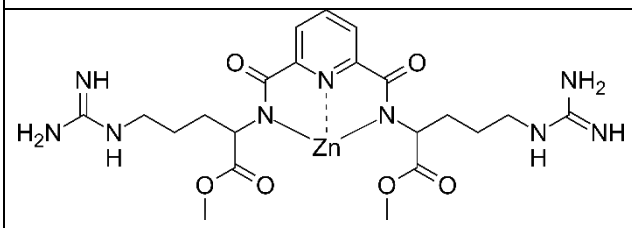
Entry	ECR Rank	Summation Rank
SP22	1	4
SP9	2	2
SP5	3	1
SP20	4	7
SP26	5	3
SP3	6	8
SP34	7	5
SP13	8	6
SP16	9	9
SP25	10	10

The benefit of the ECR is exemplified in Table 3.3 and Figure 3.8 as the exceptionally high G-score for **SP5** skews the ranking when a summation (or average) of docking scores is used. The ECR determines **SP22** to be the best-ranked molecule because it is docked well against several residues but not necessarily all of them. The top five entries as determined by ECR are presented in Table 3.4 with their structures and druglikeness parameters.

The parameters listed in Table 3.4 suggest these compounds would be more druglike than the hits obtained from HTVS presented in Table 3.2. The top five SP hits encompass only three ligands with the ligand of **SP22** and **SP5** ranking 1st and 3rd. The best SP docked chelate, **SP22**, is shown in Figure 3.9 with its interactions to residues R403, E406, Q409, K417, T500, N501, G502 and Y505 of the RBD. 6M0J was chosen to showcase the binding because the resolution on the X-ray data is excellent and the RBD is in complex with ACE2, hence residues are in position for receptor recognition. Y505 was chosen to showcase potential binding because this residue produced the best G-score when **SP22** was docked against Y449, Y453, Y489 and Y505.

The dynamic interactions between **SP22** and the RBD over 100 ns are shown in Figure 3.10. The timeline shows that contacts with Y505 and R403 are maintained over the trajectory period while the number of contacts to N501 and G502 increases as the system equilibrates. Initially, **SP22** interacts with E406 but quickly adjusts to bind D405 for the remainder of the trajectory.

Table 3.4: The structures and druglikeness parameters for the top five SP docking hits.

Structure	Entry	MW[a]	#HBA[b]	#HBD[c]	#RB[d]
	SP22	489.43	8	2	4
	SP9	507.54	12	6	2
	SP5	489.43	8	2	4
	SP20	403.39	6	2	4
	SP26	507.54	12	6	2

The G-scores obtained in Figure 3.7 and Figure 3.8 were summed for each tyrosine residue and it was found that chelates docked against Y453 and Y505 produced the highest scores across the library. Hence, Y453 and Y505 were selected for XP docking. However, it should be noted that more solvent-exposed residues Y489 and Y505 are highly likely targets. This was shown in the MD analysis of **SP34** presented in Figure 3.11. **SP34** was initially docked at Y453, then as the MD trajectory progressed, the chelate became bound to Y449 and then Y489 on the RBD. It has been shown that Y453, Y449, Y489, and Y505 are instrumental to ACE2 binding, and by targeting any of these tyrosine residues, the novel metal chelates may potentially function as antiviral fusion inhibitors by disrupting receptor recognition.

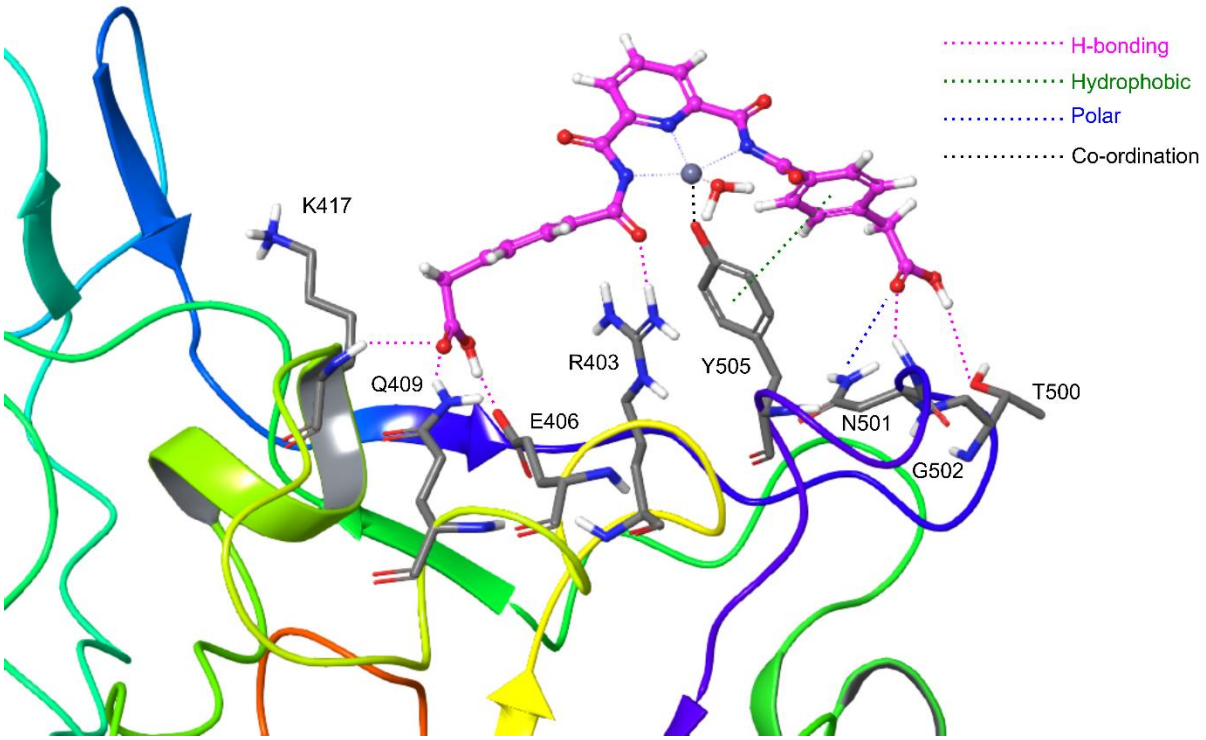


Figure 3.9: The best-ranked chelate, *SP22*, docked against the RBD of SARS-CoV-2 (6M0J). There are multiple hydrogen-bonding interactions between the chelate and RBD, stabilizing the protein-ligand complex. The Zn(II) centre is distorted square-pyramidal with Y505 forming part of the inner coordination sphere.

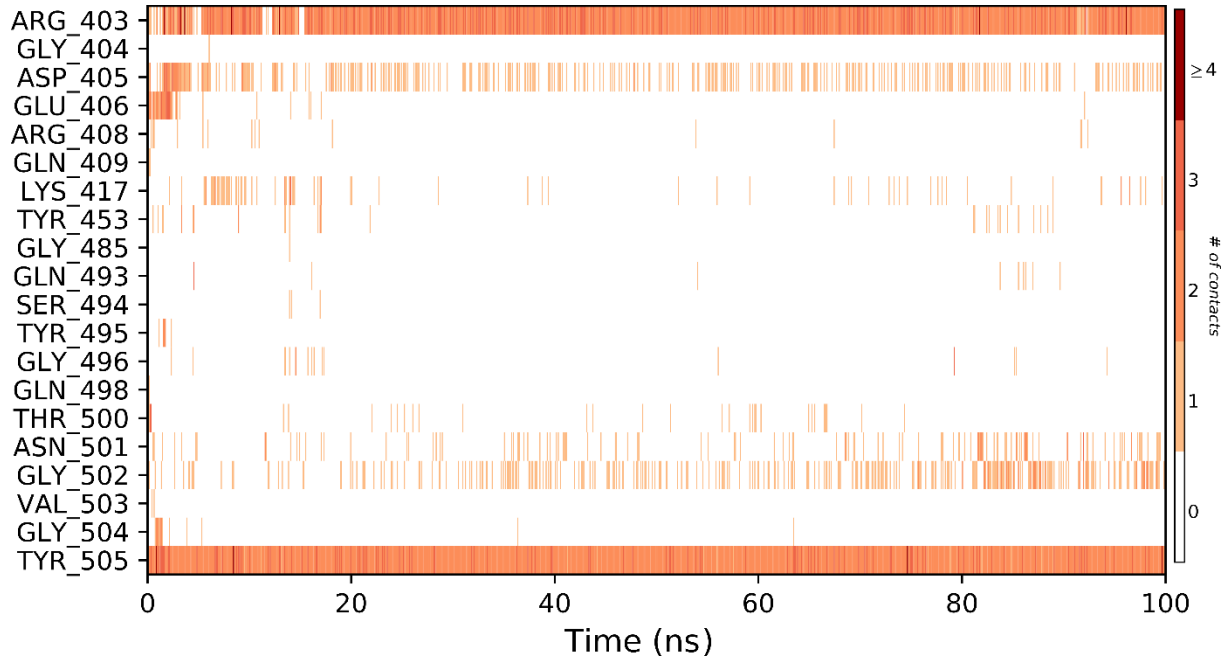


Figure 3.10: The protein-ligand contacts between *SP22* and the RBD over 100 ns.

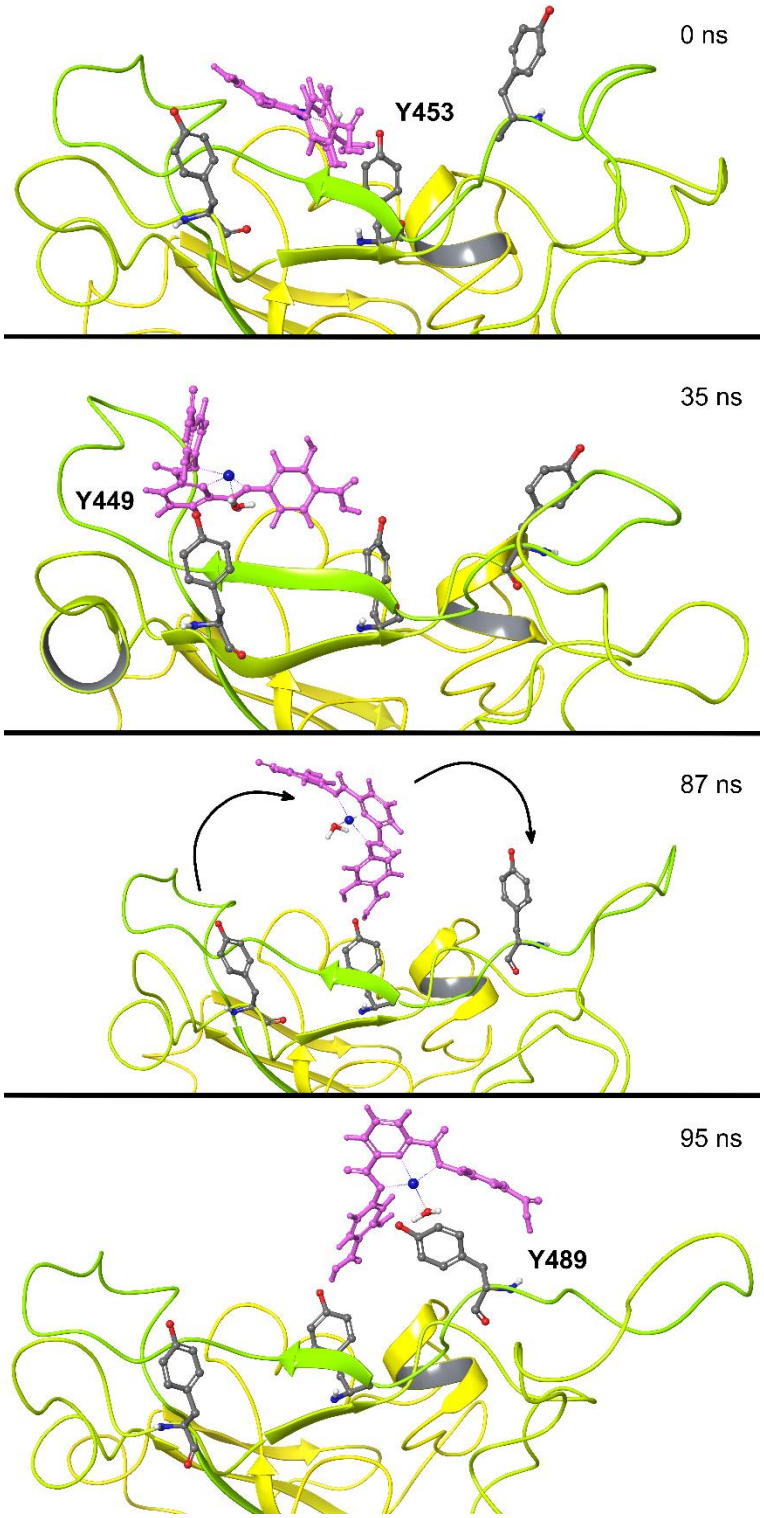


Figure 3.11: MD trajectory snapshots over 100 ns for the RBD-SP34 complex. *SP34* was initially docked against Y453 as shown at 0 ns. The dynamic fluctuations of the protein result in *SP34* departing the original binding site at Y453 and coordinating to Y449. The chelate then remains bound to solvent-exposed Y449 for 50 ns before leaving this binding site at 87 ns. The chelate then coordinates Y489 towards the end of the trajectory indicating that this is the more favourable binding site as the MD simulation has equilibrated.

3.4 XP Molecular Docking & Dynamics

The SP docking process identified Y453 and Y505 as the most favourable residue targets and hence these were selected for XP docking. The XP G-scores for the library of 56 chelates are presented in Figure 3.12 and Figure 3.13 for residues Y453 and Y505 on PDB structures 6M0J, 7DK5 and 7KJ5. It can be seen from these figures that Y453 produces better docking scores and this is because the residue is buried within the cavity of the RBD whilst Y505 is more solvent-exposed. Again, the ECR strategy was employed to determine the best-ranked chelates across the residues and protein structures, with the expected value of the exponential distribution σ taken as 28.44. The best-ranked XP entries as determined by ECR and summation of G-scores are presented in Table 3.5. The best-ranked structures and their druglikeness parameters are presented in Table 3.6.

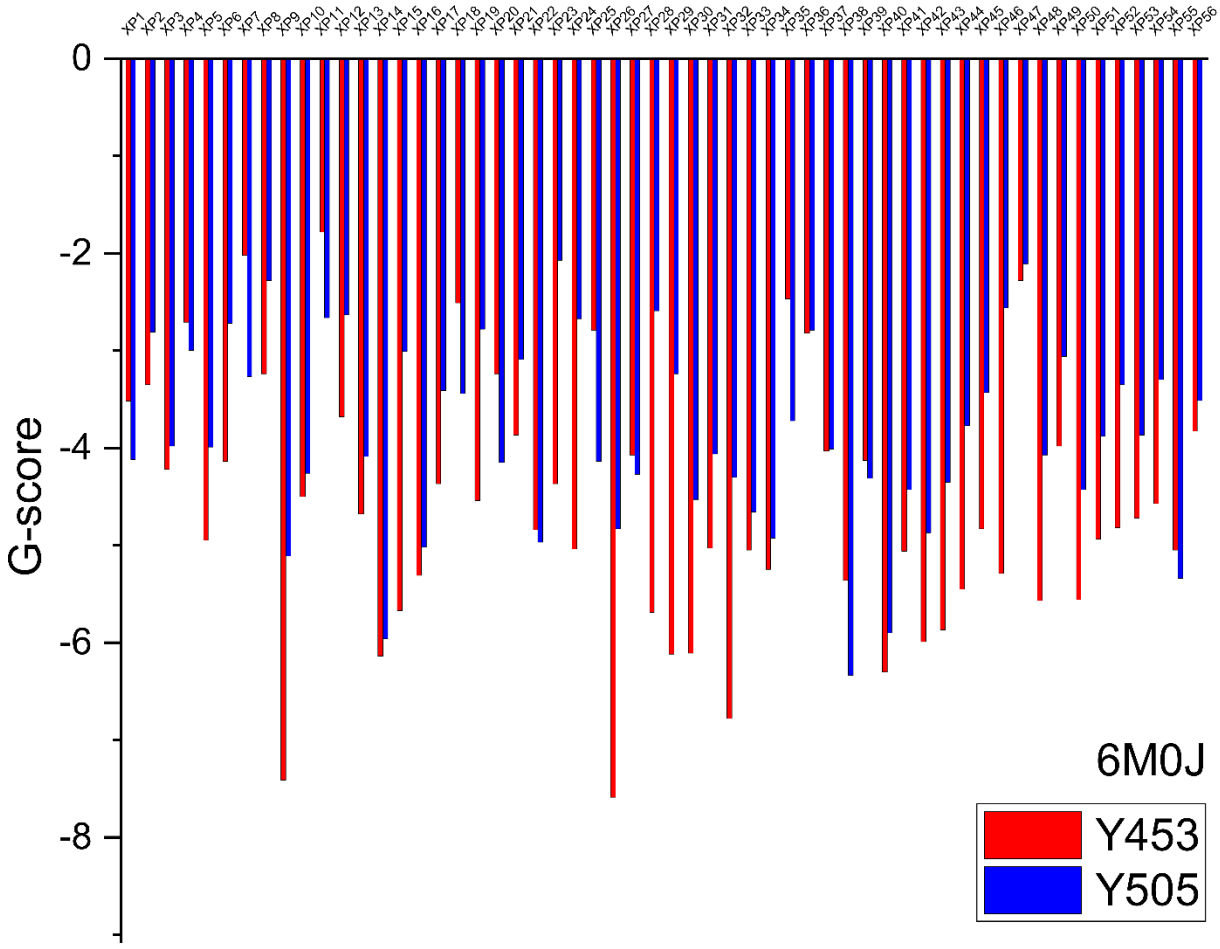


Figure 3.12: The G-scores obtained from docking entries XP1 through XP56 against 6M0J.

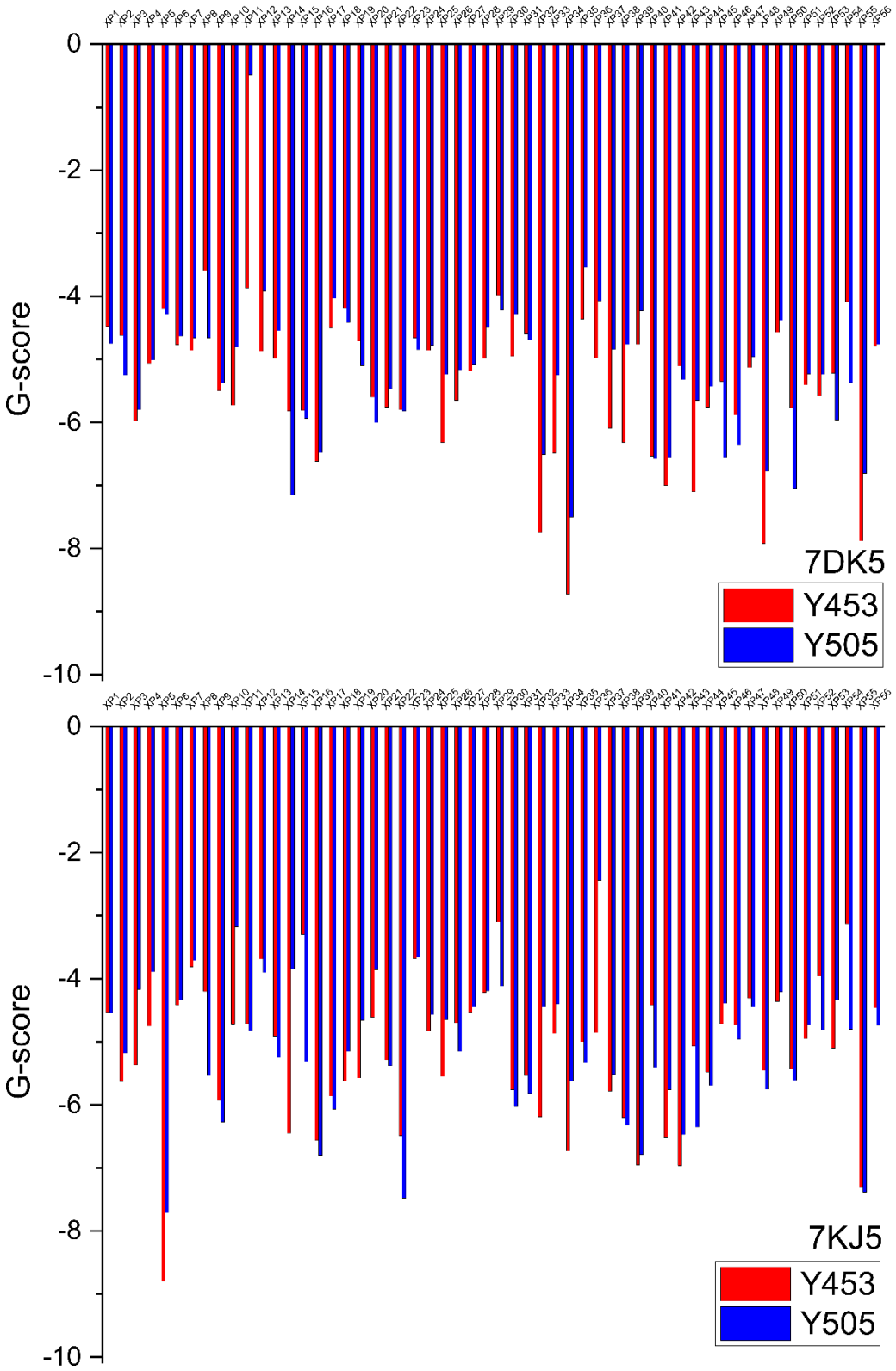
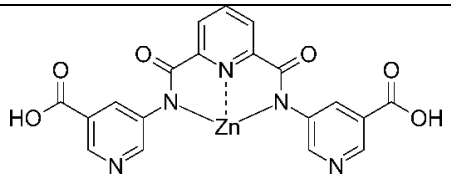
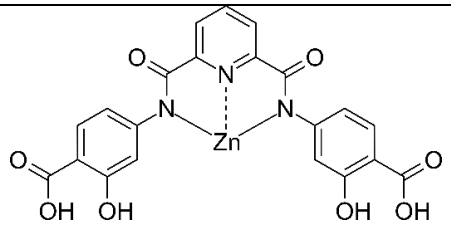


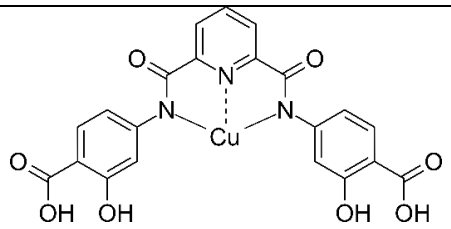
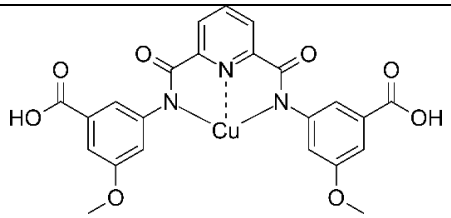
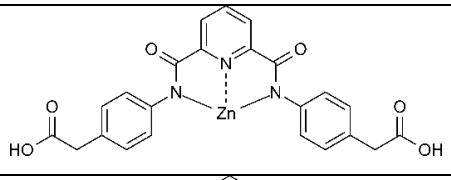
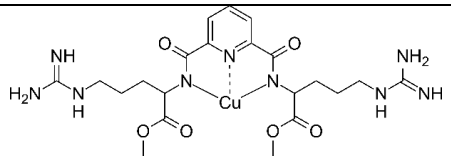
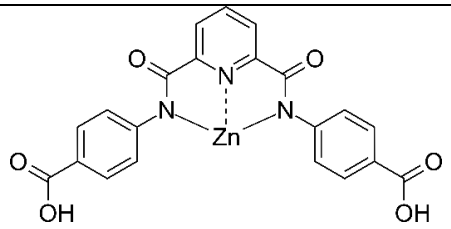
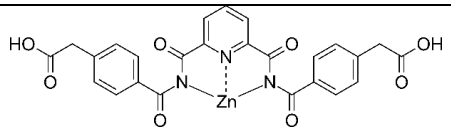
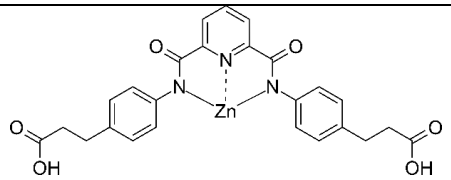
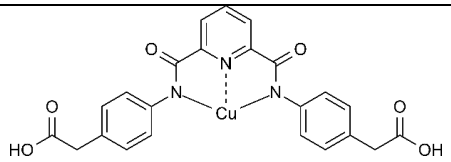
Figure 3.13: The G-scores obtained from docking entries XP1 through XP56 against 7DK5 and 7KJ5.

Table 3.5: The best-ranked entries from XP docking as determined by ECR and summation.

Entry	ECR Rank	Summation Rank
XP56	1	1
XP34	2	2
XP16	3	3
XP14	4	8
XP41	5	9
XP9	6	5
XP40	7	11
XP22	8	7
XP42	9	12
XP38	10	10
XP32	11	4
XP49	12	6

Table 3.6: The structures and druglikeness parameters for the top 10 XP hits. As was noted in the methods for ligand preparation, the current force fields employed by Schrodinger are not parameterized for metal-containing ligands. Consequently, ionization states could not be generated for the chelates and represents a current limitation in the accuracy of docking in Glide. While ionization states for carboxylic acids and guanadinium groups may affect the *in silico* affinity for the RBD, the purpose of docking was to determine ideal substitution patterns for the chelates. Hence, the docking results are valid for determining favourable substitution patterns on the aryl rings of the chelate but the final G-score may be affected by ionization states.

Structure	Entry	MW[a]	#HBA[b]	#HBD[c]	#RB[d]
	XP56	407.33	8	2	4
	XP34	437.35	8	4	4

	XP16	437.35	8	4	4
	XP14	465.41	8	2	6
	XP41	433.41	6	2	4
	XP9	507.54	12	6	2
	XP40	405.36	6	2	4
	XP22	489.43	8	2	4
	XP42	461.46	6	2	4
	XP38	433.41	6	2	4

[a] Molecular weight (MW) in g mol^{-1} of the organic framework only.
[b] Number of hydrogen-bond acceptors (HBA).
[c] Number of hydrogen-bond donors (HBD).
[d] Number of rotatable bonds (RB).

The best-ranked chelate, **XP56**, was subjected to a 100 ns MD simulation after XP docking against Y453 on 6M0J. The RBD-XP56 system was allowed to equilibrate over 100 ns and the resulting pose is presented in Figure 3.14 with its intermolecular interactions. The protein-ligand interaction timeline is presented in Figure 3.14. The timeline presented highlights key contacts between **XP56** and residues Y453 and K417 which are maintained over the trajectory period. The residues R403, Y489, and N501 make significant contact with **XP56** over the trajectory, especially toward the end of equilibration. The residues L455 and G496 maintain significant contact but show dynamic fluctuations over the 100 ns simulation.

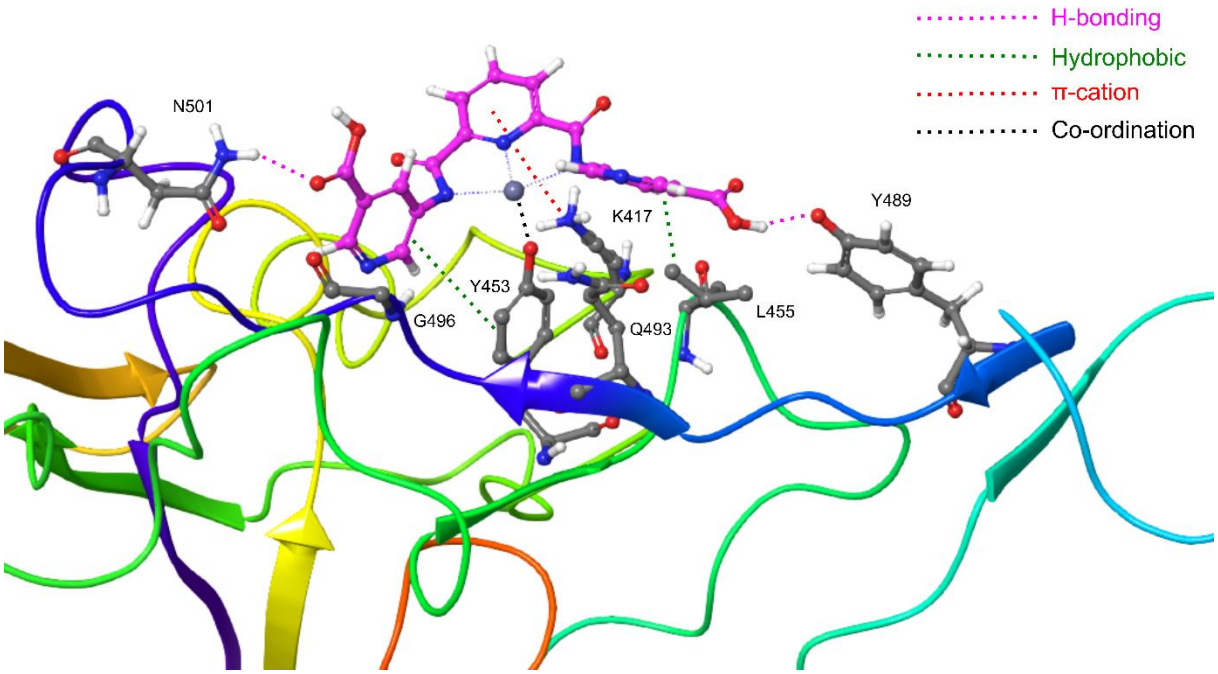


Figure 3.14: The best-ranked chelate from XP docking, *XP56*, after 100 ns MD equilibration. The ligand is coloured magenta and intermolecular interactions are listed in the legend. As was noted in the methods for docking, an anionic charge was given to each tyrosine suspected to serve as a binding site, i.e., Y453, Y449, Y489, and Y505. This was done to introduce "decoy" targets as the receptor grid was large enough to encompass the entire receptor binding motif. This gives more freedom to the docking run and does not constrain chelate binding to any particular tyrosine residue. Electrostatic forces then direct binding to the more favourable tyrosine target.

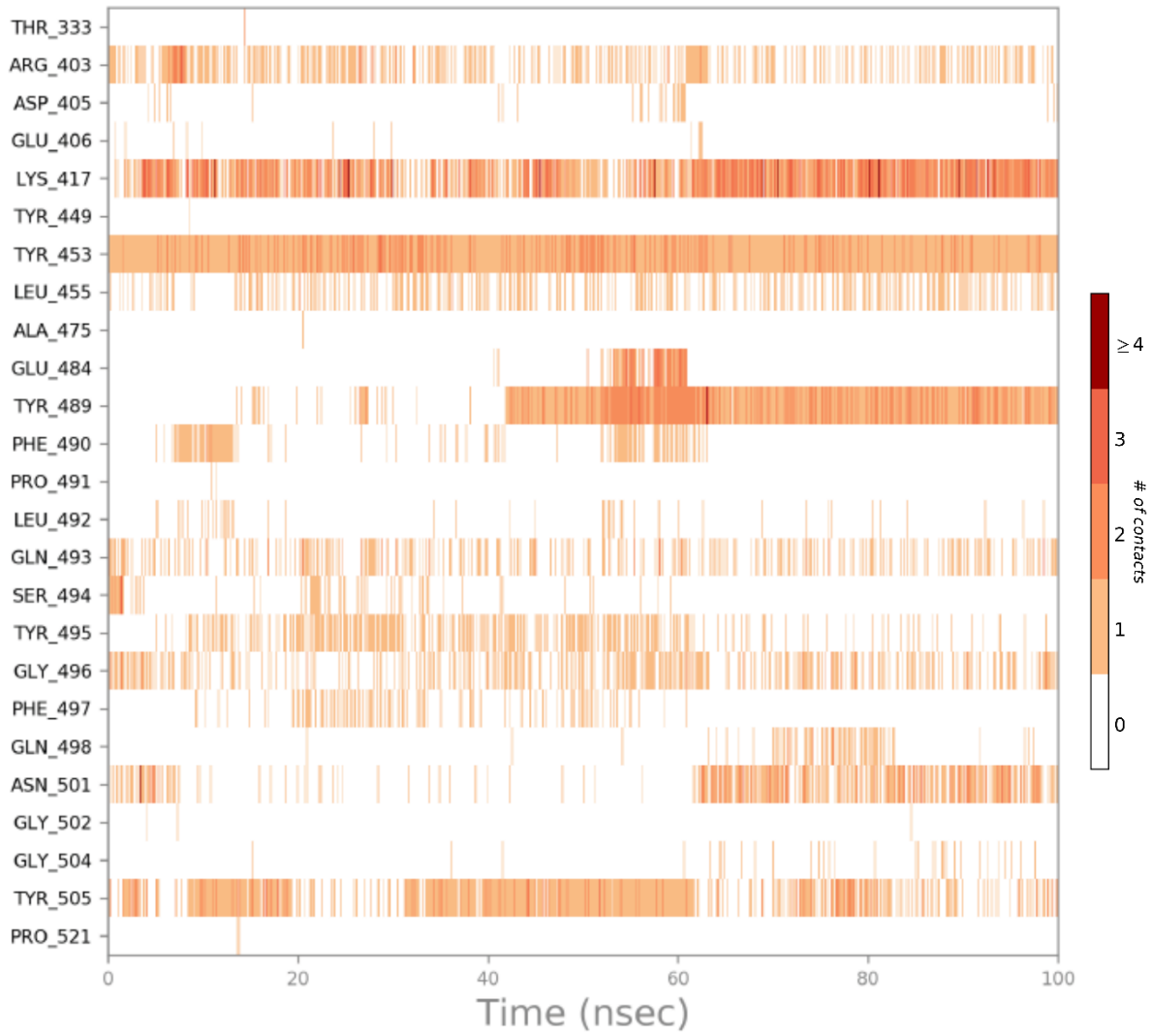


Figure 3.15: RBD-XP56 interaction timeline over 100 ns.

The structures presented in Table 3.6 encompass the 10 best-ranked chelates after XP docking, and 7 of these have functional groups substituted on the 4-position of the aryl rings that make up the amide pincer ligand. Hence, molecular docking and dynamics analysis was executed for **XP38** to determine structural features on the RBD that result in the chelates substituted at the 4-position producing the best G-scores. The best XP docked chelates with substituents in the 4-position are presented in Figure 3.16. These are **XP40**, **XP42**, **XP38**, and **XP41** and their rankings and G-scores from the individual docking run against Y453 of 6M0J are shown in Table 3.7.

.

Table 3.7: The G-scores for top-ranking entries when docked against Y453 of 6M0J.

Entry	Rank	G-score (kcal mol^{-1})
XP40	1	–6.30
XP42	2	–5.99
XP38	3	–5.36
XP41	4	–5.32

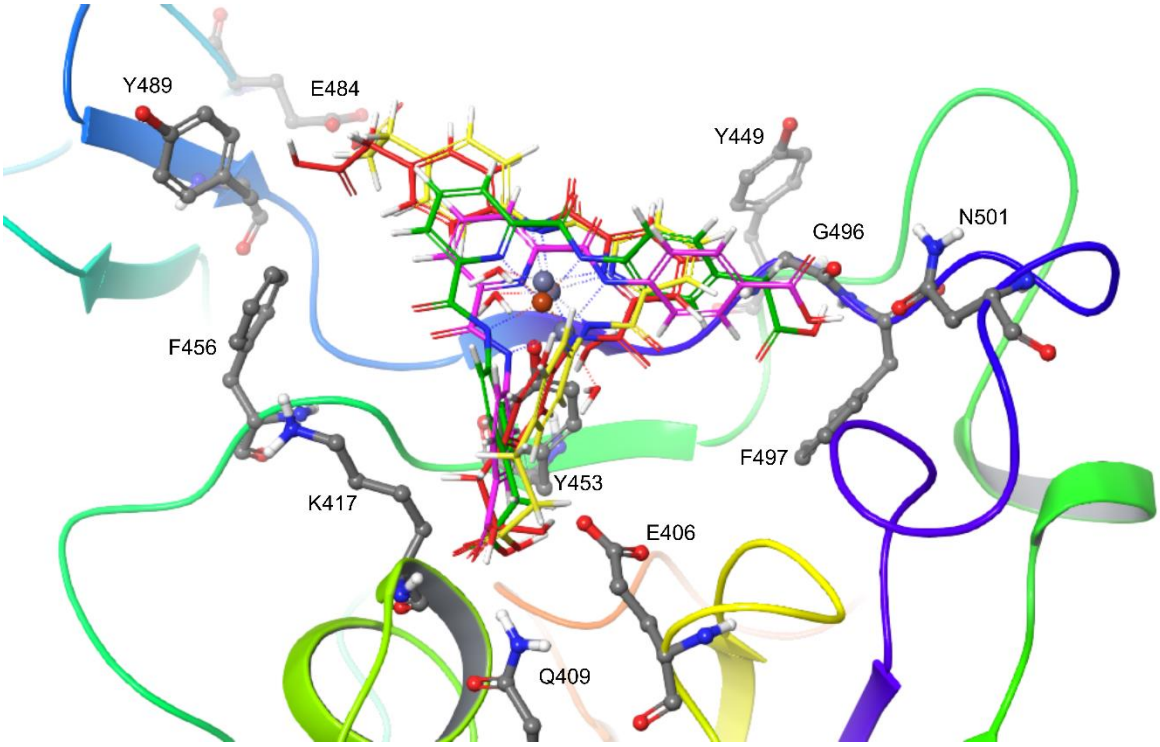


Figure 3.16: The best-docked chelates with substituents in the 4-position, *XP40* is coloured magenta, *XP42* is yellow, *XP38* is green and *XP41* is red. The Zn(II) ions have been coloured grey while Cu(II) is brown. The metal centres are all 5-coordinate with a single water molecule making the square plane and Y453 bound in the axial position. The residues on the RBD have been labelled, although some have been omitted for clarity. Y489 and Y449 were given an anionic charge to serve as "decoy" targets so that electrostatic forces were used to direct chelate binding to the most favourable residue.

It is clear from Figure 3.16 that substituents in the 4-position all occupy the same cavity on the RBD made up of residues K417, I418, E406, Q409 and Y505. The symmetrical ligands then either bind residues local to G496 or local to E484. The stability of the RBD-chelate complex is exemplified by the dynamic protein-ligand contacts presented in Figure 3.17 for **XP38**. The timeline shows that residues E406, K417, I418, and Y505 maintain contact with **XP38** over the trajectory period and once the chelate has bound this residue pocket, it is stable in solution. The interactions with I418 and Y505 are hydrogen bonds to the protein backbone while the interaction with K417 encompasses mostly ionic and hydrophobic forces.

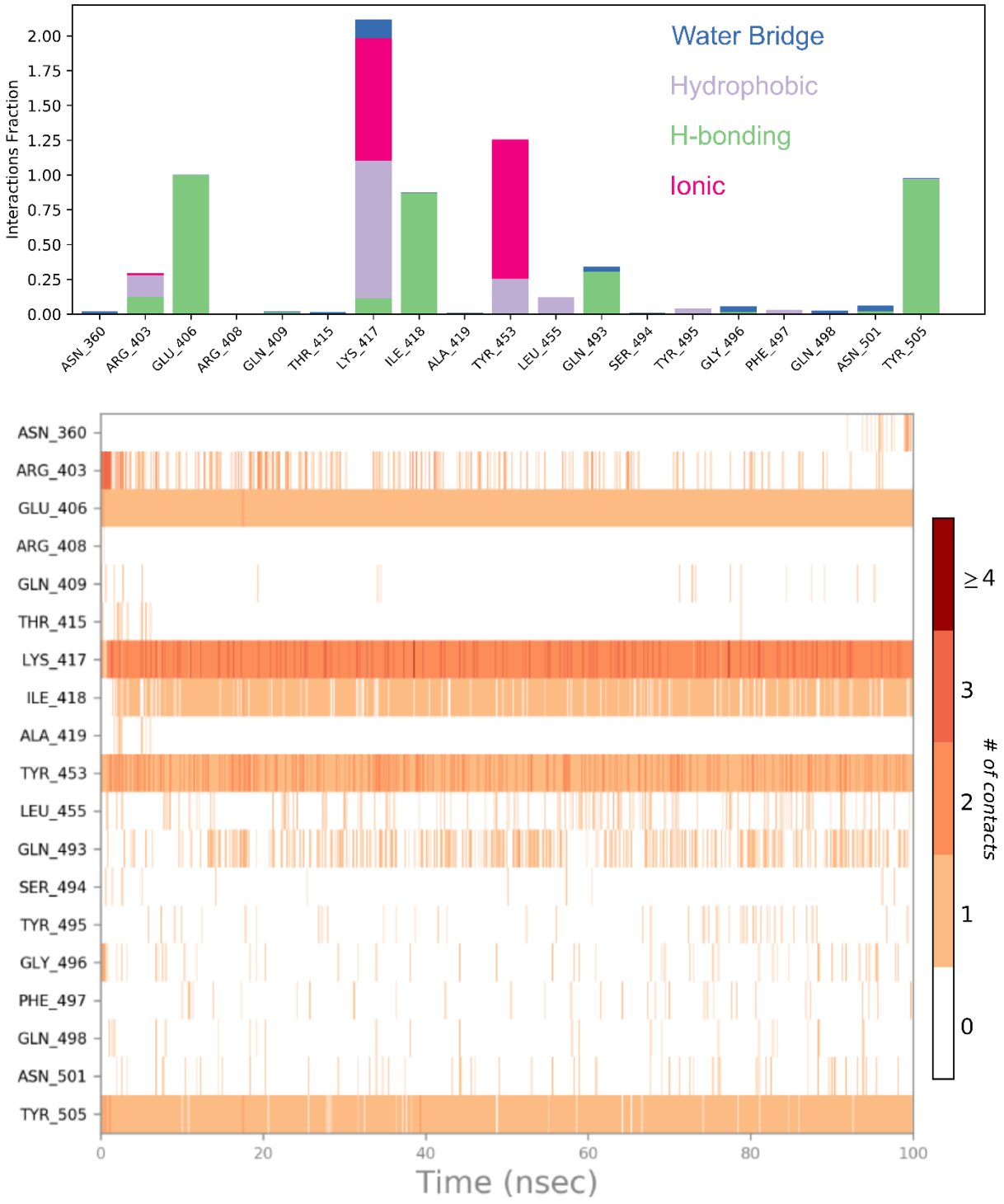


Figure 3.17: Interactions fraction and protein-ligand contacts between *XP38* and the RBD over 100 ns.

3.5 Synthesized Chelate Docking (RBD)

The results of the XP docking were used to guide synthetic efforts, and the ligands for **XP56**, **XP41**, **XP40** and **XP38** were made but metalation proved unsuccessful (Chapter 2). Hence, the ligand scaffolds were reconsidered and complexes **Cu(L5)**, **Cu(H_2L6)**, **Cu(H_2L8)**, **Cu(H_2L9)** and **Cu(L10)** were synthesized for experimental testing against the RBD and its peptide epitope. The SP docking results for the five chelates are presented in Figure 3.18 below.

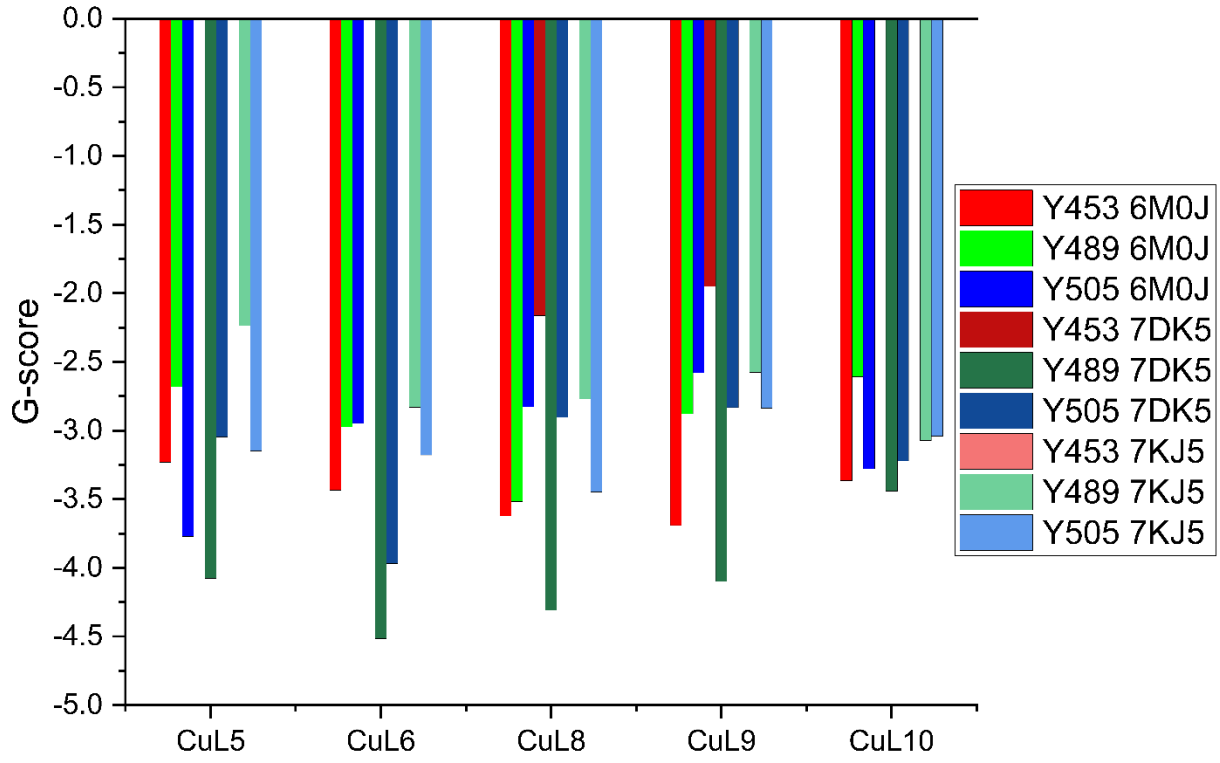
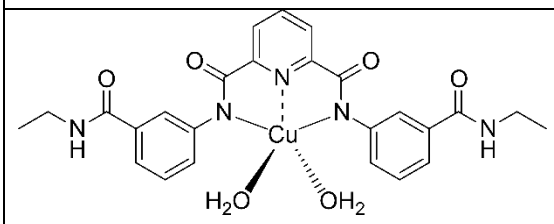
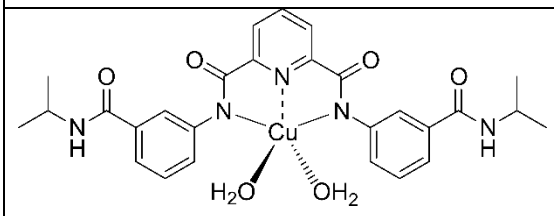
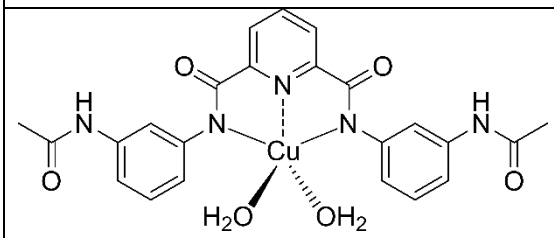
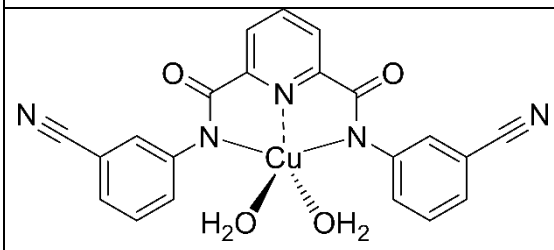
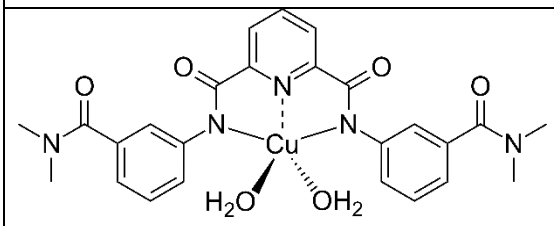


Figure 3.18: The G-scores for synthesized chelates docked against the RBD of SARS-CoV-2.

The synthesized chelates were ranked by ECR and summation of G-scores as shown in Table 3.8. It can be seen from Figure 3.18 above that the copper complexes have a higher *in silico* affinity for Y489 of the RBD. The ECR ranks **Cu(H_2L8)** as the best chelate across the various residues and protein structures, and its docked pose and interactions with the RBD at Y489 are shown in Figure 3.19.

Table 3.8: The ECR and summation rankings of the five synthesized copper chelates.

Structure	Complex	ECR Rank	Summation Rank
	$Cu(H_2L8)$	1	5
	$Cu(H_2L6)$	2	4
	$Cu(H_2L9)$	3	3
	Cu(L10)	4	1
	Cu(L5)	5	2

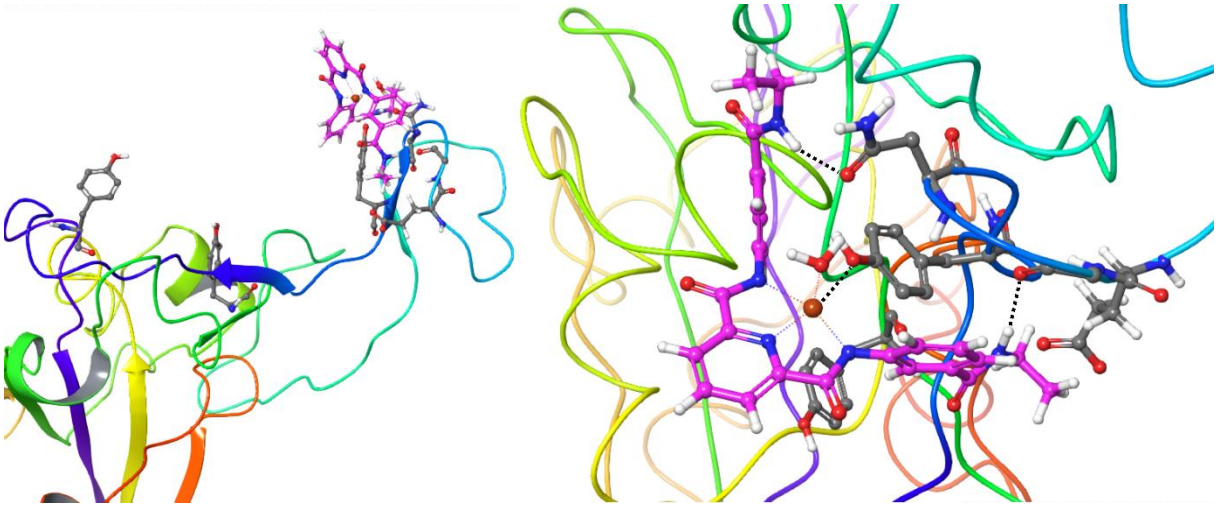


Figure 3.19: The best-ranked copper complex, Cu(H_2L8), docked against Y489 of the RBD (6M0J). The ligand is coloured magenta, and the black dashed lines are primary interactions with the protein. The copper centre is square pyramidal with Y489 making up the square plane and an aqua ligand bound in the axial position. The chelate donates two hydrogen bonds to the protein, one to the backbone at G485 and one to the side chain of N487. The ligand is further stabilized by hydrophobic forces between surrounding residues shown in Figure 3.20 below. As was noted in the methods for docking, positional constraints were used to dock the synthesized chelates. This constraint was shown by NMR to be valid. Hence, these docking runs served to delineate the binding mode between the synthesized chelates and the RBD.

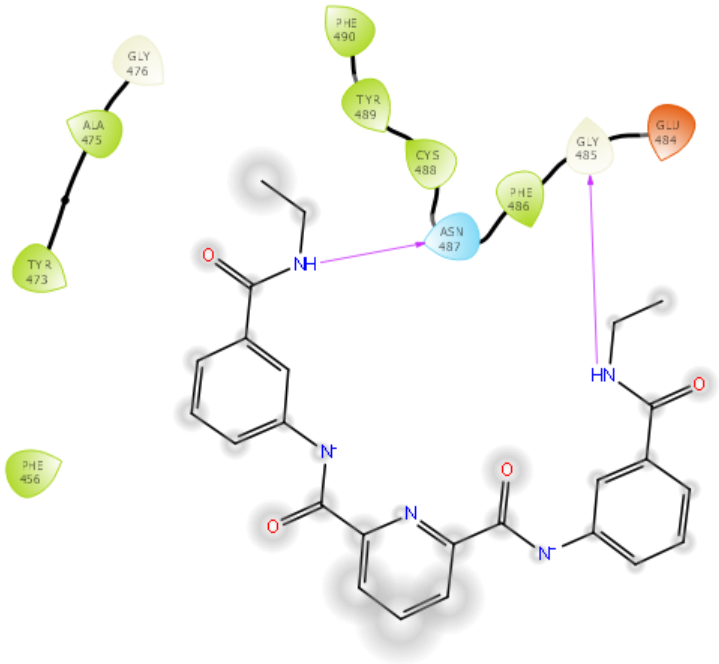


Figure 3.20: Ligand interaction diagram showing forces between Cu(H_2L8) and the RBD. Hydrophobic forces are coloured green, polar forces are blue, electrostatic forces are red, and hydrogen bonds are indicated by magenta arrows.

3.6 Synthesized Chelate Docking (Epitope)

As a preliminary proof-of-concept, the synthetic peptide sequence Ac-GVGYQP-NH_2 was purchased from Sigma-Aldrich to mimic the epitope on the RBD. This sequence corresponds to G502-V503-G504-Y505-Q506-P507 on the RBD of SARS-CoV-2. The synthesized chelates were docked against the peptide epitope and the results were compared to experimental findings. The experimental binding constants will be covered in Chapter 4 but are presented here for discussion. The G-scores, experimental K_a, and the fraction of hydrophobic interactions to tyrosine over a 100 ns MD simulation are presented in Table 3.9. The rankings of the chelates based on the values in Table 3.9 are presented in Table 3.10.

Table 3.9: G-scores for the binding of five synthesized Cu(II) chelates to the RBD target peptide epitope, the fraction of hydrophobic interactions to tyrosine over a 100 ns MD simulation, and the experimental association constant.

Complex	K_a ($\times 10^4$) M^{-1}	G-score (kcal mol^{-1})	Hydrophobic Fraction
Cu(L5)	2.38	–1.88	0.315
Cu(H_2L6)	1.76	–2.07	0.128
Cu(H_2L8)	1.59	–1.84	0.103
Cu(H_2L9)	2.10	–2.04	0.117
Cu(L10)	2.07	–2.06	0.180

Table 3.10: The rankings of the chelates based on experimental K_a, G-score, and the hydrophobic fraction of interactions.

Rank	Experimental K_a	G-score	Hydrophobic Fraction
1	Cu(L5)	Cu(H_2L6)	Cu(L5)
2	Cu(H_2L9)	Cu(L10)	Cu(L10)
3	Cu(L10)	Cu(H_2L9)	Cu(H_2L6)
4	Cu(H_2L6)	Cu(L5)	Cu(H_2L9)
5	Cu(H_2L8)	Cu(H_2L8)	Cu(H_2L8)

The MD analysis of the chelates shows that the peptide-chelate complex is unstable in solution and the chelate readily departs from its docked position at tyrosine before binding again in dynamic equilibrium. This is exemplified in the RMSD plot for **Cu(L5)** shown in Figure 3.21.

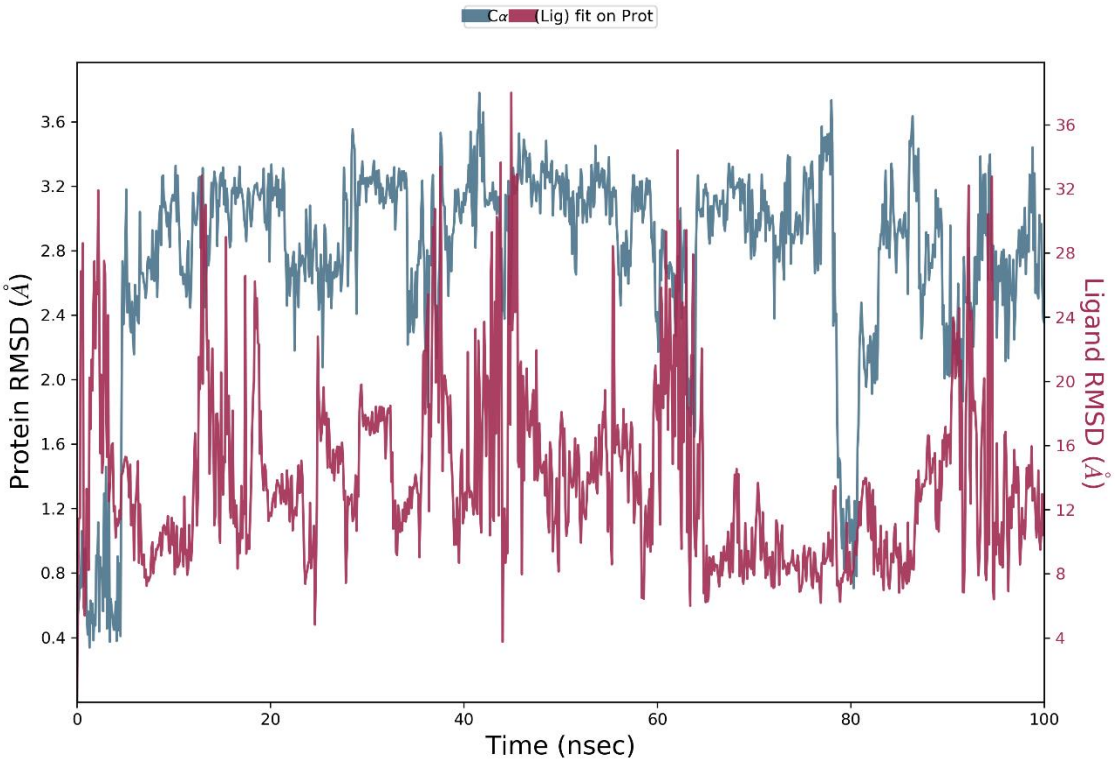


Figure 3.21: The RMSD plot for Cu(L5) and the peptide epitope. The system struggles to equilibrate and the fluctuations for the peptide RMSD indicate that the α-helical structure is unstable under the force field parameters.

The chelate departs from the binding site and enters solution where it may still make contact with tyrosine, but the copper centre is not coordinated to the phenol side chain. It will be shown in Chapter 4 that the copper complexes specifically target tyrosine and so this coordination must be modelled in the simulation. Only when the copper centre is coordinated to tyrosine, will the aryl rings of the ligand interact hydrophobically with the residue. Hence, only the hydrophobic fraction of peptide-ligand contacts has been considered to determine a ranking for the chelates. The docked peptide-Cu(L5) complex and its contacts and interactions fraction are shown in Figure 3.22.

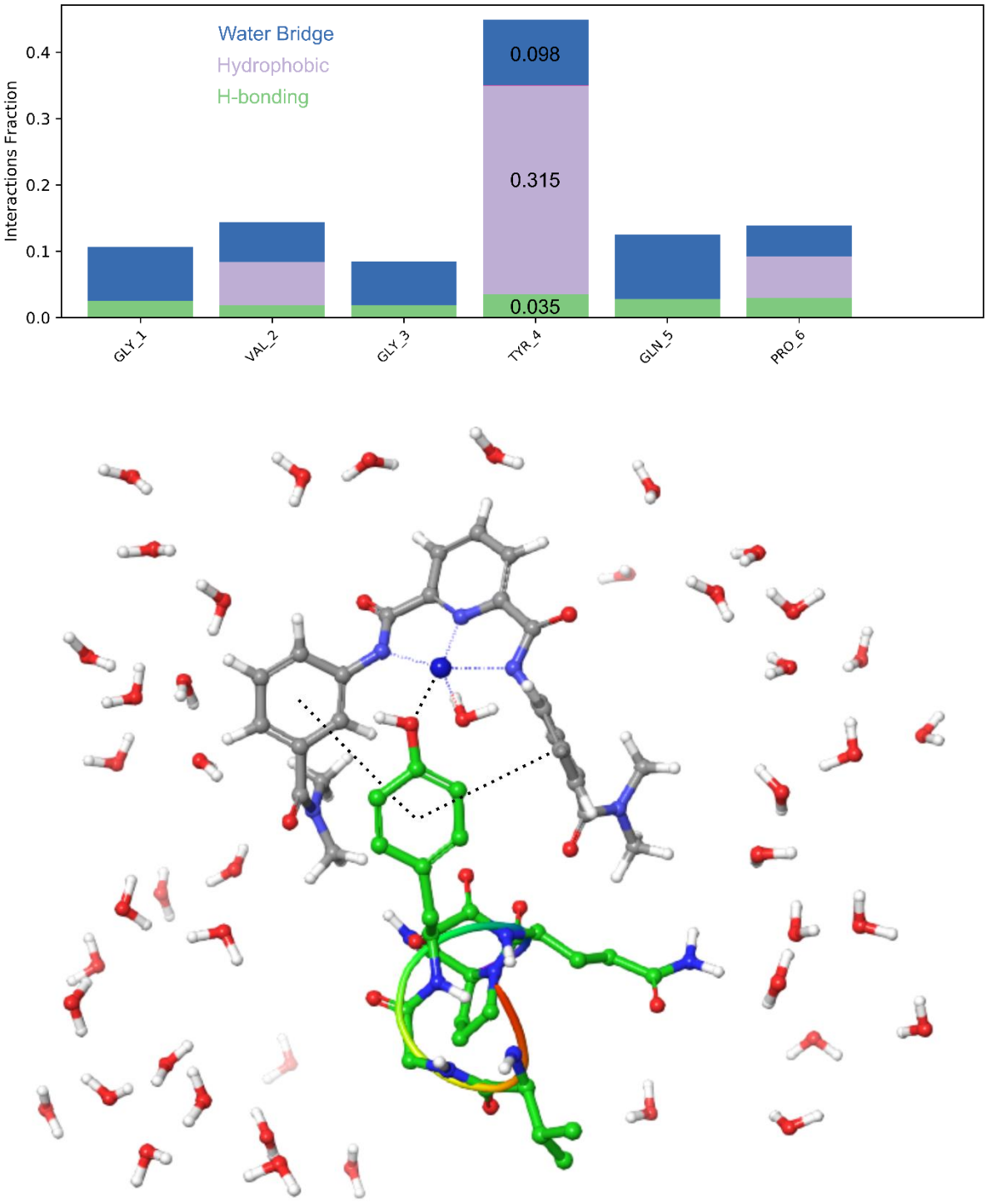


Figure 3.22: Cu(L5) docked against the peptide RBD epitope. The tyrosine is coordinated to the copper center making up the square plane of the square pyramidal metal complex. The binding is stabilized by hydrophobic forces between the aryl rings of the ligand and the phenolic residue. The hydrophobic interactions fraction is also shown and was used to determine the ranking for the chelates.

4. Conclusion

The HTVS process screened a large library of copper chelates that produced docking scores between –9 and –8 kcal mol^{-1} for the top hits. The chelates were docked at Y453 of the SARS-CoV-2 RBD (PDB: 6M0J) and it was found that the best-ranking entries all targeted residues R403, K417, Y453, L455, Q493, S493, Y495, G496 and Y505. The SP and XP docking of synthetically feasible chelates produced some docking scores approaching between –8 and –7 kcal mol^{-1} but on average the chelates' G-scores fell in the range between –6 and –4 kcal mol^{-1}. The top hits were found to possess substituents in the 4-position of the aryl ring of the pincer ligand and when these chelates were docked against Y453, the ligand frameworks all occupied the same protein pocket comprising of residues K417, I418, E406, Q409 and Y505. The best-docked ligands substituted at the 4-position were then further stabilized by hydrogen bonding to G496. These ligands also occupied the protein pocket encompassing K417, I418, E406, and Q409 when docked against Y505 with additional stabilizing interactions between the ligand and R403, D405 and G502. The top-ranking XP docked ligand was substituted in the 3-position of the aryl ring and when docked against Y453 the chelate was stabilized by interactions to K417, Y489, N501 and Y505. The best-docked ligand substituted in the 3-position was then further stabilized by hydrogen bonding to G496.

The synthesized chelates were docked against the various tyrosine residues present on the SARS-CoV-2 RBD and produced G-scores between –4 and –3 kcal mol^{-1}. The docking process identified that the copper chelates, **Cu(L5)** through **Cu(L10)**, preferentially targeted Y489 while some poses could not be generated for Y453 due to energy minimization thresholds. This is because Y453 is buried within the RBD cavity and restraints imposed on the position of Cu(II) with respect to Y453 meant that the ligand could not be favourably docked in the 3D space due to steric repulsions between the protein and ligand. Hence, it is reasonable to conclude that the chelates would favourably bind more solvent-exposed residues like Y489 and Y505. The binding mode between the copper pincer and RBD is theorized to involve a coordination bond between Cu(II) and tyrosine, with hydrogen-bond donation from the organic framework to the protein and additional stabilization due to hydrophobic forces.

References

(1) *WHO Coronavirus (COVID-19) Dashboard*. https://covid19.who.int (accessed 2023-03-15).

(2) Zhu, Y.; Yu, D.; Yan, H.; Chong, H.; He, Y. Design of Potent Membrane Fusion Inhibitors against SARS-CoV-2, an Emerging Coronavirus with High Fusogenic Activity. *J. Virol.* **2020**, *94* (14), 12.

(3) Jiang, S.; Zhang, X.; Du, L. Therapeutic Antibodies and Fusion Inhibitors Targeting the Spike Protein of SARS-CoV-2. *Expert Opin. Ther. Targets* **2021**, *25* (6), 415–421. https://doi.org/10.1080/14728222.2020.1820482.

(4) Yuan, M.; Wu, N. C.; Zhu, X.; Lee, C.-C. D.; Mok, C. K. P.; Wilson, I. A. A Highly Conserved Cryptic Epitope in the Receptor Binding Domains of SARS-CoV-2 and SARS-CoV. **2020**, 5.

(5) Yan, R.; Zhang, Y.; Li, Y.; Xia, L.; Guo, Y.; Zhou, Q. Structural Basis for the Recognition of SARS-CoV-2 by Full-Length Human ACE2. *Science* **2020**, *367* (6485), 1444–1448. https://doi.org/10.1126/science.abb2762.

(6) Lan, J.; Ge, J.; Yu, J.; Shan, S.; Zhou, H.; Fan, S.; Zhang, Q.; Shi, X.; Wang, Q.; Zhang, L.; Wang, X. Structure of the SARS-CoV-2 Spike Receptor-Binding Domain Bound to the ACE2 Receptor. *Nature* **2020**, *581* (7807), 215–220. https://doi.org/10.1038/s41586-020-2180-5.

(7) Shang, J.; Ye, G.; Shi, K.; Wan, Y.; Luo, C.; Aihara, H.; Geng, Q.; Auerbach, A.; Li, F. Structural Basis of Receptor Recognition by SARS-CoV-2. *Nature* **2020**, *581* (7807), 221–224. https://doi.org/10.1038/s41586-020-2179-y.

(8) Perlman, S. Another Decade, Another Coronavirus. *N. Engl. J. Med.* **2020**, *382* (8), 760–762. https://doi.org/10.1056/NEJMe2001126.

(9) Friesner, R. A.; Banks, J. L.; Murphy, R. B.; Halgren, T. A.; Klicic, J. J.; Mainz, D. T.; Repasky, M. P.; Knoll, E. H.; Shelley, M.; Perry, J. K.; Shaw, D. E.; Francis, P.; Shenkin, P. S. Glide: A New Approach for Rapid, Accurate Docking and Scoring. 1. Method and Assessment of Docking Accuracy. *J. Med. Chem.* **2004**, *47* (7), 1739–1749. https://doi.org/10.1021/jm0306430.

(10) Madhavi Sastry, G.; Adzhigirey, M.; Day, T.; Annabhimoju, R.; Sherman, W. Protein and Ligand Preparation: Parameters, Protocols, and Influence on Virtual Screening Enrichments. *J. Comput. Aided Mol. Des.* **2013**, *27* (3), 221–234. https://doi.org/10.1007/s10822-013-9644-8.

(11) Shelley, J. C.; Cholleti, A.; Frye, L. L.; Greenwood, J. R.; Timlin, M. R.; Uchimaya, M. Epik: A Software Program for PK a Prediction and Protonation State Generation for Drug-like Molecules. *J. Comput. Aided Mol. Des.* **2007**, *21* (12), 681–691. https://doi.org/10.1007/s10822-007-9133-z.

(12) Banks, J. L.; Beard, H. S.; Cao, Y.; Cho, A. E.; Damm, W.; Farid, R.; Felts, A. K.; Halgren, T. A.; Mainz, D. T.; Maple, J. R.; Murphy, R.; Philipp, D. M.; Repasky, M. P.; Zhang, L. Y.; Berne, B. J.; Friesner, R. A.; Gallicchio, E.; Levy, R. M. Integrated Modeling Program,

Applied Chemical Theory (IMPACT). *J. Comput. Chem.* **2005**, *26* (16), 1752–1780. https://doi.org/10.1002/jcc.20292.

(13) Zhang, C.; Wang, Y.; Zhu, Y.; Liu, C.; Gu, C.; Xu, S.; Wang, Y.; Zhou, Y.; Wang, Y.; Han, W.; Hong, X.; Yang, Y.; Zhang, X.; Wang, T.; Xu, C.; Hong, Q.; Wang, S.; Zhao, Q.; Qiao, W.; Zang, J.; Kong, L.; Wang, F.; Wang, H.; Qu, D.; Lavillette, D.; Tang, H.; Deng, Q.; Xie, Y.; Cong, Y.; Huang, Z. Development and Structural Basis of a Two-MAb Cocktail for Treating SARS-CoV-2 Infections. *Nat. Commun.* **2021**, *12* (1), 264. https://doi.org/10.1038/s41467-020-20465-w.

(14) Xiao, T.; Lu, J.; Zhang, J.; Johnson, R. I.; McKay, L. G. A.; Storm, N.; Lavine, C. L.; Peng, H.; Cai, Y.; Rits-Volloch, S.; Lu, S.; Quinlan, B. D.; Farzan, M.; Seaman, M. S.; Griffiths, A.; Chen, B. A Trimeric Human Angiotensin-Converting Enzyme 2 as an Anti-SARS-CoV-2 Agent. *Nat. Struct. Mol. Biol.* **2021**, *28* (2), 202–209. https://doi.org/10.1038/s41594-020-00549-3.

(15) Friesner, R. A.; Murphy, R. B.; Repasky, M. P.; Frye, L. L.; Greenwood, J. R.; Halgren, T. A.; Sanschagrin, P. C.; Mainz, D. T. Extra Precision Glide: Docking and Scoring Incorporating a Model of Hydrophobic Enclosure for Protein−Ligand Complexes. *J. Med. Chem.* **2006**, *49* (21), 6177–6196. https://doi.org/10.1021/jm051256o.

(16) Bowers, K. J.; Chow, D. E.; Xu, H.; Dror, R. O.; Eastwood, M. P.; Gregersen, B. A.; Klepeis, J. L.; Kolossvary, I.; Moraes, M. A.; Sacerdoti, F. D.; Salmon, J. K.; Shan, Y.; Shaw, D. E. Scalable Algorithms for Molecular Dynamics Simulations on Commodity Clusters. In *ACM/IEEE SC 2006 Conference (SC'06)*; IEEE: Tampa, FL, 2006; pp 43–43. https://doi.org/10.1109/SC.2006.54.

(17) Jorgensen, W. L.; Chandrasekhar, J.; Madura, J. D.; Impey, R. W.; Klein, M. L. Comparison of Simple Potential Functions for Simulating Liquid Water. *J. Chem. Phys.* **1983**, *79* (2), 926–935. https://doi.org/10.1063/1.445869.

(18) Jorgensen, W. L. Convergence of Monte Carlo Simulations of Liquid Water in the NPT Ensemble. *Chem. Phys. Lett.* **1982**, *92* (4), 405–410. https://doi.org/10.1016/0009-2614(82)83437-4.

(19) Lipinski, C. A. Drug-like Properties and the Causes of Poor Solubility and Poor Permeability. *J. Pharmacol. Toxicol. Methods* **2000**, *44* (1), 235–249. https://doi.org/10.1016/S1056-8719(00)00107-6.

(20) Lipinski, C. A. Lead- and Drug-like Compounds: The Rule-of-Five Revolution. *Drug Discov. Today Technol.* **2004**, *1* (4), 337–341. https://doi.org/10.1016/j.ddtec.2004.11.007.

(21) Patel, C. N.; Goswami, D.; Sivakumar, P. K.; Pandya, H. A. Repurposing of Anticancer Phytochemicals for Identifying Potential Fusion Inhibitor for SARS-CoV-2 Using Molecular Docking and Molecular Dynamics (MD) Simulations. *J. Biomol. Struct. Dyn.* **2022**, *40* (17), 7744–7761. https://doi.org/10.1080/07391102.2021.1902393.

(22) Teli, D. M.; Shah, M. B.; Chhabria, M. T. In Silico Screening of Natural Compounds as Potential Inhibitors of SARS-CoV-2 Main Protease and Spike RBD: Targets for COVID-19. *Front. Mol. Biosci.* **2021**, *7*, 599079. https://doi.org/10.3389/fmolb.2020.599079.

(23) Sinha, S. K.; Shakya, A.; Prasad, S. K.; Singh, S.; Gurav, N. S.; Prasad, R. S.; Gurav, S. S. An *in-Silico* Evaluation of Different Saikosaponins for Their Potency against SARS-CoV-2 Using NSP15 and Fusion Spike Glycoprotein as Targets. *J. Biomol. Struct. Dyn.* **2020**, 1–12. https://doi.org/10.1080/07391102.2020.1762741.

(24) Palacio-Rodríguez, K.; Lans, I.; Cavasotto, C. N.; Cossio, P. Exponential Consensus Ranking Improves the Outcome in Docking and Receptor Ensemble Docking. *Sci. Rep.* **2019**, *9* (1), 5142. https://doi.org/10.1038/s41598-019-41594-3.

(25) Wang, G.; Zhu, W. Molecular Docking for Drug Discovery and Development: A Widely Used Approach but Far from Perfect. *Future Med. Chem.* **2016**, *8* (14), 1707–1710. https://doi.org/10.4155/fmc-2016-0143.

Chapter 4

Biophysical Chemistry

1. Introduction

The biophysical properties of ligand binding to biomolecules can be studied with a variety of methods. Several techniques are used to probe binding events, including NMR, FTIR, UV-vis, CD and MS. Using a combination of these methods provides a more holistic view of the binding interaction. Additionally, fluorescence spectroscopy is widely used to study biomolecules because aromatic residues like tyrosine and tryptophan serve as fluorescent probes. Fluorescence is the emission of light from a molecule that occurs when a singlet state system returns to the ground state after excitation at a particular wavelength.[1] Fluorescence data are generally presented as the emission spectra and the technique is widely used due to the high sensitivity of detection.

Fluorescent measurements are versatile in their application and easily obtained data for appropriate systems gives a wealth of information about the biochemical processes taking place. Molecular binding events and mechanisms can be delineated from fluorescent data by using the century-old Hill equation.[2] The Hill equation is derived from the law of mass action:

$$nL + P \rightleftharpoons L_nP \tag{1}$$

and hence

$$[L_nP] = [P_0] \cdot \frac{[L]^n}{[L]^n + K_d} \tag{2}$$

where L is the ligand at variable concentration, P is the protein target at a fixed concentration, n is the stoichiometry of binding, L_nP is the protein-ligand complex, $[P_0]$ is the total protein concentration and K_d is the equilibrium dissociation constant. The Hill equation may be plotted from fluorescent data[3] using the expression:

$$\frac{F_0 - F}{F_0 - F_c} = \frac{[L]^n}{[L]^n + K_d} \tag{3}$$

where F is the measured fluorescence, F_0 is the starting fluorescence before addition of the ligand quencher and F_c is the ending fluorescence after the protein has been fully complexed. Although the Hill equation is a robust and suitable method for quantifying biomolecular binding events, the Stern-Volmer (SV) equations are the most widely used expressions for analyzing fluorescent data.[1,4,5]

The SV equation is defined as:

$$\frac{F_0}{F} = 1 + K_{SV}[Q] \tag{4}$$

where K_{SV} is the Stern-Volmer constant in units of M^{-1} and $[Q]$ is the concentration of the ligand quencher in molar units. When the quenching mechanism is known to be static or dynamic, the K_{SV} can be equated to the static quenching constant (K_S) or the dynamic quenching constant (K_D), respectively. When the quenching mechanism is known to be static, and the ligand binds the protein with 1:1 stoichiometry to form a non-fluorescent ground-state complex, the constant K_{SV} can be equated to K_a, the equilibrium association constant. The Stern-Volmer constant is also given by the following expression:

$$K_{SV} = k_q \tau_0 \tag{5}$$

where k_q is the bimolecular quenching rate constant with the units $M^{-1}\,s^{-1}$ and τ_0 is the lifetime of the fluorophore fluorescence in the absence of any quencher. The biomimetic models used in the current study include *p*-cresol and a hexapeptide epitope containing a single tyrosine. These models are presented in Figure 4.2. The lifetime of fluorescence for *p*-cresol has been reported as 1.6 ns[6, 7] while the τ_0 for free tyrosine has been reported between 3.3 and 3.8 ns[8,9,10] and will be taken as 3.6 ns for present purposes. The SARS-CoV-2 RBD has a reported τ_0 of 6.2 ns.[11]

When n, the number of binding sites, is unknown, it is not possible to perform a linear regression for equations (2) or (3) and it is appropriate to modify equation (4) to include the unknown with the SV constant now equal to the equilibrium association constant.

$$\frac{F_0}{F} = 1 + K_a[Q]^n \tag{6}$$

Then linearization is easily achieved by taking the logarithm of equation (6) to yield the modified double-log SV equation:

$$\log\frac{F_0 - F}{F} = n\log[Q] + \log K_a \tag{7}$$

When the SV equation (4) is plotted and upward curvature is observed, it is likely that dynamic quenching is affecting fluorescent emission. When only static quenching is being observed the plot of equation (4) yields a straight line. The SV equation may be modified to account for upward curvature when both static and dynamic quenching are being observed. This yields[1] the second order equation:

$$\frac{F_0}{F} = 1 + (K_D + K_S)[Q] + K_D K_S[Q]^2 \quad (8)$$

When dual quenching mechanisms are being observed, equation (8) may be modified to yield a straight line when the apparent quenching constant, K_{app}, is plotted against [Q]. The equation is defined as:

$$K_{app} = \left[\frac{F_0}{F} - 1\right]\frac{1}{[Q]} = (K_D + K_S) + K_D K_S[Q] \quad (9)$$

The fluorescent data must be properly corrected to avoid inaccurate analysis of the observed trends and one major contribution to the distortion of fluorescent data is the inner-filter effect (IFE). The IFE is greatest when components in solution strongly absorb exciting or emitting radiation and numerous corrections are available that may be applied to the appropriate experimental setup.[12,13,14] Herein, it was found that the IFE correction described by Gauthier et al.[15] was the most appropriate method for the system and experimental setup currently under study. The correction is defined by equation (10) below.

$$F_{cor} = F_{obs} \times \frac{2.3dA_{ex}}{1-10^{-dA_{ex}}} \times 10^{gA_{em}} \times \frac{2.3sA_{em}}{1-10^{-sA_{em}}} \quad (10)$$

Where F_{cor} is the corrected fluorescent intensity value, F_{obs} is the observed fluorescent intensity, A_{ex} is the total absorbance per cm of the solution at the excitation wavelength, A_{em} is the total absorbance per cm at the emission wavelength, and d, g and s are dependent on the geometry of the measurement and have been defined in the original paper as well as Figure 4.1 below. The geometry of the quartz cuvette used in the current study had dimensions 1 cm × 0.2 cm with the 1 cm path length facing the exciting radiation and emissive radiation being detected at a right-angle using a Cary Eclipse fluorimeter. There have been methods described that correct for IFE that arise from the horizontally orientated slits on the Cary Eclipse[16], however, equation (10) was found to produce better corrections without the use of mathematical scripts. Given the dimensions of the cuvette used, and the horizontal beam of the Cary Eclipse, d, g and s are 1 cm, 0 cm, and 0.2 cm respectively.

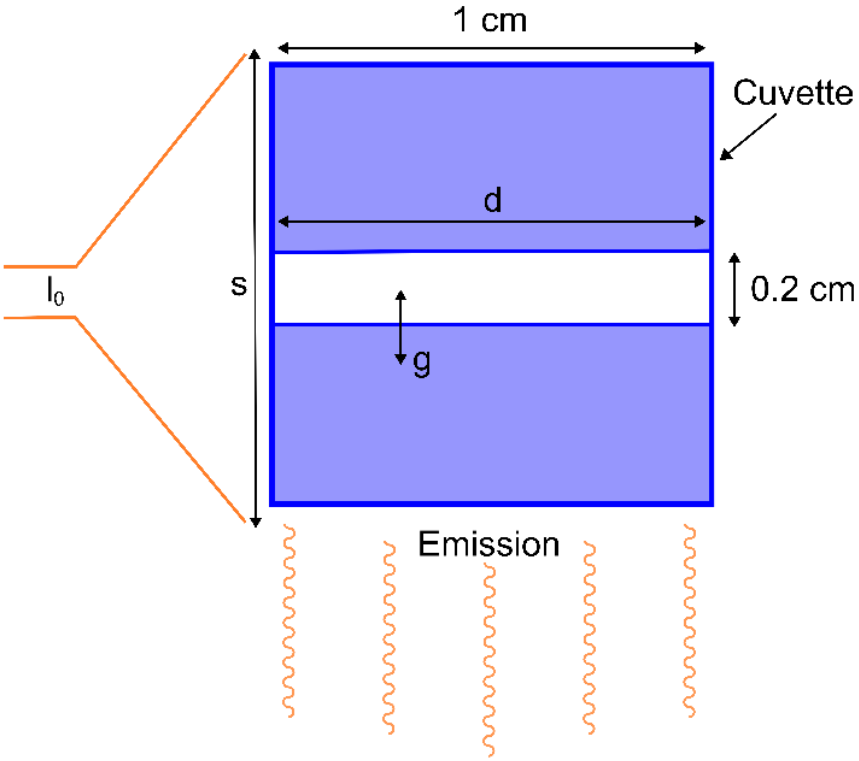


Figure 4.1: Geometry of the cuvette. I_0 is the horizontally orientated excitation beam with thickness s. The path length of the exciting radiation d = 1 cm and g is the distance from the edge of the sample beam to the edge of the cuvette. This reduces to g = 0 cm because the entire 0.2 cm emission pathlength is illuminated by the excitation beam and hence s = 0.2 cm.

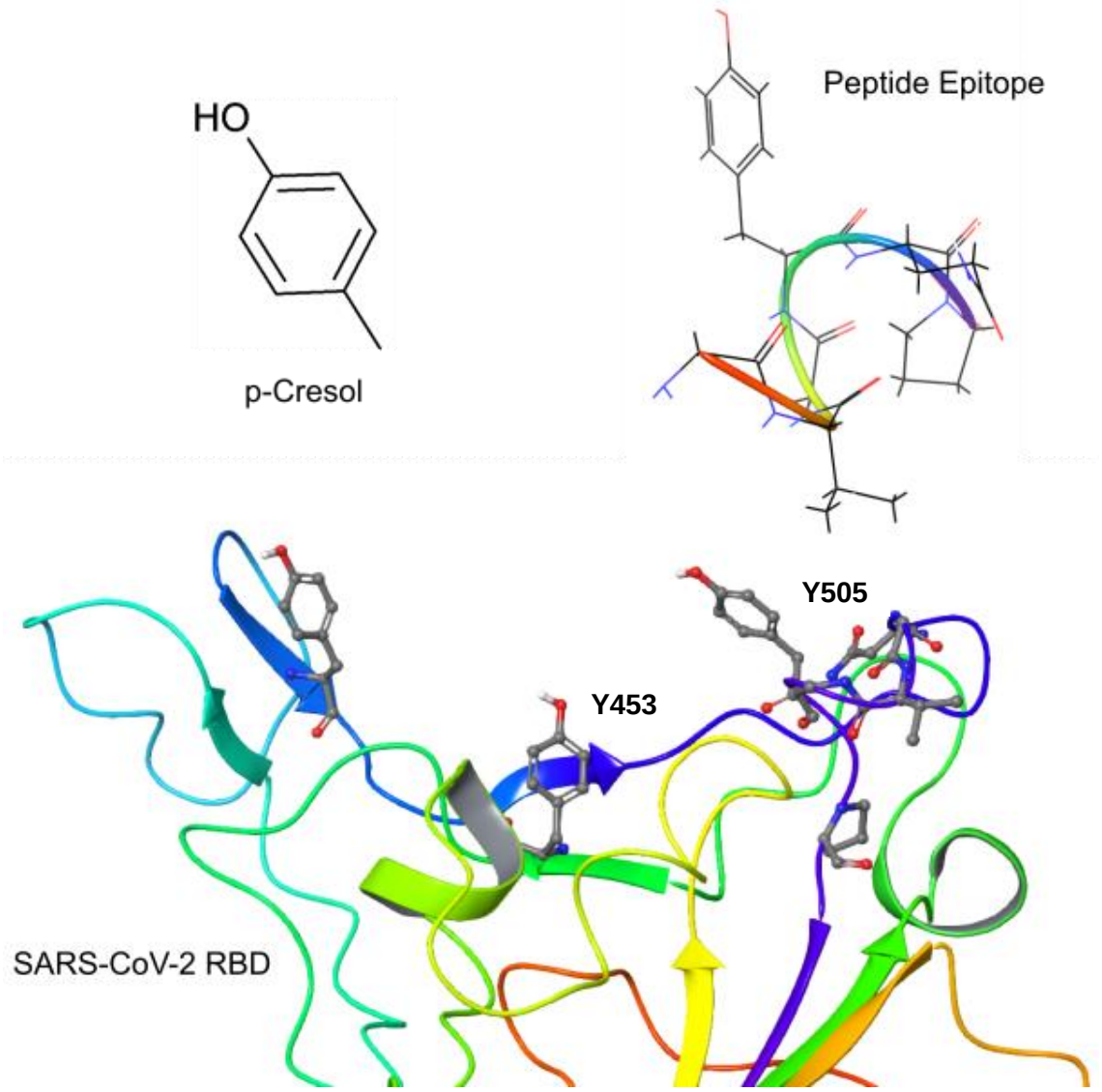


Figure 4.2: The biomimetics used to model the SARS-CoV-2 RBD. The small molecule *p*-cresol is the simplest model for tyrosine and was used to determine the Cu(II) NNN pincers' coordinative affinity for the phenol side chain. The peptide epitope used to model the RBD has the sequence GVGYQP and corresponds to G502-V503-G504-Y505-Q506-P507 on the RBD of SARS-CoV-2. The peptide epitope has been shown on the RBD as ball-and-stick structures along with solvent-exposed Y453 and Y489 which are also potential binding sites for the Cu(II) pincers studied here.

The biophysical study aimed to determine whether the Cu(II) pincers bind phenolic residues and to then quantify the binding affinity. The binding interaction was first quantified for the simplest biomimetic model, *p*-cresol, before delineating the binding event for the peptide epitope and the SARS-CoV-2 RBD. By targeting the tyrosine residues involved with ACE2 receptor recognition, the metal chelates may disrupt membrane fusion events and prevent viral infection of host cells.

2. Methods

2.1 NMR Spectroscopy

NMR data were acquired on a Bruker Advance III 500 MHz spectrometer operating at 500.13 MHz for ^{1}H and 125.31 MHz for ^{13}C. Data were acquired in D_2O as the solvent at a temperature of 296 K.

2.2 Mass Spectroscopy

Mass spectra were recorded with a Bruker compact Q-TOF high resolution mass spectrometer with Bruker Daltronics HyStar 3.2 SR4 software. Chromatograms were analysed with Bruker Compass DataAnalysis software (Version 4.3) or with MestReNova Software (Version 12.0.0-20080). Samples were prepared by weighing 1 mg of CuL5 and the peptide epitope and dissolving these components in 100 µL of HPLC grade DMSO before making up a final volume of 1 mL with UltraPure Type 1 water and subsequent 100-fold dilution with Type 1 water. The mole ratio of chelate to peptide was 1.3:1. CuL5 was chosen for MS analysis because it was the most stable chelate and demetallation in the spectrometer would be lessened.

2.3 CD Spectroscopy

Spectra were recorded on a Jasco J-1500 Circular Dichroism Spectrophotometer at 37 °C using a quartz cuvette with dimensions 1.0 × 1.0 cm over the wavelength range of 180 to 300 nm for the peptide epitope. Samples were prepared with Type 1 water only. The spectra were recorded with a data interval of 0.5 nm and with a scan rate of 500 nm/min for three accumulations and then averaged. The baseline spectrum was subtracted from the sample spectra. The peptide concentration was kept constant with [peptide] = 50 µM while the Cu(II) chelate was titrated into the cuvette over a range 7 to 120 µM. The recorded spectra were then smoothed in OriginPro 2021 using the Savitzky-Golay method using 10 points and a second order polynomial before applying the appropriate dilution factor corrections.

Spectra were recorded for the SARS-CoV-2 Delta RBD at 25 °C in 3 mM HEPES, 150 mM NaCl, 0.02% NaN_3 aqueous buffer at pH 7.4 using a quartz cuvette with dimensions 1.0 × 1.0 cm over the wavelength range of 190 to 890 nm. The spectra were recorded with a scan rate of 500 nm/min for five accumulations and then averaged. The baseline spectrum was subtracted from the sample spectra. The [RBD] was kept constant at 15 µM while the Cu(II) pincer was titrated into the protein solution. The recorded spectra were then smoothed in OriginPro 2021 using the Savitzky-Golay method using 10 points and a second order polynomial before applying the appropriate dilution factor corrections.

2.4 Fluorescence Spectroscopy

Fluorescence spectra were recorded using a Varian Cary Eclipse fluorescence spectrophotometer using the Cary Eclipse software (version 1.0(78)). Spectra were recorded for the peptide epitope and *p*-cresol at 37 °C, with an excitation wavelength of 280 nm, and the emission spectrum recorded from 290 to 390 nm. The emission spectra were occasionally recorded from 290 to 600 nm but no tyrosyl radical or tyrosinate anion emission was ever observed. Titrations involving *p*-cresol used a slit width of 5 nm for both excitation and emission, while titrations involving the peptide epitope used a slit width of 10 nm for both excitation and emission. The titrations were performed as a serial dilution of the copper complexes from 500 to 1 μM in 10 mM MOPS aqueous buffer with 10% (v/v) DMSO at 7.4 pH while keeping the *p*-cresol or peptide concentration constant at 100 μM. The recorded data were smoothed in OriginPro 2021 using the Fast Fourier Transform (FFT) Filter with 5 points and a cut-off frequency of 0.1 before applying the appropriate IFE corrections. Titrations were performed in triplicate.

Spectra were recorded for the SARS-CoV-2 Delta RBD at 37 °C, with an excitation wavelength of 280 nm, and the emission spectrum recorded from 290 to 600 nm. The excitation slit width was 5 nm and the emission slit width was 20 nm. The titrations were performed by adding 1 μL aliquots of 250 μM copper complex to a 3 μM RBD solution in 3 mM HEPES, 150 mM NaCl, 0.02% NaN_3 aqueous buffer at pH 7.4. The recorded data were smoothed in OriginPro 2021 using the Fast Fourier Transform (FFT) Filter with 5 points and a cut-off frequency of 0.1 before applying the appropriate dilution factor and IFE corrections. Titrations were performed in duplicate.

3. Results and Discussion

3.1 Biomimetic Models

Although fluorescent measurements were used to quantify the binding interactions between the Cu(II) NNN pincer library and *p*-cresol or the SARS-CoV-2 peptide epitope, it was necessary to prove that the chelates bind specifically to tyrosine by NMR spectroscopy. CuL5 and Cu(H_2L6) were chosen to showcase tyrosine recognition because the chelates are highly water-soluble. The NMR spectra obtained are shown below in Figure 4.3 and Figure 4.4 (Supporting Information S4.1-S4.3). The NMR data show that tyrosine is significantly affected by Cu(II) pincer binding. The peptide has been fully assigned and the spectra show that while tyrosine proton signals have become broader, weaker, and shifted, the remaining amino acids are largely unaffected.

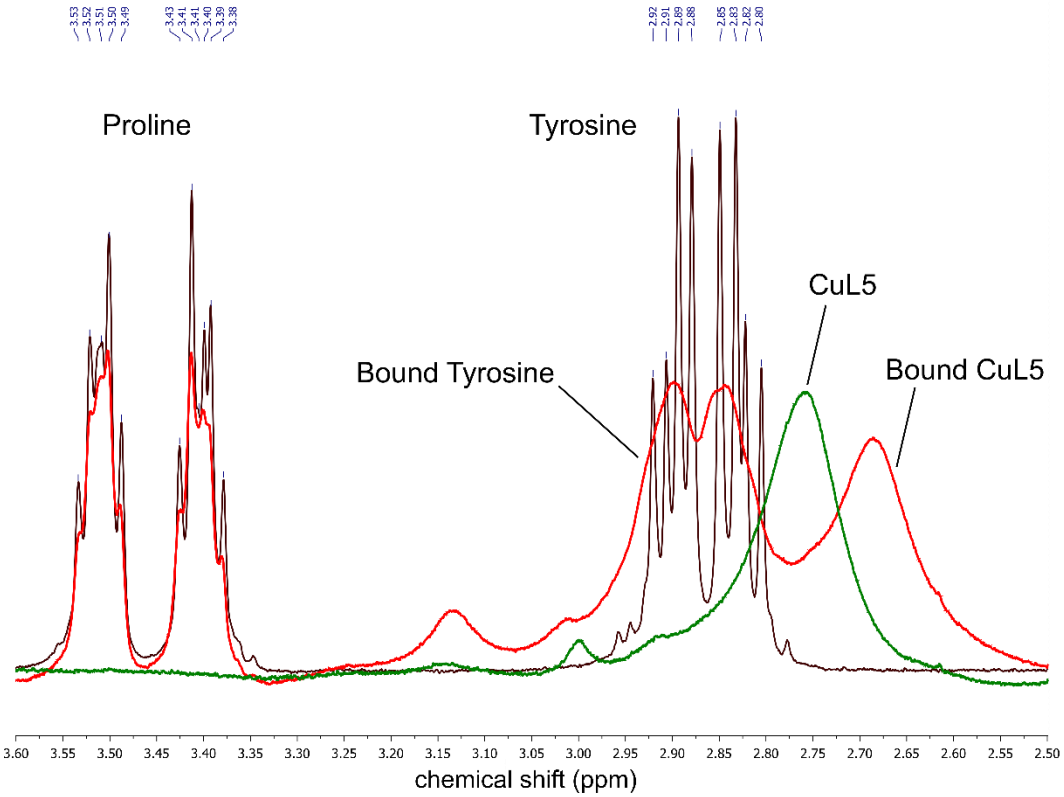


Figure 4.3: The NMR spectrum of the free peptide at a concentration of 6 mM is shown in black, the spectrum of the free complex CuL5 at 3 mM is shown in green, and the spectrum of peptide-chelate mixture is shown in red with [peptide] = 6 mM and [CuL5] = 3 mM.

There is a small downfield shift of 0.01 ppm for the aromatic tyrosine residues upon Cu(II) binding, whilst the proton signal for CuL5 shows a significant upfield shift of 0.08 ppm (Figure 4.3). This strongly indicates that upon coordination, the tyrosine donates electron density to the copper chelate.

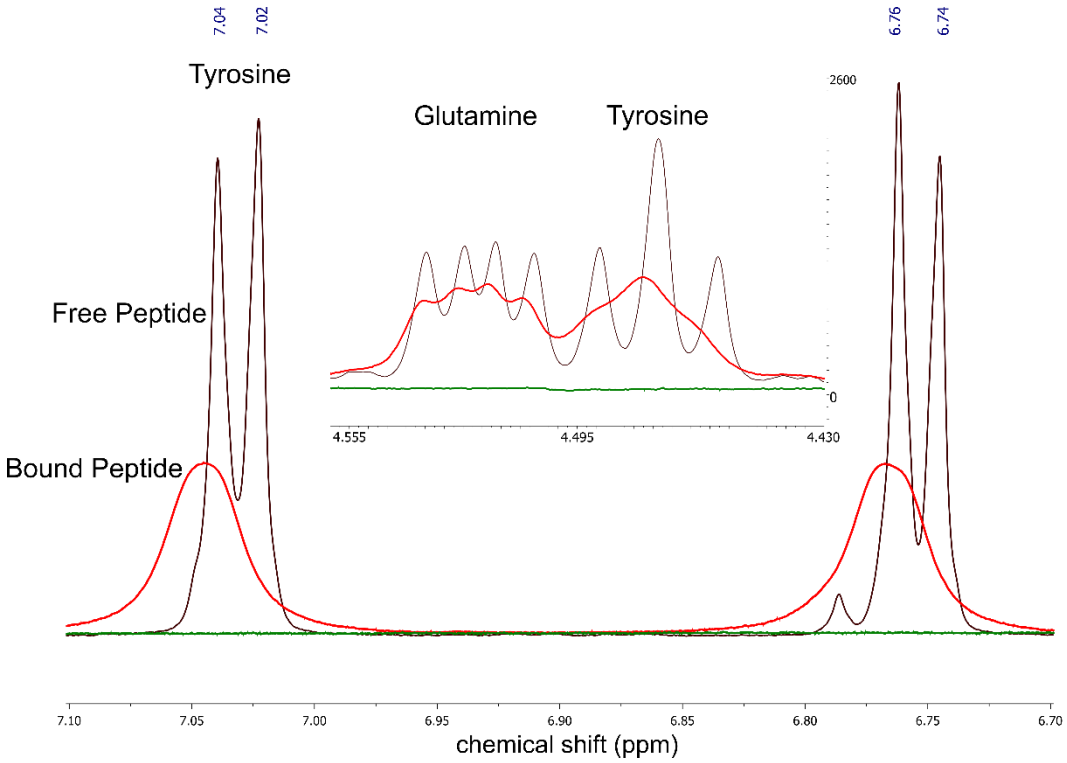


Figure 4.4: The NMR spectrum of the free peptide at a concentration of 6 mM is shown in black, the spectrum of the free complex Cu(H_2L6) at 800 µM is shown in green, and the spectrum of the peptide-chelate mixture is shown in red with [peptide] = 6 mM and [Cu(H_2L6)] = 800 µM.

The slight broadening of the proline signal in Figure 4.3 and glutamine signal in Figure 4.4 can be attributed to the paramagnetic material present in the NMR sample. Proline is directly adjacent to tyrosine and the proline signals are minimally perturbed, indicating that tyrosine is indeed the ligand binding site. The significant broadening and downfield shifts for all tyrosine signals clearly indicate that there is selective binding between this amino acid and the Cu(II) pincers. The perturbation of the aromatic tyrosine in the presence of the Cu(II) pincers was also confirmed by FTIR spectroscopy as shown in Figure 4.5.

The NMR data show that tyrosine on the peptide epitope is targeted by the Cu(II) pincers and MS data confirm that the binding stoichiometry is 1:1. The mass spectrum is presented in Figure 4.6and S4.4. The identified species from the mass spectrum indicates that the Cu(II) pincer coordinates the tyrosine, but deprotonation of the phenol does not occur. This was also checked by fluorescence spectroscopy as no tyrosyl radical[17,18] or tyrosinate anion[19] emission was ever observed under biological conditions (S4.5). Although the peptide-chelate species identified by mass spectrometry has the Cu(II) centre 4-coordinate with the NNN pincer ligand and tyrosine

making up the square-plane, UV-Vis absorbance data indicates that the Cu(II) centre is 5-coordinate under biological conditions (S4.6), with the fifth ligand likely being water.

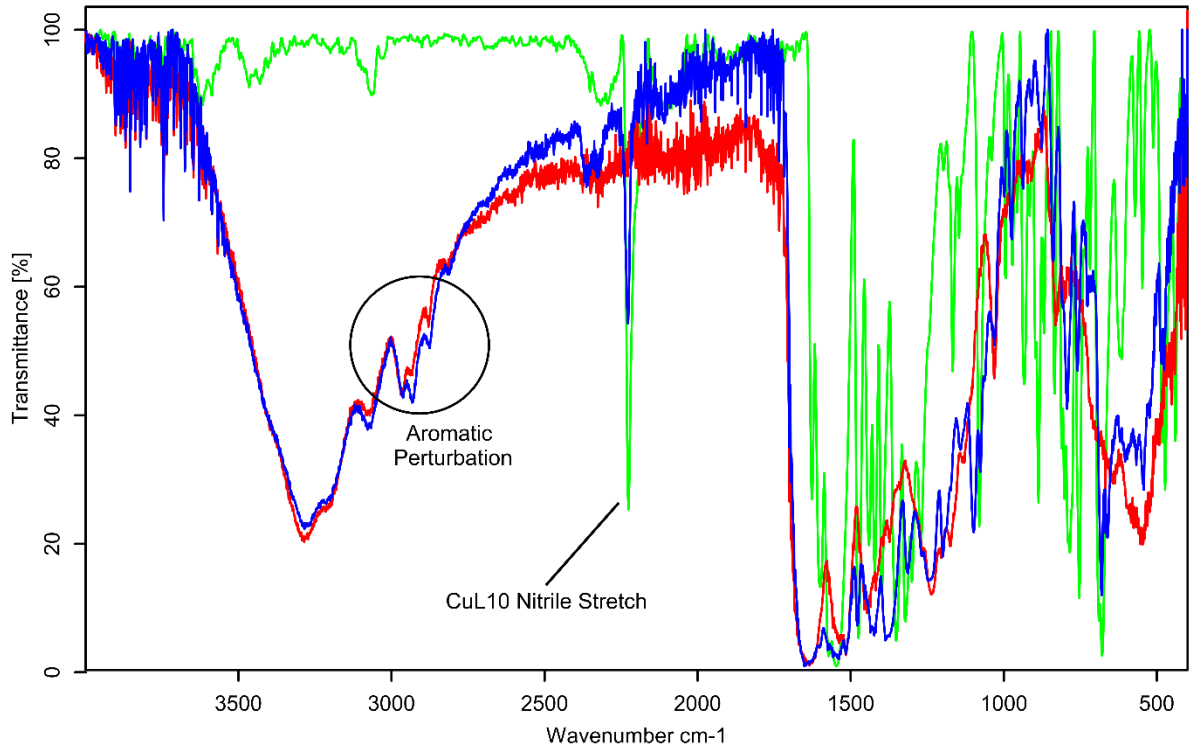


Figure 4.5: The FTIR spectra of CuL10 shown in green, the lyophilized peptide epitope shown in red, and the peptide-CuL10 lyophilized mixture shown in blue. There is a slight change in polarization of the hydroxyl stretch of the tyrosine upon coordination of the Cu(II) pincer. There is significant perturbation of the aromatic C–H stretching vibrations of the peptide upon CuL10 binding. Hence, the FTIR spectra show distinct binding specificity between tyrosine on the epitope and the Cu(II) NNN pincer.

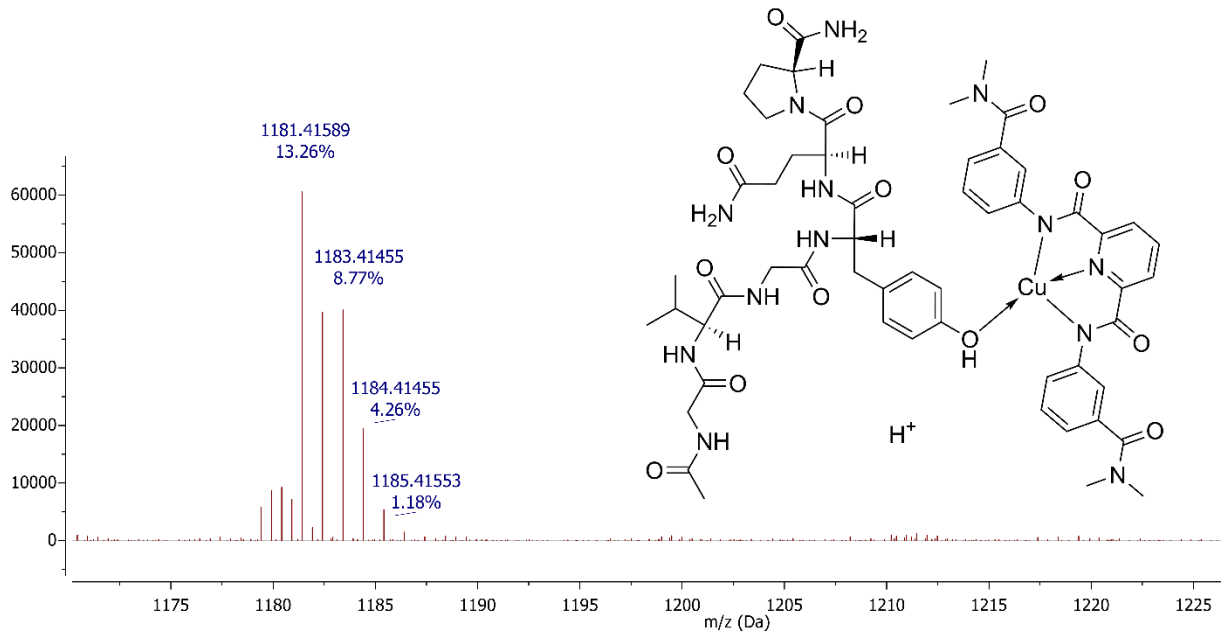


Figure 4.6: The MS detected peptide-CuL5 complex species. $[M + H]^+$: calc 1181.43501 Da; found 1181.41589 Da. The elemental formula is thus $CuN_{13}O_{13}C_{55}H_{68}$. The data confirm that the binding stoichiometry is 1:1.

Finally, before the data from fluorescence spectroscopy are presented here, CD spectroscopy was used to confirm the α-helical nature of the peptide in solution. The CD spectra of the free peptide and Cu(H_2L8) bound peptide are presented in Figure 4.7. There is obvious secondary structure as the free peptide epitope shows minima at 205 and 215 nm while the 0 mdeg axis is crossed at 200 nm with a maximum at 198 nm. The α-helix is perturbed upon titration of Cu(H_2L8) indicating that the Cu(II) pincer binds the biomolecule. When the binding between the peptide and Cu(II) pincer is saturated at high [Cu(H_2L8)], an induced CD signal is observed for the peptide-chelate complex. Hence, NMR, MS, FTIR and CD data indicate that the Cu(II) pincers selectively bind tyrosine on the α-helix with a 1:1 stoichiometry.

The parameters obtained from fluorescent data for the Cu(II) pincer binding to *p*-cresol and the SARS-CoV-2 peptide epitope are collated in Table 4.1 and Table 4.2 respectively. Cu(H_2L9) was chosen to showcase the fluorescent data for binding *p*-cresol and the peptide epitope. The processed fluorescent data for the Cu(II) pincer library binding *p*-cresol (S4.8-S4.32) and the peptide epitope (S4.33-S4.57) are presented in the Supporting Information.

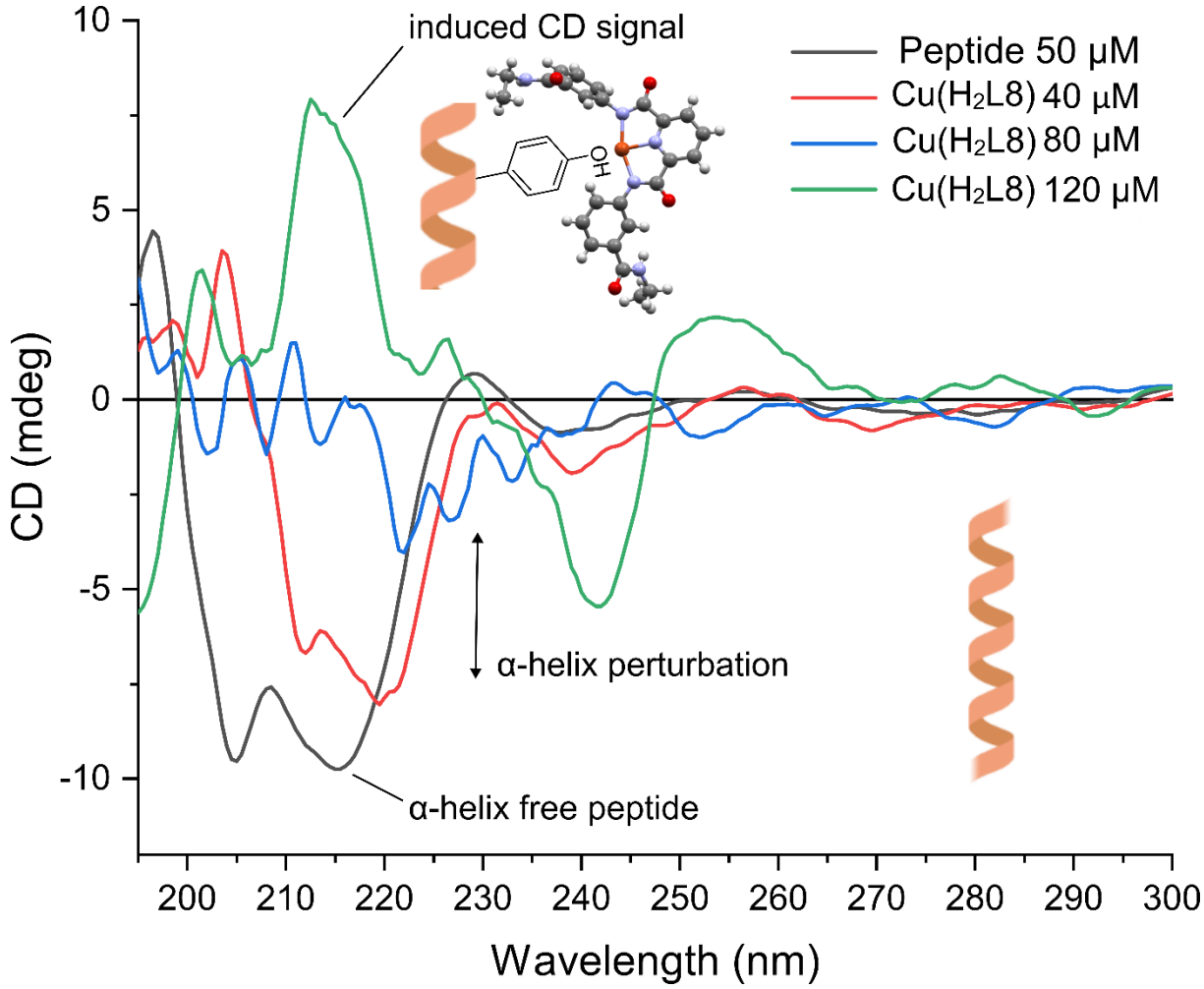


Figure 4.7: The CD spectra of the free peptide epitope and Cu(H_2L8) bound peptide. The [peptide] was kept constant at 50 μM while the [Cu(H_2L8)] was increased from 0 to 120 μM.

Table 4.1: Fluorescence quenching parameters of *p*-cresol in the presence of copper complexes. The data were obtained in MOPS aqueous buffer 10% DMSO (v/v) at pH 7.4 and 37 °C. The parameters highlighted in green are obtained from the Hill model. Those highlighted in blue are obtained from the modified double-log SV equation. The parameters highlighted in orange are obtained from the SV equation. The logK value is the logarithm of the association constant, K_a; n is the stoichiometry of binding; R^2 is the square of the correlation coefficient of the model; and k_q is the bimolecular quenching rate constant. The errors are obtained as the estimated standard deviation of the model and from the rules of propagation of uncertainty in measurement.

Cu(II) NNN Pincer Binding: *p*-Cresol					
Complex	CuL5	Cu(H_2L6)	Cu(H_2L8)	Cu(H_2L9)	CuL10
logK	3.73 ± 0.01	3.88 ± 0.01	4.12 ± 0.01	3.89 ± 0.01	3.94 ± 0.01
n	1.34 ± 0.02	1.06 ± 0.03	1.20 ± 0.01	1.28 ± 0.03	1.23 ± 0.04
R^2	0.999	0.995	0.999	0.997	0.995
logK	3.81 ± 0.3	3.84 ± 0.08	4.15 ± 0.1	3.82 ± 0.1	3.91 ± 0.1
n	1.09 ± 0.06	1.01 ± 0.02	1.03 ± 0.03	1.00 ± 0.03	1.02 ± 0.03
R^2	0.986	0.997	0.995	0.996	0.996
logK	3.72 ± 0.03	3.85 ± 0.03	4.09 ± 0.02	3.84 ± 0.01	3.88 ± 0.03
$k_q \times 10^{12}$ (M^{-1} s^{-1})	3.30 ± 0.2	4.40 ± 0.3	7.72 ± 0.4	4.33 ± 0.1	4.70 ± 0.3
R^2	0.994	0.999	0.999	0.999	0.999

Table 4.2: Fluorescence quenching parameters of the peptide epitope in the presence of copper complexes. The data were obtained in MOPS aqueous buffer 10% DMSO (v/v) at pH 7.4 and 37 °C. The parameters highlighted in green are obtained from the Hill model. Those highlighted in blue are obtained from the modified double-log SV equation. The parameters highlighted in orange are obtained from the SV equation. The logK value is the logarithm of the association constant, K_a; n is the stoichiometry of binding; R^2 is the square of the correlation coefficient of the model; and k_q is the bimolecular quenching rate constant. The errors are obtained as the estimated standard deviation of the model and from the rules of propagation of uncertainty in measurement.

Cu(II) NNN Pincer Binding: Peptide Epitope					
Complex	CuL5	Cu(H_2L6)	Cu(H_2L8)	Cu(H_2L9)	CuL10
logK	3.82 ± 0.01	3.61 ± 0.03	3.45 ± 0.04	3.88 ± 0.008	3.87 ± 0.004
n	1.11 ± 0.03	1.08 ± 0.05	0.942 ± 0.08	1.17 ± 0.02	1.27 ± 0.03
R^2	0.994	0.981	0.953	0.998	0.997
logK	3.77 ± 0.1	3.54 ± 0.2	3.27 ± 0.3	3.79 ± 0.2	3.86 ± 0.1
n	1.01 ± 0.03	0.998 ± 0.05	0.955 ± 0.07	0.995 ± 0.04	1.01 ± 0.03
R^2	0.992	0.988	0.986	0.992	0.995
logK	3.74 ± 0.01	3.62 ± 0.04	3.47 ± 0.03	3.83 ± 0.04	3.84 ± 0.03
$k_q \times 10^{12}$ (M^{-1} s^{-1})	1.53 ± 0.05	1.15 ± 0.1	0.819 ± 0.06	1.89 ± 0.2	1.93 ± 0.1
R^2	0.999	0.999	0.999	0.999	0.999

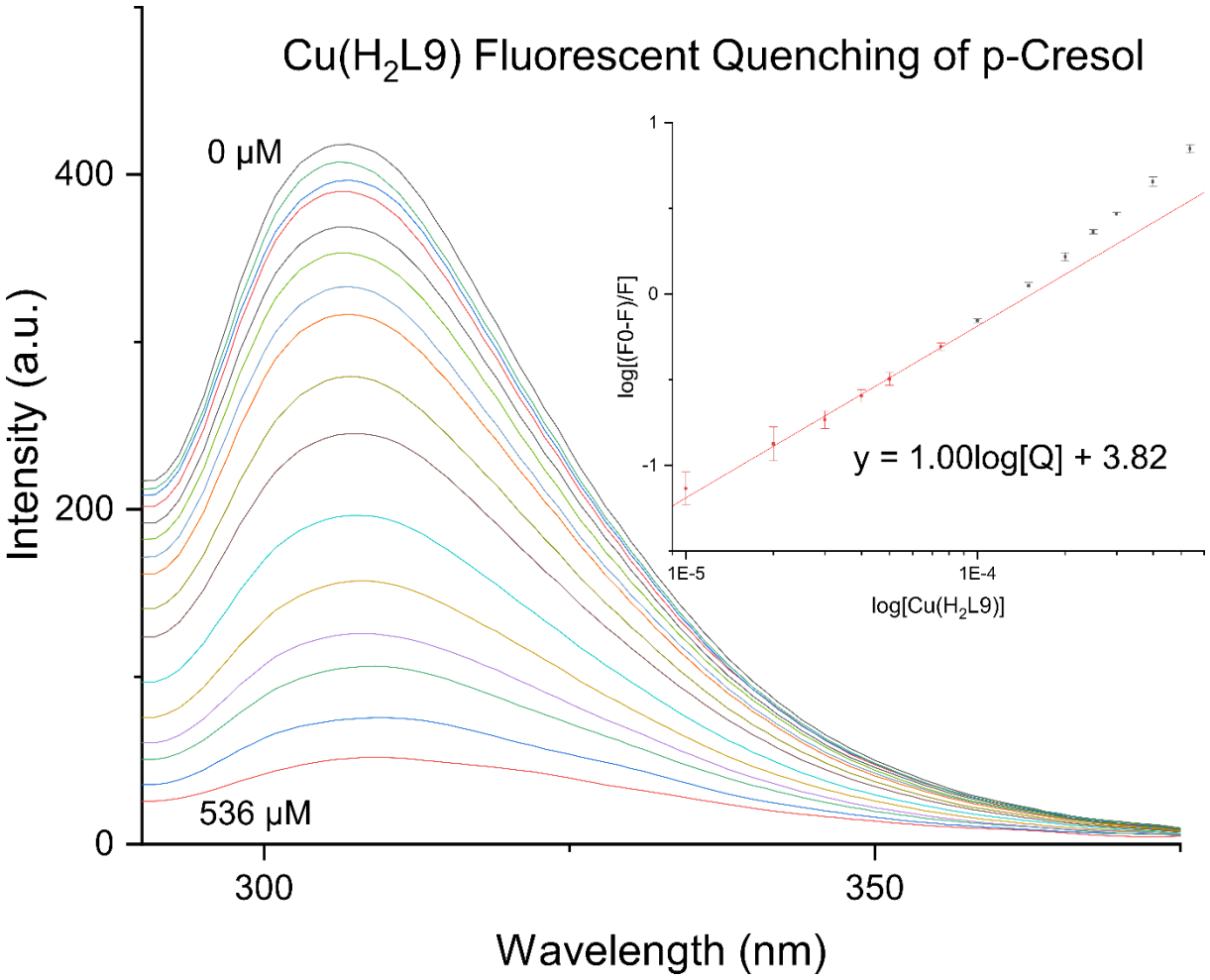


Figure 4.8: The fluorescence emission spectra of *p*-cresol at various concentrations of Cu(H_2L9). The [*p*-cresol] was kept constant at 100 µM while the [Cu(H_2L9)] was varied from 0.00 to 536 µM. The *p*-cresol fluorophore is quenched by increasing concentration of Cu(H_2L9). The inset shows the plot of the modified double-log Stern-Volmer equation where n = 1.00 and logK = 3.82. The deviation from linearity at high concentrations is due to dynamic quenching being observed.

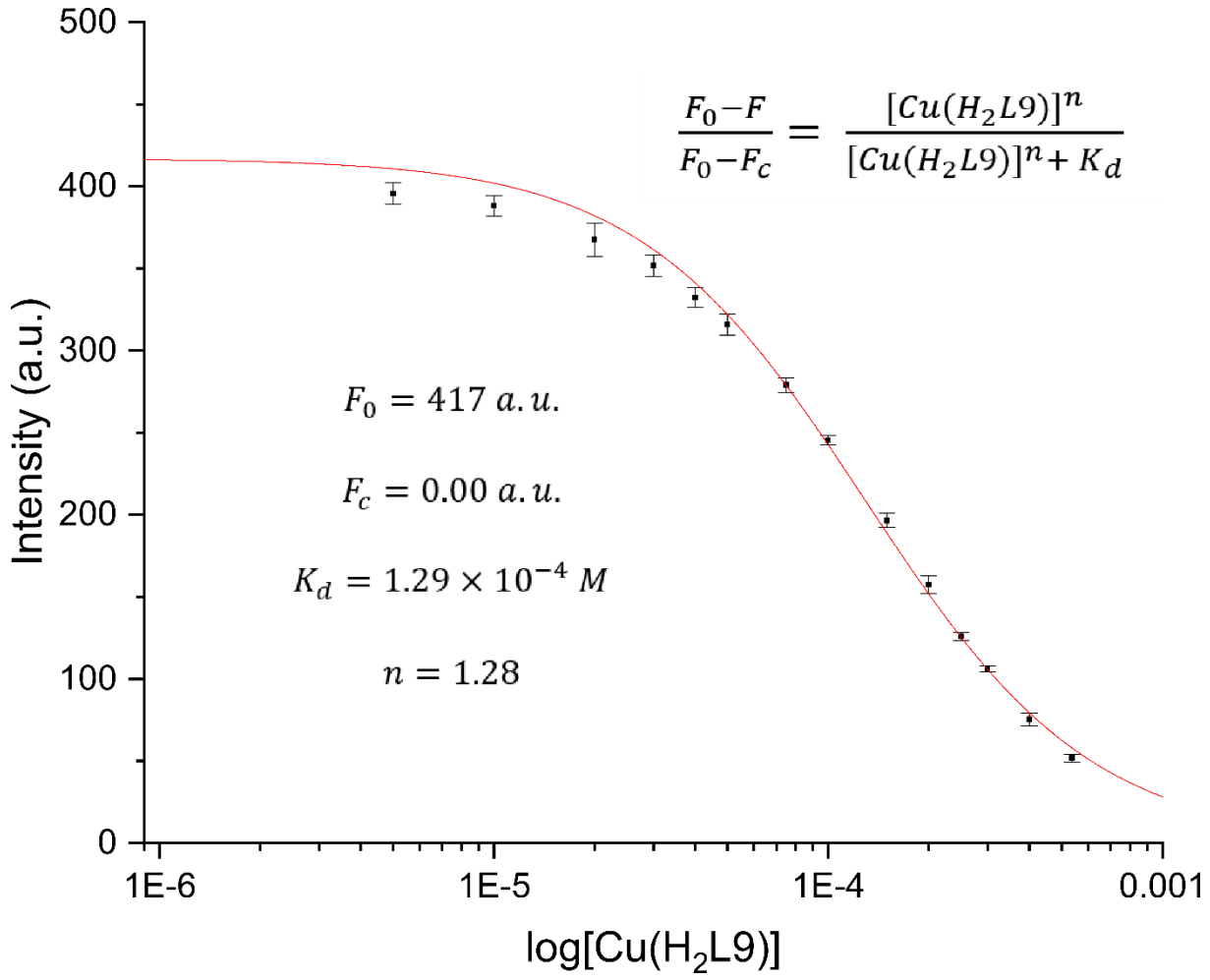


Figure 4.9: The Hill plot obtained from fluorescent intensity values at 308 nm. The [Cu(H₂L9)] was varied from 536 μM to 1.00 μM while the [*p*-cresol] was kept constant at 100 μM. The error bars are reported as the standard deviation of the intensity value at 308 nm for three independent samples.

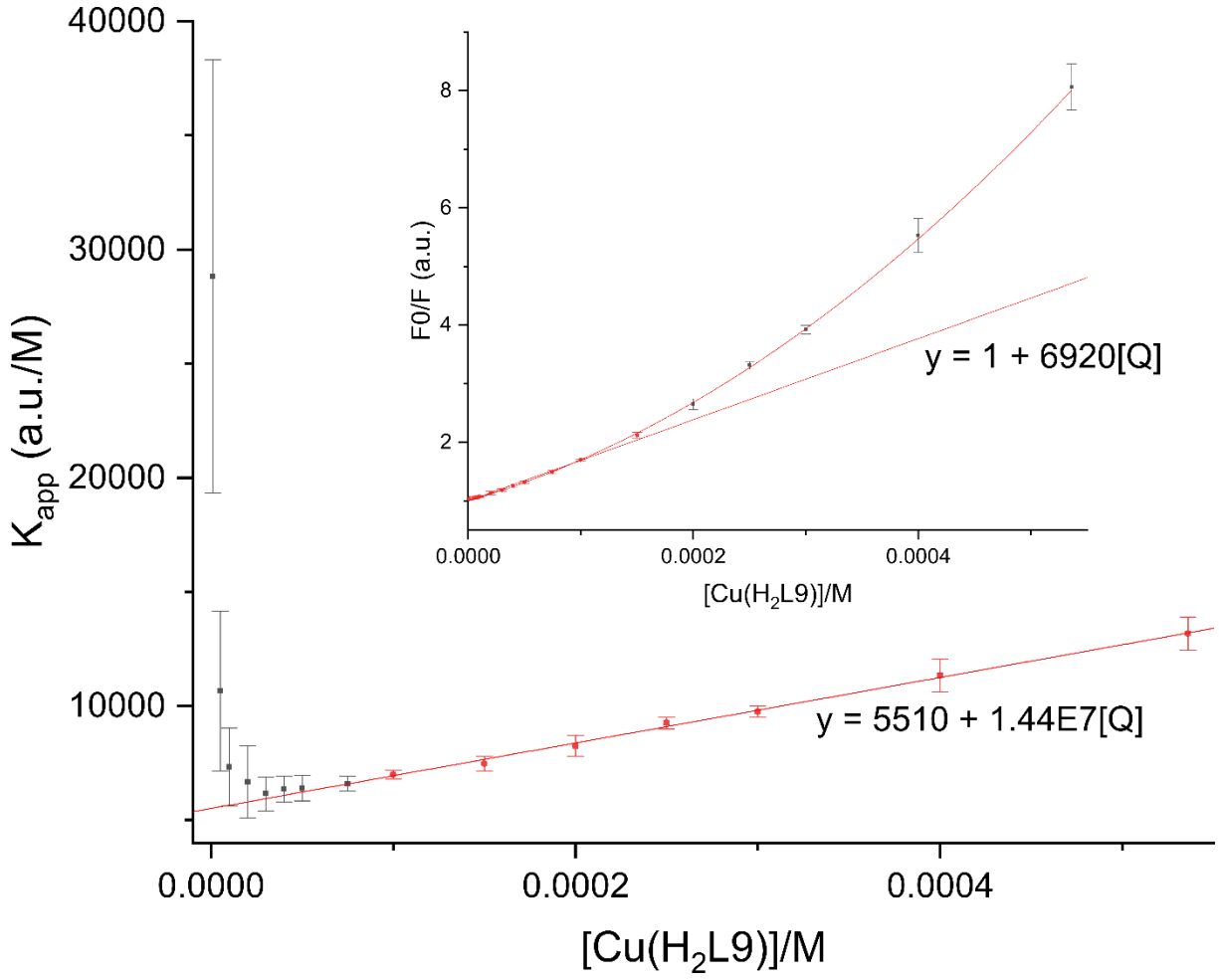


Figure 4.10: The plot of K_{app} vs [Cu(H_2L9)] obtained by titrating Cu(H_2L9) against *p*-cresol showing that dual quenching mechanisms are being observed at high concentrations of copper complex. The deviation from linearity at low [Cu(H_2L9)] indicates that only static quenching is being observed in this region. The K_{app} plot yields (K_D + K_s) = 5510 ± 110 M^{-1} and K_DK_S = 1.44×10^7 ± 4.89×10^5 M^{-1}. The inset shows the Stern-Volmer plot with the straight line plotted for low concentration data only. The SV plot yields a slope of 6920 ± 164 M^{-1} which is the K_{SV} and furthermore, the equilibrium association constant, K_a. The deviation from linearity observed for the SV plot at high concentrations of copper complex is due to dynamic quenching processes.

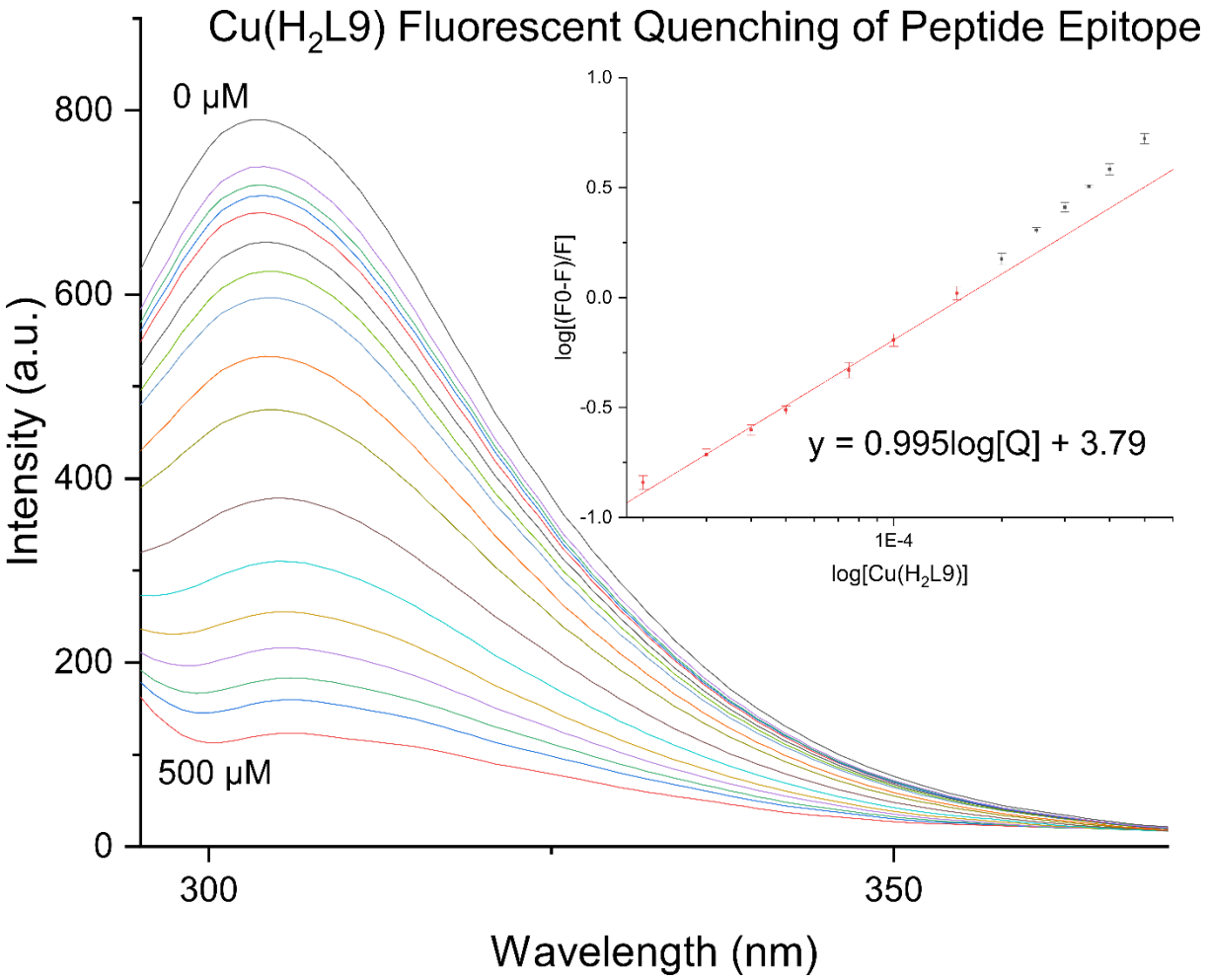


Figure 4.11: The fluorescence emission spectra of the SARS-CoV-2 peptide epitope at various concentrations of Cu(H_2L9). The [peptide] was kept constant at 100 µM while the [Cu(H_2L9)] was varied from 0.00 to 500 µM. The peptide fluorophore is quenched by increasing concentration of Cu(H_2L9). The inset shows the plot of the modified double-log Stern-Volmer equation where n = 0.995 and logK = 3.79. The deviation from linearity at high concentrations is due to dynamic quenching being observed.

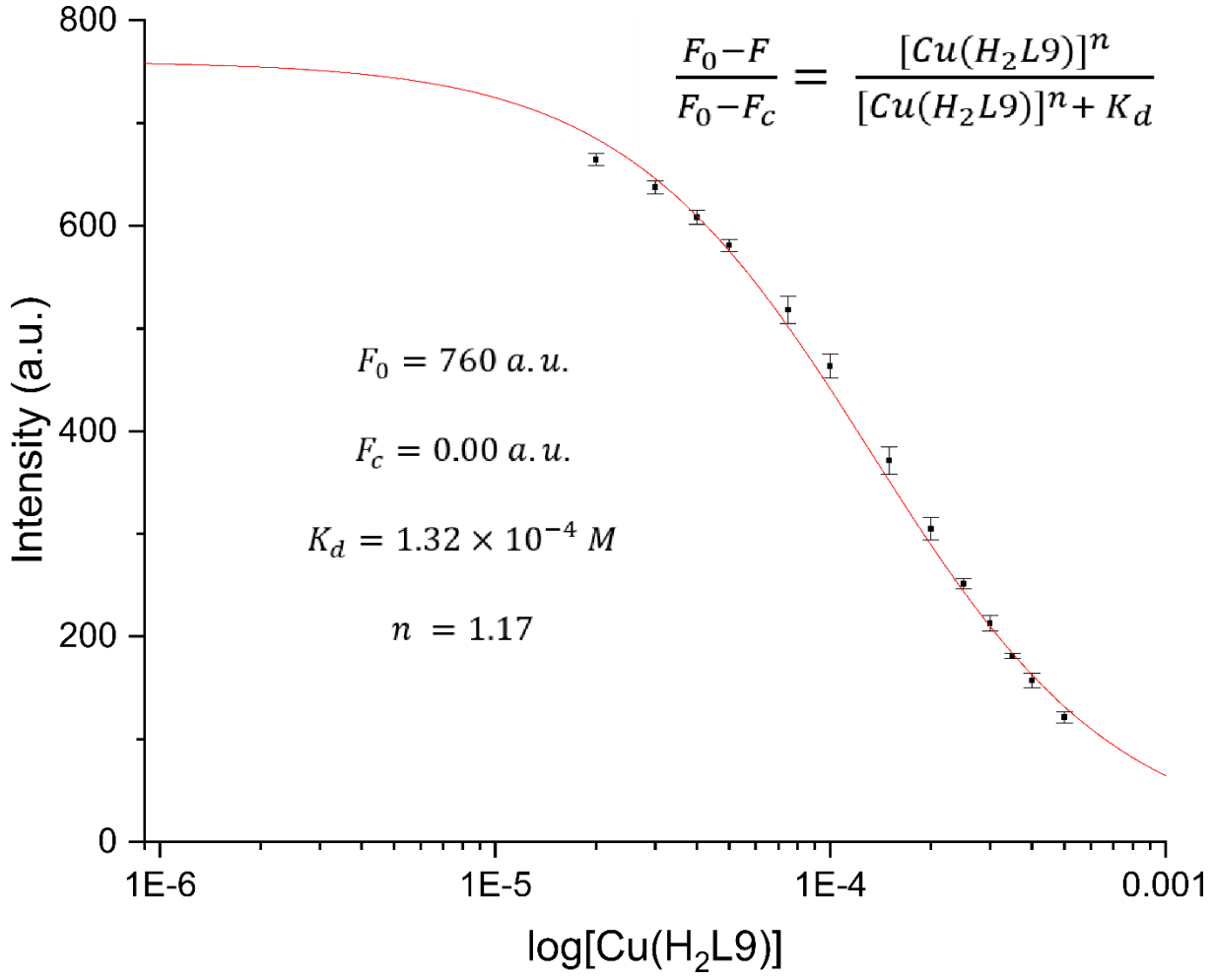


Figure 4.12: The Hill plot obtained from fluorescent intensity values at 308 nm. The [Cu(H_2L9)] was varied from 500 μM to 1.00 μM while the [peptide] was kept constant at 100 μM. The error bars are reported as the standard deviation of the intensity value at 308 nm for three independent samples.

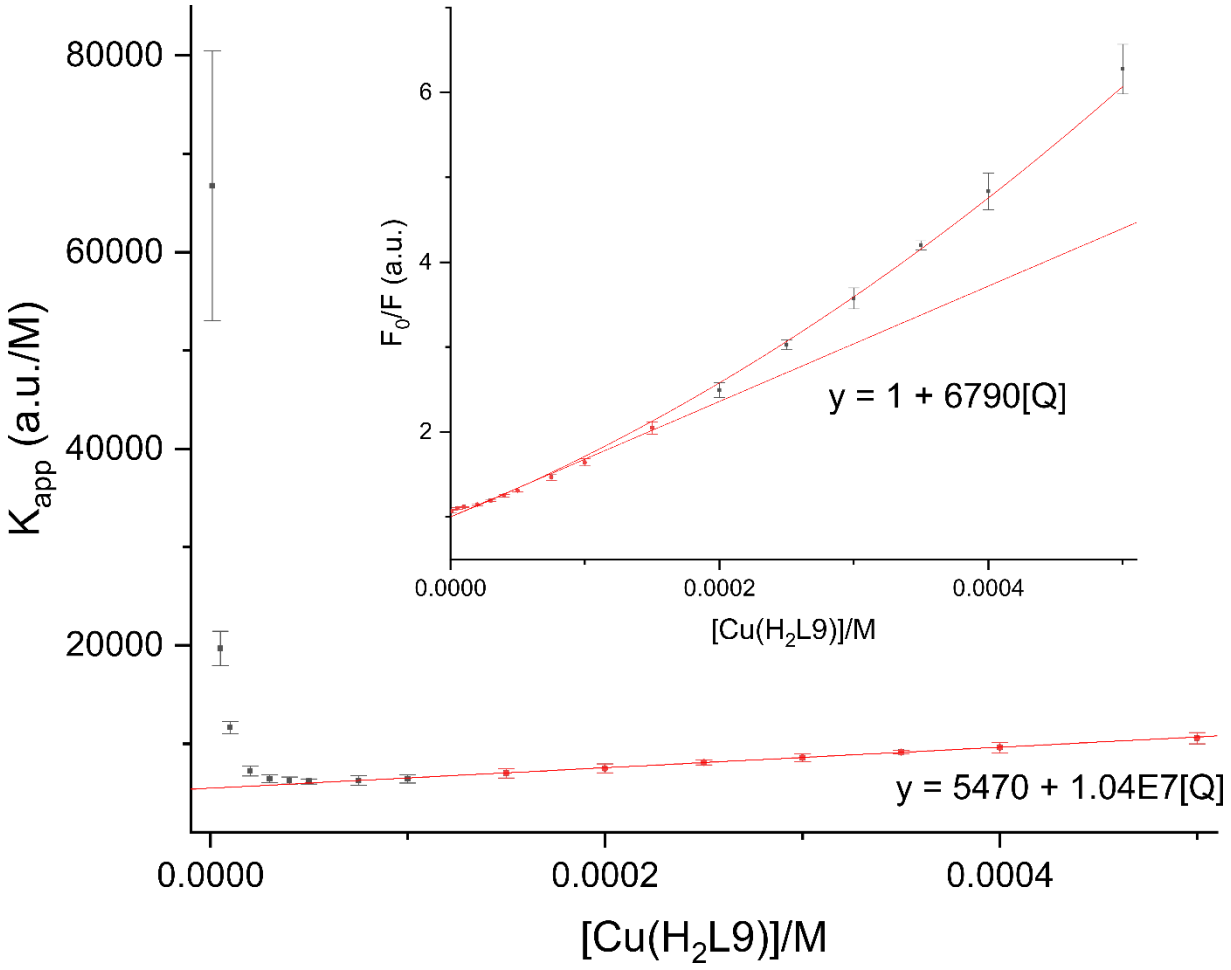


Figure 4.13: The plot of K_{app} vs [Cu(H_2L9)] obtained by titrating Cu(H_2L9) against the peptide epitope showing that dual quenching mechanisms are being observed at high concentrations of copper complex. The deviation from linearity at low [Cu(H_2L9)] indicates that only static quenching is being observed in this region. The K_{app} plot yields (K_D + K_S) = 5470 ± 81.7 M^{-1} and K_DK_S = 1.04×10^7 ± 2.56×10^5 M^{-1}. The inset shows the Stern-Volmer plot with the straight line plotted for low concentration data only. The SV plot yields a slope of 6790 ± 574 M^{-1} which is the K_{SV} and furthermore, the equilibrium association constant, K_a. The deviation from linearity observed for the SV plot at high concentrations of copper complex is due to dynamic quenching processes.

3.2 SARS-CoV-2 Delta RBD

After confirming that the copper chelates target tyrosine on the hexapeptide epitope, the binding of the Cu(II) NNN pincer to the SARS-CoV-2 Delta RBD was observed by CD spectroscopy and the results are presented in Figure 4.14. ONIOM calculations were then used to determine the binding site and coordination geometry for the CuL5-RBD interaction and are presented in Figure 4.15. The binding interaction between the copper complex and the RBD of the virus Delta variant was quantified using fluorescence spectroscopy. The data are presented in Figures 4.16-4.19 as well as S4.60-S4.64. The fluorescence quenching parameters are collated in Table 4.3.

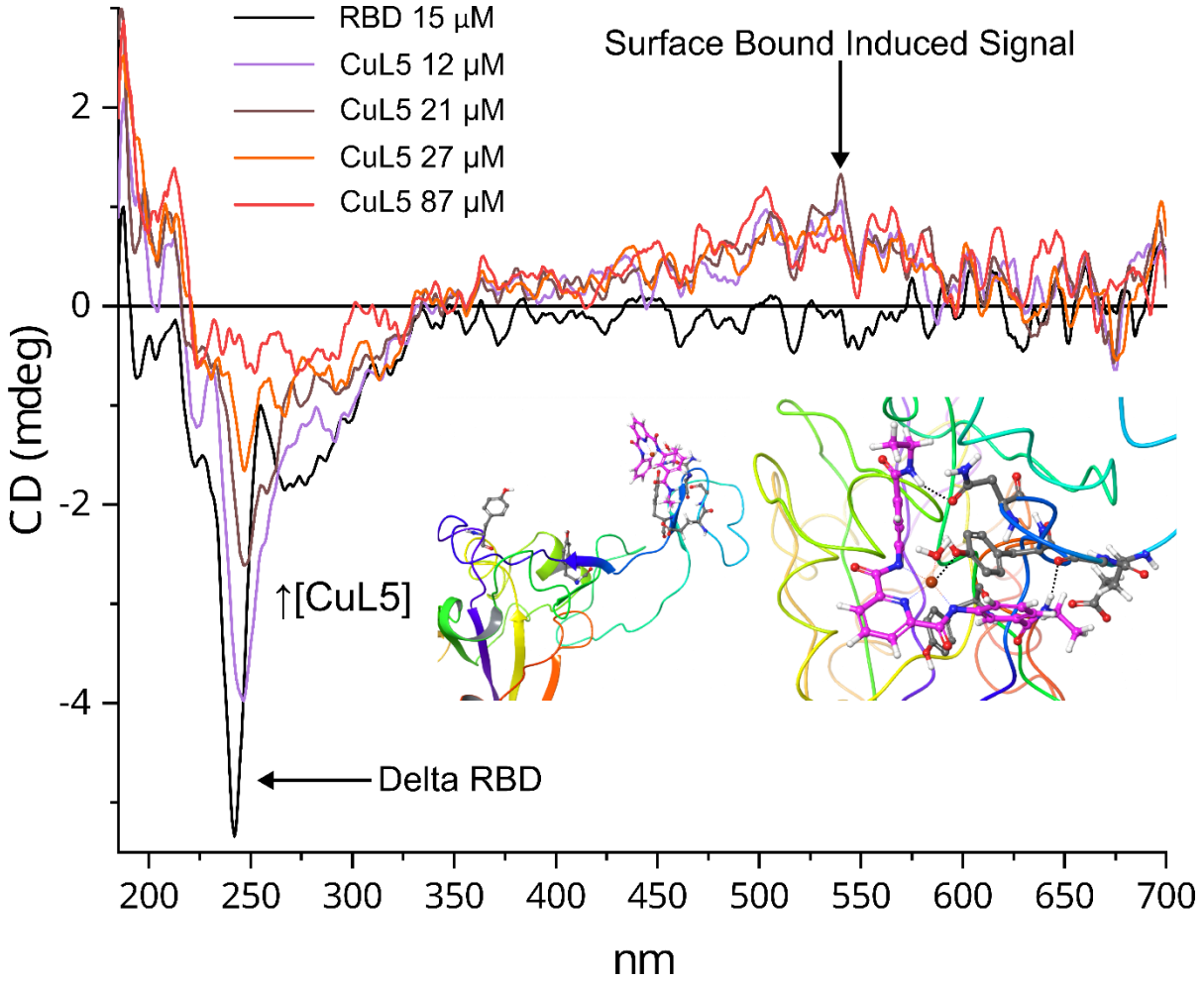


Figure 4.14: The CD spectra of SARS-CoV-2 Delta RBD in the presence of copper complex CuL5. The [RBD] was kept constant at 15 μM while titrating aliquots of CuL5 into the protein solution. The secondary structure of the protein is perturbed upon addition of the copper chelate indicating that the compound binds the biomolecule. There is a weak induced CD signal at 550 nm which indicates that the copper complex is stable and has not demetalated in the presence of RBD. Furthermore, the weak induced signal indicates that CuL5 is surface bound so that it may potentially act as a fusion inhibitor. The inset shows Cu(H_2L8) docked against Y489 of the RBD; this solvent exposed residue is the most likely target as determined by *in silico* methods.

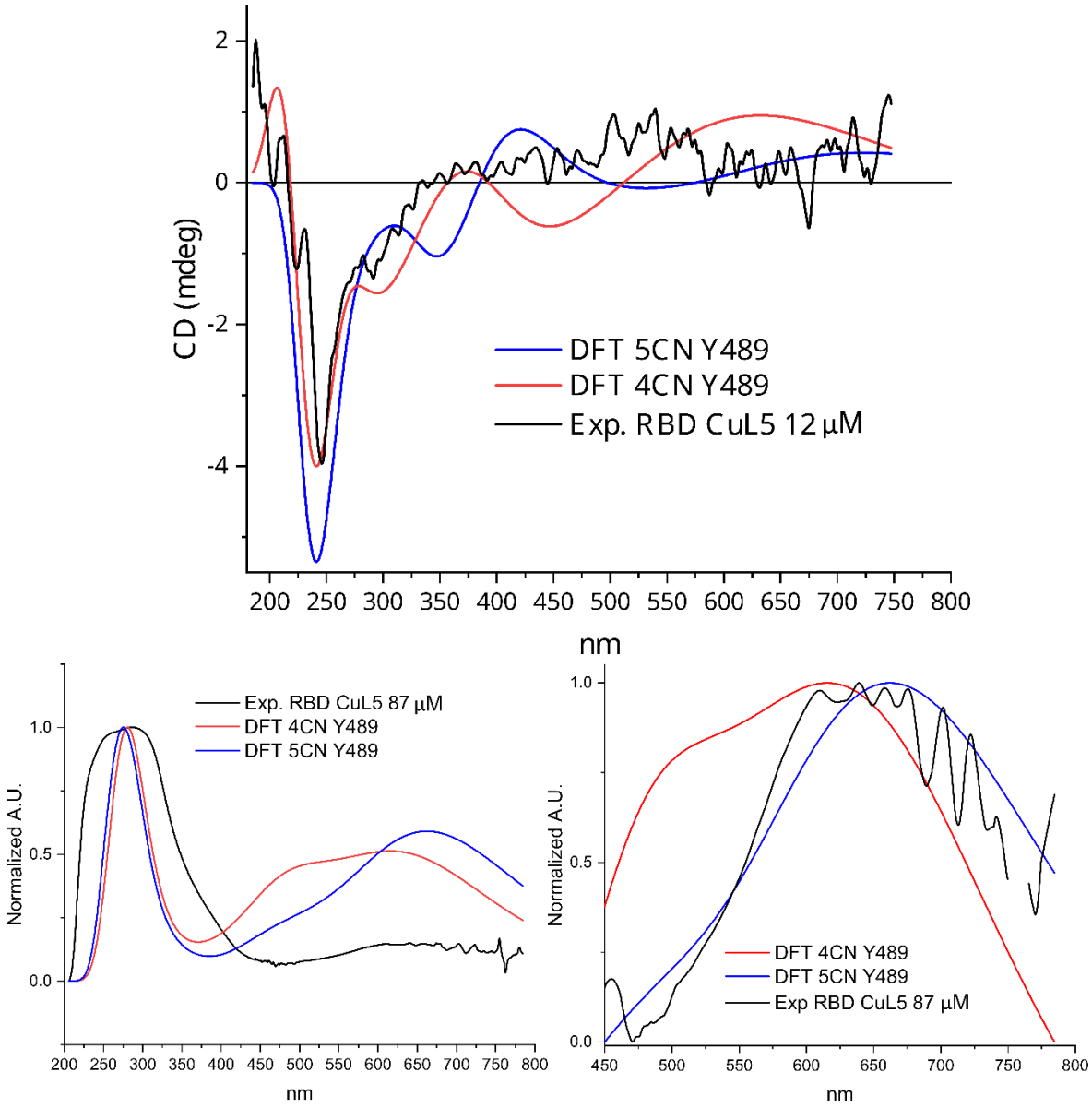


Figure 4.15: The DFT ONIOM calculated spectra and experimental CD and UV-Vis spectra of Delta RBD in complex with CuL5 (cam-b3lyp/sdd, TD-DFT n=60, with empirical dispersion correction gd3bj). The copper chelate was docked against Y489 of the Delta RBD (PDB:7V8B) either with 4-coordinate (4CN) geometry or 5-coordinate (5CN) geometry where the fourth and fifth ligands are tyrosine and water. Simulations were also calculated for Y505, Y449, and Y473, with CuL5 4CN, 5CN, and anionic (S4.58). However, the results for CuL5 docked against Y489 produced the best correlation between calculated and experimental results. The DFT calculated CD wavelengths for 5CN data were corrected by –19 nm while 4CN data was corrected by –38 nm. The DFT calculated UV-Vis data was only normalized. There is good overlap between all three CD spectra, and hence cannot comment on coordination geometry, but it is highly likely that Y489 is the binding site on the RBD. However, the UV-Vis data suggests that CuL5 is bound with 5-coordinate geometry (S4.59). The severe noise for experimental UV-Vis data is due to the dilute solutions producing absorbance values below 0.1. Experimental UV-Vis data excluded between 750 and 760 nm for normalization between 450 and 800 nm.

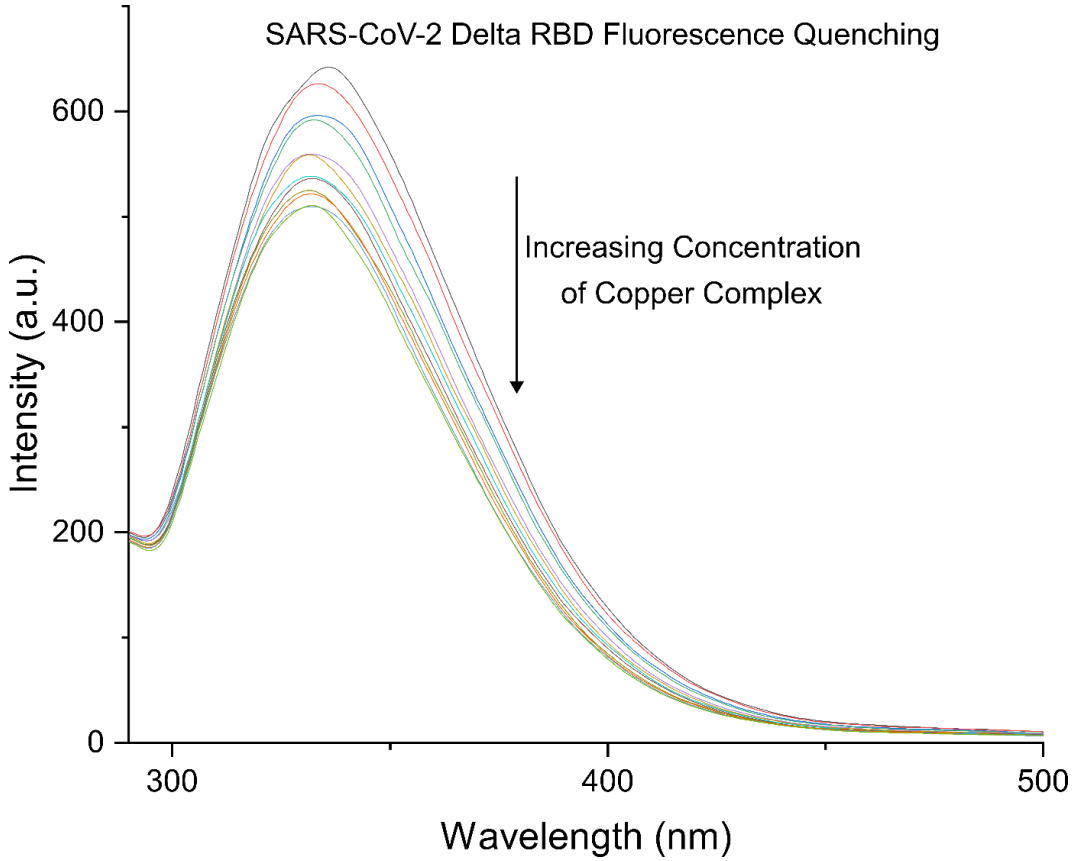


Figure 4.16: The fluorescence emission spectra of SARS-CoV-2 Delta RBD in the presence of Cu(H_2L8). The [Cu(H_2L8)] was varied from 500 nM to 5.38 μM while the [RBD] was kept constant at 3.11 μM or 0.08 mg/mL. The RBD fluorophore is quenched by increasing [Cu(H_2L8)].

Table 4.3: Fluorescence quenching parameters of the SARS-CoV-2 Delta RBD in the presence of Cu(H_2L8). The data were obtained in 3 mM HEPES, 150 mM NaCl, 0.02% NaN_3 aqueous buffer at pH 7.4 and 37 °C. The parameters highlighted in green are obtained from the Hill model. Those highlighted in blue are obtained from the modified double-log SV equation. The parameters highlighted in orange are obtained from the SV equation. The logK value is the logarithm of the association constant, K_a; n is the stoichiometry of binding; R^2 is the square of the correlation coefficient of the model; and k_q is the bimolecular quenching rate constant. The errors are obtained as the estimated standard deviation of the model and from the rules of propagation of uncertainty in measurement.

Cu(H_2L8) Binding SARS-CoV-2 Delta RBD								
logK	n	R^2	logK	n	R^2	logK	k_q ×10^{13} (M^{-1} s^{-1})	R^2
5.74 ± 0.03	1.46 ± 0.2	0.994	4.25 ± 0.5	0.887 ± 0.09	0.953	4.80 ± 0.001	1.01 ± 0.003	1

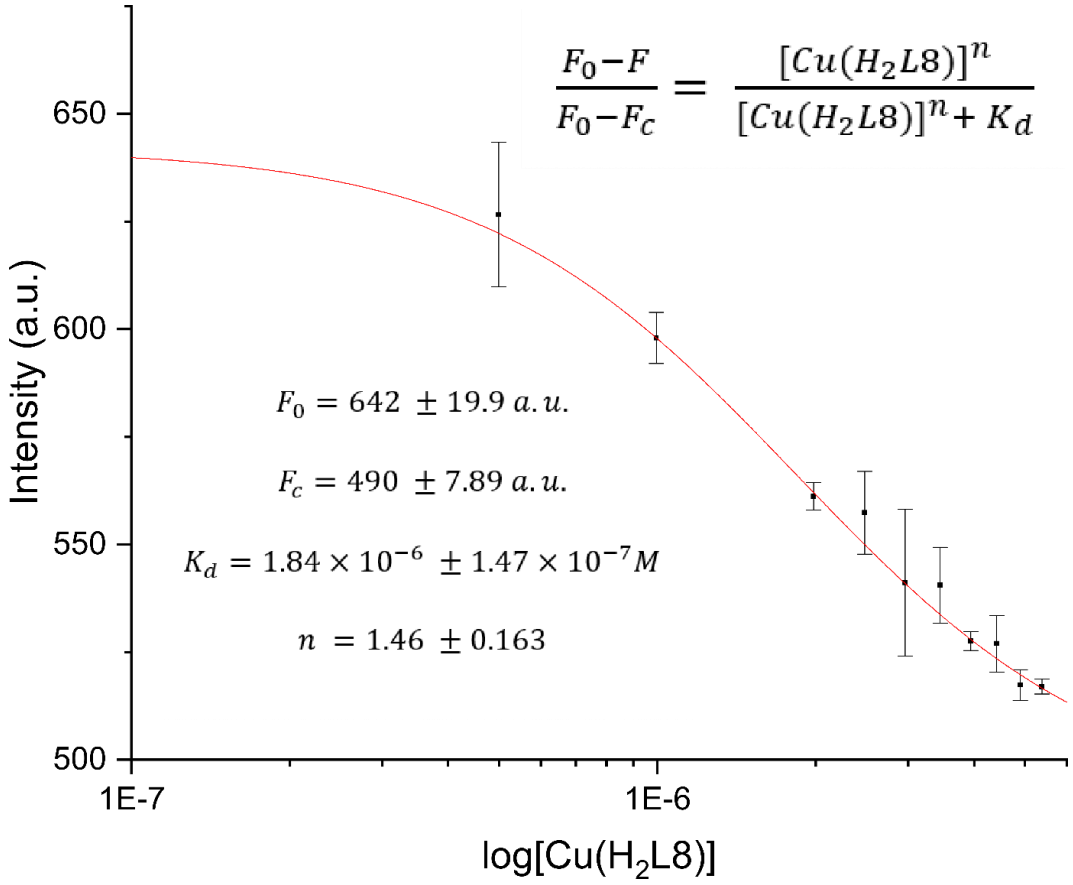


Figure 4.17: The Hill plot obtained from fluorescent intensity values at 335 nm. The [Cu(H_2L8)] was varied from 500 nM to 5.38 µM while the [RBD] was kept constant at 3.11 µM. The error bars are reported as the standard deviation of the intensity value at 335 nm for two independent samples.

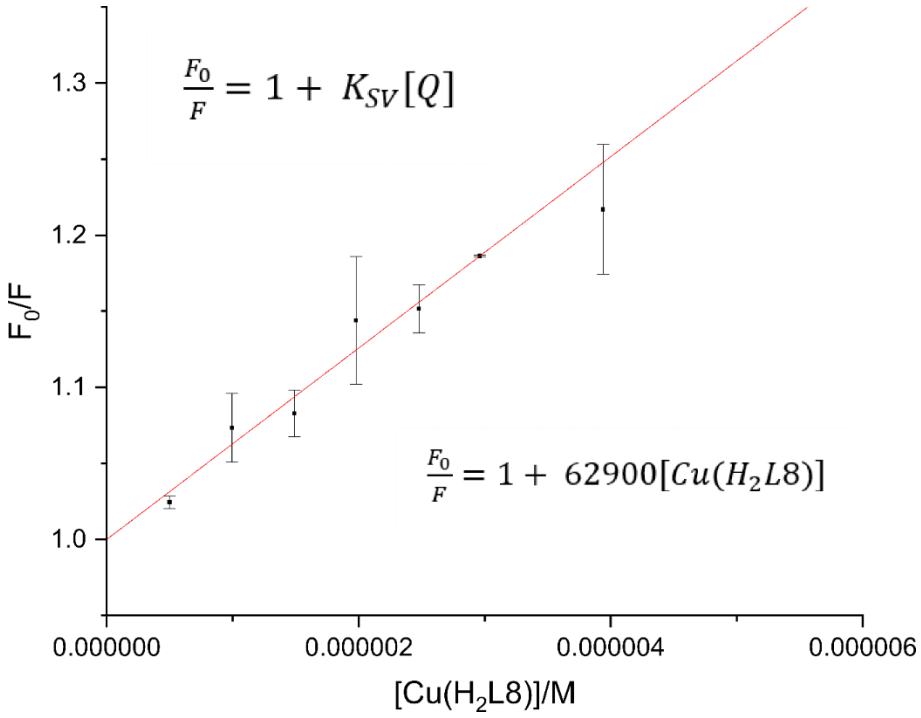


Figure 4.18: The SV plot obtained from fluorescence quenching of SARS-CoV-2 Delta RBD by Cu(H_2L8). The K_{SV} of 62900 ± 172 M^{-1} may be equated to K_a, the equilibrium association constant. The fit is really good with R^2 = 0.98.

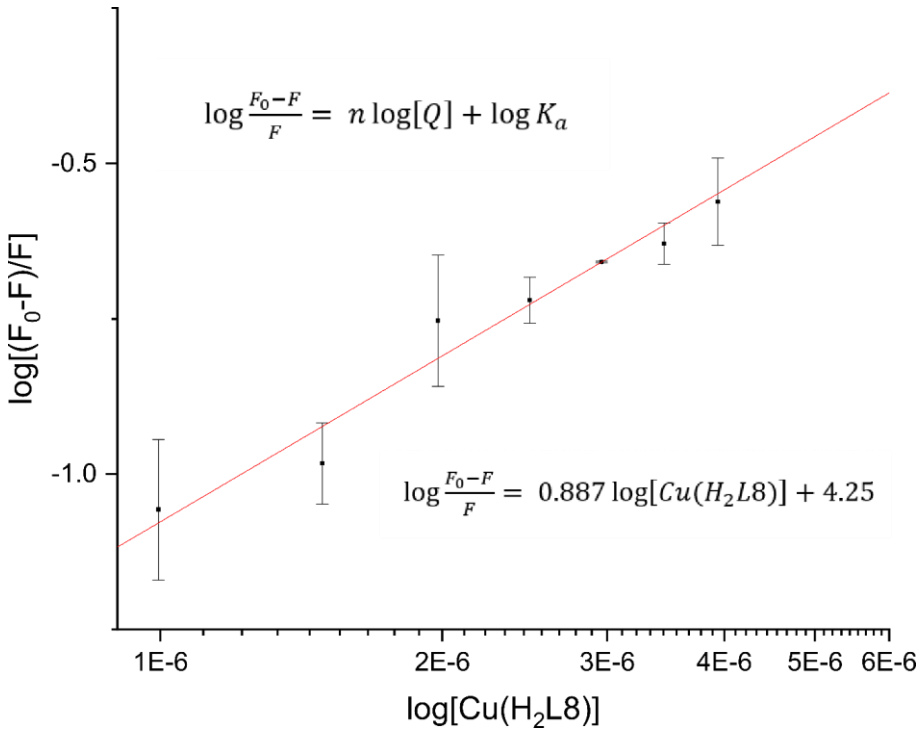


Figure 4.19: The modified double-log SV plot obtained from fluorescence quenching of SARS-CoV-2 Delta RBD by Cu(H_2L8). The straight line yields a slope of 0.887 ± 0.09 which is n, the binding stoichiometry. This suggests that the stoichiometry is approximately 1:1 Cu(H_2L8):RBD. The plot yields an intercept of 4.25 ± 0.5 which is the value of logK.

The parameters presented in Table 4.1 were obtained for the fluorescence quenching of *p*-cresol in the presence of the Cu(II) NNN pincer library. The *p*-cresol biomimetic model is the simplest model for tyrosine and the measured binding constants are essentially the coordinating affinity of the phenol side chain for the copper chelate. The stoichiometry obtained from Hill plots and modified double-log SV plots indicates that the *p*-cresol binding stoichiometry for is 1:1 for the copper complexes. The values of k_q obtained were of the order 10^{12} M^{-1} s^{-1} which is 100× more than the diffusion-controlled limit of 10^{10} M^{-1} s^{-1} when colliding components are larger than the solvent molecules.[1] When k_q is larger than 10^{10} M^{-1} s^{-1}, this indicates that quenching is due to stable complex formation and is not merely a diffusion-controlled collisional event. Although the second-order SV equations were well modelled for the data, indicating that dual quenching mechanisms are being observed, the dynamic quenching constant, K_D, could not be decomposed to find a meaningful value because the solutions to the equations yield complex numbers. However, based on the coefficients of the second-order SV plot, it can be said that the K_D is small in comparison with K_s. The value of K_s, and hence K_a, could be reliably determined from the linear first-order SV plot for the low concentration data where only static quenching is being observed as determined from the plot of K_{app} vs [Q]. The logK values obtained from the SV plots were in the range 3.72 - 4.09 which translates to a Gibbs Free energy between –22.1 and –24.3 kJ mol^{-1} at 37 °C. This Gibbs energy is essentially the coordinative bond strength between the copper pincer and the phenol ligand. Critical stability constants have been measured for various phenols and the Cu(II) ion, and depending on the phenolic group, the logK values range from 2 -12.[20]

The parameters presented in Table 4.2 were obtained for the fluorescence quenching of the peptide epitope in the presence of the copper pincer library. The peptide epitope is a biomimetic model for Y505 on the SARS-CoV-2 RBD and although the peptide has α-helical secondary structure, the biomolecule has no tertiary structure. The stoichiometry obtained from Hill plots, modified double-log plots, and MS data indicate that the peptide binding stoichiometry is 1:1 for the copper chelates. The values of k_q obtained were of the order 10^{12} M^{-1} s^{-1} which is 100× more than the diffusion-controlled limit of 10^{10} M^{-1} s^{-1}. The logK values obtained from the SV plots were in the range 3.47 – 3.84 which translates to a Gibbs Free energy between –20.6 and –22.8 kJ mol^{-1} at 37 °C. This is lower than the binding energy to *p*-cresol and thus implies that the peptide chain is sterically blocking Cu(II) pincer access to tyrosine. The small biomolecule lacks tertiary structure that extends into 3D space beyond the tyrosine residue which would facilitate additional binding interactions between the ligand and protein. Hence, the results

suggest that there are no additional binding interactions between the copper chelate and the peptide and the binding affinity is diminished due to steric repulsions between the peptide and ligand. This was also observed by molecular dynamics simulation for the peptide-CuL5 complex presented in Chapter 3, Figure 3.21.

The parameters presented in Table 4.3 were obtained for the fluorescence quenching of the SARS-CoV-2 Delta RBD in the presence of Cu(H_2L8). The stoichiometry obtained from Hill and modified double-log plots indicate that the RBD binding stoichiometry is 1:1 for Cu(H_2L8). This binding stoichiometry could not be confirmed by MS analysis because the Cu(II) pincers are unstable and readily demetallate in the spectrometer. The values of k_q obtained were of the order 10^{13} M^{-1} s^{-1} which is 1000× more than the diffusion-controlled limit of 10^{10} M^{-1} s^{-1} when colliding components are larger than the solvent molecules. When k_q is larger than 10^{10} M^{-1} s^{-1} this indicates that quenching is due to stable complex formation and is not merely a diffusion-controlled collisional event.[1] The logK value obtained from the SV plot was 4.80 which translates to a Gibbs Free energy of –28.5 kJ mol^{-1} at 37 °C. The coordinative bond strength between Cu(H_2L8) and the phenol ligand was measured to be –24.3 kJ mol^{-1} and hence the difference between binding energies to *p*-cresol and the RBD may be equated to additional interactions between the pincer ligand and the protein. Therefore, the Gibbs energy of Cu(H_2L8) binding to Delta RBD may be decomposed into a coordinating bond strength of –24.3 kJ mol^{-1} and additional hydrophobic and H-bonding forces of –4.20 kJ mol^{-1} to give a total binding energy of –28.5 kJ mol^{-1}. The *in silico* results indicate that Y489 is the preferential target on the RBD and Cu(H_2L8) binds this residue with additional stabilizing interactions to G485 and N487 (See Chapter 3, Figures 3.18 and 3.19). Hence, the dominant binding interaction is coordinative in nature with an energy of –24.3 kJ mol^{-1} and additional H-bonding interactions from the pincer ligand to the RBD at G485 and N487 with an energy of –4.20 kJ mol^{-1}. The DFT calculated CD and UV-Vis spectra presented in Figure 4.15 further support the finding that Y489 is the ligand binding site on the RBD. Additional information on the potential binding site is presented in S4.65 and S4.66.

3.3 Solution Behavior of Cu(II) Pincers

The solution behaviour of the Cu(II) NNN amide pincers was determined in aqueous media by UV-Vis spectroscopy and the results are presented in Table 4.4 and Table 4. 5. The GSH stability of CuL5 was also determined by UV-Vis spectroscopy and these results are presented in Table 4.6 and Figure 4.20. Reduction by GSH is a cellular defence strategy against xenobiotics and it is important that the metallodrug candidates are stable in the presence of high [GSH].

Table 4.4: The solubility of the copper complexes in water as determined by UV-Vis at 25 °C. The complexes are water soluble with CuL5 saturating water at 3 mM. The solubility was not determined for Cu(H_2L9) as the complex demetallates in pure water and solubility was not determined for CuL10 because the complex is very poorly water soluble.

Cu(II) NNN Pincer Water Solubility	
Complex	Water Saturation
CuL5	3.01 mM
Cu(H_2L6)	760 μM
Cu(H_2L8)	993 μM
Cu(H_2L9)	Not Determined
CuL10	Not Determined

Table 4. 5: The complex Cu(H_2L9) was observed to demetallate in water and its percent demetallation was determined by UV-Vis spectroscopy. The complex is not stable in pure water and decomposes by 6% over 24 hours. However, the complex is stable in MOPS buffer at pH 7.4 over 24 hours.

Cu(H_2L9) % Demetallation in Pure Water and MOPS Buffer After 24 Hours	
Type 1 Water	MOPS Buffer
6.4%	0%

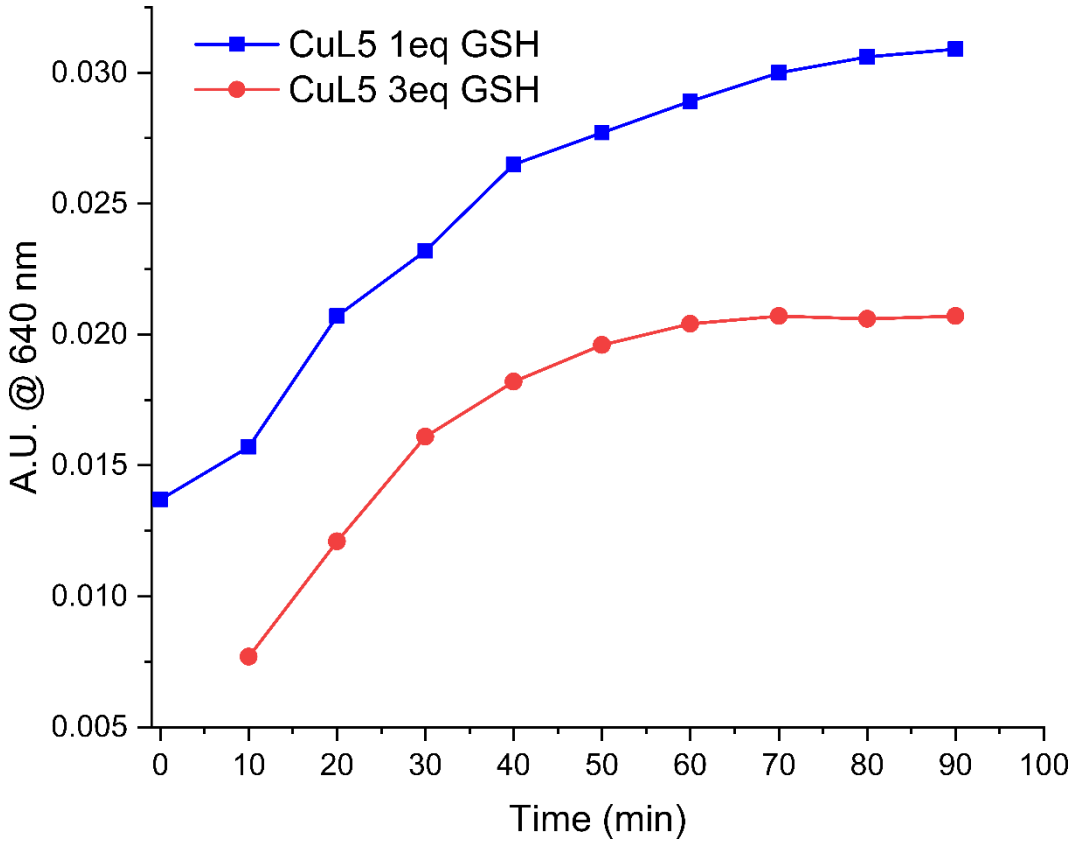


Figure 4.20: The absorbance values at 640 nm for a solution of CuL5 with 1 and 3 equivalents of glutathione (GSH). GSH is present in high concentrations in living cells and it is important that the Cu(II) chelates are GSH stable. Upon sample preparation, the solution changes from green to colourless before returning to a green colour over time.

Table 4.6: The stability of CuL5 was tested in the presence of GSH. Solutions of CuL5 were preprepared in MOPS buffer at pH 7.4 with 1 and 3 equivalents of GSH and monitored by UV-Vis spectroscopy over time. Upon sample preparation, the solution changes from green to colourless. It is suspected that GSH reduces the Cu(II) NNN pincer to a negatively charged Cu(I)L5-GSH complex before dissolved oxygen oxidizes the chelate back to its Cu(II) form. The re-oxidation process was monitored over 1.5 hours, and with 1 eq GSH, 65% of the Cu(II) chelate remains in solution while 3 eq resulted in only 33% Cu(II) chelate remaining. The experiment was run with the cuvette properly sealed and it was suspected that equilibrium was established for the oxidation process. Hence, the experiment was repeated with 7 eq of GSH but molecular oxygen was bubbled through the solution before leaving it for ∞ time and again before recording the UV-Vis spectrum. At 7 eq GSH with the solution oxygenated, the CuL5 concentration returned to 79% of its initial concentration. There were no signs of demetallation and hence it is suspected that an equilibrium exists where the Cu(I)L5-GSH complex is stable and present in measurable quantities (the difference between initial and final Cu(II) pincer concentration). The GSH stability was also tested in HEPES, NaCl buffer but resulted in instant and irreversible demetallation. Finally, the Cu(II) chelates were tested for a suitable buffer. Cu(H_2L9) was only stable in MOPS buffer, while the complex demetallated in PBS, TBS, HEPES and TA. CuL5 was stable in HEPES, MOPS, TA, and TBS but demetallated in PBS. The Cu(II) NNN pincers are highly sensitive to demetallation in HCl with compounds decomposing in 0.01M $HCl_{(aq)}$. Hence, it is unlikely the copper chelates would survive *in vitro* cell cultures and live virus data was never collected.

CuL5 GSH Stability		
Time from Sample Prep (min)	% of Starting [CuL5] 1 eq GSH	% of Starting [CuL5] 3 eq GSH
10	34.2	12.9
20	45.0	20.3
30	50.5	27.0
40	57.7	30.5
50	60.3	32.9
60	62.9	34.2
70	65.3	34.7
80	66.6	34.6
90	67.3	34.7
∞	65.14	33.2

4. Conclusion

The Cu(II) NNN amide pincers were shown to bind the biomimetic *p*-cresol model with logK values in the range of 3.72 - 4.09. This is essentially the coordinative bond strength between the phenolic group on the tyrosine target and the metal pincer. The copper chelates were then shown to specifically bind tyrosine on the hexapeptide epitope corresponding to Y505 on the SARS-CoV-2 RBD. This specificity was confirmed by NMR spectroscopy and the 1:1 binding stoichiometry was confirmed by MS analysis. A conclusion cannot be made regarding whether the tyrosine becomes deprotonated upon coordination, as tyrosyl radical and tyrosinate fluorescence emission would likely be quenched by the metal ion. However, MS and FTIR data tentatively suggest that deprotonation does not occur and the interaction is purely coordinative in nature.

CD spectroscopy was then used to show that CuL5 binds the SARS-CoV-2 Delta RBD and the weak induced signal indicates that the chelate is surface bound. The copper chelate must be surface bound on the RBD to interfere with ACE2 receptor recognition and act as a fusion inhibitor. Cu(H_2L8) was then found to bind the RBD with logK values between 4.80 and 5.74, depending on whether Hill or Stern-Volmer models were used. There are small molecules that bind the RBD with logK values between 4.5 and 7.0 and these compounds successfully act as fusion inhibitors with an IC_{50} value of about 85 μM.[21] The ligand binding site was found to be Y489 on the RBD, thus proving the concept that metal chelates may specifically target solvent-exposed protein residues, and potentially act as antiviral fusion inhibitors.

However, the copper chelates showed poor stability in various buffers and instantly decomposed in dilute solutions of HCl. Initially, the biomimetic model protein, thaumatin, was to be tested, but CuL5 immediately demetallated in a solution of the protein. While the copper chelate showed good GSH stability in MOPS buffer, the compound decomposed when GSH and NaCl were present. These findings suggest that the Cu(II) pincer would not survive *in vitro* cell cultures and hence live virus data was never collected.

References

(1) Lakowicz, J. R.; Masters, B. R. Principles of Fluorescence Spectroscopy, Third Edition. *J. Biomed. Opt.* **2008**, *13* (2), 029901. https://doi.org/10.1117/1.2904580.

(2) Gesztelyi, R.; Zsuga, J.; Kemeny-Beke, A.; Varga, B.; Juhasz, B.; Tosaki, A. The Hill Equation and the Origin of Quantitative Pharmacology. *Arch. Hist. Exact Sci.* **2012**, *66* (4), 427–438. https://doi.org/10.1007/s00407-012-0098-5.

(3) van de Weert, M.; Stella, L. Fluorescence Quenching and Ligand Binding: A Critical Discussion of a Popular Methodology. *J. Mol. Struct.* **2011**, *998* (1–3), 144–150. https://doi.org/10.1016/j.molstruc.2011.05.023.

(4) Alarcón, E.; Aspée, A.; Abuin, E. B.; Lissi, E. A. Evaluation of Solute Binding to Proteins and Intra-Protein Distances from Steady State Fluorescence Measurements. *J. Photochem. Photobiol. B* **2012**, *106*, 1–17. https://doi.org/10.1016/j.jphotobiol.2011.11.002.

(5) van de Weert, M. Fluorescence Quenching to Study Protein-Ligand Binding: Common Errors. *J. Fluoresc.* **2010**, *20* (2), 625–629. https://doi.org/10.1007/s10895-009-0572-x.

(6) Oldani, A. N.; Ferrero, J. C.; Pino, G. A. Effect of the Intermolecular Hydrogen Bond Conformation on the Structure and Reactivity of the P-Cresol(H2O)(NH3) van Der Waals Complex. *Phys. Chem. Chem. Phys.* **2009**, *11* (44), 10409. https://doi.org/10.1039/b916901f.

(7) Myszkiewicz, G.; Meerts, W. L.; Ratzer, C.; Schmitt, M. The Structure of 4-Methylphenol and Its Water Cluster Revealed by Rotationally Resolved UV Spectroscopy Using a Genetic Algorithm Approach. *J. Chem. Phys.* **2005**, *123* (4), 044304. https://doi.org/10.1063/1.1961615.

(8) Ferreira, S. T.; Stella, L.; Gratton, E. Conformational Dynamics of Bovine Cu, Zn Superoxide Dismutase Revealed by Time-Resolved Fluorescence Spectroscopy of the Single Tyrosine Residue. *Biophys. J.* **1994**, *66* (4), 1185–1196. https://doi.org/10.1016/S0006-3495(94)80901-4.

(9) Creed, D. THE PHOTOPHYSICS AND PHOTOCHEMISTRY OF THE NEAR-UV ABSORBING AMINO ACIDS-II. TYROSINE AND ITS SIMPLE DERIVATIVES. *Photochem. Photobiol.* **2008**, *39* (4), 563–575. https://doi.org/10.1111/j.1751-1097.1984.tb03891.x.

(10) Ross, J. A.; Jameson, D. M. Time-Resolved Methods in Biophysics. 8. Frequency Domain Fluorometry: Applications to Intrinsic Protein Fluorescence. *Photochem. Photobiol. Sci.* **2008**, *7* (11), 1301–1312. https://doi.org/10.1039/b804450n.

(11) Grzesiak, J.; Fellner, L.; Grünewald, K.; Kölbl, C.; Walter, A.; Horlacher, R.; Duschek, F. Fluorescence Signatures of SARS-CoV-2 Spike S1 Proteins and a Human ACE-2: Excitation-Emission Maps and Fluorescence Lifetimes. *J. Biomed. Opt.* **2022**, *27* (05). https://doi.org/10.1117/1.JBO.27.5.050501.

(12) Wang, T.; Zeng, L.-H.; Li, D.-L. A Review on the Methods for Correcting the Fluorescence Inner-Filter Effect of Fluorescence Spectrum. *Appl. Spectrosc. Rev.* **2017**, *52* (10), 883–908. https://doi.org/10.1080/05704928.2017.1345758.

(13) Weitner, T.; Friganović, T.; Šakić, D. Inner Filter Effect Correction for Fluorescence Measurements in Microplates Using Variable Vertical Axis Focus. *Anal. Chem.* **2022**, *94* (19), 7107–7114. https://doi.org/10.1021/acs.analchem.2c01031.

(14) Mendonça, A.; Rocha, A. C.; Duarte, A. C.; Santos, E. B. H. The Inner Filter Effects and Their Correction in Fluorescence Spectra of Salt Marsh Humic Matter. *Anal. Chim. Acta* **2013**, *788*, 99–107. https://doi.org/10.1016/j.aca.2013.05.051.

(15) Gauthier, T. D.; Shane, E. C.; Guerin, W. F.; Seitz, W. Rudolf.; Grant, C. L. Fluorescence Quenching Method for Determining Equilibrium Constants for Polycyclic Aromatic Hydrocarbons Binding to Dissolved Humic Materials. *Environ. Sci. Technol.* **1986**, *20* (11), 1162–1166. https://doi.org/10.1021/es00153a012.

(16) Kasparek, A.; Smyk, B. A New Approach to the Old Problem: Inner Filter Effect Type I and II in Fluorescence. *Spectrochim. Acta. A. Mol. Biomol. Spectrosc.* **2018**, *198*, 297–303. https://doi.org/10.1016/j.saa.2018.03.027.

(17) Ignasiak, M.; Frackowiak, K.; Pedzinski, T.; Davies, M. J.; Marciniak, B. Unexpected Light Emission from Tyrosyl Radicals as a Probe for Tyrosine Oxidation. *Free Radic. Biol. Med.* **2020**, *153*, 12–16. https://doi.org/10.1016/j.freeradbiomed.2020.03.022.

(18) Wojcik, A.; Łukaszewicz, A.; Brede, O.; Marciniak, B. Competitive Photosensitized Oxidation of Tyrosine and Methionine Residues in Enkephalins and Their Model Peptides. *J. Photochem. Photobiol. Chem.* **2008**, *198* (1), 111–118. https://doi.org/10.1016/j.jphotochem.2008.02.027.

(19) Prendergast, F. G.; Hampton, P. D.; Jones, B. Characteristics of Tyrosinate Fluorescence Emission in .Alpha.- and .Beta.-Purothionins. *Biochemistry* **1984**, *23* (26), 6690–6697. https://doi.org/10.1021/bi00321a063.

(20) Martell, A. E.; Smith, R. M. *Other Organic Ligands*; Springer US: Boston, MA, 1977. https://doi.org/10.1007/978-1-4757-1568-2.

(21) Wang, L.; Wu, Y.; Yao, S.; Ge, H.; Zhu, Y.; Chen, K.; Chen, W.; Zhang, Y.; Zhu, W.; Wang, H.; Guo, Y.; Ma, P.; Ren, P.; Zhang, X.; Li, H.; Ali, M. A.; Xu, W.; Jiang, H.; Zhang, L.; Zhu, L.; Ye, Y.; Shang, W.; Bai, F. Discovery of Potential Small Molecular SARS-CoV-2 Entry Blockers Targeting the Spike Protein. *Acta Pharmacol. Sin.* **2022**, *43* (4), 788–796. https://doi.org/10.1038/s41401-021-00735-z.

Chapter 5

Crystallography

1. Introduction

X-ray crystallography experiments provide detailed structural information that allows chemical bonding and metal ion geometry to be precisely delineated. The Cu(II) NNN amide pincers presented here were designed to target solvent-exposed tyrosine residues as labile water molecules at the Cu(II) centre may exchange upon binding of the phenolic side chain. The solid-state structures enable the elucidation of binding modes of these chelates in biological systems. A search of the CSD[1] yielded three crystal structures[2,3] of a Cu(II) NNN amide pincer coordinated to phenol and these have been presented in Figure 5.1 with the inner coordination sphere bond lengths. The Cu–O_{phenol} bond is considerably shorter than the remaining bonds that make up the square plane and this indicates that tyrosine may avidly bind the metal centre. Indeed, the binding constants for the interaction between phenol and the Cu(II) NNN amide pincers were found to be around logK = 4 and were presented in Chapter 4. The crystal structures also indicate that in addition to coordinating forces, the phenol is stabilised at the metal centre by hydrophobic interactions between the aromatic ligand and aryl rings present on the chelate.

The Cu(II) pincers presented here all crystallized as cyclic supermolecules with hexameric geometry. Other Cu(II) metallocycle hexamers have been found in literature and will be presented here for discussion. The superstructure published by Lloyd *et al.*[4] has been presented in Figure 5.2 and follows the same cyclic bonding pattern as the Cu(II) metallocycles studied in this work. The cyclic coordination follows the pattern Cu(II)–C=O_{amide}–Cu(II) where the amide carbonyl of the complex acts a bridging ligand between copper centres that results in S_6 symmetry for the supermolecule. The bridging moiety involves three atoms and results in a 24-membered hexanuclear cyclic assembly which is stabilised by a synergistic combination of intramolecular coordination and aromatic interactions.

The metallocycle published by Hossain *et al.*[5] has been presented in Figure 5.3 and follows the bonding pattern Cu(II)–N_{diazo}–Cu(II). The diazo bridging group coordinates in a bidentate fashion that results in S_6 symmetry for the supermolecule. The bridging moiety involves two atoms and

results in an 18 membered hexanuclear metalladiazamacrocyle. The third Cu(II) metallocycle presented here was published by Fu *et al.*[6] has been shown in Figure 5.4. The cyclic coordination follows the pattern Cu(II)–N–C–N–C–C–O–Cu(II) where the bridging group involves a (1*H*-benzimidazol-1-yl)acetic acid moiety. The six atom bridging group results in a 42 membered hexanuclear metallocycle with S_6 symmetry. The final Cu(II) hexamer presented here was published by Higa *et al.*[7] and is shown in Figure 5.5. The cyclic coordination follows the pattern Cu(II)–$N_{imidazole}$–Cu(II) which results in S_6 symmetry for the supermolecule. The bridging imidazole connects each copper centre through three atoms and results in a 24-membered cyclic assembly.

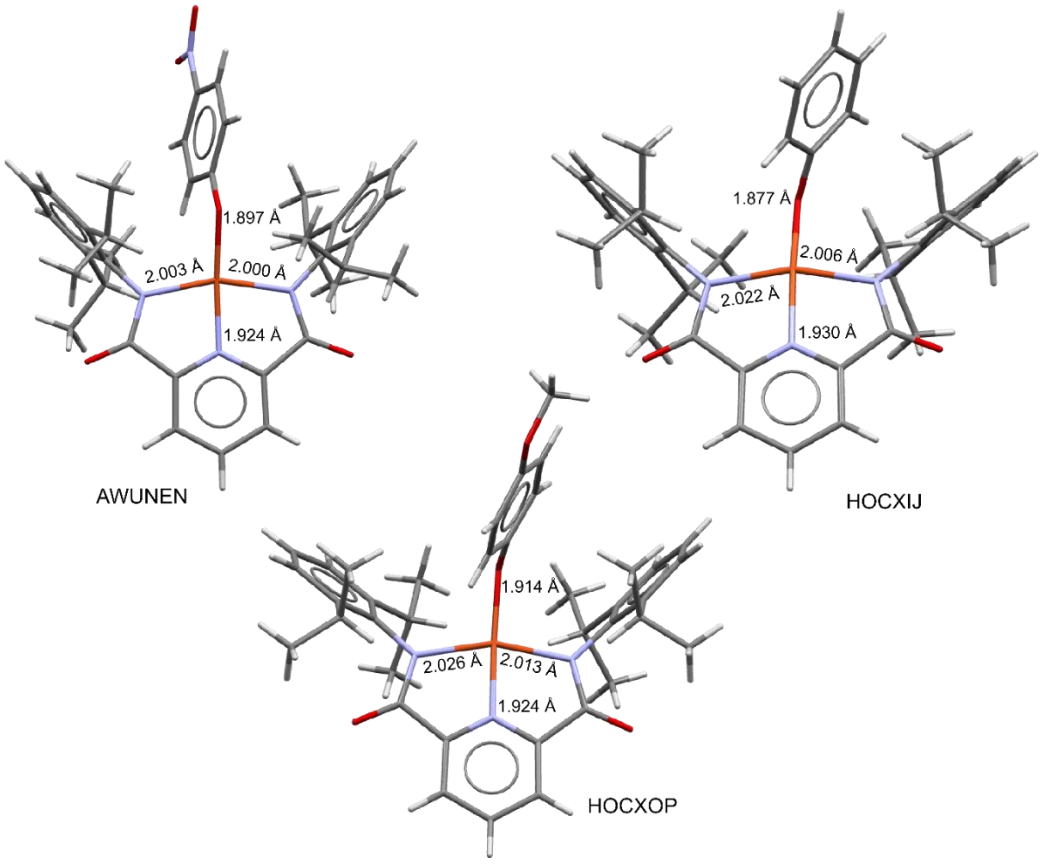


Figure 5.1: The crystal structures of a Cu(II) NNN amide pincer coordinated to various phenols. The structures have been labelled with their CSD reference codes. The phenol group serves as a biomimetic model for tyrosine and indicates the possible binding mode when the chelate has bound the solvent exposed residue on the SARS-CoV-2 receptor binding domain. The phenol coordinates in the equatorial position such that there is overlap of the paramagnetic $3d_{x^2-y^2}$ orbital and the aromatic π-system. This has been observed by NMR and was presented in Chapter 4. Additional stability is afforded by hydrophobic interactions between the phenol and the aryl rings present on the chelate.

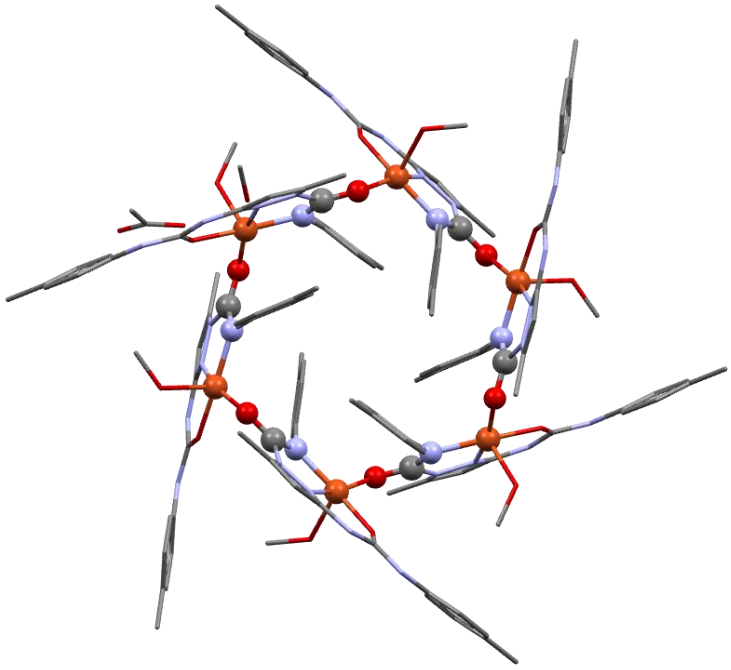


Figure 5.2: The Cu(II) hexamer published by Lloyd *et al.*[4] with the coordination pattern shown as ball-and-stick models. The cyclic coordination follows the pattern Cu(II)–C=O$_{amide}$–Cu(II). Standard colours have been used for atoms, i.e., grey for carbon, red for oxygen, blue for nitrogen, bronze for copper.

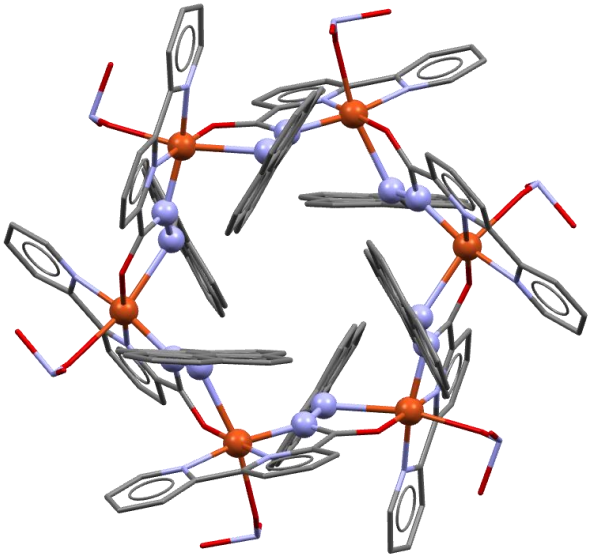


Figure 5.3: The copper metallocycle published by Hossain *et al.*[5] with the cyclic coordination pattern Cu(II)–N$_{diazo}$–Cu(II) shown as ball-and-stick models. Standard colours have been used for atoms, i.e., grey for carbon, red for oxygen, blue for nitrogen, bronze for copper.

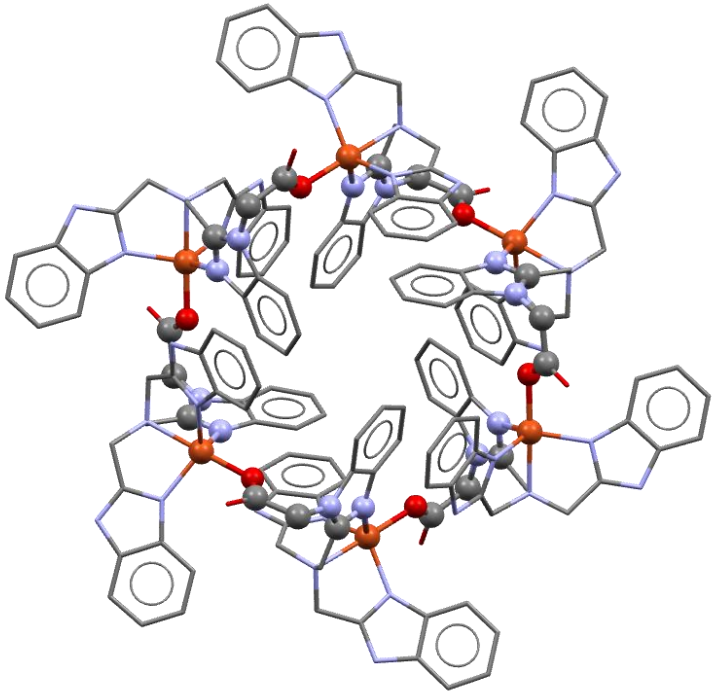


Figure 5.4: The Cu(II) superstructure published by Fu *et al.*[6] with the coordination pattern shown as ball-and-stick models. The (1*H*-benzimidazol-1-yl)acetic acid moiety serves as a bridging group between metal centres. Standard colours have been used for atoms, i.e., grey for carbon, red for oxygen, blue for nitrogen, bronze for copper.

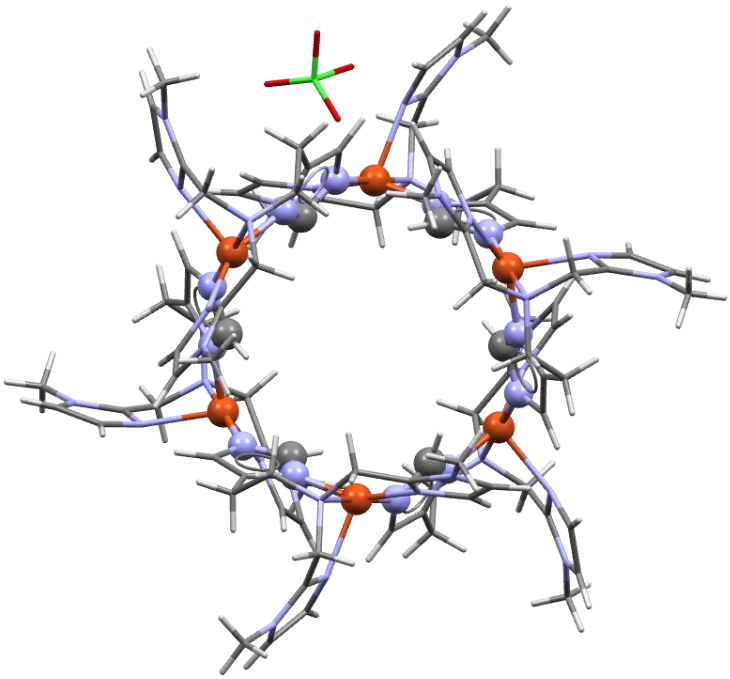


Figure 5.5: The hexanuclear cyclic assembly published by Higa *et al.*[7] with the coordination pattern Cu(II)–$N_{imidazole}$–Cu(II) shown as ball-and-stick models. Standard colours have been used for atoms, i.e., grey for carbon, red for oxygen, blue for nitrogen, bronze for copper.

2. Methods

Intensity data for CuL2 “blue” and “green” were collected on a BRUKER D8 Venture PHOTON II pixel array area detector with Mo Kα graphite monochromated sealed X-ray source (50kV, 30 mA) while the remaining structures were collected on a Bruker D8 Venture Bio PHOTON III diffractometer with a Mo Kα IμS DIAMOND source (50 kV, 1.4 mA). The collection method involved ω- and φ-scans, with either 768 × 1024 (PHOTON II) or 1536 × 1024 (PHOTON III) bit data frames. The unit cell and full data set were collected using APEX4[8]; SAINT was used to integrate the data, and SADABS was used to make empirical absorption corrections and scale the data. Space group assignments were made using XPREP on all compounds. Using Olex2[9], the crystal structures were solved with the ShelXT[10] structure solution program using Intrinsic Phasing and refined with the ShelXL[11] refinement package using Least Squares minimization. Non-hydrogen atoms were first refined isotropically followed by anisotropic refinement by full-matrix least-squares calculations based on F^2. The IUCr cif check reports have been collated in the Supporting Information.

3. Results & Analysis

3.1 CuL2 “blue”

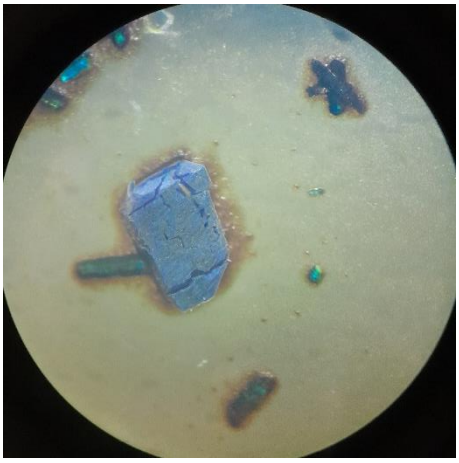


Figure 5.6: Crystals of CuL2 “blue” grown by evaporating a saturated pyridine solution.

A blue block of $C_{92}H_{88.04}Cu_2N_{16}O_{18.02}$ with approximate dimensions 0.219 mm x 0.332 mm x 0.359 mm was used and the X-ray intensity data were measured (λ = 0.71073 Å). $C_{92}H_{88.04}Cu_2N_{16}O_{18.02}$ (*M* = 1833.22 g/mol): triclinic, space group *P*-1 (no. 2), *a* = 15.3159(6) Å, *b* = 16.8888(7) Å, *c* = 18.9152(7) Å, *α* = 97.9570(10)°, *β* = 113.0810(10)°, *γ* = 96.638(2)°, *V* = 4379.6(3) Å^3, *Z* = 2, *T* = 153.0 K, μ(MoKα) = 0.565 mm^{-1}, *Dcalc* = 1.390 g/cm^3, 437150 reflections measured (5.052° ≤ 2Θ ≤ 61.482°), 26824 unique (R_{int} = 0.1246, R_{sigma} = 0.0634) which were used in all calculations. The final R_1 was 0.0487 (I > 2σ(I)) and wR_2 was 0.1302 (all data). The integration of the data using a triclinic unit cell yielded a total of 434176 reflections to a maximum θ angle of 30.74° (0.70 Å resolution), of which 26823 were independent (average redundancy 16.187, completeness = 98.3%, R_{int} = 11.16%, R_{sig} = 5.14%) and 17197 (64.11%) were greater than 2σ(F^2). The final cell constants are based upon the refinement of the XYZ-centroids of reflections above 20 σ(I). Data were corrected for absorption effects using the Multi-Scan method (SADABS). The ratio of minimum to maximum apparent transmission was 0.950. The calculated minimum and maximum transmission coefficients (based on crystal size) are 0.8230 and 0.8860. The final anisotropic full-matrix least-squares refinement on F^2 with 1241 variables converged at R1 = 5.02%, for the observed data and wR2 = 12.39% for all data.

CuL2 “blue” crystallised over a few weeks in the triclinic space group *P*-1 with two dinuclear copper “cage” complexes in the unit cell and the asymmetric unit described by a single dinuclear chelate. The asymmetric unit and “cage” structure are presented in Figure 5.7. There is an ordered H-bonding network between six co-crystalized water molecules that have occupied the cavity of the dinuclear copper cage. Additionally, there are four molecules of pyridine that have co-crystalized in the unit cell and this affects the solvatochromism observed for the CuL2 compound. The crystal is deep blue when pyridine has co-crystallized in the lattice. However, as will be shown shortly, the crystal is green when no pyridine is present in the lattice.

The inner coordination sphere for each square pyramidal metal center has bond lengths Cu–$O_{carboxylate}$ that average *ca.* 1.945 ± 0.003 Å while the pyridine ligands that make up the square plane have bonds Cu–N_{pyr} *ca.* 2.038 ± 0.004 Å. The short Cu–$O_{carboxylate}$ bond reflects the σ-donor ability of the anionic donor and the preference of the Cu(II) ion for the carboxylate functional group. Hence, when the chelate is synthesized with equivalent ratios of metal and

ligand, the Cu(II) ion preferentially binds the carboxylates, leaving the NNN amide pincer cleft unoccupied. The axially coordinated pyridine has a bond length *ca.* 2.29 Å indicating that the electron dense square plane repels ligands approaching the axial position. The dinuclear cage structure $Cu_2(L2)_2$ is formed in preference to CuL2 because the carboxylates afford charge neutrality, and the ligand is less strained when coordinated as $Cu_2(L2)_2$.

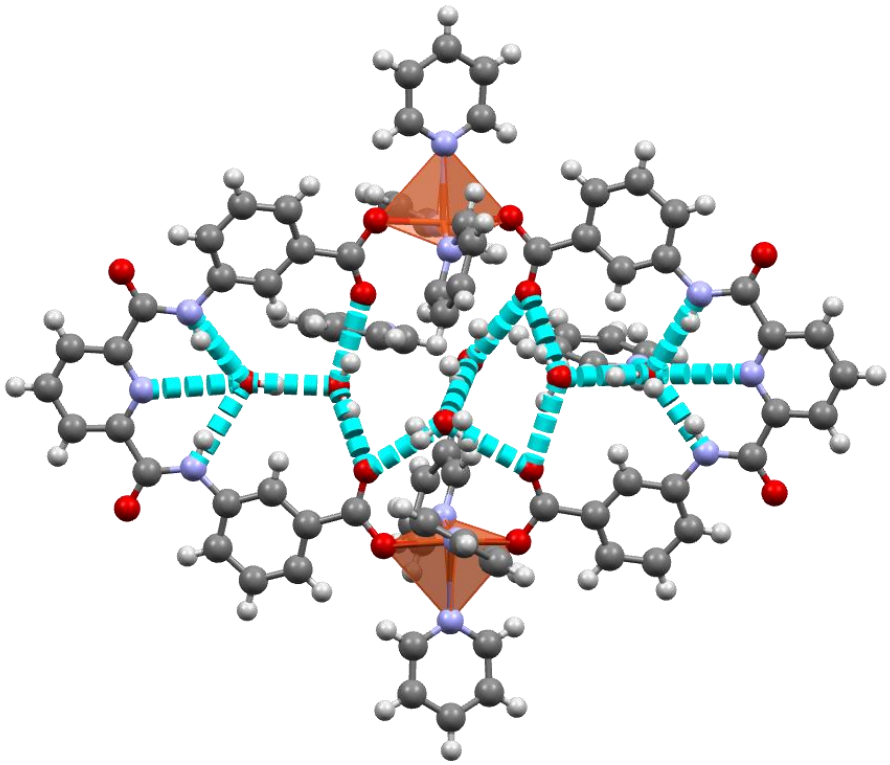


Figure 5.7: The asymmetric unit of CuL2 "blue" showing the dinuclear cage structure and co-crystallized solvent molecules. The square pyramidal copper centers have been shown as polyhedrons. There are six water molecules and four pyridines, two have been omitted for clarity. The internal H-bond network has been shown as cyan cylinders.

The crystal packing is efficient as there are no voids in the lattice and various intermolecular forces exist between dinuclear chelates. This has been shown in Figure 5.8. The extensive H-bonding network extends between cage structures and facilitates packing in the lattice. Additionally, there are C–H···π, C–H···O, and π···π interactions between molecules that allow the structure to efficiently pack into the lattice.

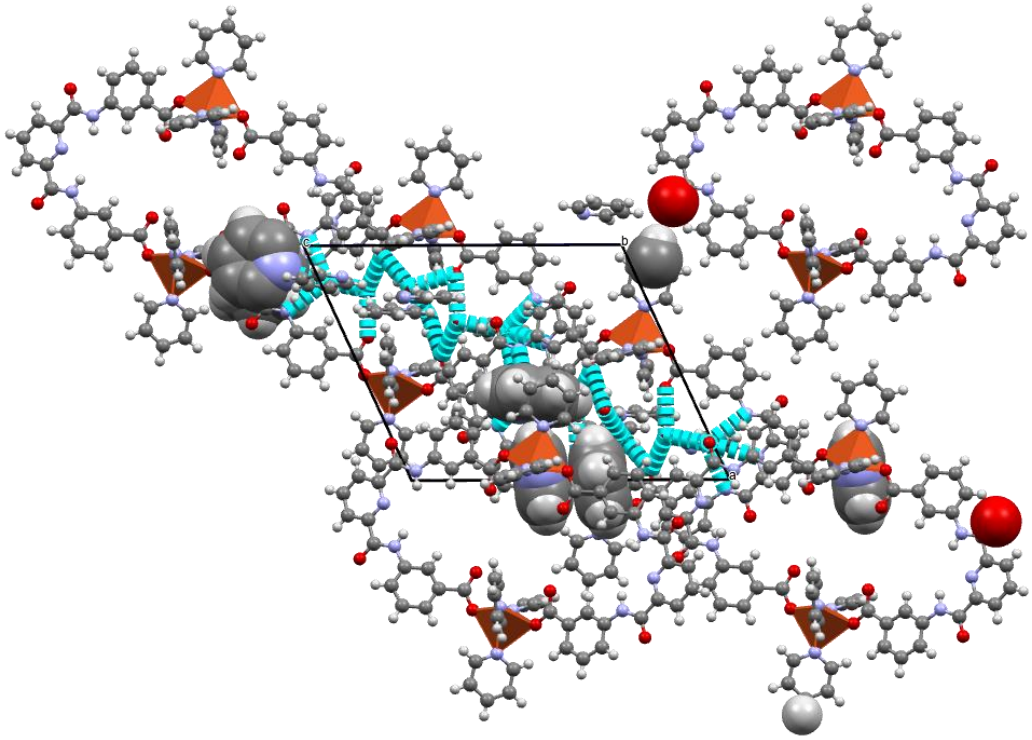


Figure 5.8: The intermolecular forces and unit cell of CuL2 “blue”. The C–H···π, C–H···O, and π···π interactions have been shown as space-fill models while the H-bonding network has been shown as cyan cylinders. There are additional, and numerous, close contacts that further facilitate packing of the cage structure into the crystal lattice.

3.2 CuL2 “green”

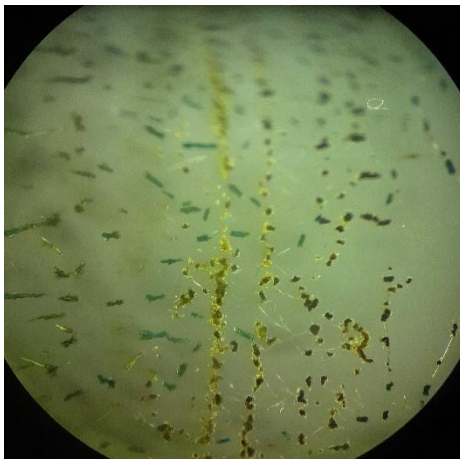


Figure 5.9: Crystals of CuL2 “green” grown from a saturated pyridine solution.

A clear green needle-like crystal of $C_{72}H_{68}Cu_2N_{12}O_{18}$ with approximate dimensions 0.100 mm x 0.178 mm x 0.328 mm, was used and the X-ray intensity data were measured (λ = 0.71073 Å). $C_{72}H_{68}Cu_2N_{12}O_{18}$ (*M* = 1516.46 g/mol): monoclinic, space group $P2_1/c$ (no. 14), *a* = 8.6922(5) Å, *b* = 27.6985(15) Å, *c* = 15.2690(8) Å, *β* = 105.377(2)°, *V* = 3544.6(3) Å^3, *Z* = 2, *T* = 153.0 K, μ(MoKα) = 0.680 mm^{-1}, *Dcalc* = 1.421 g/cm^3, 143320 reflections measured (4.86° ≤ 2Θ ≤ 61.332°), 10934 unique (R_{int} = 0.1169, R_{sigma} = 0.0698) which were used in all calculations. The final R_1 was 0.0557 (I > 2σ(I)) and wR_2 was 0.1430 (all data). The integration of the data using a monoclinic unit cell yielded a total of 143320 reflections to a maximum θ angle of 30.67° (0.70 Å resolution), of which 10934 were independent (average redundancy 13.108, completeness = 99.6%, R_{int} = 11.69%, R_{sig} = 6.98%) and 7092 (64.86%) were greater than 2σ(F^2). The final cell constants are based upon the refinement of the XYZ-centroids of reflections above 20 σ(I). Data were corrected for absorption effects using the Multi-Scan method (SADABS). The ratio of minimum to maximum apparent transmission was 0.950. The calculated minimum and maximum transmission coefficients (based on crystal size) are 0.8080 and 0.9350. The final anisotropic full-matrix least-squares refinement on F^2 with 478 variables converged at R1 = 5.57%, for the observed data and wR2 = 14.30% for all data.

CuL2 “green” crystallized over a few weeks in the monoclinic space group $P2_1/c$ with two dinuclear copper “cage” structures in the unit cell and the asymmetric unit described by half of a dinuclear complex. The copper cage structure is presented in Figure 5.10 and shows three co-crystallized water molecules. There is a H-bonding network between waters that have occupied the cage cavity and a single water molecule that acts a H-bond donor to the carbonyl of a neighboring cage complex, facilitating intermolecular interactions and packing of the chelates into the crystal lattice. The short bond lengths Cu–$O_{carboxylate}$ average *ca.* 1.952 ± 0.002 Å indicating that the Cu(II) ion favourably binds carboxylates over amidates. The Cu–N_{pyr} mean distance is 2.023 ± 0.008 Å for the pyridine molecules that make up the square plane of the square pyramidal complex. The solvatochromic phenomena observed for CuL2 “green” and CuL2 “blue” are explained by differences in co-crystallized solvent molecules.

The “blue” crystal contains six water molecules and four pyridine rings while the “green” crystal contains only three co-crystalized waters, and it is this difference that results in the solvatochromatic effect observed. The phenomenon may be delineated with the use of DFT

however this was not pursued because it was not aligned with the original aims of the project. Nevertheless, the structure was computed at the B3LYP/LanL2DZ level of theory, and the spin-density was found to occupy the $3d_{x^2-y^2}$ orbital located at the copper centre and making up the square plane. The molecular overlay of crystal and computed structures and the spin-density plot are presented in Figure 5.11. Finally, the intermolecular forces that facilitate packing of the chelates are presented in Figure 5.12. The intermolecular interactions are dominated by H-bonding between chelates that results in efficient packing of the cage structures as no voids are present in the crystal.

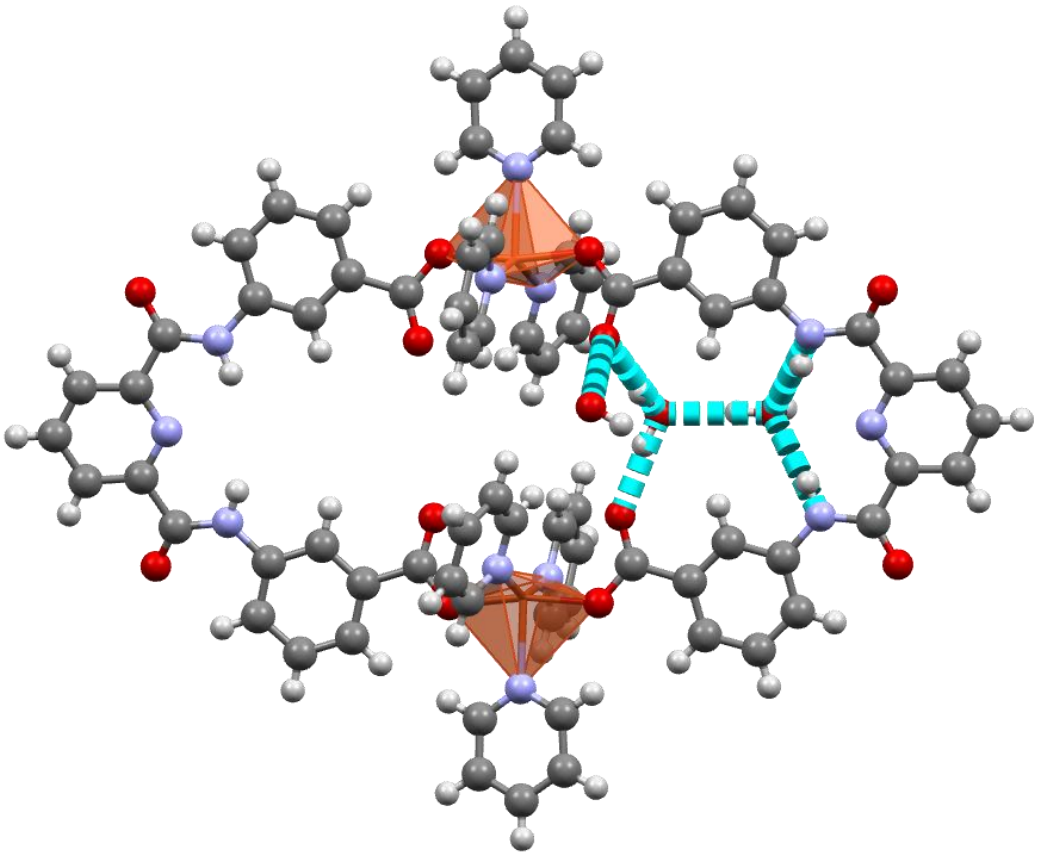


Figure 5.10: The dinuclear cage structure of CuL2 "green" has co-crystalized with three water molecules. A single water molecule is shown that acts as a H-bond donor to the carbonyl of a neighboring chelate and facilitates packing of the complexes into the lattice.

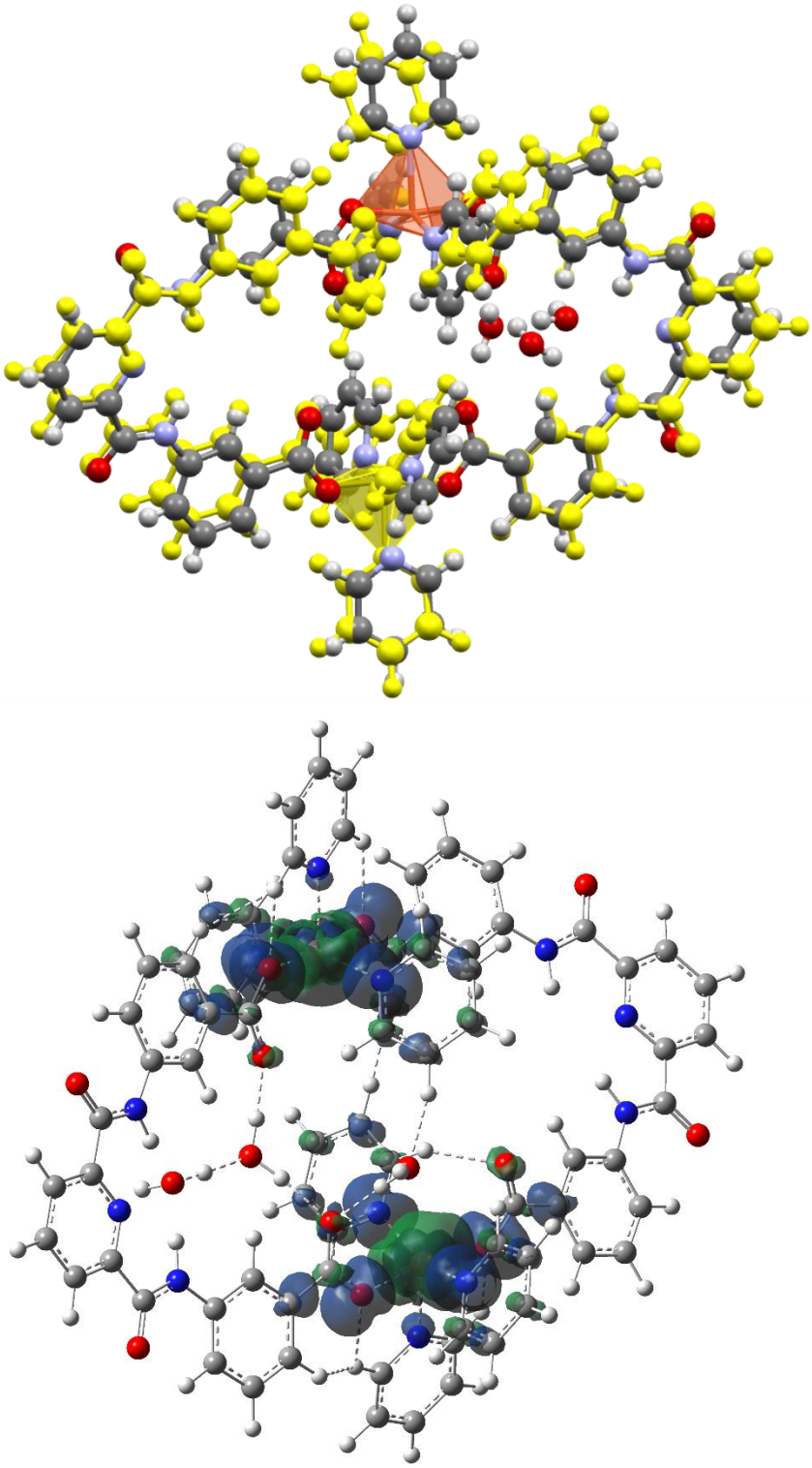


Figure 5.11: (Top) The molecular overlay of computed structure (shown in yellow) and X-ray crystal structure, R^2 = 0.86 Å. (Bottom) The spin-density plot for CuL2 "green" shows significant $3d_{x^2-y^2}$ character and occupies the square plane of the metal center.

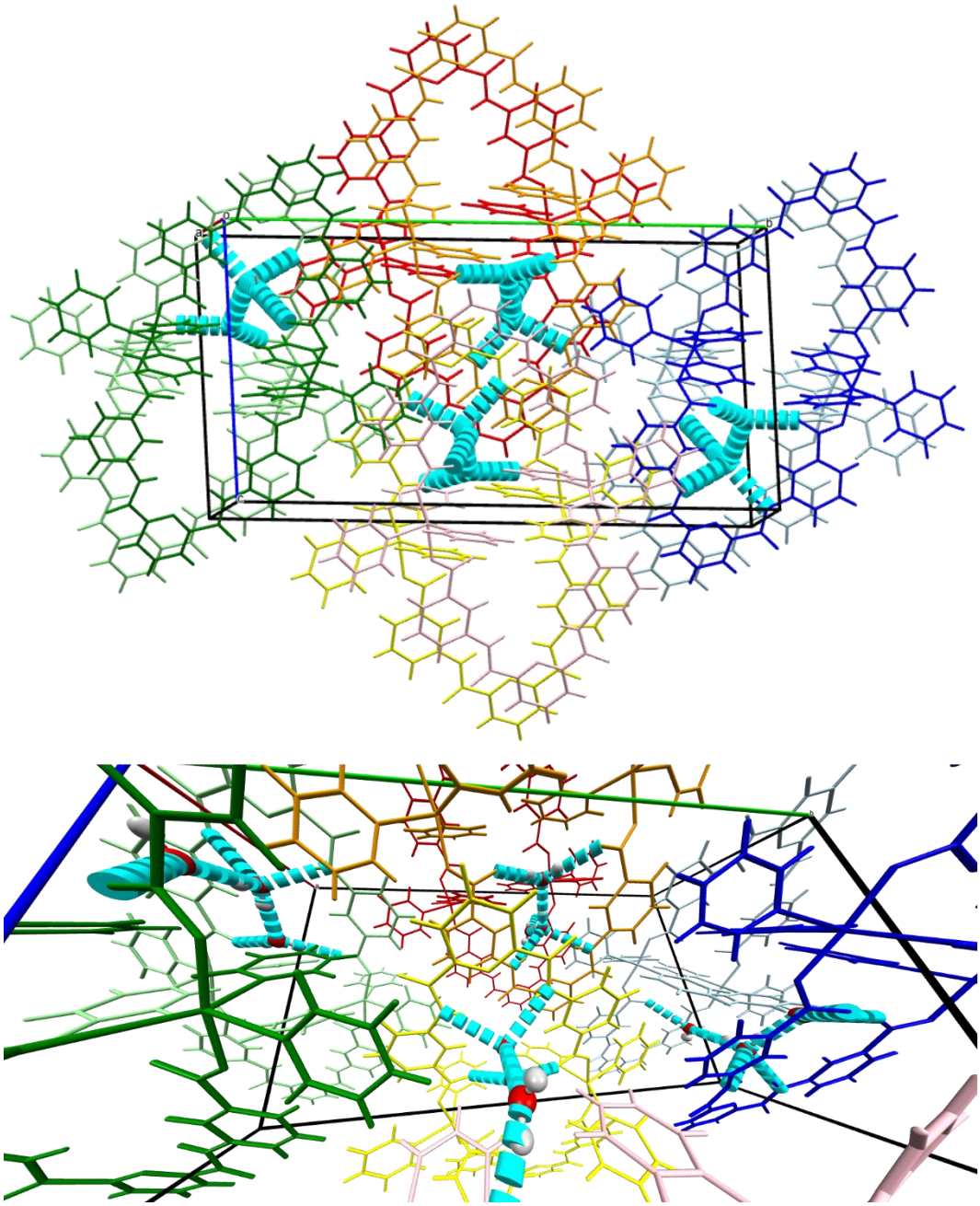


Figure 5.12: The unit cell and packing of CuL2 “green” is shown with neighboring cage structures colored differently. The H-bonding network extends between three water molecules that occupy the cage cavity and the carbonyl of an adjacent chelate. These strong intermolecular interactions result in efficient crystal packing as no voids are present in the lattice.

3.3 CuL3

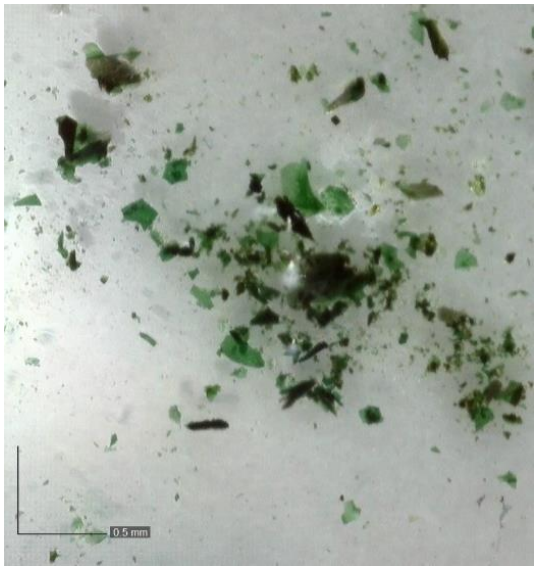


Figure 5.13: Crystals of CuL3 grown from a saturated pyridine solution.

A translucent dark green, plate-like crystal of $C_{72}H_{56}Cu_4N_{12}O_{14}$ with approximate dimensions 0.114 mm x 0.240 mm x 0.301 mm was used and the X-ray intensity data were measured (λ = 0.71073 Å). $C_{72}H_{56}Cu_4N_{12}O_{14}$ (*M* = 1567.44 g/mol): monoclinic, space group *C*2 (no. 5), *a* = 36.605(5) Å, *b* = 16.354(2) Å, *c* = 16.399(2) Å, *β* = 111.797(4)°, *V* = 9116(2) Å^3, *Z* = 4, *T* = 173.00 K, μ(MoKα) = 0.977 mm^{-1}, *Dcalc* = 1.142 g/cm^3, 79338 reflections measured (2.764° ≤ 2Θ ≤ 50°), 15612 unique (R_{int} = 0.1950, R_{sigma} = 0.1385) which were used in all calculations. The final R_1 was 0.0743 (I > 2σ(I)) and wR_2 was 0.2289 (all data). A total of 902 frames were collected. The total exposure time was 3.11 hours. The frames were integrated with the Bruker SAINT software package using a narrow-frame algorithm. The integration of the data using a monoclinic unit cell yielded a total of 124396 reflections to a maximum θ angle of 25.48° (0.83 Å resolution). The final cell constants are based upon the refinement of the XYZ-centroids of 7191 reflections above 20 σ(I) with 4.794° < 2θ < 50.18°. Data were corrected for absorption effects using the Multi-Scan method (SADABS). The ratio of minimum to maximum apparent transmission was 0.614.

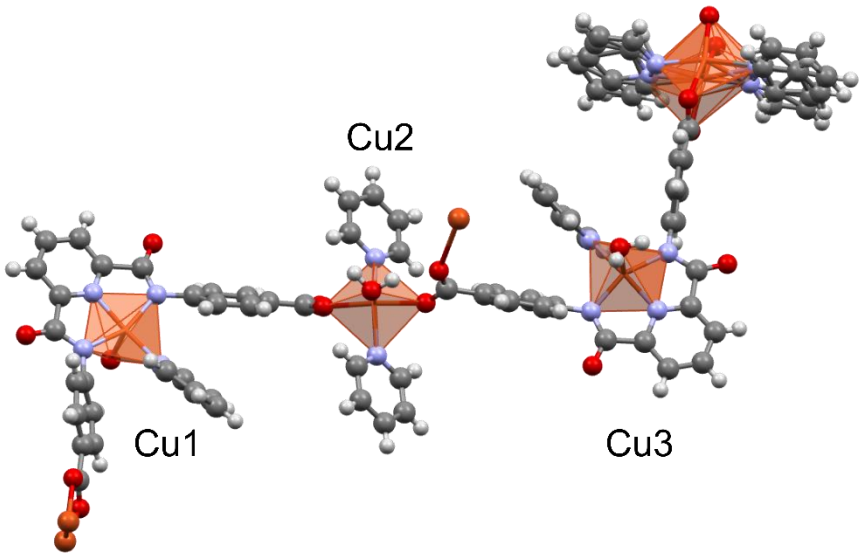


Figure 5.14: The asymmetric unit of CuL3 is described by a tetramer of the MOF polymer.

CuL3 crystallized over two days in the monoclinic space group *C*2 with four molecules of $C_{72}H_{56}Cu_4N_{12}O_{14}$ in the unit cell and the asymmetric unit described by a single tetramer. The asymmetric unit has been presented in Figure 5.14 and inner coordination sphere bond lengths have been collated in Table 5.1. The bond lengths for Cu2 and the anionic carboxylate oxygen donors ($O_{carboxylate}$), are significantly shorter than anionic amidate bonds ($N_{amidate}$) to Cu1 and Cu3. This indicates that the Cu(II) ion preferentially binds carboxylates over amidates and provides rationale for the off-target synthesis of NNN amide pincers that have been functionalized with carboxylic acids (See Chapter 2 and CuL2 presented here).

The $O_{carboxylate}$ ligands coordinate Cu2 to make up the square plane of the square pyramidal metal center, and hence the atomic $3d_{x^2-y^2}$ orbital is principally involved with overlap of these ligands. The delocalization of this paramagnetic orbital is favored for the $O_{carboxylate}$ ligand as the bond lengths Cu–$O_{carboxylate}$ are *ca.* 1.95 Å while the bonds to the $N_{amidate}$ ligand (Cu–$N_{amidate}$) are *ca.* 2.00 Å. The delocalization of electron density from the Cartesian *xy* plane allows axially coordinated ligands to approach closer to the metal centre. This is evident as Cu2 with $O_{carboxylate}$ donors has an axially coordinated aqua ligand with a bond length Cu–OH_2 of 2.217 Å while Cu3 is bound by $N_{amidate}$ ligands and has an axially coordinated water molecule with a bond length Cu–OH_2 of 2.326 Å. The final indication that $O_{carboxylate}$ donors are better ligands for Cu(II) than $N_{amidate}$ ligands is found in the bond length comparison of anionic and neutral donors at the metal centre. While neutral donors have comparable bond lengths to anionic donors for Cu2 and the carboxylate complex, the anionic donor bond lengths for Cu3 and the amidate complex are significantly longer than neutral donors. Hence, with bond lengths Cu–$N_{amidate}$ *ca.* 2 Å, it is reasonable to conclude that $N_{amidate}$ is a poorer ligand than $O_{carboxylate}$ and provides rational for the off-target synthesis and poor stability of the NNN amide copper pincers studied in this work.

CuL3 crystallised as a 2D metal-organic framework (MOF) and the packing of the polymer in the lattice is presented in Figure 5.15. The MOF polymer extends parallel to the crystallographic c-axis and the coordination along this axis has been presented in Figure 5.14. The polymer also extends parallel to the crystallographic b-axis where the coordination involves an axially coordinated C=O at Cu1. This bond, Cu–$O_{carbonyl}$, is particularly long at 2.618 Å and reflects the tensional restriction imposed as the C=O containing tetramer must approach the axial position of an adjacent polymer. The intermolecular forces along the a-axis comprise of only close contacts which facilitate packing of the MOF into the crystal lattice. The MOF is arranged such that large voids exist as infinite channels that extend parallel to the crystallographic c-axis (Figure 5.16). The void volume is large at 29.5% (2690 $Å^3$) of the unit cell volume.

Table 5.1: The inner coordination bond lengths in Angstroms for the CuL3 tetramer. The bond lengths have been reported with the estimated standard deviation of the least significant digits given in parenthesis. Cu4 has been omitted due to the disorder at this metal center.

Bond	Cu1	Cu2	Cu3
Cu–$N_{pyr}1$	1.908(9)	1.936(9)	1.927(9)
Cu–$N_{pyr}2$	1.977(9)	2.024(9)	1.989(9)
Cu–Anion1 (N or O)	1.985(9)	1.928(11)	1.985(9)
Cu–Anion2 (N or O)	2.021(9)	1.963(9)	2.034(9)
Cu–Axial	2.618(9)	2.217(11)	2.326(12)

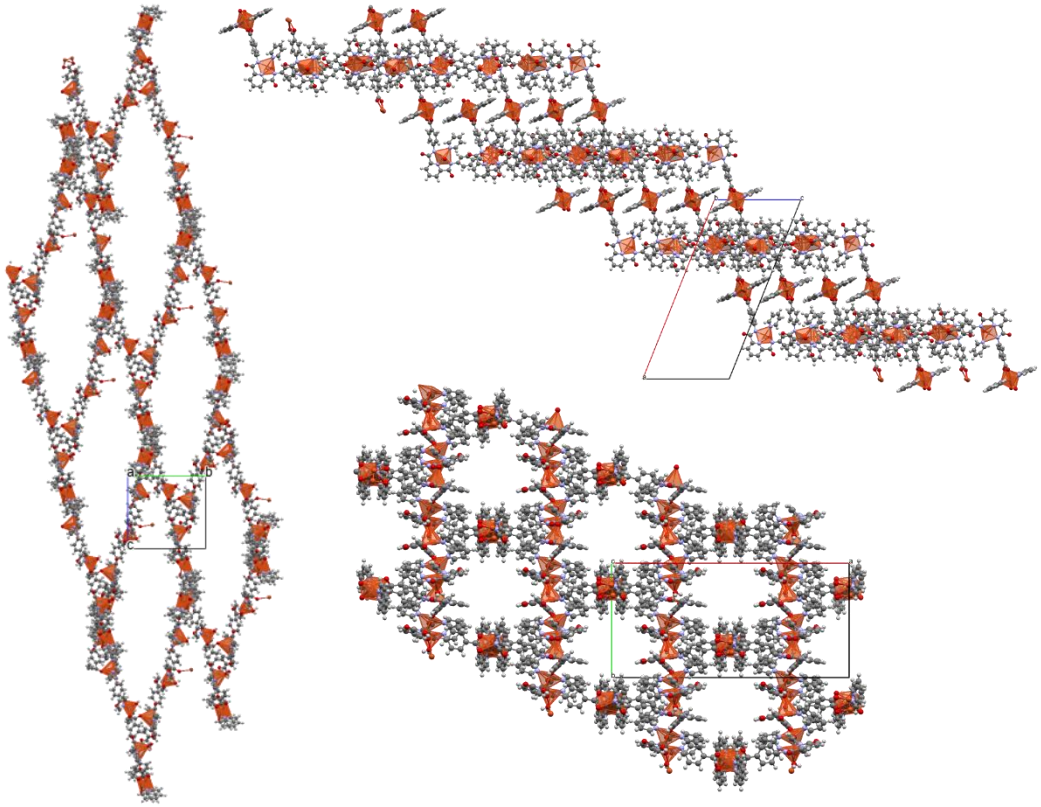


Figure 5.15: The unit cell of CuL3 showing the 2D MOF polymer. There is metal coordination that extends the polymer parallel to the crystallographic b- and c-axes while close contacts facilitate packing parallel to the a-axis. The unit cell is viewed down the a-axis (left), b-axis (top), and c-axis (bottom).

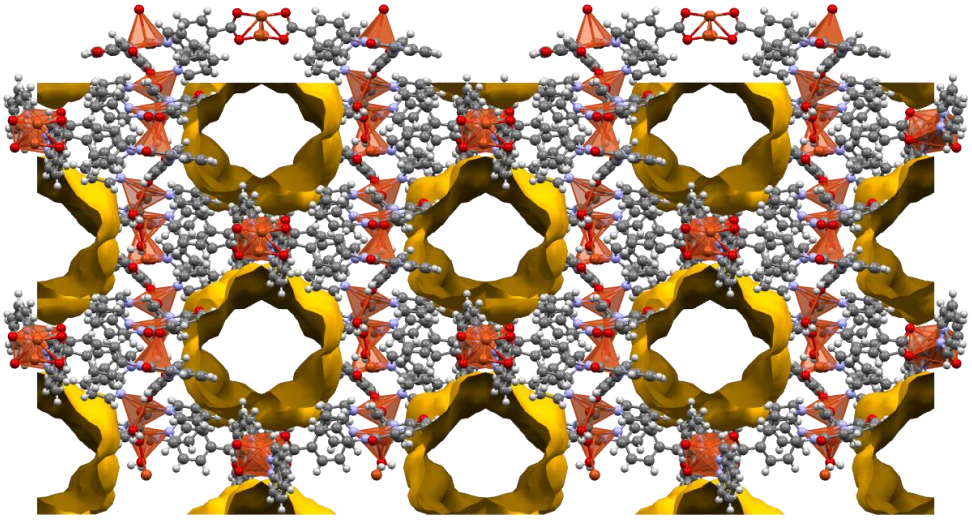


Figure 5.16: The voids that extend through the lattice of CuL3 as infinite channels parallel to the crystallographic c-axis.

3.4 CuL5

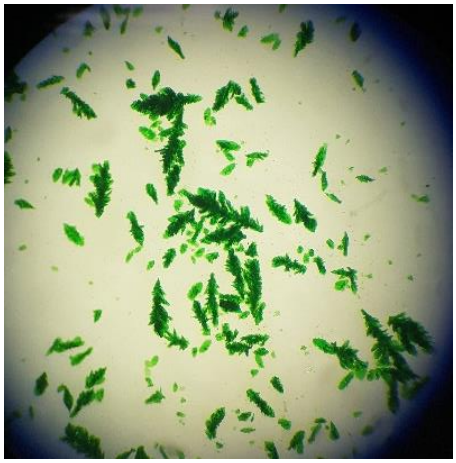


Figure 5.17: Crystals of CuL5 viewed under the microscope.

A dark-green, plate-like crystal with dimensions 0.065 mm x 0.218 mm x 0.292 mm was used and the X-ray intensity data were measured (λ = 0.71073 Å). $C_{156}H_{162}Cu_6N_{30}O_{30}$ (*M* = 3318.39 g/mol): monoclinic, space group *C*2/*c* (no. 15), *a* = 33.5199(11) Å, *b* = 19.1604(6) Å, *c* = 28.5691(10) Å, *β* = 105.9930(10)°, *V* = 17638.5(10) Å^3, *Z* = 4, *T* = 153.0 K, μ(MoKα) = 0.783 mm^{-1}, *Dcalc* = 1.250 g/cm^3, 515044 reflections measured (2.472° ≤ 2Θ ≤ 61.124°), 26998 unique (R_{int} = 0.0696, R_{sigma} = 0.0274) which were used in all calculations. The final R_1 was 0.0484 (I > 2σ(I)) and wR_2 was 0.1369 (all data). A total of 2543 frames were collected. The total exposure time was 6.11 hours. The frames were integrated with the Bruker SAINT software package using a narrow-frame algorithm. The integration of the data using a monoclinic unit cell yielded a total of 644508 reflections to a maximum θ angle of 30.61° (0.70 Å resolution). The final cell constants are based upon the refinement of the XYZ-centroids of 9947 reflections above 20 σ(I) with 4.347° < 2θ < 60.36°. Data were corrected for absorption effects using the Numerical Mu Calculated method (SADABS). The ratio of minimum to maximum apparent transmission was 0.888.

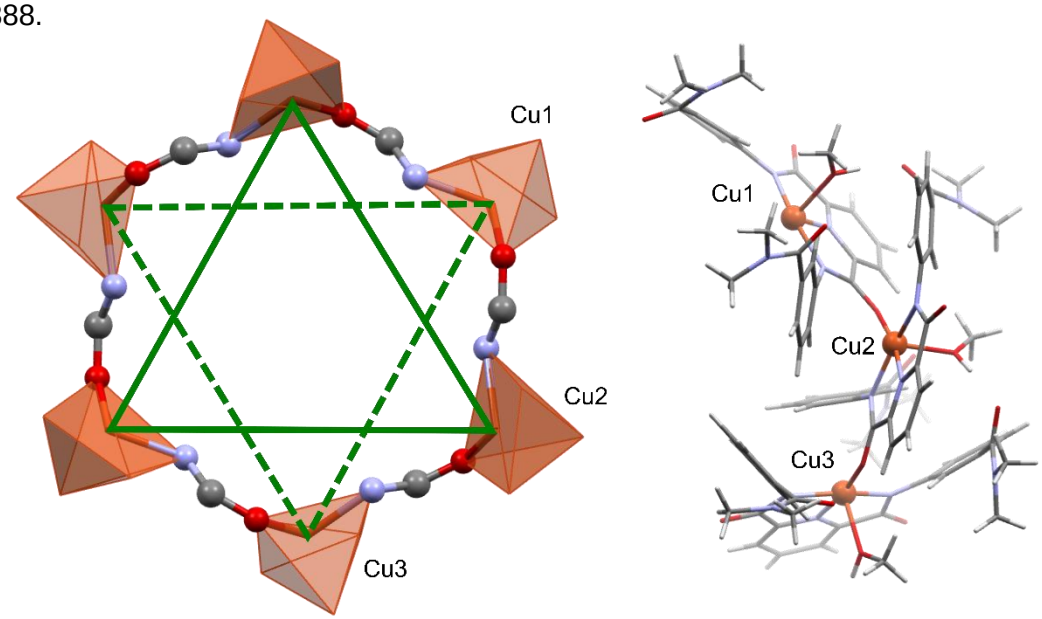


Figure 5.18: The coordination pattern that generates the 24-membered hexanuclear copper carboxamide macrocycle with S_2 symmetry. The metal centers are 5-coordinate square pyramidal and are shown as polyhedrons. The mean plane for the hexamer lies in the plane of the six nitrogens that make up the cyclic pattern. There are three Cu(II) centers that lie in a plane above the mean plane (solid green) and three Cu(II) centers that lie in a plane below the mean plane (dashed green). The asymmetric unit is shown on the right.

CuL5 crystallized in the monoclinic space group *C*2/*c* with four copper metallocycles in the unit cell and the asymmetric unit described by three monomers of the hexamer. The hexanuclear copper macrocycle coordination pattern is shown in Figure 5.18. The coordination follows the pattern Cu(II)–N–C=O_{amide}–Cu(II) where the amide carbonyl of the complex acts a bridging ligand between copper centres that results in S_2 symmetry. The mean plane of the metallocycle lies in the plane of the six nitrogens that make up the coordination pattern and three alternating Cu(II) centres lie in a plane above, and below, the mean plane. The plane-to-plane distance between the Cu(II) triads is 1.62 Å and the metallocycle mean plane bisects this interplanar distance.

The inner coordination sphere of the Cu(II) centres adopt square pyramidal geometry and is shown in Figure 5.19. The bond lengths that make up the inner coordination sphere are collated in Table 5.2 and are presented as an average of the three monomers that make up the asymmetric unit. The tridentate ligand chelates Cu(II) through N_{pyr} and two N_{amide} while a fourth exogenous ligand coordinates to make up the square plane. The atomic $3d_{x^2-y^2}$ orbital lies in the square plane where the x-axis is colinear with the N_{pyr}–Cu bond and the y-axis is colinear with the N_{amide}–Cu–N_{amide} bond. The bond lengths between Cu(II) and the neutral donor atoms N_{pyr} and $O_{carbonyl}$ are 1.92 and 1.93 Å respectively, while the anionic N_{amide} donors have bond lengths to Cu(II) *ca.* 2.05 Å and reflects the repulsive forces that exist between the anionic donors themselves as well as the metal center. The strong interelectronic repulsions between Cu(II) and the four donor atoms of the square plane raise the energy of the $3d_{x^2-y^2}$ paramagnetic orbital and promote electronic delocalization. This is reflected in the bond lengths of the amide carbonyls that make up the chelate ring and serve as bridging ligands between metal centers.

The amide C=O that forms part of the chelate ring, but is not a bridging group, has an average bond length of 1.248 ± 0.001 Å. However, when the amide C=O acts a bridging group and forms a Cu–$O_{carbonyl}$ bond, the bond length increases to an average of 1.267 ± 0.003 Å. This increase in C=O bond length is due to electron density from the $3d_{x^2-y^2}$ orbital occupying vacant σ* orbitals on the carbonyl, thereby decreasing repulsive forces in the metal-based orbital. There is additional overlap between the atomic $3d_{xy}$ orbital and π* molecular orbitals of the carbonyl, resulting in bond length elongation for the bridging moiety. The orbital analysis has been presented in Figure 5.20. The electron dense square plane repels ligands approaching on the z-axis of the Cartesian coordinate system centered on the metal, that is, ligands approaching the $3d_{z^2}$ orbital are repelled due to high electron density in the xy plane. This is reflected in the Cu–$O_{solvent}$ bond length of 2.296 Å; this axially coordinated ligand has the longest bond length out of

the five donor atoms that make up the square pyramidal geometry. Furthermore, the coordinated methanol solvent has a short O–H bond length of 0.871 Å, which indicates that electron density on the donor oxygen atom is being repelled by the $3d_{z^2}$ orbital such that internuclear repulsion is diminished in the O–H bond.

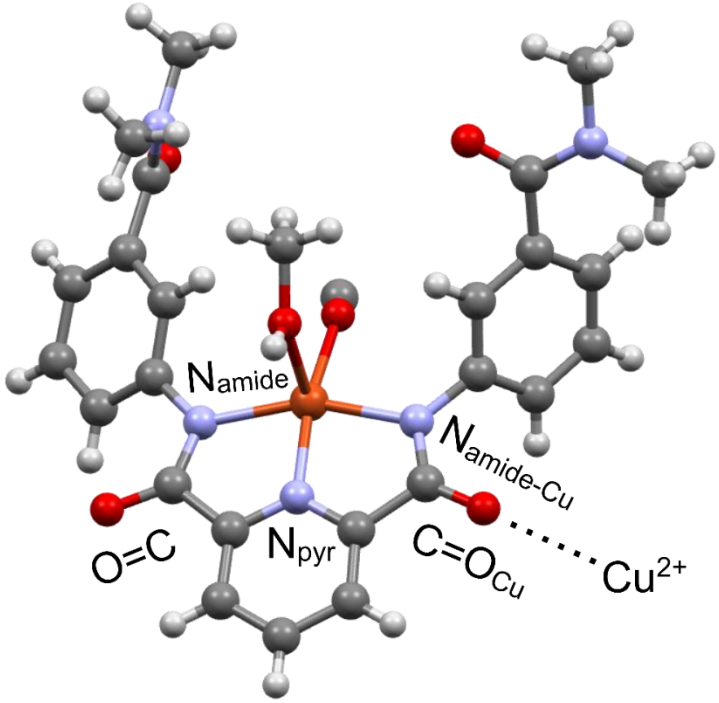


Figure 5.19: A single monomer of CuL5 that makes up the metallocycle hexamer. The inner coordination sphere is square pyramidal and donor nitrogens are labelled where N_{pyr} is the pyridine nitrogen and N_{amide} is the amide anionic nitrogen. The label $N_{amide\text{-}Cu}$ refers to the anionic nitrogen that forms the amide that is coordinated to a neighboring complex of CuL5. The carbonyls that make up the chelate ring are distinguished as C=O and $C{=}O_{Cu}$ where the latter refers to the carbonyl that acts as a bridge between metal centers of the hexamer.

Table 5.2: The bond lengths for the inner coordination sphere of CuL5 as well as carbonyl bonds that make up the tridentate chelate ring. The asymmetric unit of the crystal contains three Cu(II) centers, and the bond lengths are presented as the average with the error reported as the standard deviation of three independent bond length measurements.

Bond	Length (Å)
$Cu–N_{pyr}$	1.920 ± 0.007
$Cu–N_{amide}$	2.045 ± 0.01
$Cu–N_{amide\text{-}Cu}$	2.059 ± 0.003
$Cu–O_{carbonyl}$	1.931 ± 0.01
$Cu–O_{solvent}$	2.296 ± 0.02
C=O	1.248 ± 0.001
$C{=}O_{Cu}$	1.267 ± 0.003

The metallocycle hexamer is held together by a synergistic combination of intramolecular forces that facilitate the tensional integrity observed for the supramolecular assembly. These forces include coordinative bonding through the cyclic structure, hydrogen bonding, van der Waals forces, C–H···π[12] and d···π[13,14] interactions, the latter two interactions have been defined in Figure 5.21. The C–H···π interactions have been defined in literature, however, the d···π interaction has been defined here by the author.

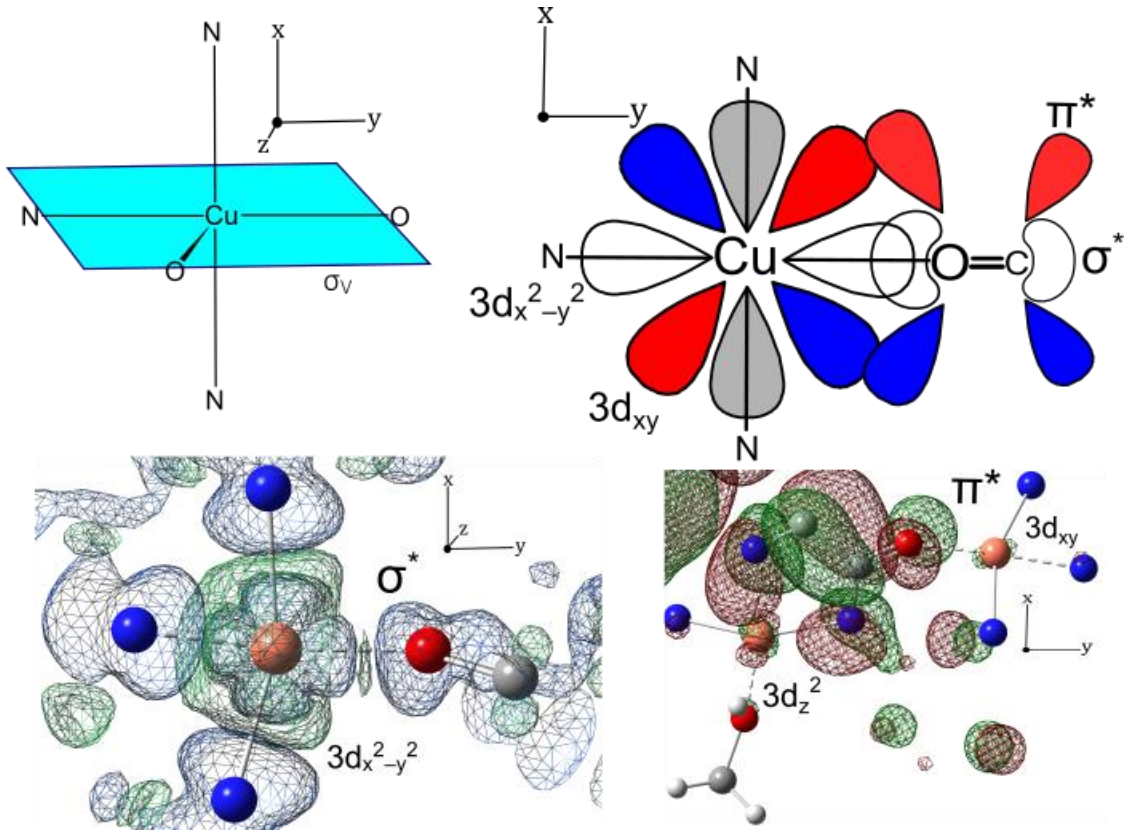


Figure 5.20: The inner coordination sphere of CuL5 is shown in the top left, and the only symmetry element is a vertical mirror plane, σ_V. The mirror plane defines the Cartesian z-axis as the principal z-axis is collinear with the highest symmetry element. As a result, the x-axis is perpendicular to the z-axis and collinear with highest number of identical atoms, i.e., the two N_{amide}. That leaves the y-axis to pass through N_{pyr} and $O_{carbonyl}$. The bridging carbonyl interaction is then shown on the top right. The bonding involves predominately σ-overlap of the metal-based $3d_{x^2-y^2}$ atomic orbital and σ* molecular orbital of the carbonyl. There is additional bonding involving π-overlap of the metal-based $3d_{xy}$ atomic orbital and the π* molecular orbitals of the carbonyl. This donation of electron density from the metal-based orbitals into antibonding orbitals of the carbonyl causes the bond length to increase for the bridging moiety. This was confirmed with DFT, as the spin-density plot in the bottom left of the figure shows significant $3d_{x^2-y^2}$ character as well as σ-overlap between copper and the carbonyl. The π-overlap between carbonyl π* molecular orbitals and the atomic $3d_{xy}$ orbital was observed for the LUMO of the asymmetric unit of CuL5. Additionally, the axially coordinated solvent molecule shows significant $3d_{z^2}$ character, substantiating the claim that the z-axis is collinear with the axial position.

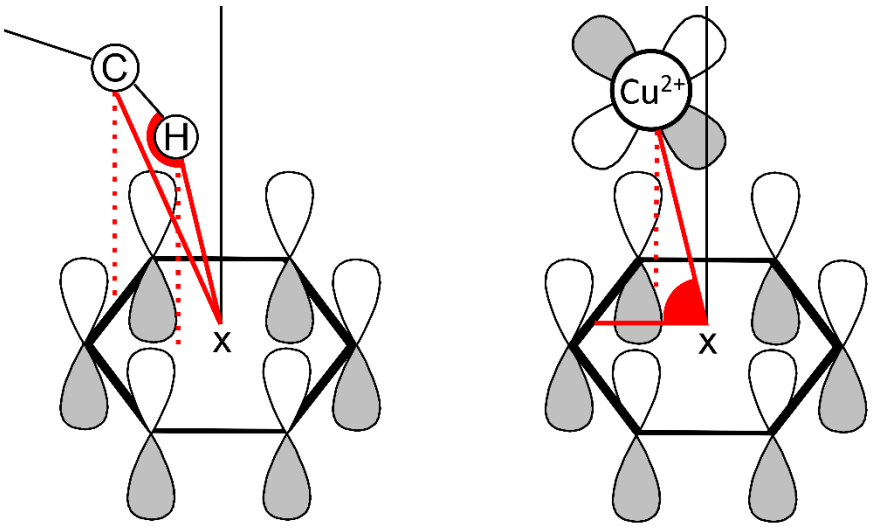


Figure 5.21: The geometry of C–H···π and d···π interactions. The centroid of the aromatic ring is marked "x" and the normal to the aromatic plane is shown as a solid black line. The atom-to-centroid distances are marked by solid red lines while atom-to-plane distances are marked by dashed red lines. The angles that define the interaction have been marked in red. The C–H···π interaction has optimal overlap when the angle at hydrogen ∠C–H–X approaches 180°. The metal d···π interaction has optimal overlap when the angle at the centroid ∠C–X–M approaches 90°. The angle is defined by selecting the atom in the aromatic ring closest to the metal centre, the centroid of the ring, and the metal centre itself. When the d···π interaction has optimal overlap all angles ∠C–X–M will approach 90° as the d_{z^2} orbital approaches the centroid of the aromatic ring. When the d···π interaction angle ∠C–X–M is acute, but greater than 45°, the d_{xz} and d_{yz} orbitals are orientated for favourable overlap with the π molecular orbitals of the aromatic ring. Hence, C–H···π interactions will be described by the atom-to-plane distance between the hydrogen atom and the aromatic plane as well as the angle at hydrogen ∠C–H–X. Furthermore, d···π interactions will be described by the atom-to-plane distance in angstroms between the metal centre and the aromatic plane as well as the angle at the centroid ∠C–X–M.

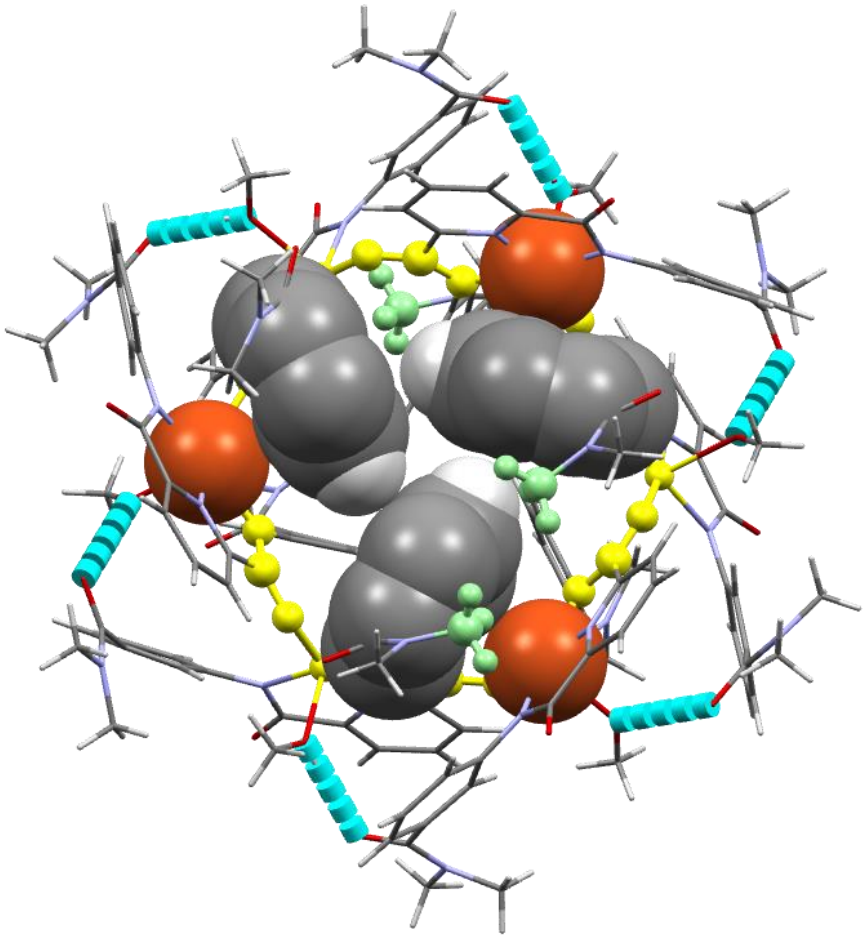


Figure 5.22: The intramolecular interactions stabilizing the CuL5 metallocycle hexamer. The repeating coordination pattern has been shown in yellow while H-bonds are shown as dashed cyan cylinders. The Cu(II) triad that lies above the mean plane of the macrocycle has been shown as space-fill model with C–H···π and d···π interactions to aromatic rings of adjacent chelates shown. There are numerous disordered van der Waals interactions, one interaction has been shown at the green-highlighted methyl groups.

The tensional integrity of the CuL5 metallocycle has been highlighted in Figure 5.22 above. The strongest forces holding the cyclic structure together are the coordinating bonds that result in the pattern Cu(II)–N–C=O_{amide}–Cu(II). The short bond lengths Cu–$O_{carbonyl}$ *ca.* 1.93 Å indicate that negative charge from the amidate nitrogen has been delocalized into the carbonyl oxygen making it a better σ-donor and resulting in the short bond length of this bridging molecular moiety. Additionally, six intramolecular H-bonds exist between an axially coordinated methanol and the dimethylamide carbonyl of a neighbouring chelate monomer. There are numerous disordered van der Waals interactions that exist between hydrophobic groups in the metallocycle, notably between methyl groups of the substituted aryl rings where the bond distance is 2.7 Å. This has been highlighted in Figure 5.22 where the interaction exists above and below the mean plane of the metallocycle and is related by inversion through the centroid of

the supramolecular assembly. Finally, significant C–H···π and d···π interactions are observed to stabilize the cyclic assembly. These interactions have been shown in Figure 5.22 where the bonding exists between the Cu(II) triad that lies above the mean plane of the metallocycle and aromatic rings of neighbouring chelate monomers. These C–H···π and d···π interactions are inverted about the centroid of the hexamer and exist between the Cu(II) triad that lies below the mean plane. The aromatic rings that serve as d···π acceptors on one face of the aromatic ring, function as C–H···π acceptors on the reflected face. This self-recognition and intramolecular stabilisation are shown in Figure 5.23 where the C–H···π and d···π bond lengths and angles have been shown. Notably, all atom-to-plane distances are less than 3 Å which indicates that although the bonding may be weak, it is significant. Also noteworthy is the fact that d···π bond angles vary between about 50° and 60°, suggesting that atomic $3d_{xz}$ and $3d_{yz}$ orbitals are principally involved with d-π overlap.

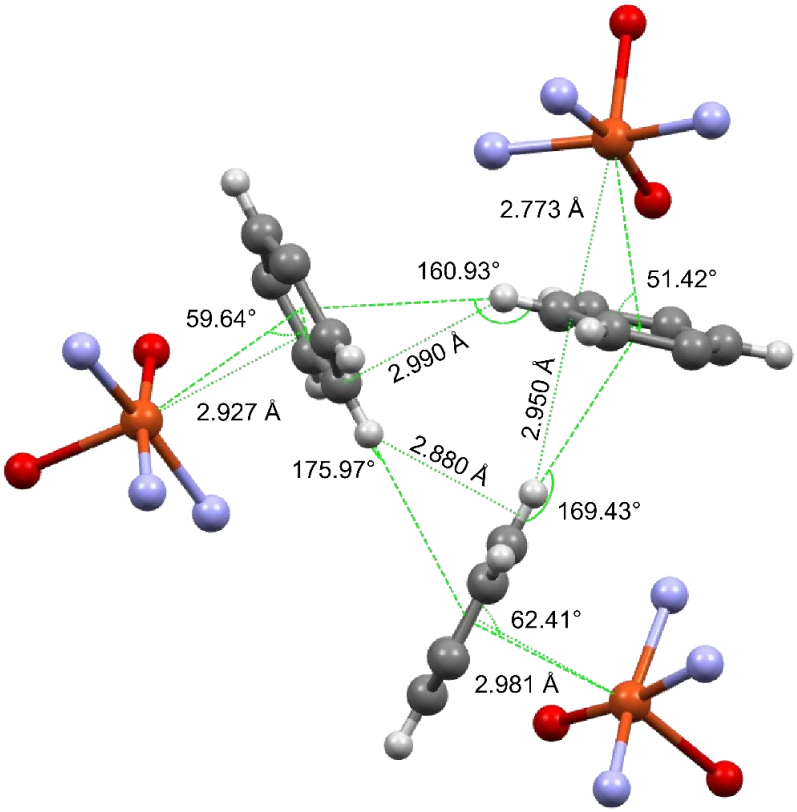


Figure 5.23: The bond lengths and angles of the intramolecular C–H···π and d···π interactions that stabilize the CuL5 cyclic assembly.

Finally, because the aromatic rings participate in C–H···π and d···π interactions, they are unavailable for π···π stacking and no such interaction is observed to stabilize the metallocycle. Hence, numerous forces stabilize the supramolecular assembly through intramolecular interactions. There are significantly fewer intermolecular interactions that facilitate packing of the cyclic hexamers in the lattice. The intermolecular interactions between supermolecules are shown in Figure 5.24 as well as the voids that extend as infinite channels through the crystal lattice.

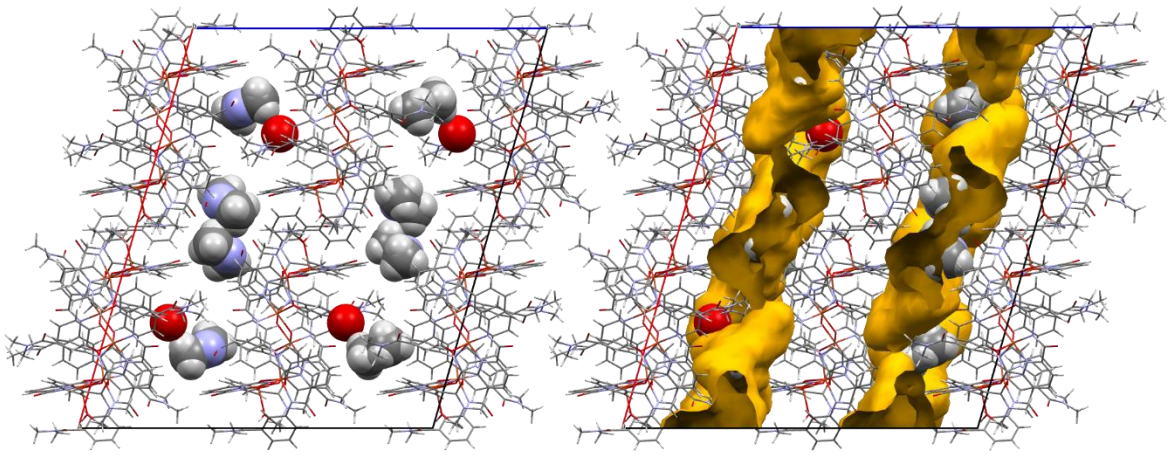


Figure 5.24: The unit cell of CuL5 as viewed down the crystallographic b-axis. The intermolecular forces that stabilize the packing of hexamers in the lattice are shown as space-fill models. The voids present in the crystal are also shown and these extend as infinite channels parallel to the crystallographic a-axis.

The intermolecular forces that facilitate packing of supermolecules in the lattice involve only van der Waals forces and C–H···O hydrogen bonds. These interactions exist between hexamers in the *ab* plane with C–H···O bonds at 2.540 Å and van der Waals H···H distance of 1.855 Å. There are short contacts that exist between hexamers in the *bc* plane which further stabilize packing of the supermolecule in the crystal lattice. The unit cell contains four metallocycles and has a volume of V = 17638.5 Å^3 of which 18.4 % (3243 Å^3) is void volume.

3.5 Cu(H_2L6) "kinetic"

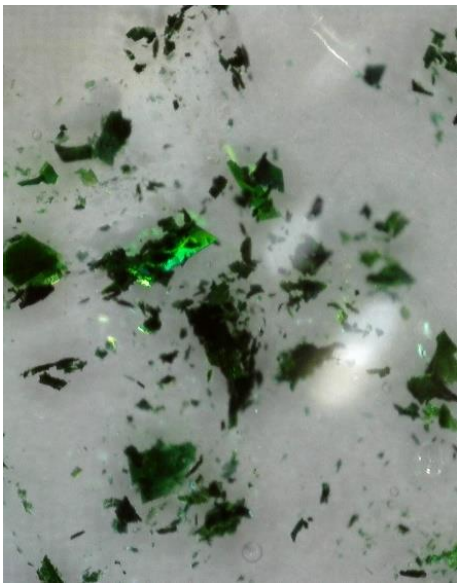


Figure 5.25: Crystals of Cu(H_2L6) grown over 6 weeks and viewed under the microscope.

A dark green, prism-like crystal of $C_{172}H_{202}Cu_6N_{30}O_{34}$ with approximate dimensions 0.364 mm x 0.438 mm x 0.750 mm was used and the X-ray intensity data were measured (λ = 0.71073 Å). $C_{172}H_{202}Cu_6N_{30}O_{34}$ (*M* = 3614.86 g/mol): monoclinic, space group $P2_1/c$ (no. 14), *a* = 19.4579(12) Å, *b* = 30.8216(17) Å, *c* = 18.4247(10) Å, *β* = 105.596(2)°, *V* = 10642.9(11) Å^3, *Z* = 2, *T* = 153.00 K, μ(MoKα) = 0.655 mm^{-1}, *Dcalc* = 1.128 g/cm^3, 1565432 reflections measured (3.422° ≤ 2Θ ≤ 52.898°), 21828 unique (R_{int} = 0.0846, R_{sigma} = 0.0182) which were used in all calculations. The final R_1 was 0.0789 (I > 2σ(I)) and wR_2 was 0.2110 (all data). A total of 5162 frames were collected. The total exposure time was 10.05 hours. The frames were integrated with the Bruker SAINT software package using a narrow-frame algorithm. The integration of the data using a monoclinic unit cell yielded a total of 816720 reflections to a maximum θ angle of 25.73° (0.82 Å resolution). The final cell constants are based upon the refinement of the XYZ-centroids of 9923 reflections above 20 σ(I) with 4.434° < 2θ < 51.33°. Data were corrected for absorption effects using the Multi-Scan method (SADABS). The ratio of minimum to maximum apparent transmission was 0.835.

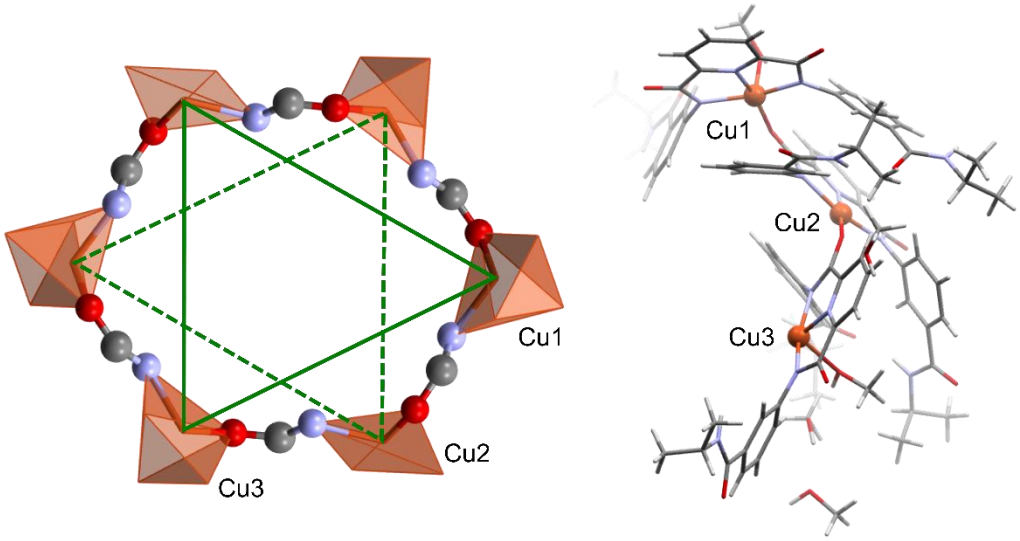


Figure 5.26: The coordination pattern that generates the 24-membered hexanuclear copper carboxamide metallocycle with S_2 symmetry. The metal centers are 5-coordinate square pyramidal or 4-coordinate square planar and are shown as polyhedrons. The mean plane for the hexamer lies in the plane of the six nitrogens that make up the cyclic pattern. There are three Cu(II) centers that lie in a plane above the mean plane (solid green) and three Cu(II) centers that lie in a plane below the mean plane (dashed green). Each Cu(II) triad has two neighboring metal centers square pyramidal with the third being square planar. Asymmetric unit shown on the right.

Cu(H_2L6) “kinetic” crystallized over 6 weeks in the monoclinic space group $P2_1/c$ with two copper metallocycles in the unit cell and the asymmetric unit described by three monomers of the hexamer. The hexanuclear copper macrocycle coordination is shown in Figure 5.26 and follows the bonding pattern Cu(II)–N–C=O_{amide}–Cu(II) which results in S_2 symmetry for the supermolecule. The mean plane of the metallocycle lies in the plane of the six nitrogens that make up the coordination pattern and three alternating Cu(II) centres lie in a plane above ,and below, the mean plane. The plane-to-plane distance between the Cu(II) triads is 1.16 Å and the metallocycle mean plane bisects this interplanar distance.

The inner coordination sphere for the Cu(II) centres adopt square pyramidal or square planar geometry and these bond lengths have been collated in Table 5.3. The tridentate ligand chelates Cu(II) through N_{pyr} and two N_{amide} while a fourth exogenous ligand coordinates to make up the square plane. The atomic $3d_{x^2-y^2}$ orbital lies in the square plane and overlaps with π* orbitals of the bridging carbonyl that facilitates metallocycle formation. This is evident in the bond lengths of the carbonyls that form part of the inner chelate ring. The amide carbonyl has an average C=O bond length of 1.241 ± 0.006 Å when it is not acting as a bridging ligand, however, when the C=O coordinates Cu(II) its bond length increases to an average of 1.264 ± 0.007 Å indicating that electron density from the paramagnetic $3d_{x^2-y^2}$ orbital has occupied σ* orbitals on the carbonyl.

The electron dense square plane repels ligands approaching on the z-axis of the Cartesian coordinate system placed on the metal centre, that is, ligands approaching the $3d_{z^2}$ orbital are repelled due to high electron density in the xy plane. Additionally, the $3d_{z^2}$ orbital is fully occupied resulting in interelectronic repulsion between the metal-based orbital and the incoming lone pair of the solvent molecule. This is reflected in the long bond lengths of the axially coordinated solvent molecules *ca.* 2.29 Å and the fact that the asymmetric unit contains three Cu(II) centers where two are 5-coordinate and one is 4-coordinate. The average bond lengths for the square pyramidal metal centers are Cu–N_{pyr} (1.920 Å), Cu–N_{amide} (2.021 Å), Cu–$N_{amide\text{-}Cu}$ (2.054 Å), and Cu–$O_{carbonyl}$ (1.947 Å). However, bond lengths for the square planar metal centre are Cu–N_{pyr} (1.911 Å), Cu–N_{amide} (1.992 Å), Cu–$N_{amide\text{-}Cu}$ (2.013 Å), and Cu–$O_{carbonyl}$ (1.899 Å). Hence, bond lengths in the square plane increase when an axially coordinated ligand overlaps with the $3d_{z^2}$ orbital, because interelectronic repulsion is increased at the metal center. Furthermore, the coordinated methanol solvent has a short O–H bond length of 0.883 Å, which indicates that electron density on the donor oxygen atom is being repelled by the $3d_{z^2}$ orbital such that internuclear repulsion is diminished in the O–H bond.

Table 5.3: The bond lengths for the inner coordination sphere of Cu(H_2L6) as well as carbonyl bonds that make up the tridentate chelate ring system. The asymmetric unit of the crystal contains three Cu(II) centers, and the bond lengths are presented as the average with the error reported as the standard deviation of three independent bond length measurements or two independent measurements for bonds to axially coordinated solvent.

Bond	Length (Å)
$Cu–N_{pyr}$	1.917 ± 0.005
$Cu–N_{amide}$	2.011 ± 0.02
$Cu–N_{amide\text{-}Cu}$	2.040 ± 0.02
$Cu–O_{carbonyl}$	1.931 ± 0.03
$Cu–O_{solvent}$	2.296 ± 0.05
C=O	1.241 ± 0.006
$C=O_{Cu}$	1.264 ± 0.007

The Cu(H_2L6) hexanuclear copper carboxamide macrocyclic assembly is stabilized by intramolecular forces acting in concert to enable the tensegrity observed for the super structure. These forces are dominated by coordinating bonds that repeat to form the cyclic assembly, with additional stabilization from H-bonds, van der Waals forces, C–H···π and d···π interactions. These intramolecular interactions have been shown in Figure 5.27. The coordinating bonds are especially strong with $Cu–O_{carbonyl}$ bond lengths averaging 1.931 ± 0.03 Å. This is an indication of the synergistic interplay between σ-donation, improved by the delocalization of the negative amidate charge onto the carbonyl oxygen, and π-backdonation from the atomic $3d_{xy}$ orbital into the π* molecular orbital located on the carbonyl. Additionally, there are six intramolecular H-bonds stabilizing the hexamer where the isopropyl amide of one monomer acts as a H-bond donor while the adjacent monomer accepts the H-bond through the carbonyl of the isopropyl amide moiety. Three intramolecular H-bonds exist in a plane above the plane of the Cu(II) triad and the mean plane of the metallocycle, while three intramolecular H-bonds exist in a plane below the Cu(II) triad plane and the mean plane.

Finally, additional intramolecular stabilization of the assembly is afforded by significant C–H···π and d···π interactions. These have been shown as space-fill models in Figure 5.27 while the bond lengths and angles for the C–H···π and d···π interactions have been presented in Figure 5.28. These interactions that exist between metal centres of the Cu(II) triad above the mean plane are inverted about the centroid of the metallocycle and exist between metal centres of the Cu(II) triad below the mean plane. The most significant d···π interaction is observed between the 4-coordinate square planar copper centre and the aromatic ring of the adjacent Cu(H_2L6)

monomer, with an atom-to-plane distance of 2.814 Å and an ∠C–X–M of 61.64°. The lack of an axially coordinated ligand allows the aromatic π-system to approach closer to the square planar metal centre because interelectronic repulsion is diminished when a fifth ligand is absent.

While aromatic rings may participate in dual C–H···π and d···π interactions, the former is absent between isopropyl benzamide rings when the benzamide moiety participates in intramolecular H-bonding. The C–H···π interaction is notably absent in Figure 5.27 and Figure 5.28 where each aromatic ring of the triad participates in d···π bonding but only two C–H···π interactions are observed. The third C–H···π bond does not form because intramolecular H-bonds pull the benzamide rings in opposite directions and the potential energy of the cyclic assembly is lowered by favourable H-bond formation more than by C–H···π bond formation.

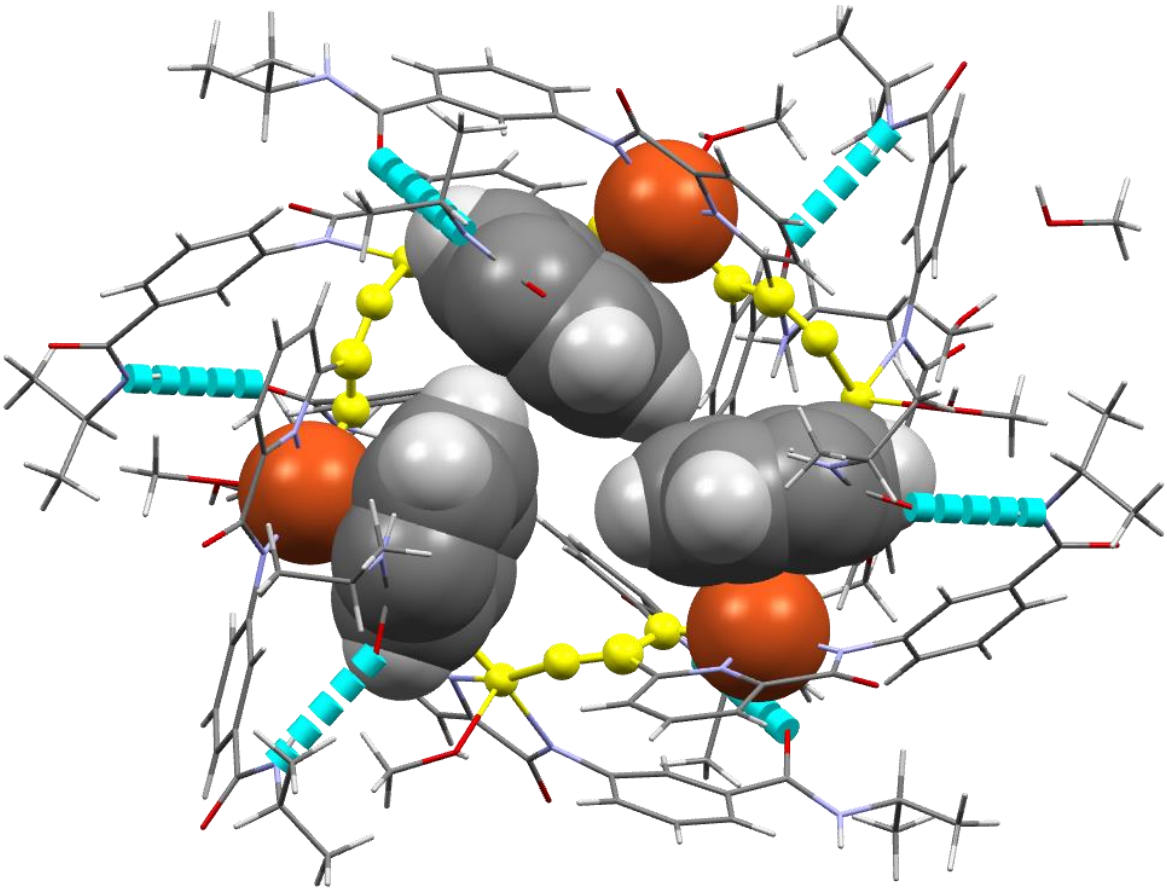


Figure 5.27: The intramolecular interactions stabilizing the Cu(H_2L6) "kinetic" metallocycle hexamer. The repeating coordination pattern has been shown in yellow while H-bonds are shown as dashed cyan cylinders. The Cu(II) triad that lies above the mean plane of the macrocycle has been shown as space-fill model with C–H···π and d···π interactions to aromatic rings of adjacent chelates shown.

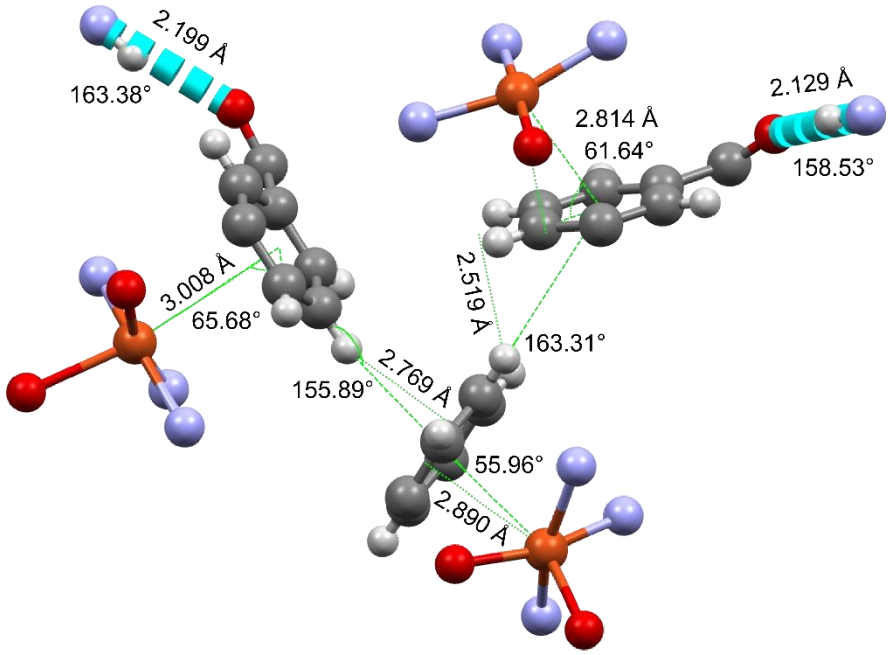


Figure 5.28: The bond lengths and angles of the intramolecular C–H···π and d···π interactions that stabilize the Cu(H_2L6) cyclic assembly. The H-bonds that prevent C–H···π bond formation have been shown as cyan cylinders with the H-bond bond length and angle.

Therefore, a synergistic interplay of various intramolecular forces stabilizes the cyclic supermolecule and permit the tensional integrity observed for the assembly. There are notably fewer intermolecular interactions that facilitate packing of the supermolecules in the lattice, and hence, there is significant void volume in the crystal. The intermolecular interactions between cyclic hexamers are shown in Figure 5.29 as well as the voids that extend as infinite channels through the crystal lattice. The hexamers pack in the lattice along the *ac* plane through an intermolecular H-bonding network between three molecules of methanol. The H-bond network extends from an axially coordinated methanol, through two co-crystalized methanol molecules, and the carbonyl of an isopropyl benzamide of a neighbouring supermolecule. The hexamers also pack along the *ac* plane through van der Waals interactions between isopropyl groups of adjacent macrocycles. These van der Waal forces also facilitate packing in the *ab* plane along with short contacts between neighbouring hexamers. The unit cell for Cu(H_2L6) "kinetic" contains two supermolecules and has a volume V = 10642.9 Å^3 of which 20.1% (2143 Å^3) is void volume.

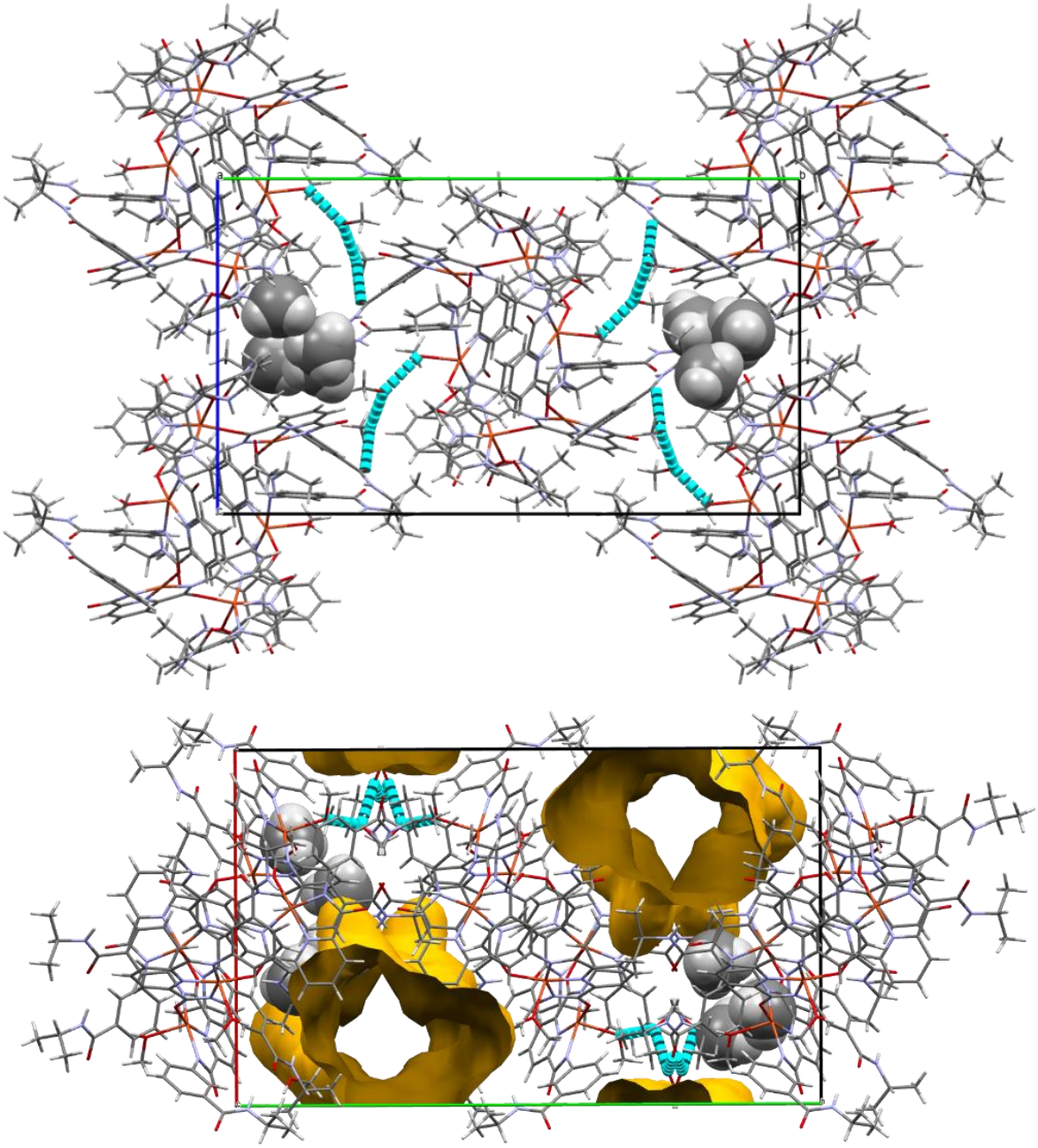


Figure 5.29: (Top) The unit cell of Cu(H_2L6) as viewed down the crystallographic a-axis. The intermolecular forces that stabilize the packing of hexamers in the lattice are shown as space-fill models for van der Waals forces and cyan cylinders for the H-bonding network. (Bottom) The voids as viewed down the crystallographic c-axis extend as infinite channels through the lattice.

3.6 Cu(H_2L6) "thermodynamic"

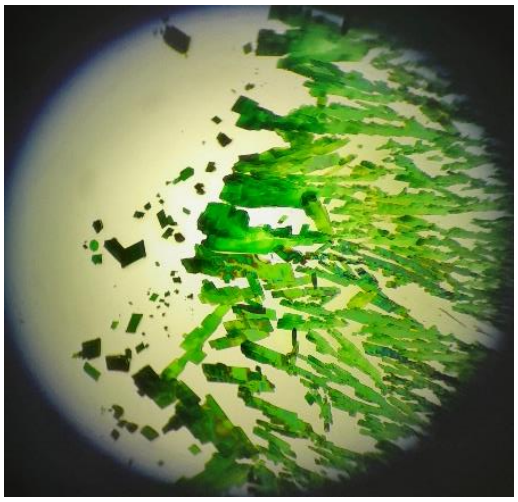


Figure 5.30: Crystals of Cu(H_2L6) grown over 6 months and viewed under the microscope.

A clear green cubic plate-like crystal of $C_{163.27}H_{169.64}Cu_6N_{30}O_{26.55}$ with dimensions 0.060 mm x 0.095 mm x 0.174 mm was used and the X-ray intensity data were measured (λ = 0.71073 Å). $C_{163.27}H_{169.64}Cu_6N_{30}O_{26.55}$ (*M* = 3358.20 g/mol): triclinic, space group *P*-1 (no. 2), *a* = 16.5532(8) Å, *b* = 17.7078(8) Å, *c* = 17.8111(8) Å, *α* = 61.632(2)°, *β* = 74.172(2)°, *γ* = 83.485(2)°, *V* = 4418.9(4) Å^3, *Z* = 1, *T* = 173.00 K, μ(MoKα) = 0.781 mm^{-1}, *Dcalc* = 1.262 g/cm^3, 227279 reflections measured (3.622° ≤ 2Θ ≤ 53.448°), 18564 unique (R_{int} = 0.1730, R_{sigma} = 0.0732) which were used in all calculations. The final R_1 was 0.0661 (I > 2σ(I)) and wR_2 was 0.2152 (all data). The total exposure time was 3.66 hours. The frames were integrated with the Bruker SAINT software package using a narrow-frame algorithm. The integration of the data using a triclinic unit cell yielded a total of 290456 reflections to a maximum θ angle of 26.72° (0.79 Å resolution). The final cell constants are based upon the refinement of the XYZ-centroids of 9947 reflections above 20 σ(I) with 4.535° < 2θ < 47.68°. Data were corrected for absorption effects using the Multi-Scan method (SADABS). The ratio of minimum to maximum apparent transmission was 0.855.

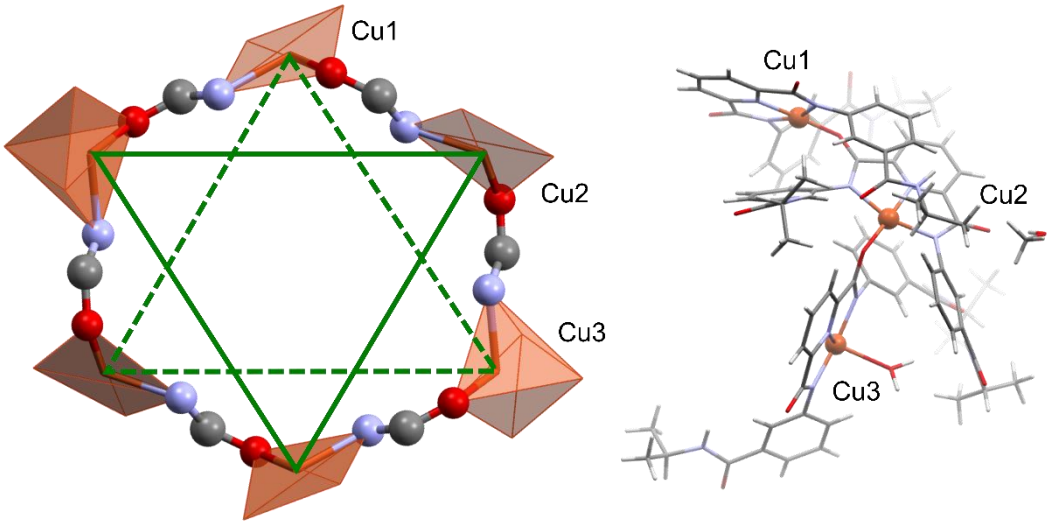


Figure 5.31: The coordination pattern that generates the 24-membered hexanuclear copper carboxamide metallocycle with S_2 symmetry. The metal centers are 5-coordinate square pyramidal or 4-coordinate square planar and are shown as polyhedrons. The mean plane for the hexamer lies in the plane of the six nitrogens that make up the cyclic pattern. There are three Cu(II) centers that lie in a plane above the mean plane (solid green) and three Cu(II) centers that lie in a plane below the mean plane (dashed green). Each Cu(II) triad has two neighboring metal centers square planar with the third being square pyramidal. Asymmetric unit shown on the right.

Cu(H_2L6) “thermodynamic” crystallized over 6 months in the triclinic space group *P*-1 with a single supermolecule in the unit cell and the asymmetric unit described by three monomers of the hexamer. The hexanuclear copper macrocycle coordination is shown in Figure 5.31 and follows the bonding pattern Cu(II)–N–C=O_{amide}–Cu(II) which results in S_2 symmetry for the supermolecule. The mean plane of the metallocycle lies in the plane of the six nitrogens that make up the coordination pattern and three alternating Cu(II) centres lie in a plane above, and below, the mean plane. The plane-to-plane distance between the Cu(II) triads is 1.21 Å and the metallocycle mean plane bisects this interplanar distance.

The inner coordination sphere for the Cu(II) ion adopts either 4-coordinate square planar or 5-coordinate square pyramidal geometry. The bond lengths for the inner coordination sphere for each geometry are collated in Table 5.4. The bond lengths between geometries are mostly the same apart from the Cu–$O_{carbonyl}$ bond, which is 1.934 Å for the 5-coordinate complex and 1.917 Å for the 4-coordinate complex. This is because the diminished interelectronic repulsion of the square planar complex allows the C=O of a neighbouring chelate to approach closer to the metal centre. Hence, when Cu(II) centres adopt square planar geometry, the metallocycle tightens as the bonds that make up the coordination pattern Cu(II)–N–C=O_{amide}–Cu(II) shorten. The C=O of an adjacent chelate approaches the Cu(II) centre to make up the square plane and hence there is overlap between the atomic $3d_{x^2-y^2}$ orbital and the σ* molecular orbital of the bridging C=O. This is evident as the C=O bond length increases from 1.241 Å to 1.270 Å when acting as a bridging group coordinated to copper, delocalizing the paramagnetic electron density, and lowering the energy of the reactive $3d_{x^2-y^2}$ orbital.

The hexanuclear assembly is stabilized by various intramolecular interactions that facilitate metallocycle formation. These intramolecular interactions have been shown in Figure 5.32 and it is the coordinating dative covalent bonds which dominate to stabilize the cyclic superstructure. The Cu–$O_{carbonyl}$ bond lengths average 1.923 ± 0.01 Å and reflect the enhanced σ-donor ability of the C=O as the amidate negative charge is delocalized into the carbonyl bond. Additional stabilization of the cyclic assembly is afforded by intramolecular H-bonding, C–H···π and d···π interactions, the latter two’s bond lengths and angles have been presented in Figure 5.33. Notably, all atom-to-plane distances are 2.7 Å or less for d···π interactions indicating significant overlap between atomic $3d_{z^2}$, $3d_{xz}$, and $3d_{yz}$ orbitals and the aromatic π-system. The d···π angles are *ca.* 56° suggesting that atomic $3d_{xz}$ and $3d_{yz}$ orbitals are principally involved with d···π overlap. The C–H···π atom-to-plane distances are all less than 2.9 Å indicating that the stabilizing interaction is significant.

Table 5.4: The bond lengths for the inner coordination sphere of Cu(H_2L6) "thermodynamic" as well as carbonyl bonds that make up the tridentate chelate ring. The asymmetric unit of the crystal contains three Cu(II) centers, and the bond lengths are reported for the square planar geometry as the average and standard variation of two independent bond measurements. There is only one Cu(II) center with square pyramidal geometry and its inner sphere bond lengths have also been presented.

Bond	Pyramidal Length (Å)	Planar Length (Å)
Cu–N_{pyr}	1.907	1.902 ± 0.005
Cu–N_{amide}	1.976	1.977 ± 0.001
Cu–$N_{amide\text{-}Cu}$	2.021	2.019 ± 0.02
Cu–$O_{carbonyl}$	1.934	1.917 ± 0.01
Cu–$O_{solvent}$	2.372	Not Applicable
C=O	1.241	1.235 ± 0.008
C=O_{Cu}	1.270	1.269 ± 0.003

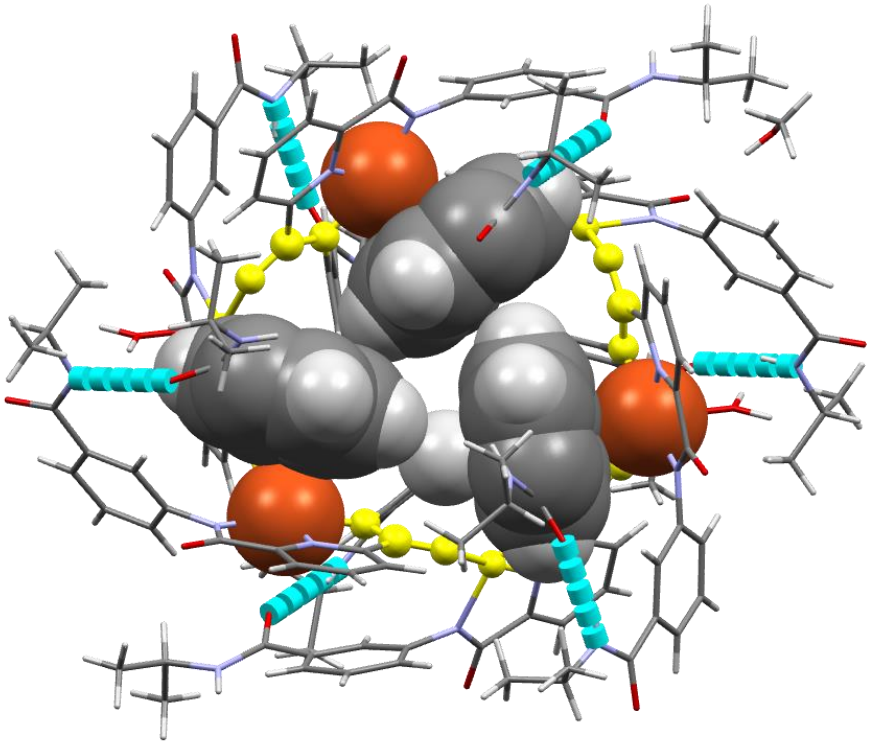


Figure 5.32: The intramolecular interactions stabilizing the Cu(H_2L6) "thermodynamic" metallocycle hexamer. The repeating coordination pattern has been shown in yellow while H-bonds are shown as dashed cyan cylinders. The Cu(II) triad that lies above the mean plane of the macrocycle has been shown as space-fill model with C–H···π and d···π interactions to aromatic rings of adjacent chelates shown.

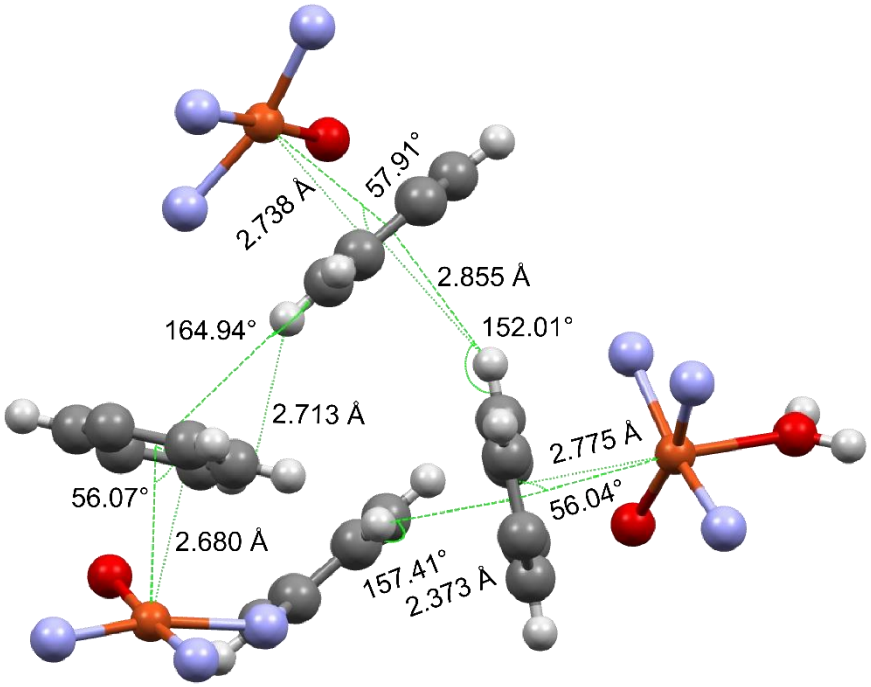


Figure 5.33: The bond lengths and angles of the intramolecular C–H···π and d···π interactions that stabilize the Cu(H_2L6) "thermodynamic" cyclic assembly.

Finally, six intramolecular H-bonds exists between isopropyl benzamide groups, with three alternating H-bonds above the mean plane of the metallocycle, and three below, which are related by inversion through the centroid of the cyclic assembly. In addition to coordinating forces, H-bonding, C–H···π and d···π interactions, there are van der Waals forces which stabilise the supermolecule through intramolecular recognition.

The packing of the cyclic structure into the lattice is directed through intermolecular interactions between supermolecules in the crystal. These have been shown in Figure 5.34 and are dominated by short contacts between hexamers in the *ab*, *bc*, and *ac* planes. Additional van der Waals forces and C–H···O bonds facilitate packing in the *bc* plane while H-bonding exists in the *ac* plane between the co-crystallized methanol of one unit cell and the carbonyl of a hexamer in the adjacent unit cell. The packing of supermolecules is efficient for Cu(H_2L6) "thermodynamic" as the unit cell contains only one hexamer with a cell volume V = 4418.9 Å^3 of which 6.7% (294 Å^3) is void volume.

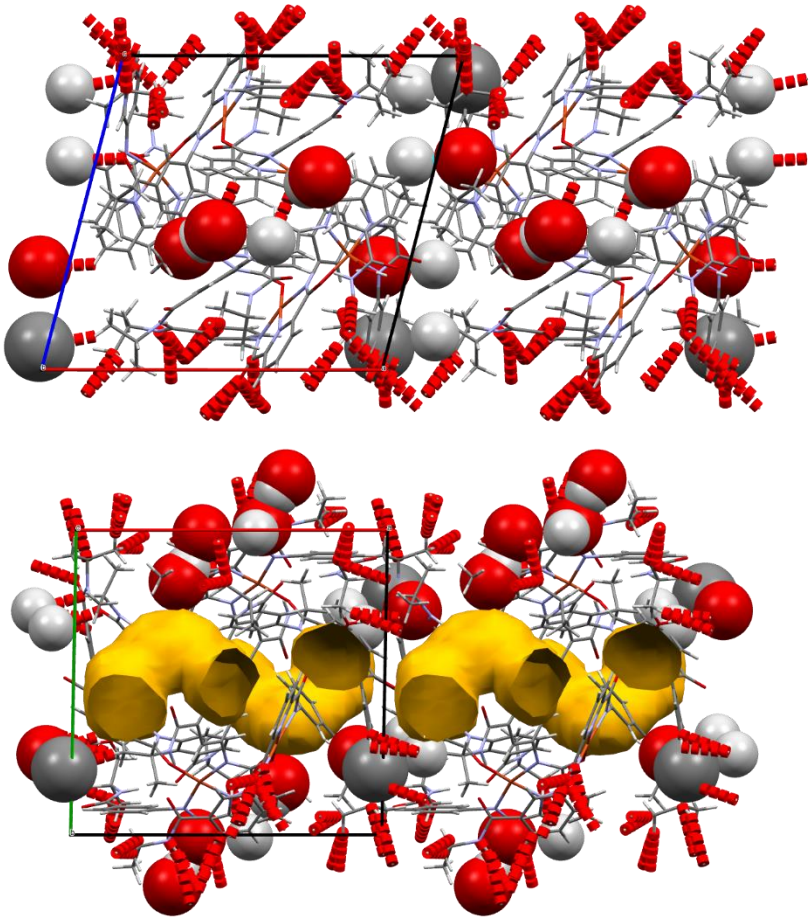


Figure 5.34: (Top) The unit cell of Cu(H_2L6) "thermodynamic" as viewed down the crystallographic b-axis. The short contacts between hexamers are shown as dashed red cylinders while C–H···O and van der Waals interactions between supermolecules in the *bc* plane have been shown as space-fill models. (Bottom) The unit cell viewed down the crystallographic c-axis shown with the voids that exist as doughnut-shaped pockets in the lattice. Also shown as space-fill models are the intermolecular interactions in the *ac* plane between the co-crystallized methanol of one unit cell H-bonded to the carbonyl of a chelate in the adjacent unit cell.

3.7 Cu(H_2L8) "kinetic"

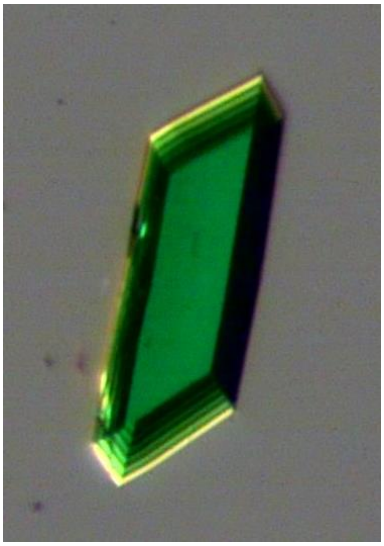


Figure 5.35: A single crystal of Cu(H_2L8) "kinetic" grown from an ethanol/methanol mixture.

A clear intense green, block-like crystal of $C_{180}H_{212.94}Cu_6N_{30}O_{40}$ with approximate dimensions 0.056 mm x 0.102 mm x 0.350 mm was used and the X-ray intensity data were measured (λ = 0.71073 Å). $C_{180}H_{212.94}Cu_6N_{30}O_{40}$ (*M* = 3817.97 g/mol): triclinic, space group *P*-1 (no. 2), *a* = 16.1679(16) Å, *b* = 18.1100(14) Å, *c* = 18.7602(17) Å, *α* = 77.450(3)°, *β* = 78.909(4)°, *γ* = 71.509(4)°, *V* = 5039.5(8) Å^3, *Z* = 1, *T* = 150.00 K, μ(MoKα) = 0.698 mm^{-1}, *Dcalc* = 1.258 g/cm^3, 165694 reflections measured (3.554° ≤ 2Θ ≤ 51.998°), 19808 unique (R_{int} = 0.0809, R_{sigma} = 0.0470) which were used in all calculations. The final R_1 was 0.1092 (I > 2σ(I)) and wR_2 was 0.2834 (all data). A total of 1500 frames were collected. The total exposure time was 8.15 hours. The frames were integrated with the Bruker SAINT software package using a narrow-frame algorithm. The integration of the data using a triclinic unit cell yielded a total of 334769 reflections to a maximum θ angle of 28.76° (0.74 Å resolution). The final cell constants are based upon the refinement of the XYZ-centroids of 9933 reflections above 20 σ(I) with 4.488° < 2θ < 55.68°. Data were corrected for absorption effects using the Multi-Scan method (SADABS). The ratio of minimum to maximum apparent transmission was 0.782.

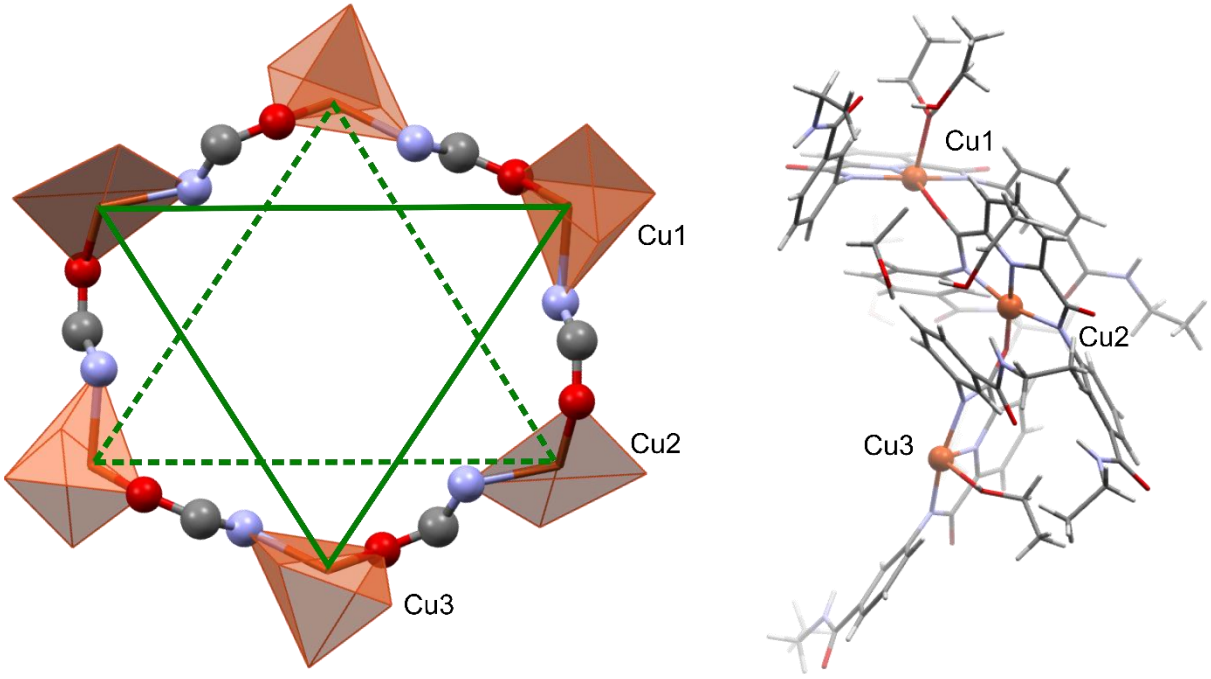


Figure 5.36: The coordination pattern for Cu(H_2L8) "kinetic" that generates the cyclic hexamer. The asymmetric unit is shown on the right.

Cu(H_2L8) “kinetic” crystalized over 6 weeks in the triclinic space group *P*-1 with one metallocycle in the unit cell and the asymmetric unit described by three monomers of the hexamer. The hexanuclear copper macrocycle coordination is shown in Figure 5.36 and follows the bonding pattern Cu(II)–N–C=O_{amide}–Cu(II) which results in S_2 symmetry for the supermolecule. The metal centers are 5-coordinate square pyramidal or 4-coordinate square planar and are shown as polyhedrons. The mean plane for the hexamer lies in the plane of the six nitrogens that make up the cyclic pattern. There are three Cu(II) centers that lie in a plane above the mean plane (solid green) and three Cu(II) centers that lie in a plane below the mean plane (dashed green). The Cu(II) triads are related to each other by inversion through the centroid of the metallocycle and the plane-to-plane distance between triads is 1.17 Å.

The inner coordination sphere for the Cu(II) ion adopts either 4-coordinate square planar or 5-coordinate square pyramidal geometry with ethanol axial ligands. The bond lengths for the inner coordination sphere for each geometry are collated in Table 5.5. The bond lengths for the anionic N_{amide} donors are significantly shorter for the square planar metal centre and this reflects the diminished interelectronic repulsion in the absence of an axially coordinated ligand. The electron dense square plane repels ligands approaching the axial position as the Cu–$O_{solvent}$ bonds are the longest at *ca.* 2.26 Å. The Cu–$O_{carbonyl}$ bond for the square planar monomer is considerably shorter than the square pyramidal monomers at 1.904 Å, and this is because the C=O can approach closer to the metal centre when an axially coordinated ligand is absent and repulsive forces lessened. The Cu–$O_{carbonyl}$ bond is instrumental for metallocycle organization and is formed by a synergistic interplay between σ-donation and π-backdonation. The σ-donor ability of the C=O is improved by delocalization of the amidate negative charge into the carbonyl, and π-backdonation from the atomic $3d_{xy}$ orbital into π* molecular orbitals on the carbonyl is evident as the C=O bond increases from 1.249 Å to 1.277 Å when coordinated to copper.

While the Cu–$O_{carbonyl}$ bond is the dominant intramolecular stabilising force for the metallocycle, additional interactions impart the tensional integrity observed for the supermolecule. The intramolecular forces stabilising the Cu(H_2L8) “kinetic” cyclic assembly have been presented in Figure 5.37. These include intramolecular H-bonding between ethylamide groups on adjacent chelates, where three H-bonds exist above and below the mean plane of the metallocycle and are related by inversion through the centroid of the cyclic assembly. There are significant C–H···π and d···π interactions which have been presented in Figure 5.38 with the relevant bond lengths and angles. A notable d···π interaction is observed between the square planar metal

Table 5.5: The inner coordination sphere bond lengths for Cu(H_2L8) "kinetic" are reported as the average and standard deviation for two bond measurements at the square pyramidal metal centers. The bond lengths for the square planar chelate monomer has been reported with the error of the X-ray measurement.

Bond	Pyramidal Length (Å)	Planar Length (Å)
$Cu–N_{pyr}$	1.886 ± 0.02	1.903(6)
$Cu–N_{amide}$	2.026 ± 0.009	1.992(6)
$Cu–N_{amide\text{-}Cu}$	2.062 ± 0.005	2.028(5)
$Cu–O_{carbonyl}$	1.943 ± 0.03	1.904(4)
$Cu–O_{solvent}$	2.260 ± 0.02	Not Applicable
C=O	1.249 ± 0.008	1.244(9)
$C=O_{Cu}$	1.277 ± 0.01	1.260(7)

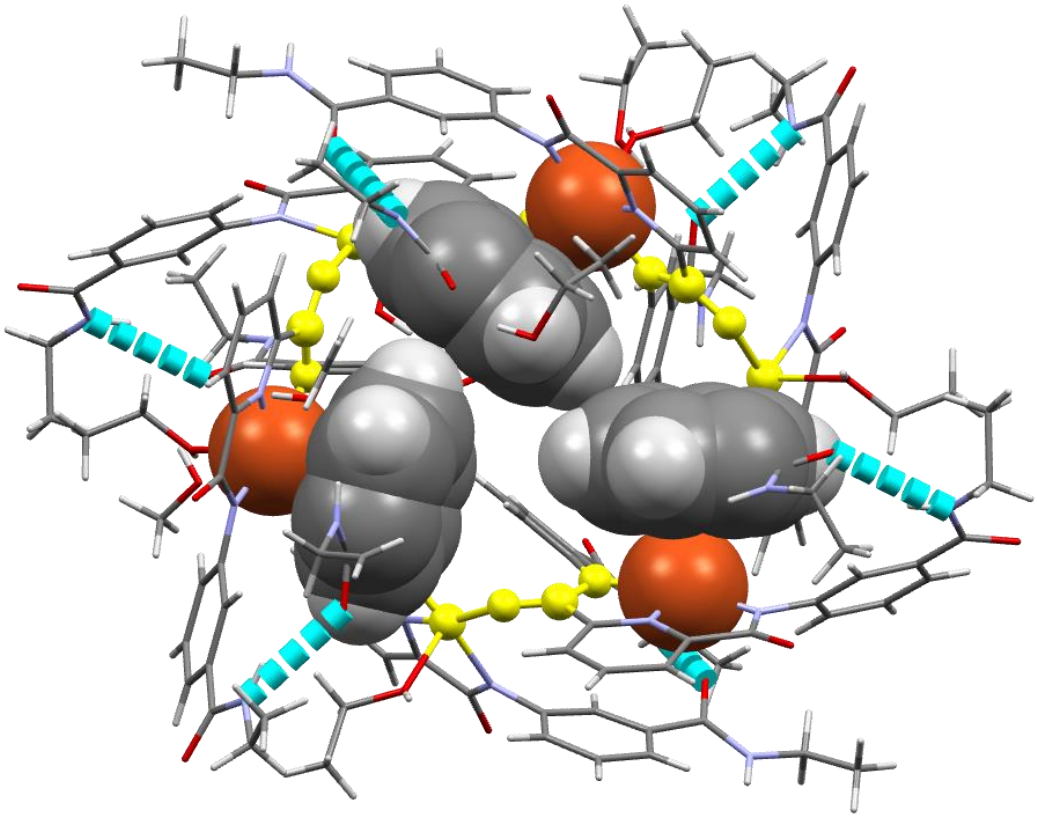


Figure 5.37: The intramolecular interactions imparting the tensegrity observed for the Cu(H_2L8) "kinetic" supermolecule. The cyclic coordination pattern has been shown in yellow while intramolecular H-bonds between ethylamide groups are shown as cyan cylinders. The C–H···π and d···π interactions have been shown as space-fill models.

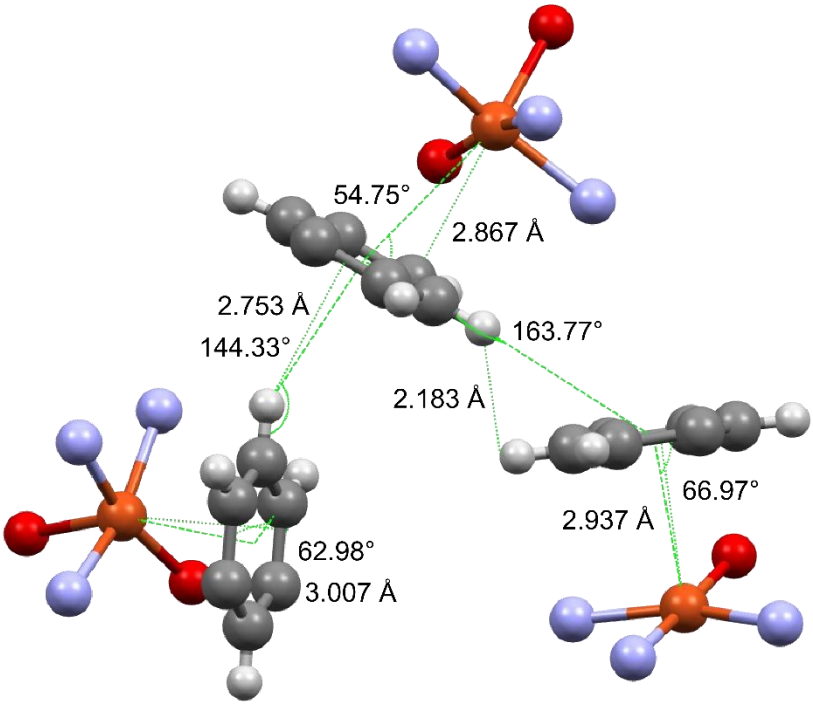


Figure 5.38: The C–H···π and d···π interactions observed for Cu(H_2L8) "kinetic" with the relevant bond lengths and angles.

centre and the aromatic ring with a ∠C–X–M angle of 66.97°. This angle is closest to 90° because in the absence of an axially coordinated ligand, interelectronic repulsion is reduced such that the π-system may approach closer to the metal centre and overlap with atomic $3d_z^2$, $3d_{xz}$ and $3d_{yz}$ orbitals.

The intermolecular forces that facilitate packing of the supermolecules in the lattice have been presented in Figure 5.39. While the ethylamide groups participate in intramolecular H-bonding, the ethylamide group functioning as the H-bond acceptor is still available to act as a H-bond donor in intermolecular interactions. These ethylamide groups H-bond to co-crystalized ethanol in neighbouring unit cells and enable packing of the supermolecules along the crystallographic *ab* plane. There is also H-bonding between amides and carbonyls of adjacent hexamers that pack the supermolecules in the *ac* plane. The crystal packing along the *bc* plane is directed by van der Waals forces between ethyl chains on neighbouring hexamers. Finally, the voids present in the lattice have been presented in Figure 5.40 and occupy a volume of 479 $Å^3$ which is 9.5% of the unit cell volume.

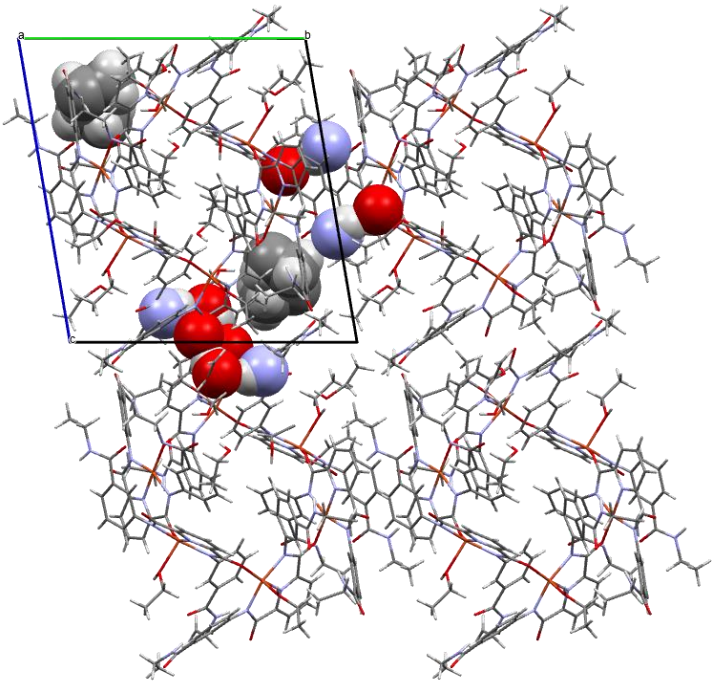


Figure 5.39: The unit cell of Cu(H_2L8) "kinetic" as viewed down the crystallographic a-axis. The intermolecular forces that facilitate packing of the hexamers have been shown as space-fill models and comprise of H-bonding and van der Waals forces.

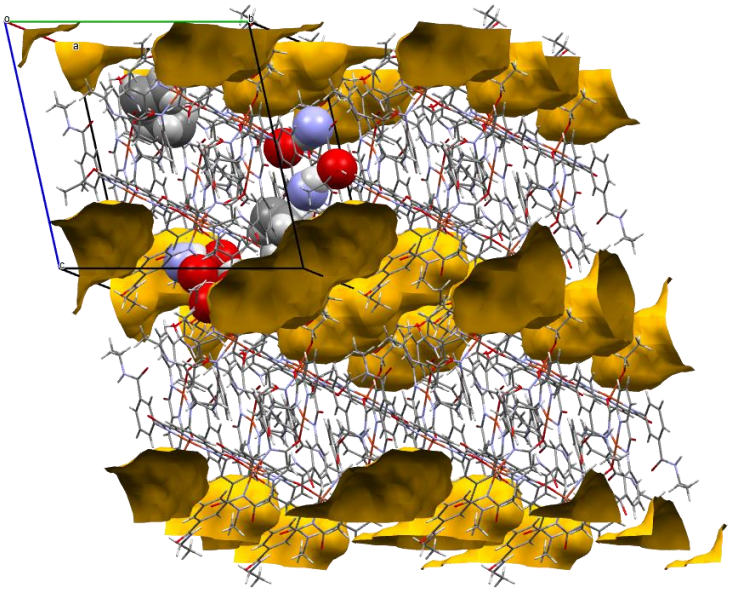


Figure 5.40: The voids present in the lattice of Cu(H_2L8) "kinetic" occupy the corners of the triclinic unit cell.

3.8 Cu(H_2L8) "thermodynamic"

A green needle of $C_{158}H_{250}Cu_6N_{30}O_{72}$ with approximate dimensions 0.059 mm x 0.064 mm x 0.222 mm was used and the X-ray intensity data were measured (λ = 0.71073 Å). $C_{158}H_{250}Cu_6N_{30}O_{72}$ (*M* = 4103.11 g/mol): monoclinic, space group $P2_1/c$ (no. 14), *a* = 18.5376(16) Å, *b* = 31.145(2) Å, *c* = 17.8471(15) Å, *β* = 105.794(2)°, *V* = 9914.9(14) Å^3, *Z* = 2, *T* = 173.0 K, μ(MoKα) = 0.726 mm^{-1}, *Dcalc* = 1.374 g/cm^3, 34499 reflections measured (3.098° ≤ 2Θ ≤ 49.998°), 17447 unique (R_{int} = 0.0610, R_{sigma} = 0.0958) which were used in all calculations. The final R_1 was 0.1066 (I > 2σ(I)) and wR_2 was 0.2485 (all data). A total of 1890 frames were collected. The total exposure time was 19.23 hours. The frames were integrated with the Bruker SAINT software package using a narrow-frame algorithm. The integration of the data using a monoclinic unit cell yielded a total of 705379 reflections to a maximum θ angle of 25.45° (0.83 Å resolution). The final cell constants are based upon the refinement of the XYZ-centroids of 9724 reflections above 20 σ(I) with 4.539° < 2θ < 40.09°. Data were corrected for absorption effects using the Multi-Scan method (TWINABS). The ratio of minimum to maximum apparent transmission was 0.268.

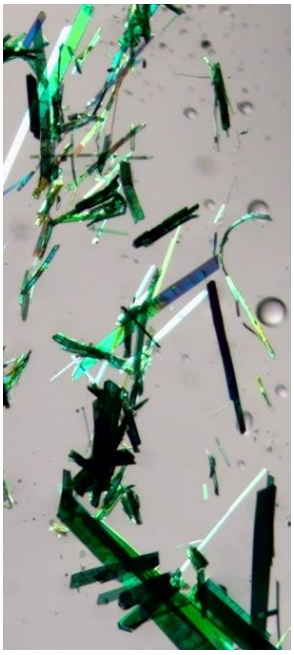


Figure 5.41: Crystals of Cu(H_2L8) grown from methanol overnight and stored for 6 months before data collection.

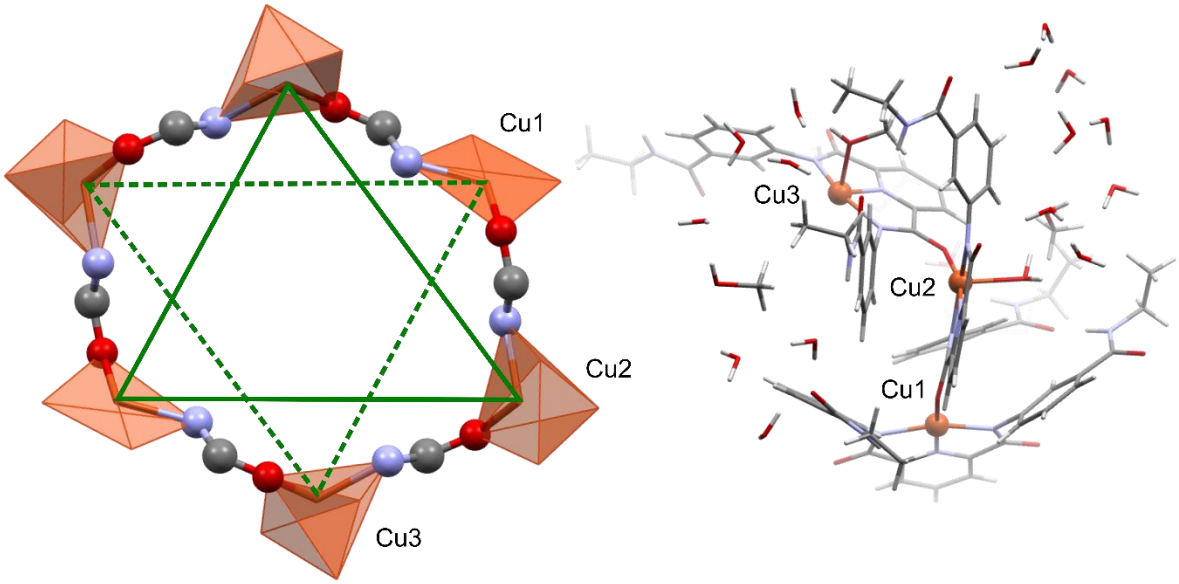


Figure 5.42: The coordination pattern for Cu(H_2L8) "thermodynamic" that generates the cyclic hexamer. The asymmetric unit is shown on the right with co-crystalized solvent.

Cu(H_2L8) “thermodynamic” crystalized overnight and was stored in the mother liquor for 6 months before data collection. The compound crystalized in the monoclinic space group $P2_1/c$ with two metallocycles in the unit cell and the asymmetric unit described by three monomers of the hexamer. The asymmetric unit also contains 19 co-crystalized water molecules and three methanol molecules. The hexanuclear copper macrocycle coordination is shown in Figure 5.42 and follows the bonding pattern Cu(II)–N–C=O_{amide}–Cu(II) which results in S_2 symmetry for the supermolecule. The metal centers are 5-coordinate square pyramidal with axially coordinated methanol or 4-coordinate square planar and are shown as polyhedrons. The mean plane for the hexamer lies in the plane of the six nitrogens that make up the cyclic pattern. There are three Cu(II) centers that lie in a plane above the mean plane (solid green) and three Cu(II) centers that lie in a plane below the mean plane (dashed green). The Cu(II) triads are related to each other by inversion through the centroid of the metallocycle and the plane-to-plane distance between triads is 1.13 Å.

The inner coordination sphere bond lengths for Cu(H_2L8) “thermodynamic” have been collated in Table 5.6 for each of the two metal geometries present in the asymmetric unit. All bonds that make up the square plane are shorter for the square planar monomer than the 5-coordinate complex and this reflects the diminished interelectronic repulsion at the metal centre in the absence of an axially coordinated ligand. The bond length for the carboxamide carbonyls is longer for the square pyramidal monomers and indicates increased delocalization of the amidate negative charge into the π-orbitals of the C=O. Hence, σ-donor ability of the C=O is increased for square pyramidal complexes as the axially coordinated ligand pushes electron density from the square plane into the molecular orbitals of the chelate. The cyclic bonding is constructed through Cu–$O_{carbonyl}$ bonds which display significant overlap of the atomic $3d_{x^2-y^2}$ orbital and σ* molecular orbitals of the C=O as the bond length of this bridging group increases significantly when coordinated to Cu(II). The intramolecular Cu–$O_{carbonyl}$ coordination is shown in Figure 5.43 with other significant interactions that stabilize the Cu(H_2L8) metallocycle. There is intramolecular C–H···π and d···π bonding (Figure 5.44) as well as H-bonding between ethylamide groups on adjacent monomers. Additional tensegrity is imparted to the cyclic assembly by a H-bonding network that exists between co-crystalized water molecules and the metallocycle. The network extends from an axially coordinated water molecule (which acts as a H-bond donor), through 8 co-crystalized water molecules and a single methanol, before the network H-bonds to carbonyls on adjacent chelates which serve as H-bond acceptors.

Table 5.6: The inner coordination sphere bond lengths for Cu(H_2L8) "thermodynamic". The square pyramidal bond lengths have been reported as the average and standard deviation of two independent measurements in the asymmetric unit. The square planar bond lengths have been reported with the error of the X-ray measurement.

Bond	Pyramidal Length (Å)	Planar Length (Å)
$Cu–N_{pyr}$	1.917 ± 0.003	1.902(5)
$Cu–N_{amide}$	2.010 ± 0.005	1.984(5)
$Cu–N_{amide\text{-}Cu}$	2.047 ± 0.002	2.023(5)
$Cu–O_{carbonyl}$	1.949 ± 0.01	1.912(4)
$Cu–O_{solvent}$	2.264 ± 0.05	Not Applicable
C=O	1.258 ± 0.004	1.241(8)
$C=O_{Cu}$	1.270 ± 0.004	1.266(7)

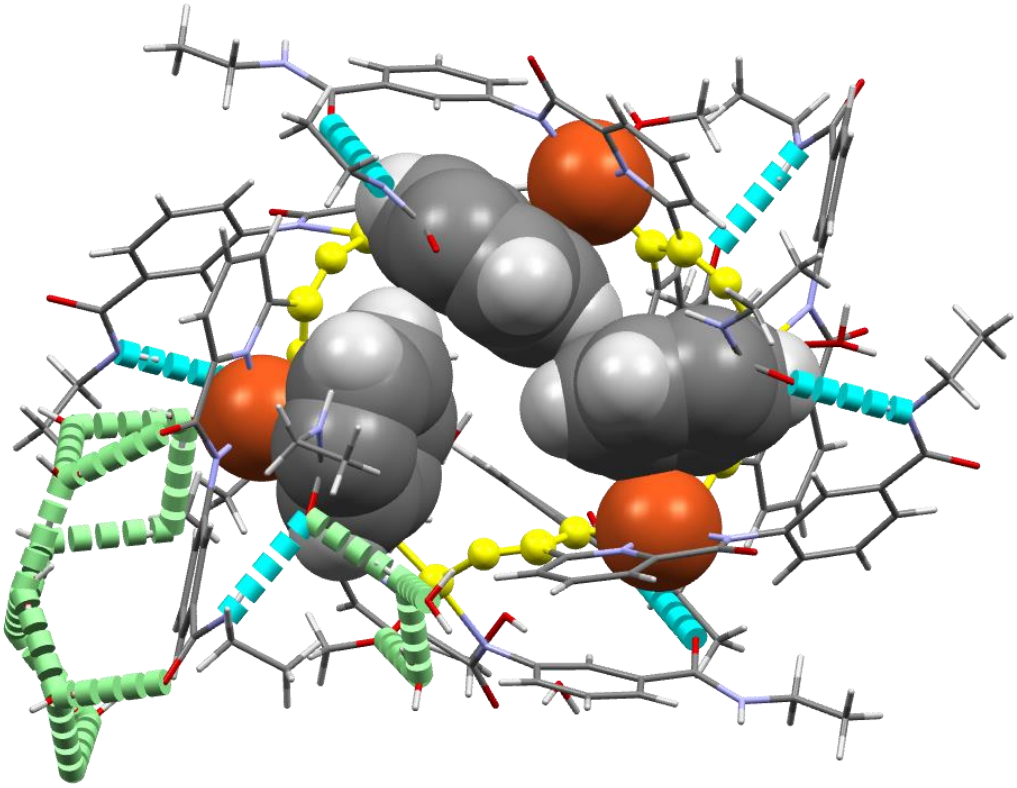


Figure 5.43: The intramolecular forces stabilizing the Cu(H_2L8) cyclic assembly. The coordination pattern has been highlighted in yellow while C–H···π and d···π interactions have been shown as space-fill models. The intramolecular H-bonding between ethylamide groups has been shown as cyan cylinders while H-bonding to co-crystalized water has been shown as green cylinders. The H-bonding network between the hexamer and water molecules is shown to extend from an axially coordinated solvent molecule and H-bond through waters before bonding carbonyls on adjacent chelates.

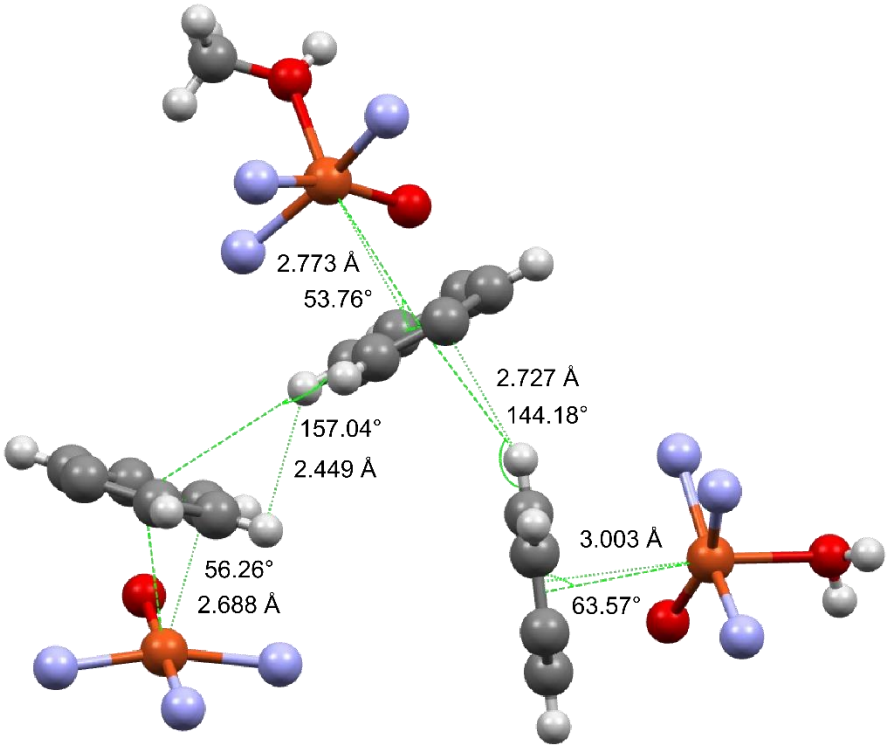


Figure 5.44: The C–H···π and d···π interaction bond lengths and angles for Cu(H_2L8) "thermodynamic".

The intermolecular forces between supermolecules that facilitate packing are comprised almost entirely of H-bonding. The 19 co-crystalized water molecules are instrumental in forming an extensive H-bonding network between supermolecules in neighbouring unit cells. The unit cell and packing of Cu(H_2L8) "thermodynamic" are presented in Figure 5.45. The crystal structure of Cu(H_2L8) "thermodynamic" is dynamic and it must be noted that the crystals were grown overnight and then stored for 6 months before data collection. Over this time, the crystal altered its structure as water entered the lattice while the crystal annealed. The absorption of water was observed by FTIR and this spectrum along with the suspected annealing process is presented in Figure 5.46. The crystals that were grown overnight were truly terrible diffractors and the structure was never solved, however, after water entered the lattice, the crystal structure was elucidated. After the thermodynamic annealing process, the potential energy of the solid-state system was lowered and produced a better diffracting crystal.

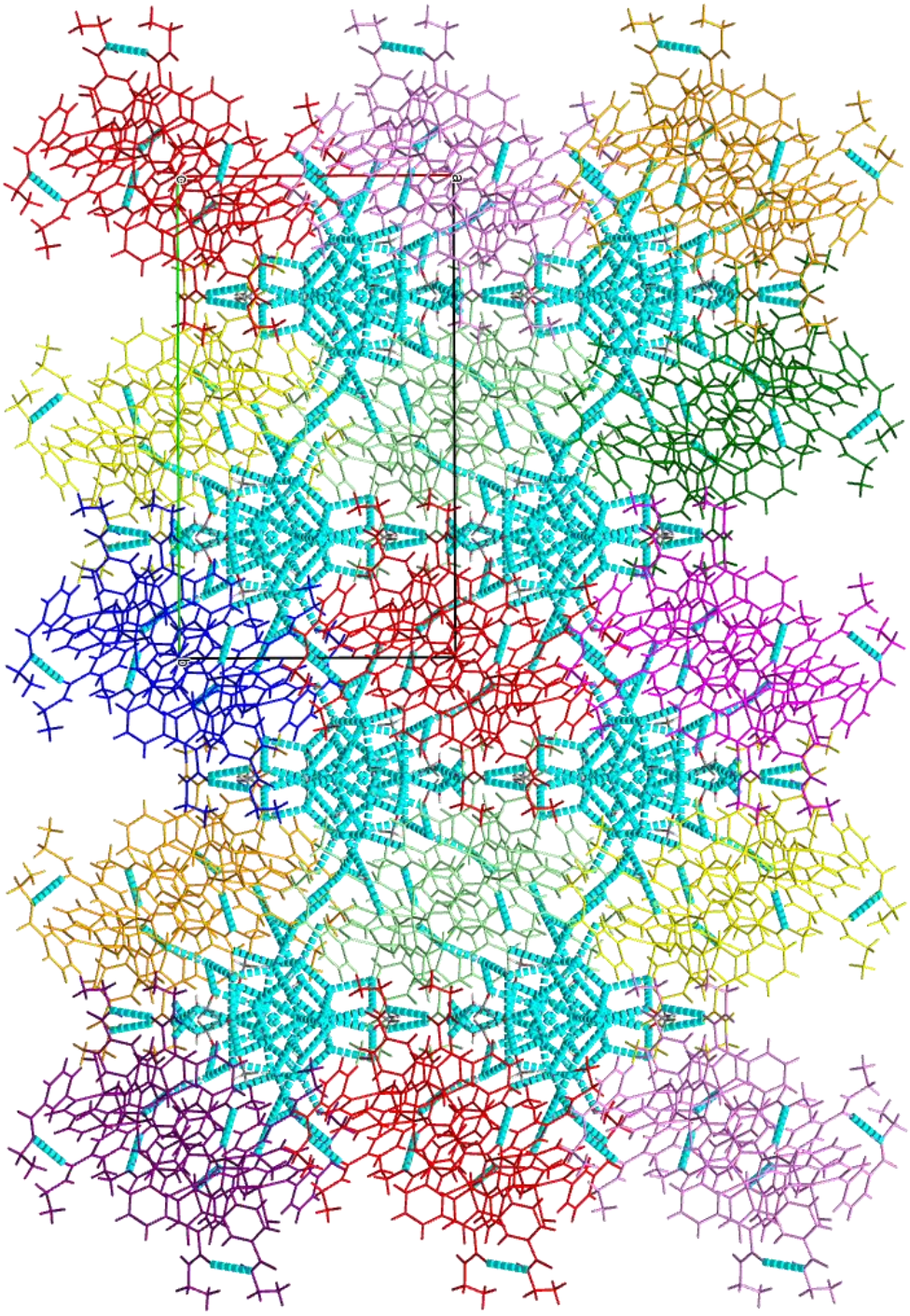


Figure 5.45: The unit cell of Cu(H_2L8) "thermodynamic" as viewed down the crystallographic c-axis. The adjacent supermolecules have been colored differently. The extensive H-bonding network has been shown as cyan cylinders and exists between co-crystalized solvent molecules and neighboring hexamers. The network enables efficient packing as the unit cell volume is only 0.1% void volume.

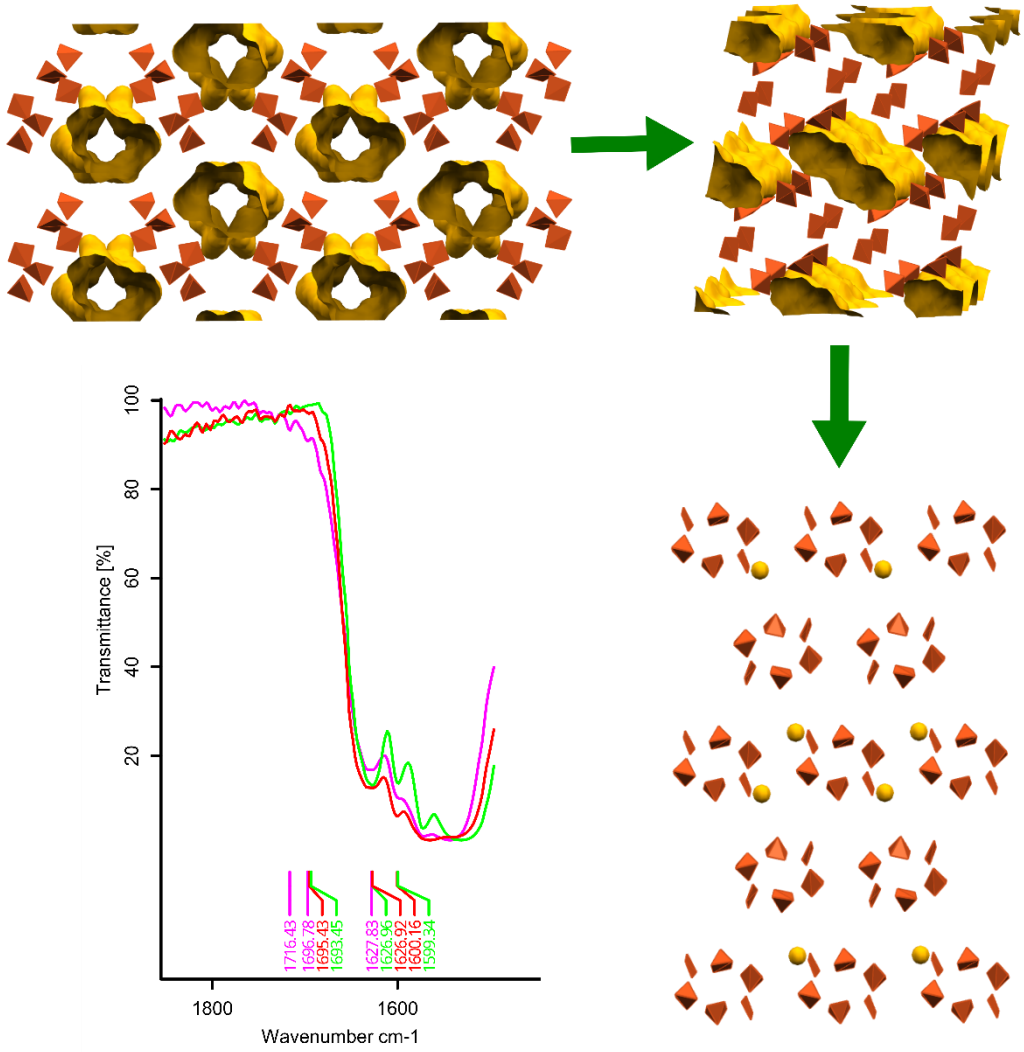


Figure 5.46: The hypothesized annealing process for Cu(H_2L8) "thermodynamic" and the FTIR spectrum confirming that water enters the crystal over time. The FTIR spectrum shows Cu(H_2L8) powder sample in red, while crystals grown overnight are shown in green and crystals stored for 6 months are shown in pink. The peak at 1696 cm^{-1} indicates O–H wagging from water that has entered the lattice and co-crystalized. The annealing process begins in the top left of the figure, where kinetic crystals of Cu(H_2L8) grown overnight are suspected to possess large voids that extend as infinite channels. The annealing process then compresses the voids into amorphous pockets that trap solvent. As the process continues, these pockets compress further into small spheres that occupy only 0.1% of the unit cell volume. After the thermodynamic process has completed, the crystal is packed efficiently, and the potential energy of the solid-state system has been lowered. The structure of the kinetic crystals grown overnight was never elucidated and hence the annealing process is speculative. The voids shown as infinite channels are drawn from the structure of Cu(H_2L6) "kinetic", which differs from Cu(H_2L8) by only a single methyl group on the chelate and was grown from methanol. The voids shown as amorphous pockets have been drawn from Cu(H_2L8) "kinetic" which was grown from an ethanol/methanol mixture. The voids for Cu(H_2L8) "thermodynamic" have been presented and the crystal was grown from a methanol solution.

3.9 Cu(H_2L9) "kinetic"

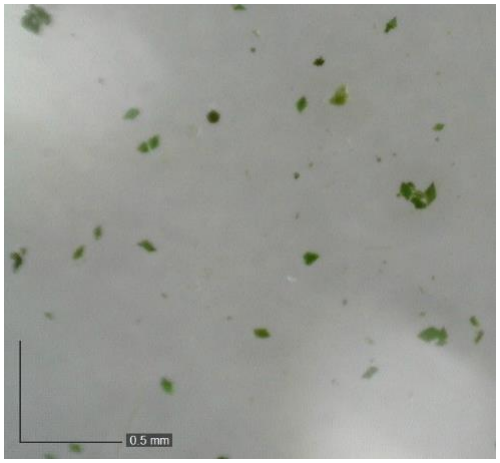


Figure 5.47: Crystals of Cu(H_2L9) "kinetic" grown from an ethanol solution over 6 weeks.

A green fragile, thin, and plate-like crystal with dimensions 0.047 mm x 0.109 mm x 0.258 mm was used and the X-ray intensity data were measured (λ = 0.71073 Å). $C_{146}H_{124}Cu_6N_{30}O_{42}$ (M = 3351.98 g/mol): triclinic, space group P-1 (no. 2), a = 17.3373(17) Å, b = 17.5903(15) Å, c = 18.4520(17) Å, α = 87.522(3)°, β = 71.113(4)°, γ = 75.760(3)°, V = 5156.6(8) Å^3, Z = 1, T = 173.00 K, μ(MoKα) = 0.675 mm^{-1}, $Dcalc$ = 1.079 g/cm^3, 218203 reflections measured (2.39° ≤ 2Θ ≤ 49.998°), 18148 unique (R_{int} = 0.6441, R_{sigma} = 0.3293) which were used in all calculations. The final R_1 was 0.1181 (I > 2σ(I)) and wR_2 was 0.3808 (all data). A total of 1427 frames were collected. The total exposure time was 11.96 hours. The frames were integrated with the Bruker SAINT software package using a narrow-frame algorithm. The integration of the data using a triclinic unit cell yielded a total of 316536 reflections to a maximum θ angle of 28.64° (0.74 Å resolution). The final cell constants are based upon the refinement of the XYZ-centroids of 9926 reflections above 20 σ(I) with 4.67° < 2θ < 48.19°. Data were corrected for absorption effects using the Multi-Scan method (SADABS). The ratio of minimum to maximum apparent transmission was 0.735.

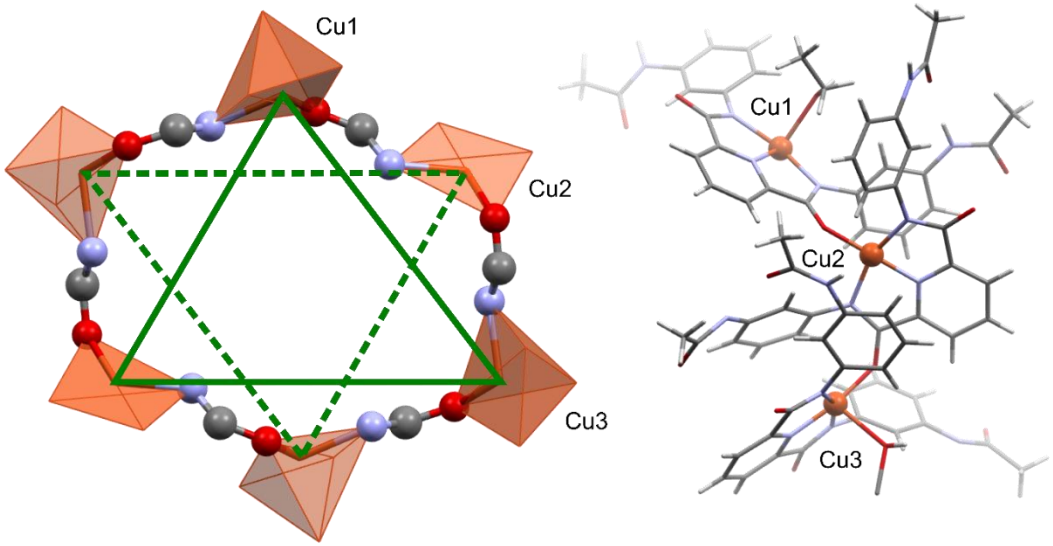


Figure 5.48: The coordination pattern that generates the 24-membered hexanuclear copper carboxamide macrocycle with S_2 symmetry. The metal centers are 5-coordinate square pyramidal or 4-coordinate square planar and are shown as polyhedrons. The mean plane for the hexamer lies in the plane of the six nitrogens that make up the cyclic pattern. There are three Cu(II) centers that lie in a plane above the mean plane (solid green) and three Cu(II) centers that lie in a plane below the mean plane (dashed green). Each Cu(II) triad has two neighboring metal centers square pyramidal with the third being square planar. The asymmetric unit is shown on the right.

Cu(H_2L9) “kinetic” crystalized over 6 weeks in the triclinic space group *P*-1 with one supermolecule in the unit cell and the asymmetric unit described by three monomers of the hexamer. The hexanuclear copper macrocycle coordination is shown in Figure 5.48 and follows the bonding pattern Cu(II)–N–C=O_{amide}–Cu(II) which results in S_2 symmetry for the supermolecule. The plane-to-plane distance between the Cu(II) triads is 1.29 Å and the metallocycle mean plane bisects this interplanar distance.

The asymmetric unit of the crystal contains three Cu(II) centres of which two are square pyramidal with ethanol and methanol axially coordinated and one is square planar. The bond lengths for the inner coordination sphere have been collated in Table 5.7 and show that bond lengths for the 4-coordinate metal centre are significantly shorter than the 5-coordinate complexes. This is because when a fifth axially coordinated ligand is absent, the diminished interelectronic repulsion at the metal allows incoming ligands to approach closer when making up the square plane. The most notable differences between geometries are the Cu–N_{pyr} and Cu–$O_{carbonyl}$ bonds which are *ca.* 0.035 Å shorter for the square planar metal centre. Hence, when 4-coordinate chelates form part of the hexamer, the metallocycle tightens as the bonds that make up the coordination pattern Cu(II)–N–C=O_{amide}–Cu(II) shorten. The $O_{carbonyl}$ that acts as a bridging group approaches Cu(II) to make up the square plane, overlapping with the atomic $3d_{x^2-y^2}$ orbital such that electronic delocalization populates σ* molecular orbitals on the C=O. This is evident as the C=O bond length increases from 1.240 Å to 1.274 Å when coordinated to copper. An exception is evident in Table 5.7 where the uncoordinated C=O_{amide} of the square planar chelate has a longer bond length than the coordinated C=$O_{amide\text{-}Cu}$. This is because the uncoordinated C=O_{amide} is exposed to a pocket in the lattice that is occupied by solvent H-bonded to the carbonyl. The poor quality of the crystal data did not allow these co-crystalized solvent molecules to be properly modelled, and hence H-bonded oxygens may be part of water, methanol, or ethanol molecules.

The hexanuclear assembly is stabilized by various intramolecular forces and these have been presented in Figure 5.49 and are notably similar to the metallocycles presented here thus far. The dominating forces that direct metallocycle formation are coordinative in nature, with the Cu–$O_{carbonyl}$ bonds that make up the coordination pattern averaging 1.927 Å across the asymmetric unit. Intramolecular H-bond formation is also a significant stabilising force that exists between acetamide groups of adjacent chelates, where there are six in total and each triad is related by inversion through the centroid of the cyclic assembly. Finally, C–H···π and d···π interactions

further stabilize the superstructure and these bond parameters have been presented in Figure 5.50.

Table 5.7: Bond lengths for the inner coordination sphere of Cu(H_2L9) "kinetic" as well as carbonyl bonds that make up the tridentate chelate ring. The asymmetric unit of the crystal contains three Cu(II) centers, and the bond lengths are reported for the square pyramidal geometry as the average and standard variation of two independent bond measurements. There is only one Cu(II) center with square planar geometry and its inner sphere bond lengths have also been presented.

Bond	Pyramidal Length (Å)	Planar Length (Å)
Cu–N_{pyr}	1.917 ± 0.02	1.881
Cu–N_{amide}	2.022 ± 0.01	1.988
Cu–$N_{amide\text{-}Cu}$	2.038 ± 0.01	2.034
Cu–$O_{carbonyl}$	1.939 ± 0.01	1.904
Cu–$O_{solvent}$	2.323 ± 0.02	Not Applicable
C=O	1.240 ± 0.008	1.285
C=O_{Cu}	1.274 ± 0.02	1.276

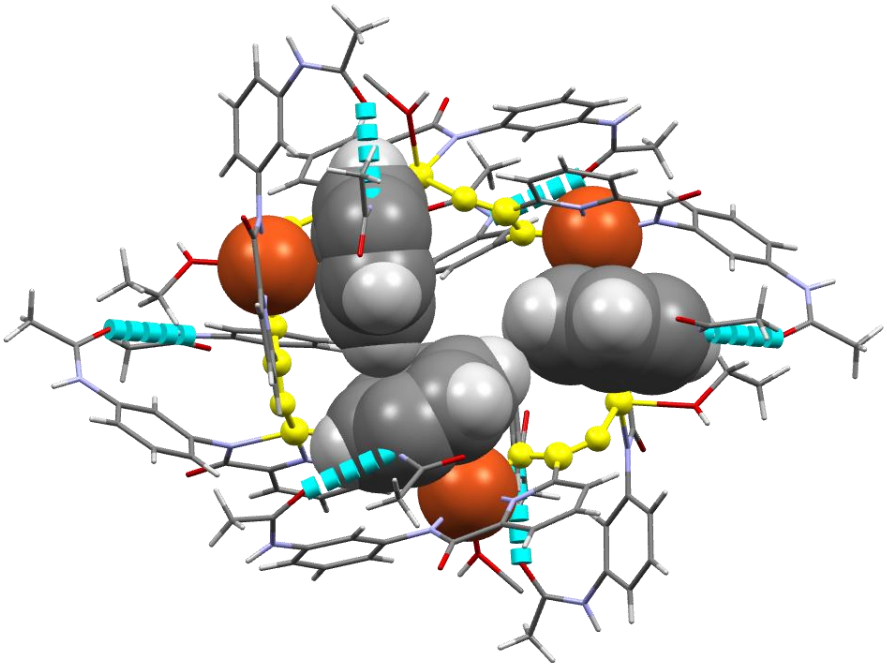


Figure 5.49: The intramolecular forces stabilizing the cyclic assembly of Cu(H_2L9) "kinetic". The coordination pattern has been highlighted yellow while H-bonds between acetamide groups of neighboring chelates have been shown as cyan cylinders. The C–H···π and d···π intramolecular interactions have been shown as space-fill models. Additionally, there are numerous disordered van der Waals forces that exist between monomers of the supermolecule.

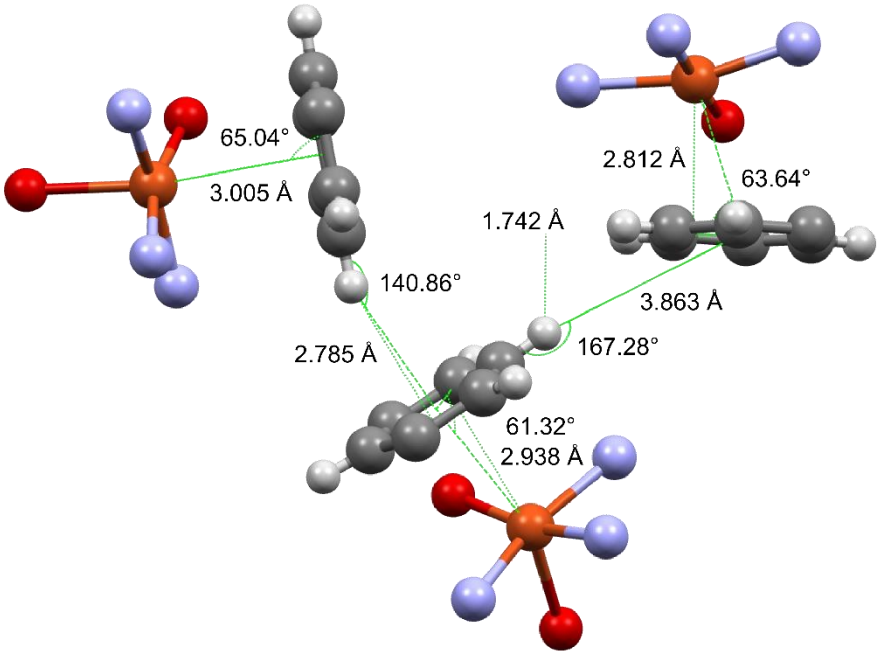


Figure 5.50: The C–H···π and d···π bond lengths and angles for the Cu(H_2L9) "kinetic" cyclic superstructure. The most significant d···π interaction is observed for the square planar chelate which has an atom-to-plane distance of 2.8 Å and indicates that in the absence of an axially coordinated ligand, the metal centre may approach closer to the π-system for more favourable overlap of atomic d-orbitals and molecular orbitals of the aromatic ring.

The packing of Cu(H_2L9) in the crystal lattice is directed by intermolecular interactions, notably H-bonding and close contacts comprising of van der Waals forces. These intermolecular forces and the crystal packing of Cu(H_2L9) "kinetic" have been shown in Figure 5.51. There is H-bonding between the acetamide of one supermolecule and the carbonyl of another supermolecule in the adjacent unit cell which facilitates packing in the *ac* plane. There is also a H-bonding network that facilitates packing in the *ab* plane and exists between the carbonyl of an acetamide and three co-crystalized oxygen-containing solvent molecules. These solvent molecules have not been properly modelled due to the poor quality of the crystal data but are likely water. The intermolecular interactions that facilitate packing in the *bc* plane comprise of close contacts between methyl groups of the acetamides on neighbouring metallocycles. There are also significant close contacts in the *ab* and *ac* planes. The crystal packing of Cu(H_2L9) "kinetic" is inefficient as the unit cell contains one supermolecule with a volume of V = 5156.6 Å^3 of which 29.2% (1504 Å^3) is void volume. The voids extend in two dimensions as infinite channels through the crystal lattice.

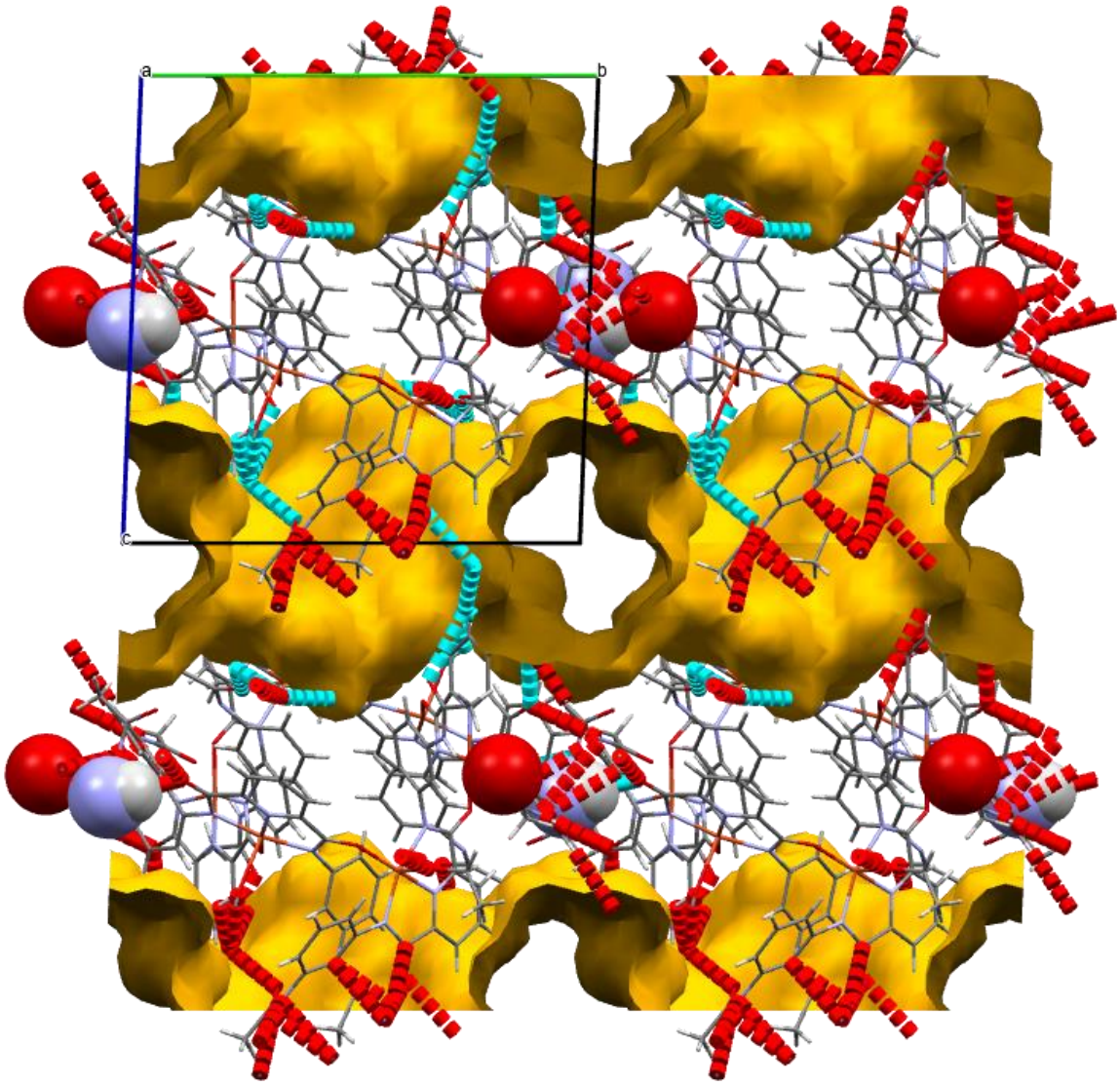


Figure 5.51: The unit cell of Cu(H_2L9) as viewed down the crystallographic a-axis. The H-bonding between the acetamide of one supermolecule and the carbonyl of another is shown as space-fill models and exist along the *ac* plane. The H-bonding network between co-crystalized solvent molecules and neighboring supermolecules has been shown as cyan cylinders and exist along the *ab* plane. Additional close contacts have been shown as red cylinders. The void volume has been shown in yellow and is considerable at 29% of the unit cell volume. The voids extend through the lattice as infinite channels in two dimensions parallel to the crystallographic a- and b-axes.

3.10 Cu(H_2L9) "thermodynamic"

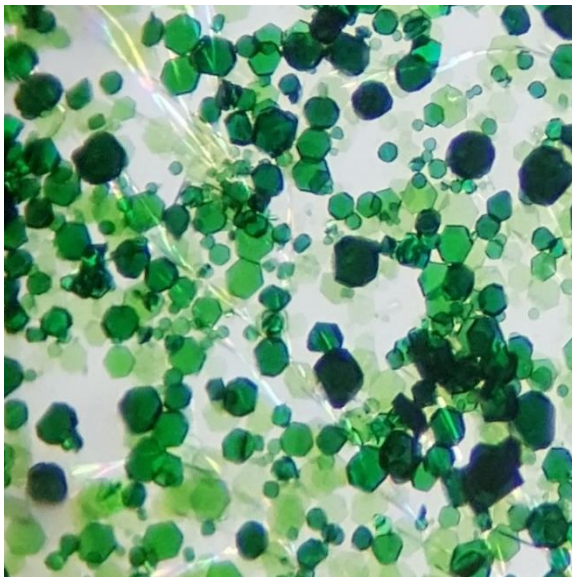


Figure 5.52: Crystals of Cu(H_2L9) "thermodynamic" grown by vapor diffusion of DCM into a methanol solution over 6 months.

A green hexagonal plate-like gem with dimensions 0.073 mm x 0.090 mm x 0.124 mm was used and the X-ray intensity data were measured (λ = 0.71073 Å). $C_{138}H_{165.666667}Cu_6N_{30}O_{49.833333}$ (*M* = 3423.30 g/mol): trigonal, space group *R*-3 (no. 148), *a* = 18.3593(9) Å, *c* = 39.415(3) Å, *V* = 11505.5(14) Å^3, *Z* = 3, *T* = 173.00 K, μ(MoKα) = 0.912 mm^{-1}, *Dcalc* = 1.482 g/cm^3, 237319 reflections measured (4.438° ≤ 2Θ ≤ 56.726°), 6397 unique (R_{int} = 0.0756, R_{sigma} = 0.0208) which were used in all calculations. The final R_1 was 0.0375 (I > 2σ(I)) and wR_2 was 0.1063 (all data). A total of 4462 frames were collected. The total exposure time was 17.19 hours. The frames were integrated with the Bruker SAINT software package using a narrow-frame algorithm. The integration of the data using a rhombohedral unit cell yielded a total of 284226 reflections to a maximum θ angle of 28.36° (0.75 Å resolution). The final cell constants are based upon the refinement of the XYZ-centroids of 9612 reflections above 20 σ(I) with 5.227° < 2θ < 56.38°. Data were corrected for absorption effects using the Multi-Scan method (SADABS). The ratio of minimum to maximum apparent transmission was 0.781.

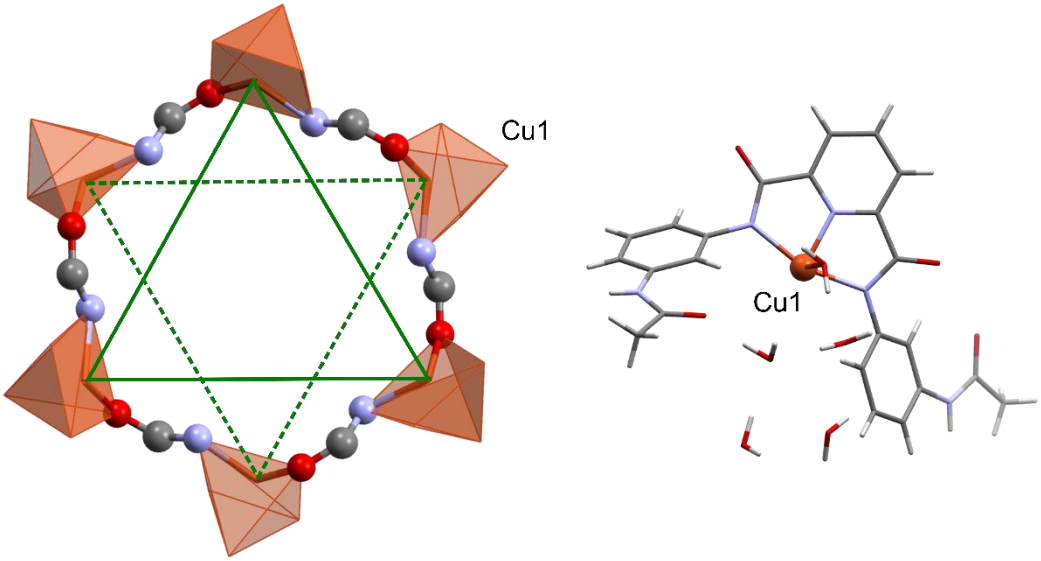


Figure 5.53: The coordination pattern that generates the 24-membered hexanuclear copper carboxamide macrocycle with S_6 symmetry. The metal centers are 5-coordinate square pyramidal and are shown as polyhedrons. The mean plane for the hexamer lies in the plane of the six nitrogens that make up the cyclic pattern. There are three Cu(II) centers that lie in a plane above the mean plane (solid green) and three Cu(II) centers that lie in a plane below the mean plane (dashed green). The asymmetric unit shown on the right.

Cu(H_2L9) “thermodynamic” crystalized over 6 months in the trigonal space group *R*-3 with three supermolecules in the unit cell and the asymmetric unit described by a single monomer of the hexamer. The hexanuclear copper macrocycle coordination is shown in Figure 5.53 and follows the bonding pattern Cu(II)–N–C=O_{amide}–Cu(II) which results in S_6 symmetry for the supermolecule. The plane-to-plane distance between the Cu(II) triads is 1.55 Å and the metallocycle mean plane bisects this interplanar distance.

The asymmetric unit of the crystal is described by a single monomer of the hexamer and the bond lengths for the inner coordination sphere have been collated in Table 5.8. The ligand chelates the metal ion through N_{pyr} and two anionic N_{amide} donors while a fourth exogenous ligand coordinates to make up the square plane. A single solvent molecule is axially coordinated to make up the final square pyramidal geometry. The bond lengths for the anionic donors are *ca.* 2.0 Å while the neutral atom donors that make up the square plane have bond lengths *ca.* 1.9 Å. This reflects the interelectronic repulsion experienced between the metal ion and the anionic donors as well as the negatively charged donors themselves. The long bond length of the axially coordinated water molecule *ca.* 2.4 Å indicates that the fully occupied $3d_z^2$ orbital is repelling the incoming lone pair of the solvent molecule. Additionally, ligands approaching the atomic $3d_z^2$ orbital are repelled due to high electron density in the Cartesian *xy* plane. This plane is occupied by the atomic $3d_{x^2-y^2}$ orbital which delocalizes into vacant orbitals on the coordinated ligand, in this case, the C=O of an adjacent chelate. The delocalization of this high energy paramagnetic orbital into the σ* molecular orbitals of the C=O is evident as the bond length increases from 1.250 Å to 1.266 Å when the C=O is coordinated to Cu(II). The C=O_{amide} has enhanced σ-donor ability as the negative charge of the amidate is delocalized onto the $O_{carbonyl}$, and the synergistic interplay between σ-donation and π-backdonation is evident in the short Cu–$O_{carbonyl}$ bond at 1.905 Å.

The Cu–$O_{carbonyl}$ bond is a crucial intramolecular interaction that facilitates metallocycle formation. The intramolecular forces stabilising the superstructure are presented in Figure 5.54 and include coordinating forces, van der Waals, C–H···π and d···π interactions. The dominating force is coordinative in nature with short bonds between atoms that make up the Cu(II)–N–C=O_{amide}–Cu(II) cyclic pattern. Notably, although H-bond donors and acceptors are present on the chelate, these moieties are not involved with intramolecular H-bond formation There are, however, significant intramolecular C–H···π and d···π interactions which have been presented in Figure 5.55 with the bond lengths and angles. All atom-to-plane distances are less than 2.9 Å indicating significant overlap with the aromatic π-systems. The d···π bond angles are *ca.* 58°

suggesting that atomic $3d_{xz}$ and $3d_{yz}$ orbitals are principally involved with d···π overlap on the aromatic ring. Although intramolecular H-bond formation is absent, the chelates are involved with intermolecular H-bonding which facilitates packing of the supermolecules in the crystal lattice.

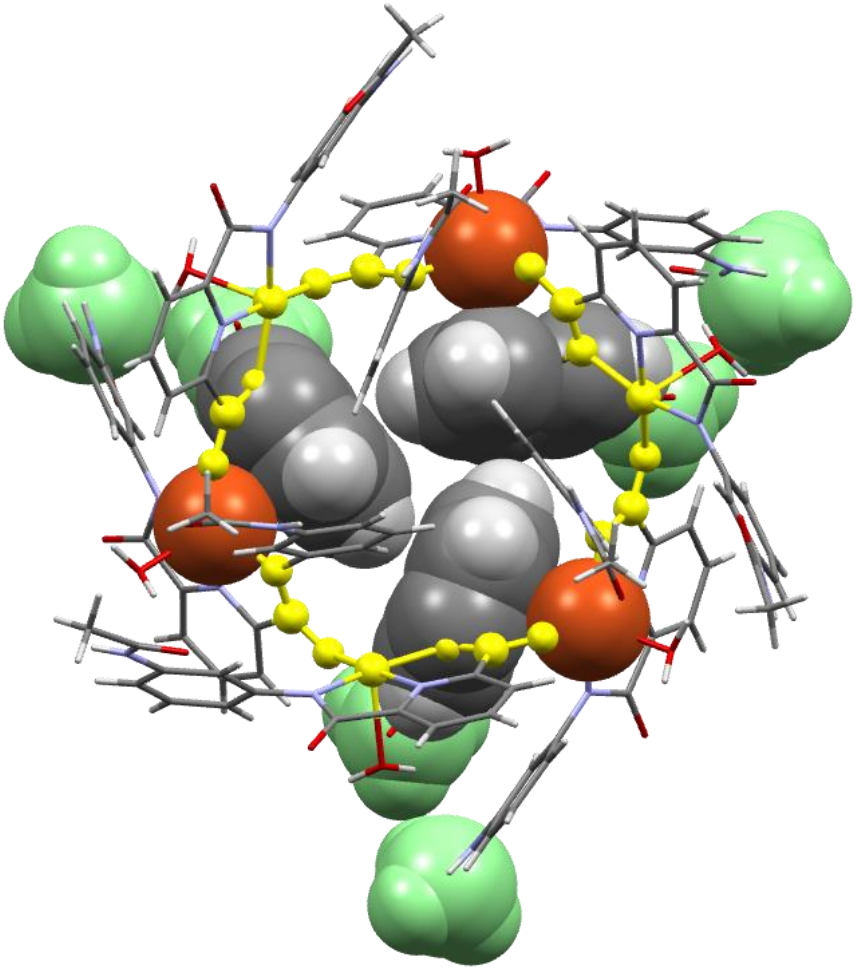


Figure 5.54: The intramolecular interactions stabilizing the Cu(H_2L9) "thermodynamic" supermolecular assembly. The coordination pattern has been shown as yellow atoms and follows the sequence Cu(II)–N–C=O_{amide}–Cu(II). There are C–H···π and d···π interactions which have been shown as space-fill models for one of the Cu(II) triads. The interactions are related to the second Cu(II) triad by inversion through the centroid of the metallocycle. Additional stabilization of the assembly is afforded by van der Waals interactions (shown in green) between acetyl groups of neighbouring chelates. Notably, intramolecular H-bonding is absent and instead the H-bond donors and acceptors participate in intermolecular recognition and packing of supermolecules into the crystal lattice.

Table 5.8: Bond lengths that make up the inner coordination sphere for Cu(H_2L9) "thermodynamic". The bond lengths have been reported with the standard deviation of the X-ray measurement.

Bond	Length (Å)
Cu–N_{pyr}	1.9073(14)
Cu–N_{amide}	2.0562(14)
Cu–$N_{amide-Cu}$	2.0346(14)
Cu–$O_{carbonyl}$	1.9058(11)
Cu–$O_{solvent}$	2.4037(15)
C=O	1.250(2)
C=O_{Cu}	1.266(2)

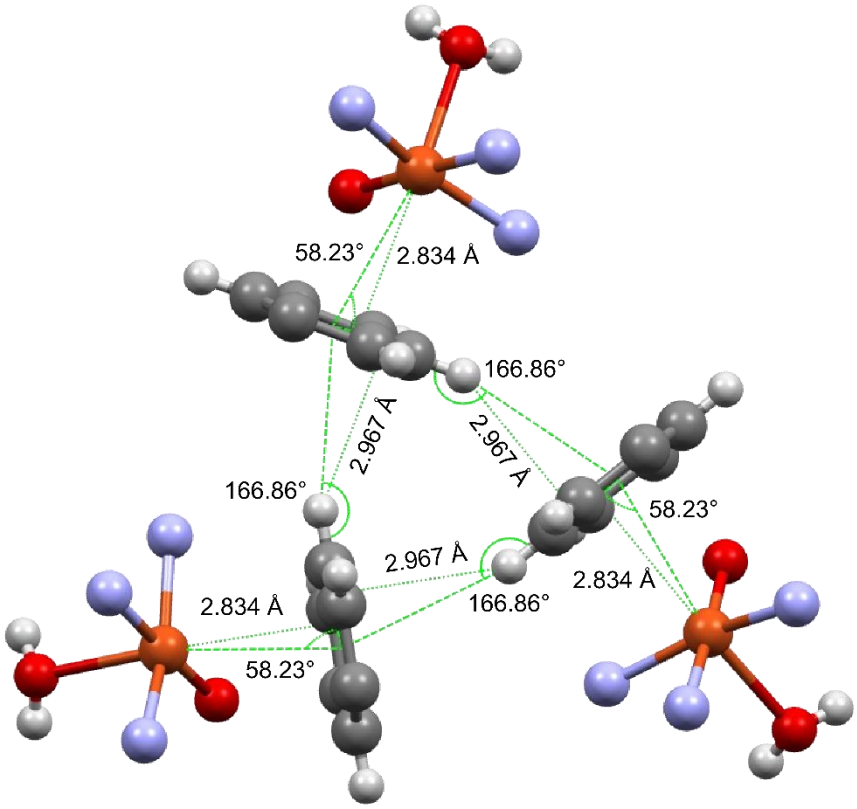


Figure 5.55: The C–H···π and d···π interaction bond lengths and angles. The bond parameters for each interaction are identical for the Cu(II) triad and reflects the symmetry of the crystal. The d···π interactions are significant with an atom-to-plane distance of 2.834 Å.

The intermolecular forces that facilitate packing of Cu(H_2L9) “thermodynamic” into the crystal lattice have been shown in Figure 5.57. The figure shows the unit cell as viewed down the crystallographic c-axis. The H-bonding network extends between a single monomer of the hexamer and four co-crystallized water molecules that from part of the asymmetric unit. The intermolecular H-bonding network facilitates packing of the supermolecules along all dimensions of the lattice, that is, along the *ab*, *bc* and *ac* planes of the crystal. There are additional intermolecular H-bonds between acetamide moieties on neighbouring supermolecules. The extensive intermolecular H-bonding ensure efficient packing of Cu(H_2L9) “thermodynamic” into the lattice and hence the unit cell contains three supermolecules with a volume of V = 11505.5 Å^3 of which only 0.1% (13 Å^3) is void volume. The crystals of Cu(H_2L9) “thermodynamic” are admirable as the symmetry of the microstructure is observed for the macrostructure. The packing of supermolecules is shown in Figure 5.56 and the S_6 symmetry observed for the macrocycle in the crystal lattice is also observed for the macrostructure itself as the green crystals grow into hexagonal prisms over 6 months.

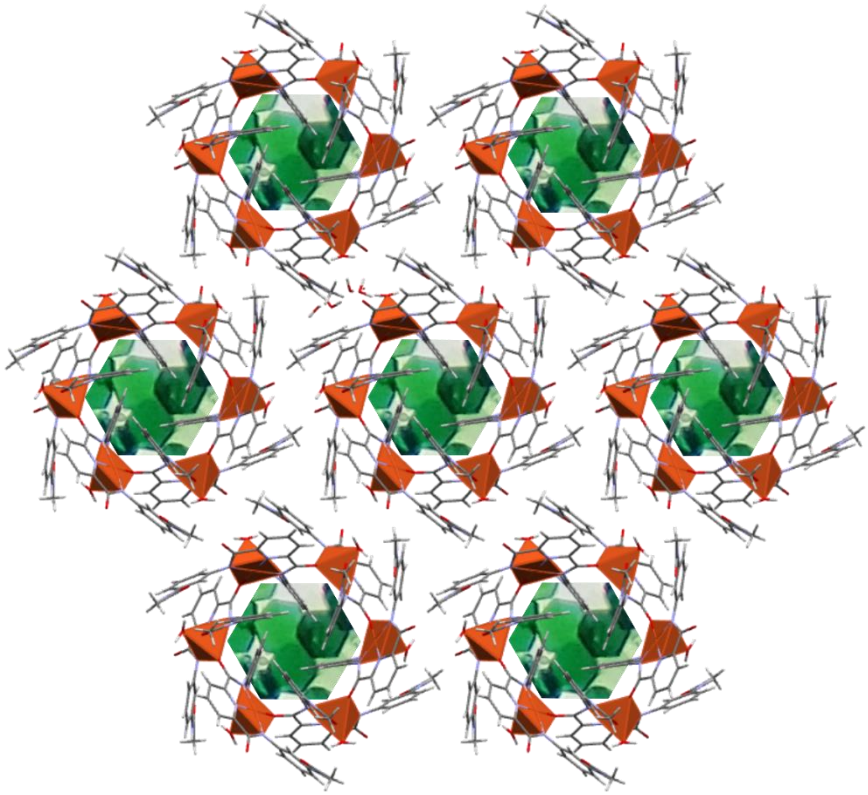


Figure 5.56: The microstructure of the supermolecule is observed for the macrostructure of the crystal.

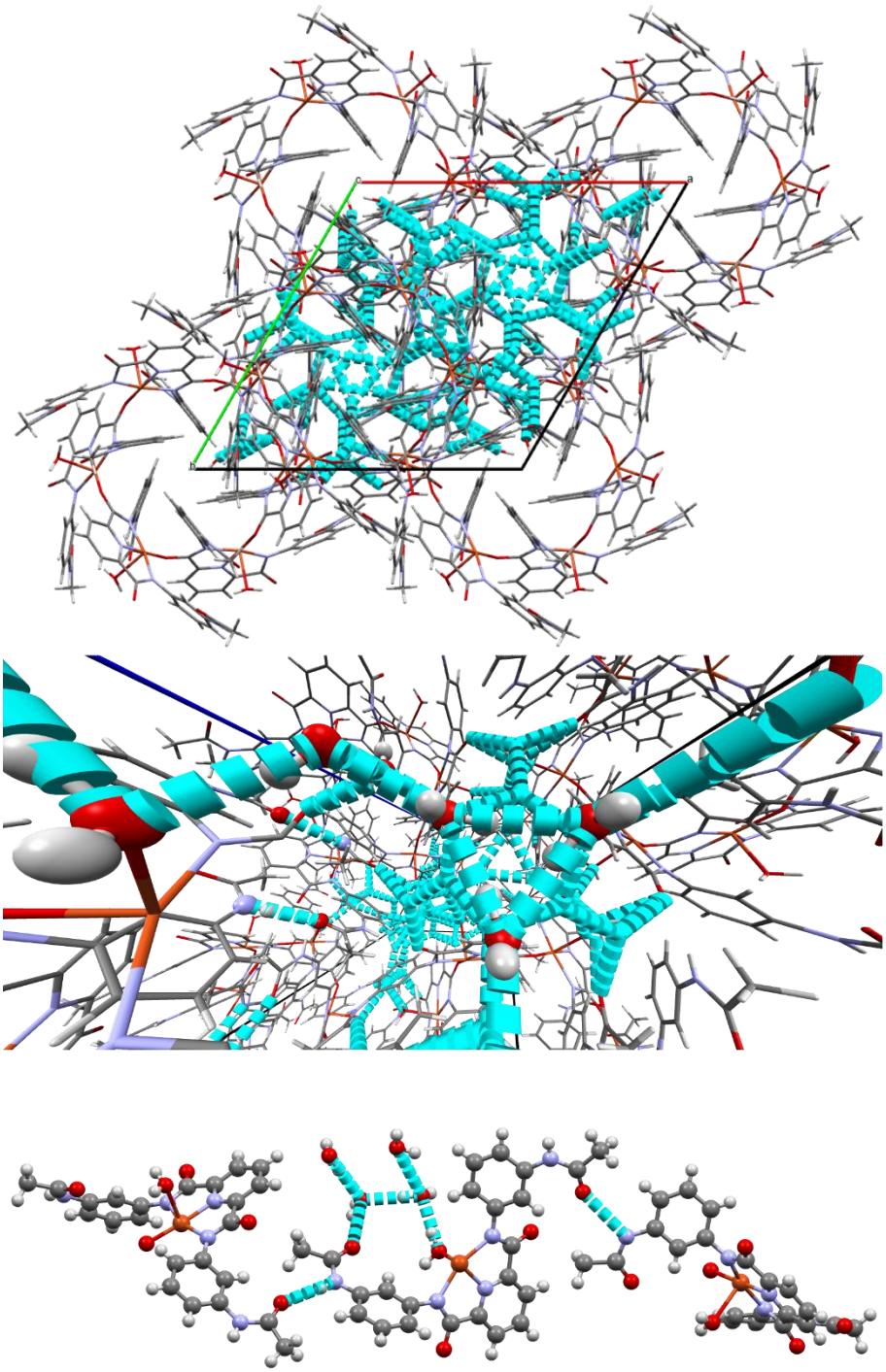


Figure 5.57: (Top) The unit cell of Cu(H_2L9) "thermodynamic" viewed down the crystallographic c-axis. (Middel) The H-bonding network between acetamide moieties of neighboring supermolecules and co-crystallized water that extends through all dimensions of the lattice. (Bottom) The monomer that describes the asymmetric unit H-bonded to four water molecules and two adjacent chelates of a hexamer.

3.11 CuL10

A green, prism-like crystal of $C_{128}H_{78}Cu_6N_{30}O_{16}$ with approximate dimensions 0.044 mm x 0.063 mm x 0.110 mm was used and the X-ray intensity data were measured (λ = 0.71073 Å). $C_{128}H_{78}Cu_6N_{30}O_{16}$ (*M* = 2673.44 g/mol): triclinic, space group *P*-1 (no. 2), *a* = 12.8621(7) Å, *b* = 14.6778(8) Å, *c* = 17.1404(9) Å, *α* = 76.085(2)°, *β* = 70.053(2)°, *γ* = 81.249(2)°, *V* = 2943.8(3) Å^3, *Z* = 1, *T* = 173.0 K, μ(MoKα) = 1.145 mm^{-1}, *Dcalc* = 1.508 g/cm^3, 427398 reflections measured (4.23° ≤ 2Θ ≤ 56.834°), 14733 unique (R_{int} = 0.1383, R_{sigma} = 0.0338) which were used in all calculations. The final R_1 was 0.0430 (I > 2σ(I)) and wR_2 was 0.1228 (all data). A total of 929 frames were collected. The total exposure time was 1.21 hours. The frames were integrated with the Bruker SAINT software package using a narrow-frame algorithm. The integration of the data using a triclinic unit cell yielded a total of 579024 reflections to a maximum θ angle of 28.47° (0.75 Å resolution). The final cell constants are based upon the refinement of the XYZ-centroids of 9965 reflections above 20 σ(I) with 4.596° < 2θ < 55.32°. Data were corrected for absorption effects using the Multi-Scan method (SADABS). The ratio of minimum to maximum apparent transmission was 0.894.

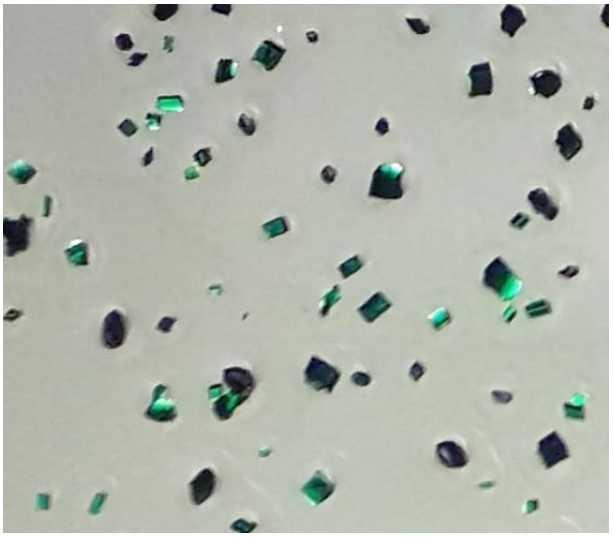


Figure 5.58: Crystals of CuL10 grown by evaporation from a methanol/ethyl acetate mixture.

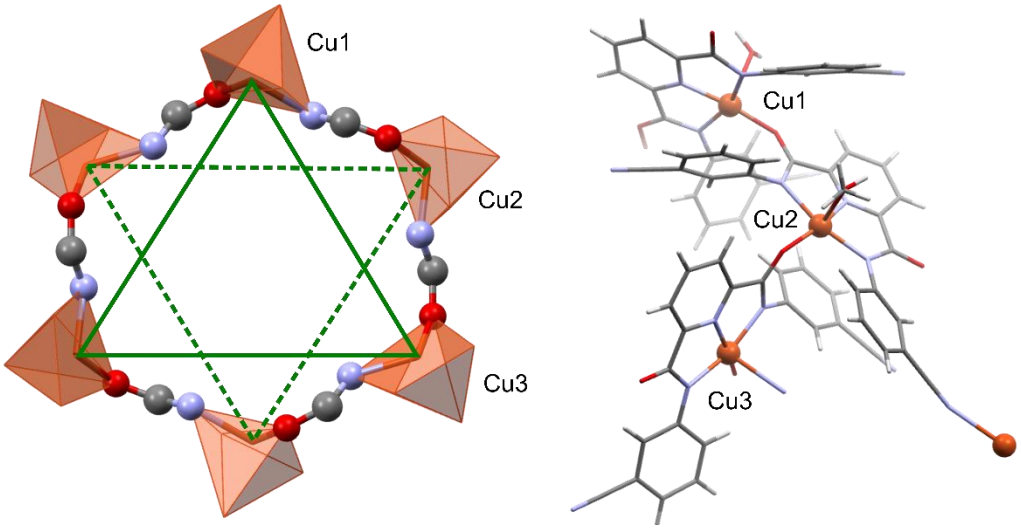


Figure 5.59: The coordination pattern for CuL10 that results in S_2 symmetry for the metallocycle. The asymmetric unit is shown on the right with the coordinating bond that results in an extended polymeric crystal structure.

CuL10 crystalized over a few weeks in the triclinic space group *P*-1 with a single supermolecule in the unit cell and the asymmetric unit described by three monomers of the hexamer. The coordination pattern that generates the 24-membered hexanuclear copper carboxamide macrocycle with S_2 symmetry is shown in Figure 5.59. The metal centers are 5-coordinate square pyramidal and are shown as polyhedrons. The mean plane for the hexamer lies in the plane of the six nitrogens that make up the cyclic pattern. There are three Cu(II) centers that lie in a plane above the mean plane (solid green) and three Cu(II) centers that lie in a plane below the mean plane (dashed green). The plane-to-plane distance between Cu(II) triads is 1.55 Å and the metallocycle mean plane bisects this interplanar distance.

The asymmetric unit of the crystal is described by three monomers of the hexamer and hence the inner coordination sphere bond lengths have been collated in Table 5.9 as the average of three independent bond length measurements. Notably, the bond lengths for anionic N_{amide} donors are significantly longer than the neutral N_{pyr} and $O_{carbonyl}$ donors. This indicates that interelectronic repulsion between the anionic donors themselves as well as the metal centre diminish the bond strength and hence increase bond length. Significant π-backbonding is observed as the C=O bond length increases from 1.240 Å to 1.268 Å when coordinated to Cu(II), indicating that electron density from the reactive atomic $3d_{x^2-y^2}$ orbital is delocalized from the square plane into σ* molecular orbitals present on the bridging C=O. The Cu–$O_{carbonyl}$ bond is formed by a synergistic interplay of σ-donation and π-backbonding, the former is enhanced by delocalization of the amidate negative charge onto the carbonyl oxygen, and hence the bond length is short at 1.928 Å. This coordinating bond is the dominant intramolecular force stabilising the cyclic assembly.

Additional intramolecular forces stabilise the metallocycle and these have been presented in Figure 5.60. The interactions include coordinating forces which make up the cyclic Cu(II)–N–C=O_{amide}–Cu(II) bonding pattern as well as C–H···π and d···π interactions which have been presented in Figure 5.61 with the relevant bond lengths and angles. The d···π interactions are significant as all atom-to-plane distances are less than 3 Å, while the bond angles between 56° and 64° suggest that atomic $3d_{xz}$ and $3d_{yz}$ orbitals are principally involved with overlap of the aromatic π-system. There are various disordered van der Waals forces and π···π stacking interactions evident in the space-fill model presented in Figure 5.62. Although the CuL10 metallocycle presented here is the only structure to display intramolecular π···π stacking, these interactions are weak as centroid-to-plane distances (Figure 5.63) between aromatic rings vary between 3.4 Å and 4.0 Å.

Table 5.9: The inner coordination sphere bond lengths for CuL10 have been reported as the average of three measurements at each metal center that describes the asymmetric unit. The bond lengths for the axially coordinated ligands have been reported with the standard deviation of the X-ray measurement.

Bond	Length (Å)
$Cu–N_{pyr}$	1.909 ± 0.003
$Cu–N_{amide}$	2.028 ± 0.01
$Cu–N_{amide\text{-}Cu}$	2.057 ± 0.01
$Cu–O_{carbonyl}$	1.928 ± 0.02
C=O	1.240 ± 0.003
$C=O_{Cu}$	1.268 ± 0.006
$Cu–OH_2$	2.389(2)
Cu–MeOH	2.302(2)
Cu–N≡C	2.461(3)

The intermolecular forces for CuL10 are particularly interesting as the molecules pack in the lattice by coordinating Cu(II) in the axial position through the nitrile group present on an adjacent chelate. This Cu–N≡C bond is 2.461 Å and allows the supermolecules to pack efficiently as they form an infinite metal-organic polymer consisting of metallocycle hexamers. This strong bond between supermolecules results in poor water solubility for the complex and hence biological work requires the use of DMSO to solubilise the copper chelate. The intermolecular forces have been presented in Figure 5.64 as space-fill models along with the voids present in the lattice. These forces include coordination of a nitrile group to the axial position of Cu(II) which facilitates packing of the supermolecules in the crystallographic *ac* plane. There is also Cu–N≡C intermolecular coordination in the *bc* plane along with C–H···O interactions which further enables packing of supermolecules. The intermolecular interactions along the *ab* plane involve H-bonding between nitrile groups and axially coordinated water or methanol. The packing of CuL10 is efficient as the unit cell contains one supermolecule and has a volume V = 2943.8 $Å^3$ of which 5.5% (161 $Å^3$) is void volume. The voids exist as chicken-nugget-shaped pockets at the corners of the unit cell.

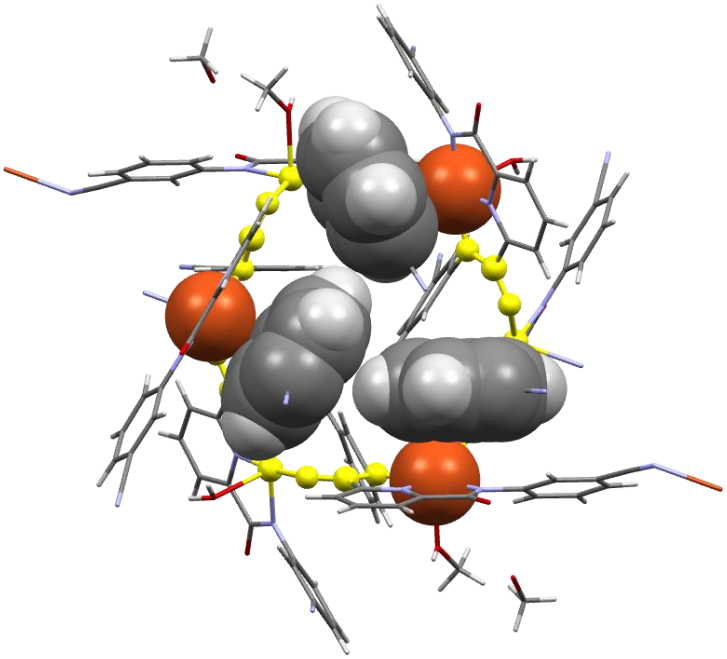


Figure 5.60: The intramolecular interactions stabilizing the CuL10 metallocycle. The coordination pattern has been shown as yellow atoms and follows the sequence Cu(II)–N–C=O_{amide}–Cu(II). There are C–H···π and d···π interactions which have been shown as space-fill models for one of the Cu(II) triads. The interactions are related to the second Cu(II) triad by inversion through the centroid of the metallocycle.

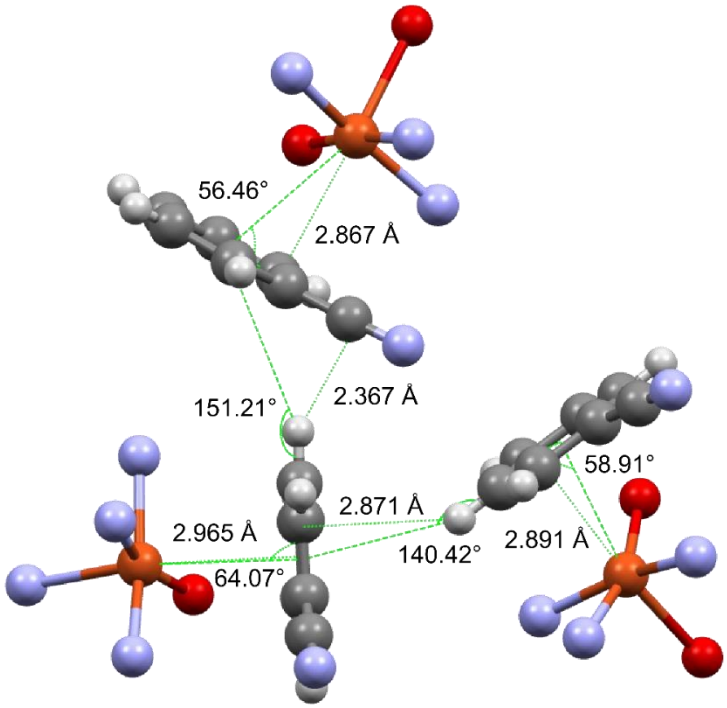


Figure 5.61: The C–H···π and d···π bond lengths and angles for CuL10.

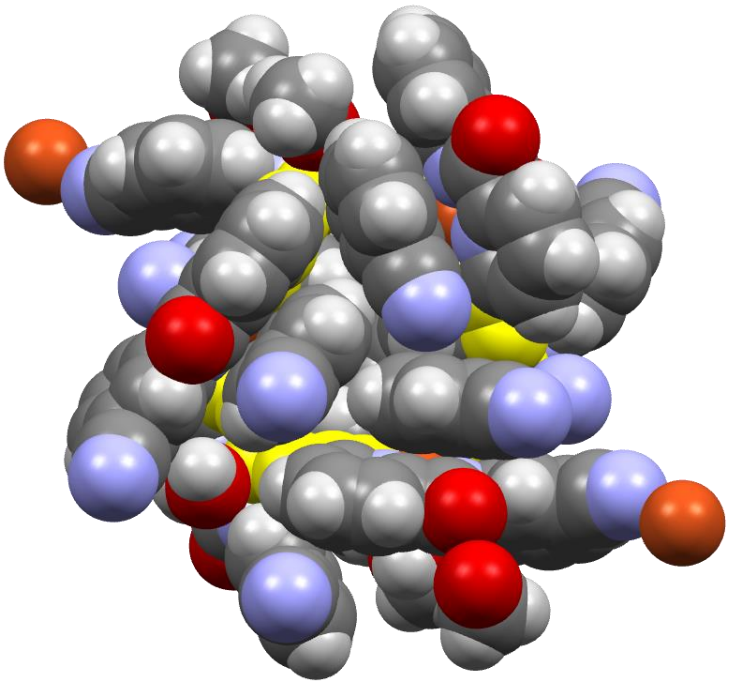


Figure 5.62: Space-filling model of the CuL10 metallocycle highlighting the various van der Waals forces imparting tensional integrity to the cyclic assembly. Additional π···π stacking is evident between aromatic pyridine rings and adjacent aryl groups.

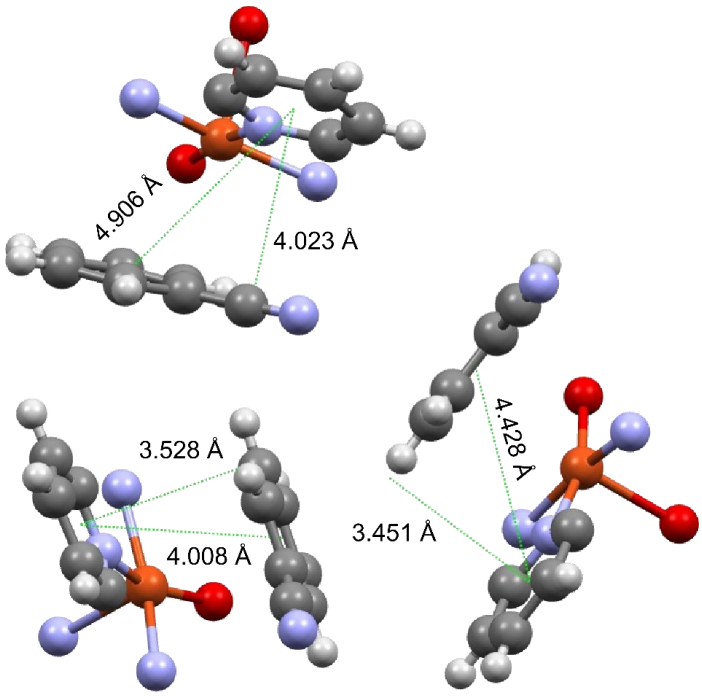


Figure 5.63: The centroid-to-centroid and centroid-to-plane distances between aromatic groups participating in π···π stacking within the CuL10 supermolecule.

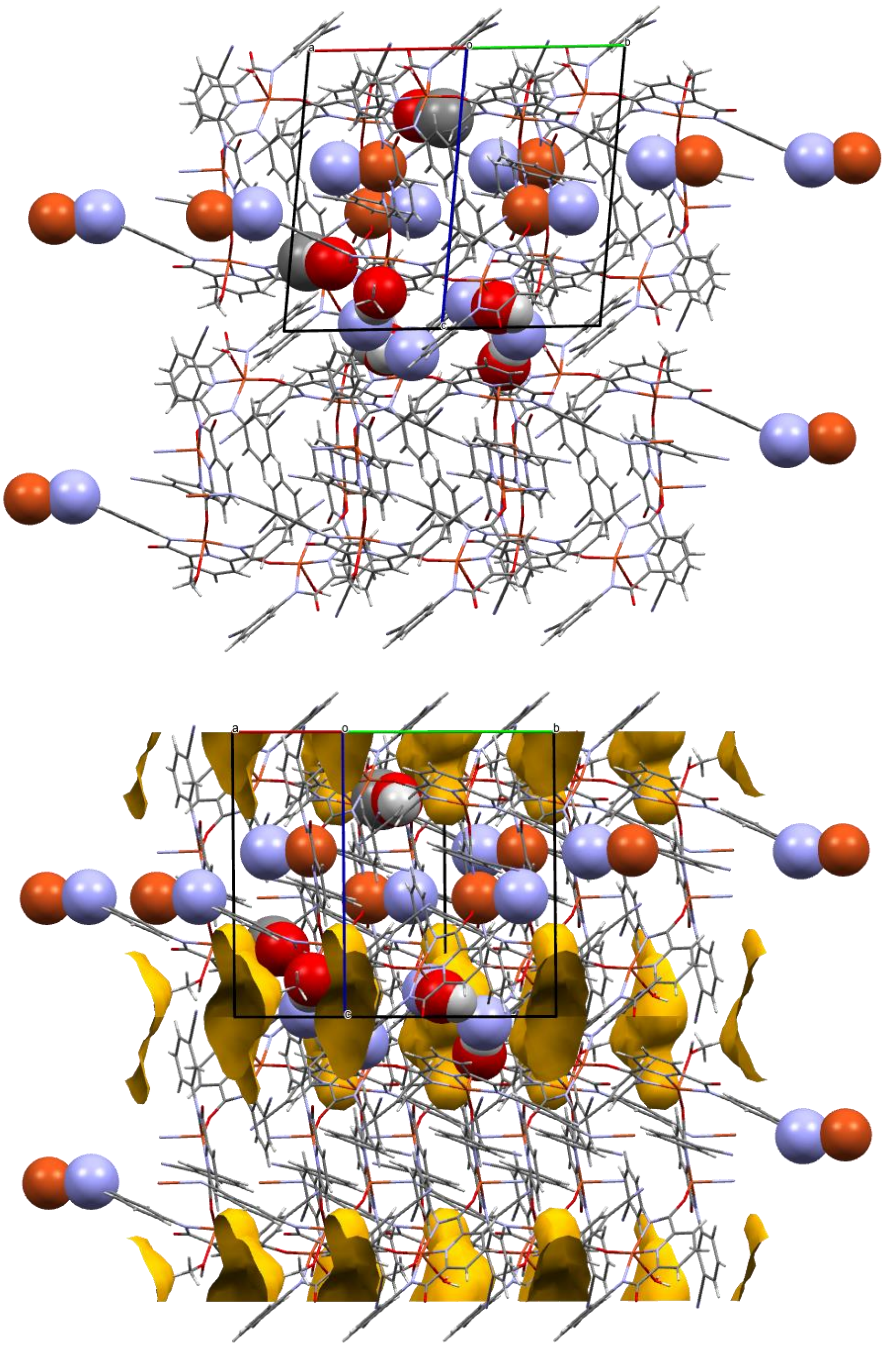


Figure 5.64: The unit cell and packing of CuL10 supermolecules in the crystal lattice. The intermolecular interactions have been shown as space-fill models and comprise of coordinating bonds that extend the hexamers as infinite polymers through the lattice. Additional C–H···O and H-bonding interactions further facilitate packing of the complex. The voids present in the crystal have also been shown and exist at the corners of the unit cell.

4. Discussion & Conclusion

Although the bonding analysis has been presented here based on Crystal Field Theory, the atomic orbital contributions to bonding have been confirmed by DFT methods. The asymmetric unit of CuL5 was optimized at the B3LYP/LanL2DZ level of theory and the computed structure is shown in Figure 5.65 with the paramagnetic spin density orbitals.

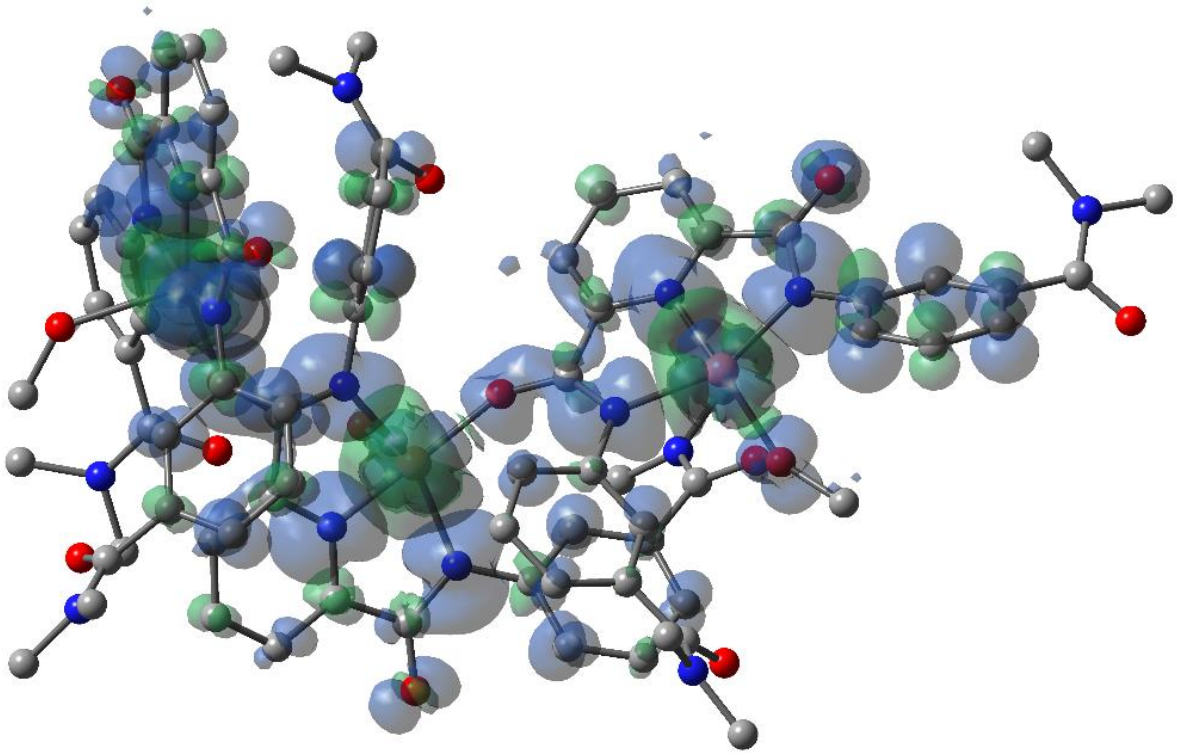


Figure 5.65: The asymmetric unit of CuL5 optimized at the B3LYP/LanL2DZ level of theory. The structure was computed with quartet multiplicity and the paramagnetic spin density was found to be located at each of the three Cu(II) centres that make up the asymmetric unit. The paramagnetic spin density is localized in the square plane of the metal centre and shows significant $3d_{x^2-y^2}$ character. Alpha spin is blue and beta spin is green.

The DFT output shows significant $3d_{x^2-y^2}$ character in the square plane of the Cu(II) center as well as spin density localized on the bridging carbonyl which is crucial to metallocycle formation. Although the paramagnetic electron density is delocalized across the monomers of the asymmetric unit, it is unlikely that antiferromagnetic coupling is taking effect over the three bridging atoms between metal centers. The spin density plot shows that paramagnetic electron density is delocalized into the aromatic rings of the ligand and reflects the energy lowering of the metal-based orbitals as a result of the nephelauxetic effect. The coordination pattern Cu(II)–$C{=}O_{amide}$–Cu(II) that drives metallocycle formation is dominated by $3d_{x^2-y^2}$ character as shown in Figure 5.66

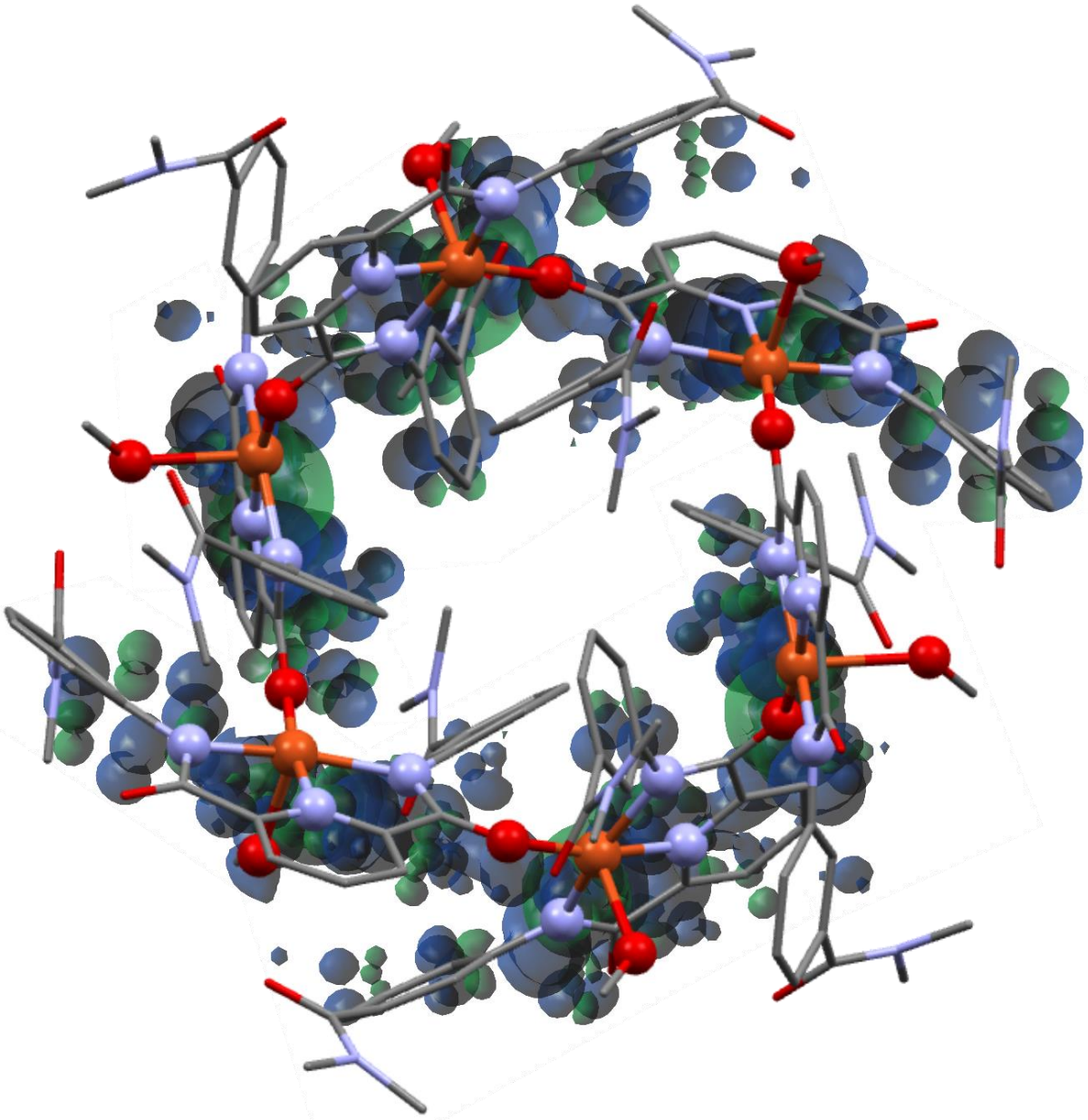


Figure 5.66: The CuL5 metallocycle hexamer shown with paramagnetic spin density orbitals. The spin density is located at each of the six copper centers and shows significant $3d_{x^2-y^2}$ character. The delocalization of this reactive orbital into vacant orbitals of the equatorially coordinated ligand is instrumental to metallocycle formation. The figure was created from the optimized asymmetric unit and crystal structure of CuL5.

The Cu(II) based atomic $3d_{x^2-y^2}$ orbital is instrumental to metallocycle formation and the resulting coordinating forces impart significant tensional integrity to the cyclic assembly. The hexameric architecture is crucial to stabilize the cyclic structure and in the absence of neighboring monomers the superstructure begins to unfold. This is evident in the DFT calculated structures of the asymmetric unit and a dimer of CuL5 which have been presented in

Figure 5.67. The figure begins in the top-left where the molecular overlay of the crystal structure and DFT calculated structure of CuL5 is shown. The asymmetric unit is well described by DFT with a correlation coefficient R^2 of 1.73 Å. The central monomer of the calculated asymmetric unit has the best overlay because the tensional forces acting on the chelate are present in the crystal structure. The overlay of the outer monomers begins to show conformational changes between calculated and crystal structures as the aryl rings are allowed to freely rotate. In the absence of the full hexameric structure, the calculated structure does not possess the necessary intramolecular forces to stabilise the metallocycle, and hence a lower potential energy is reached as the chelate begins to unfold from its cyclic conformation. This is evident in the DFT calculated structure of a CuL5 dimer as shown in the top-right of the figure. The dimer severely lacks intramolecular recognition from neighbouring chelates and hence, in the absence of the necessary tensional forces, the dimer conformation unravels, and the aryl rings rotate to avoid steric clashes. This structure can be considered a transition state for the dissolution and monomerization of the hexamer in aqueous media.

The crystal contains large solvent-accessible voids and hence water may enter the lattice and interact with the cyclic superstructures. As water enters the crystal, the molecules disrupt the intramolecular recognition and destabilise the cyclic assembly. The water molecules break intramolecular H-bonds and disrupt van der Waals interactions that stabilise the metallocycle, furthermore, nucleophilic attack of water at the Cu(II) centre may substitute the $Cu–O_{carbonyl}$ bond and break the cyclic coordination pattern that is so crucial to hexamer formation. Consequently, there is concomitant release of chelate monomers into solution upon aqua ligand substitution at the Cu(II) centre. The dissolution and monomerization of the hexamers in aqueous media were confirmed by UV-vis spectroscopy and DFT methods. The spectra show the normalized UV-vis absorbance for experimental (red) and calculated (black) aqueous solutions of CuL5. The calculated spectrum was computed at the B3LYP/LanL2DZ level of theory, with a self-consistent reaction field simulating water and solving for 20 excited states. The inset shows the spectra normalized over the wavelength range 500-800 nm and highlights the electronic transition at 640 nm which is responsible for the deep green color of the CuL5 solution. The chelate monomer was optimized with two aqua ligands and distorted square pyramidal geometry; the resulting calculated spectrum shows excellent agreement with the experimental spectrum and indicates that this is the solution species. The absorbance at 640 nm was found to be the HOMO→LUMO electronic transition which contributes 71% to the absorbance. The transition involves mostly intraligand charge transfer with some ligand-to-metal character.

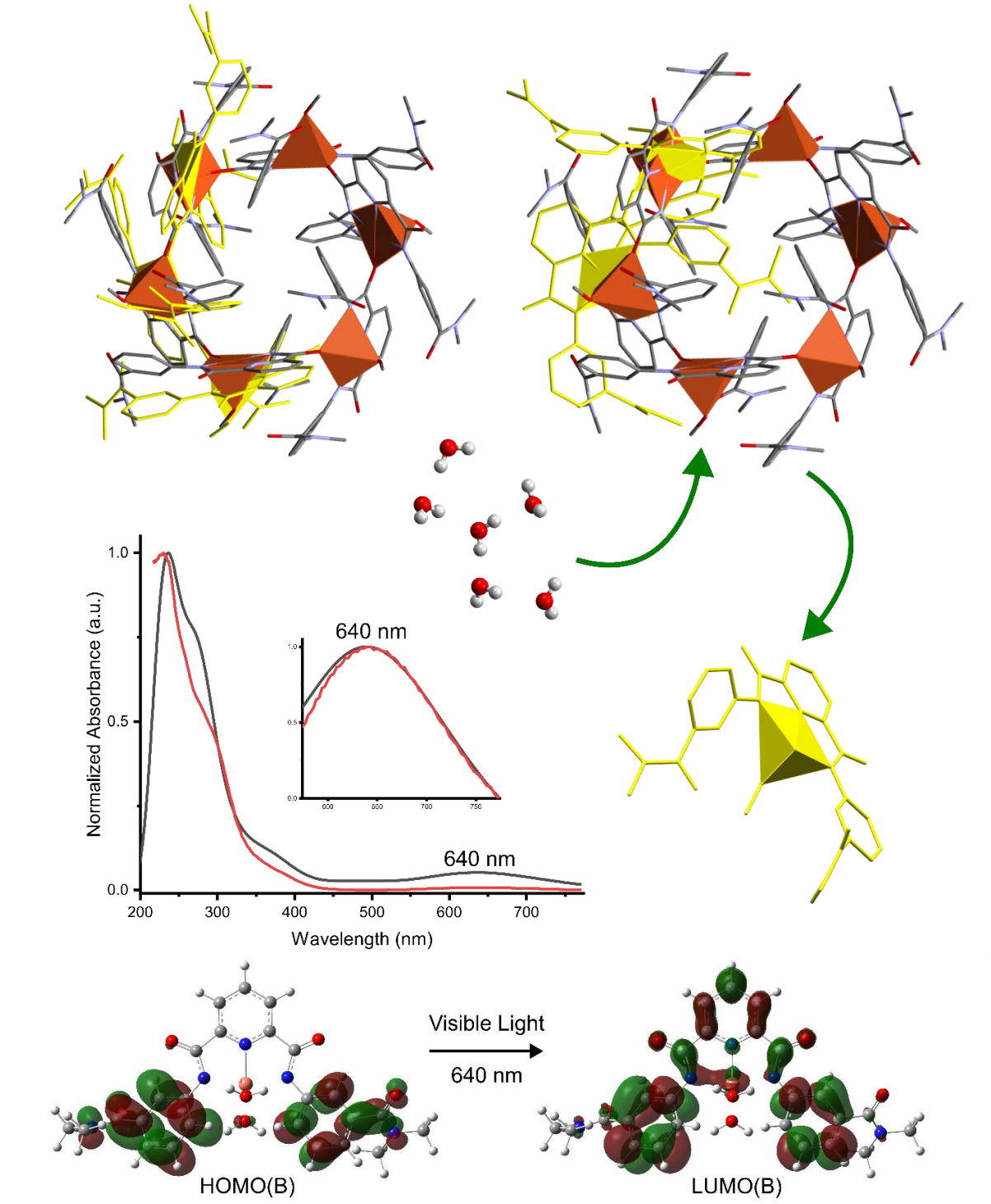
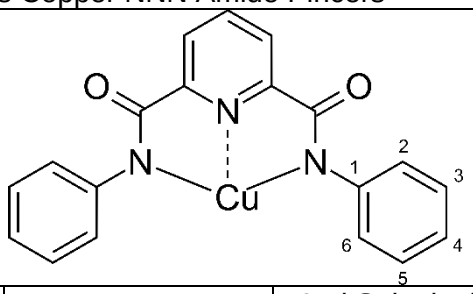


Figure 5.67: The molecular overlay of DFT calculated structures (yellow) and crystal structure. The dissolution mechanism has been shown as water may substitute at the Cu(II) center and release monomers into solution. The experimental UV-vis spectrum (red) shows excellent agreement with the DFT calculated spectrum (black). The HOMO→LUMO transition at 640 nm has also been shown. The DFT wavelength data was adjusted by –152 nm.

The Cu(II) NNN amide pincers presented here all adopt hexameric cyclic coordination in the solid-state. A CSD search of the general amide pincer scaffold yielded 69 results, and these have been presented in Table 5.10. The table shows the search query submitted to the CSD, the coordination number at the metal center, the charge on the copper ion, and the substitution on the aryl rings. The search filtered out structures with R_1 > 7.5%.

Table 5.10: CSD results upon submission of the search query. The aryl substitution positions have been labelled on the query structure. Reference codes highlighted in green represent structures that possess H-bond donors on the chelate.

CSD Analysis Copper NNN Amide Pincers				
Search Query				
CSD Reference Code	Coordination Number	Charge	Aryl Substitution Pos.	Extended Structure
AWUNEN	4	Anion	2,6	Monomer
DOWSAM	5	Anion	2,6	Monomer
DUVCAA	5	Anion	2,6	Monomer
DUVCEE	4	Anion	2,6	Monomer
EFAFID	5	Neutral	2,6	Monomer
EFAFOJ	5	Neutral	2,6	Monomer
EFAKAA	4	Anion	2,6	Monomer
HIHQEW	5	Neutral	2,6	Monomer
HIHVIF	4	Anion	2,6	Monomer
HIYWAQ	4	Anion	2,6	Monomer
HOCXIJ	4	Anion	2,6	Monomer
HOCXOP	4	Anion	2,6	Monomer
HUCFET	5	Neutral	2	Monomer
HUTMUH	5	Neutral	2,6	Monomer
HUTNUI	4	Neutral	2,6	Monomer
IBEXEU	4	Anion	2,6	Monomer
IBEXIY	4	Anion	2,6	Monomer
IBEXOE	4	Neutral	2,6	Monomer
IBEXUK	4	Neutral	2,6	Monomer
JOSQAJ	5	Neutral	2	Monomer
KAJLIT	4	Anion	2,4,6	Monomer
KAJLOZ	5	Neutral	2,4,6	Monomer
KAJLUF	5	Neutral	2,4,6	Monomer
KAJMAM	4	Neutral	2,4,6	Monomer
MEQQEF	5	Neutral	2	Monomer
MIHJEU	4	Anion	2,6	Monomer
MIHJIY	4	Anion	2,6	Monomer

MIJFUI	4	Anion	3	Dimer
MIMDAQ	5	Neutral	2	Dimer
MIMDEU	4	Neutral/Anion	2	Dimer
MIMFIA	4	Anion	2	Dimer
MOWCUZ	5	Anion	2,6	Monomer
OSIDAW	4	Neutral	2,6	Monomer
QOCXIS	4	Anion	2	Dimer
QOFLAB	4	Anion	2,6	Monomer
QOFLIJ	4	Anion	2,6	Monomer
QOFLOP	5	Anion	2,6	Monomer
QOFLUV	4	Anion	None	Dimer
QOFMAC	4	Anion	3	Dimer
QOFMEG	4	Anion	2,6	Monomer
QOFMIK	4	Anion	2,6	Monomer
REKYOX	4	Anion	2,6	Monomer
REKYUD	4	Anion	2,6	Monomer
REVQEQ	5	Neutral	2	Monomer
SEQZAR	4	Neutral	3	Monomer
SEQZOF	4	Anion	3	Monomer
SEQZUL	4	Anion	3	Monomer
TEGVOT	4	Anion	2,6	Monomer
TEGVUZ	4	Anion	2,6	Monomer
TOZFEW	5	Anion	2,6	Monomer
UGAKOF	4	Anion	2,4,6	Dimer
UGALIA	4	Anion	2,4,6	Monomer
UGALOG	4	Neutral	2,4,6	Monomer
VOLPOD	4	Anion	2	Monomer
VOLPUJ	4	Neutral	2	Dimer
VULDEO	4	Anion	2,6	Monomer
VULDIS	4	Anion	2,6	Monomer
VULDOY	4	Anion	2,6	Monomer
VULDUE	4	Neutral [Cu(III)]	2,6	Monomer
VULFAM	4	Neutral [Cu(III)]	2,6	Monomer
VULFEQ	4	Neutral [Cu(III)]	2,6	Monomer
WOHSIV	4	Anion	None	Dimer
WOHSOB	4	Anion	None	Dimer
XIVGOY	5	Anion	2	Monomer
XIVGUE	5	Anion	2	Monomer
ZAZBUX	5	Neutral	2	Monomer
ZAZCAE	4	Neutral	2	Monomer
ZOFPOZ	4	Neutral	2	Monomer
ZOFPUF	4	Neutral	2	Monomer
CuL5	5	Neutral	3	Hexamer
Cu(H_2L6)	4/5	Neutral	3	Hexamer
Cu(H_2L8)	4/5	Neutral	3	Hexamer
Cu(H_2L9)	4/5	Neutral	3	Hexamer
CuL10	5	Neutral	3	Hexamer

The 69 copper NNN amide pincers contain only 5 structures (7.2%) where the aryl ring has been substituted on the 3-position. All 5 of these structures contain dinucleating ligands. Most structures (88%) contain ligands where the aryl ring has been substituted on the 2- and 6-positions or 2-,4-and 6-positions. The copper pincers prefer 4-coordinate geometry with 50 structures (72%) being 4-coordinate and the remaining structures adopting 5-coordinate geometry. The 4-coordinate copper pincers are mostly anionic with 36 structures (72%) of 50 structures with 4-coordinate geometry being anionic and the remaining being neutral. The 5-coordinate copper pincers are mostly neutral (57%) with the remaining being anionic. Only 10 structures contain pincer ligands with H-bond donors (14% of total). None of the structures adopt the metallocycle architecture observed for the Cu(II) NNN amide pincers presented in this work. It is suspected that metallocycle formation requires the aryl ring to be substituted in the 3- or 4-position so that the substituents do not sterically block metallocycle formation. The steric requirements for hexamer formation are presented in Figure 5.68.

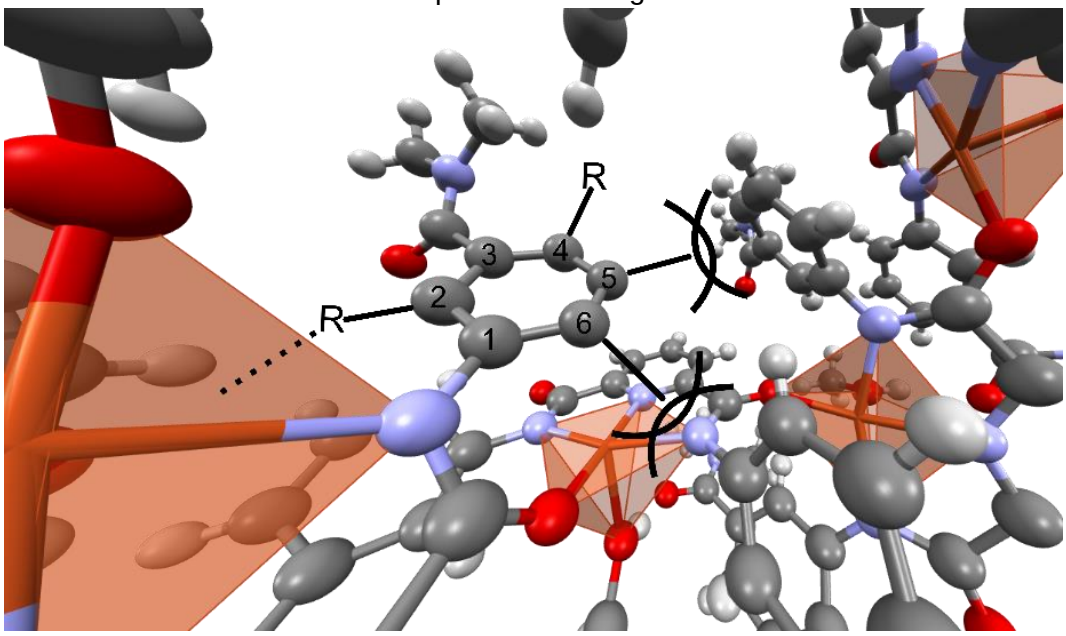


Figure 5.68: The steric requirements for Cu(II) NNN amide pincer metallocycle formation. When the aryl ring is substituted in the 4-position there are no steric repulsions, and the structure may adopt cyclic hexameric coordination as reported by Lloyd *et al*.[4] Substitution in the 2- and 6-position results in steric hinderance and metallocycles do not form, while substitution at the 2-position only results in intramolecular recognition at the Cu(II) center which prevents hexamer formation. The aryl ring substituted in the 3-position permits cyclic assembly but not when the 3- and 5-positions are substituted.

The metallocycle follows the bonding pattern Cu(II)–N–C=O_{amide}–Cu(II) and so all 69 CSD structures possess the necessary coordination pattern yet none of them form cyclic supermolecules. It is suggested here that this is because 88% of structures are substituted in

the 2-,6-position and the substituents sterically block coordination from one copper pincer to another. When only the 2-position is substituted, the CSD structures do not adopt a hexameric geometry because there is intramolecular self-recognition between the substituent and the Cu(II) center, or alternatively, the complex is anionic and electrostatic forces dominate the solid-state architecture. The structures that possess no substitution on the aryl rings do not form cyclic supermolecules because they are all anionic. The CSD structures with aryl rings substituted in the 3-position are dinucleating structures and hence the flexibility of these ligands is reduced such that metallocycle formation does not occur. Although H-bond donors are present on the copper pincer ligands presented here, intramolecular H-bond donation is not a requirement for metallocycle formation but does reduce the void volume because H-bond donation exists between supermolecules packed in the crystal lattice.

The coordination mode of the Cu(II) NNN amide pincer is presented in Figure 5.69 with the general requirements that permit metallocycle hexamer formation. Firstly, the ligand must be suitably functionalized to avoid steric repulsions. The copper complex must also be neutral and have an open face that is available for coordination by a neighboring monomer. The variable geometry of the copper ion permits supramolecular coordination as bridging groups may adopt favorable conformations around the metal center. The metallocycles presented here contain the Cu(II) ion with square planar, square pyramidal, trigonal bipyramidal[6] and octahedral[5] geometries depending on the ligand's steric requirements and the metal center's electronic requirements.

The pincers presented here coordinate Cu(II) through anionic amidate donors which increase electron density at the metal center through σ-donation. The interelectronic repulsion is relieved at the metal centre upon coordination of a π-acceptor that functions as a bridging group. Therefore, electronic requirements of the metal facilitate metallocycle formation as electron density is balanced through a synergistic interplay of σ- and π-effects. Hence, a general coordination pattern for the copper hexamers may be presented as Cu(II)–X_n**π***–Cu(II), where X represents n number of any bridging atoms and the bridging group must be a π-acceptor. This depends on the electronics at the Cu(II) centre, as seen in the structure reported by Fu *et al.*[6] When the ligand coordinates Cu(II) through only one anionic donor, and the ligand is a good π-acceptor, the electron deficient metal centre may coordinate to a bridging σ-donor moiety. Hence, the general coordination pattern may be presented as Cu(II)–X_n**σ**–Cu(II), where X represents n number of any bridging atoms that contains a good σ-donor. Ultimately, electron density at the metal centre must be appropriately balanced through σ- and π-effects for the

general Cu(II)–X_n–Cu(II) cyclic coordination pattern to form. The size of the metallocycle follows the simple arithmetic sequence 6 + 6n, where n is the number of bridging atoms. Hence, an 18-membered metallocycle is formed when two bridging atoms are present, and 24-membered when three bridging atoms are present, and so on.

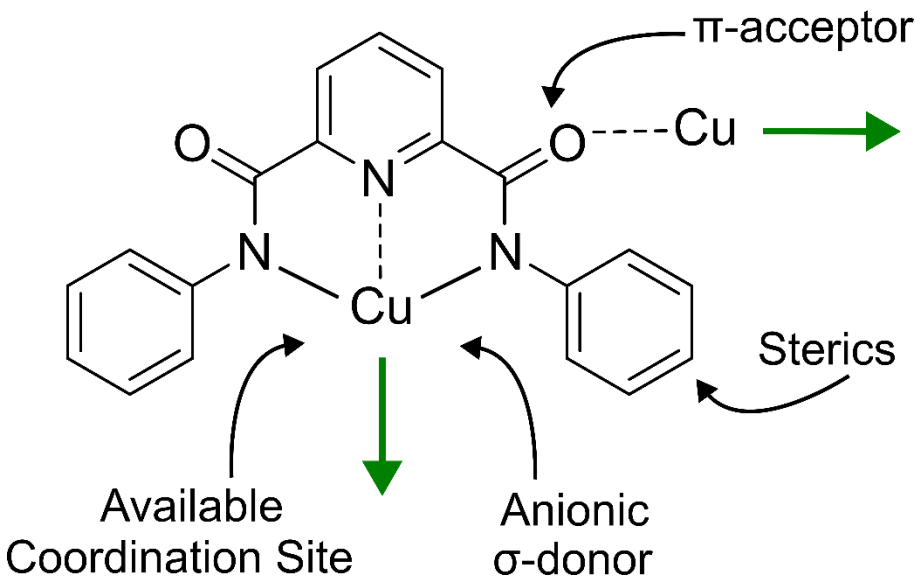


Figure 5.69: The general coordination mode for the Cu(II) NNN amide pincer. The metal center requires an available coordination site for the metallocycle to form and the ligand should not sterically hinder hexamer assembly. The electronic requirements of the metal center must be met through a finely balanced interplay between σ- and π-effects.

We now turn to discuss aspects of the metallocycle crystal structures solved in the present work. The crystal data, refinement details, and structural aspects of the Cu(II) hexamers are collated in Table 5.11 and Table 5.12 . The void volume of the crystal serves as a marker for how efficiently the supermolecules have packed in the lattice. The void volume is reduced for "thermodynamic" structures as the slower crystal growth time allows the solid-state system to reach a lower potential energy with Cu(H_2L9) showing a 29% reduction in void volume compared to the "kinetic" structure. A notable exception is CuL5 which contains a large void volume because the intermolecular interactions that facilitate packing are dominated by weak van der Waals forces.

The metal centers display variable coordination numbers with no preference between "thermodynamic" and "kinetic" structures. Cu(H_2L6) "kinetic" contains two metal centres that are 4-coordinate while the "thermodynamic" structure contains four square planar Cu(II) centres. Cu(H_2L9) "kinetic" contains four metal centres that are 5-coordinate while the "thermodynamic"

Table 5.11: Crystal data, refinement details, and structural aspects for metallocycles CuL5, Cu(H_2L6), and Cu(H_2L8) "kinetic". The metal centers are reported as "4×5CN 2×4CN" which is read as "four 5-coordinate geometry and two 4-coordinate geometry".

Complex	CuL5	Cu(H_2L6) "kinetic"	Cu(H_2L6) "thermo."	Cu(H_2L8) "kinetic"
Formula	$C_{156}H_{162}Cu_6N_{30}O_{30}$	$C_{172}H_{202}Cu_6N_{30}O_{34}$	$C_{163}H_{169}Cu_6N_{30}O_{26}$	$C_{180}H_{212}Cu_6N_{30}O_{40}$
Space Group	*C*2/*c*	*P*2$_1$/*c*	*P*-1	*P*-1
Z	4	2	1	1
Cell Volume (Å^3)	17638.5(10)	10642.9(11)	4418.9(4)	5039.5(8)
Void Volume (%)	18.4	20.1	6.7	9.5
Growth	6 weeks	6 weeks	6 months	6 weeks
Metal Centres	6×5CN	4×5CN 2×4CN	2×5CN 4×4CN	4×5CN 2×4CN
Axial Ligands	Methanol	Methanol	Water	Ethanol
Exposure (hrs)	6.11	10.05	3.66	8.15
Disordered?	No	Yes	Yes	Yes
R_1 (%)	4.84	7.89	6.61	10.92

Table 5.12: Crystal data, refinement details, and structural aspects for metallocycles Cu(H_2L8) "thermodynamic", Cu(H_2L9), and CuL10. The metal centers are reported as "4×5CN 2×4CN" which is read as "four 5-coordinate geometry and two 4-coordinate geometry".

Complex	Cu(H_2L8) "thermo."	Cu(H_2L9) "kinetic"	Cu(H_2L9) "thermo."	CuL10
Formula	$C_{158}H_{250}Cu_6N_{30}O_{72}$	$C_{146}H_{124}Cu_6N_{30}O_{42}$	$C_{138}H_{165}Cu_6N_{30}O_{49}$	$C_{128}H_{78}Cu_6N_{30}O_{16}$
Space Group	*P*2$_1$/*c*	*P*-1	*R*-3	*P*-1
Z	2	1	3	1
Cell Volume (Å^3)	9914.9(14)	5156.6(8)	11505.5(14)	2943.8(3)
Void Volume (%)	0.1	29.2	0.1	5.5
Growth	6 months	6 weeks	6 months	6 weeks
Metal Centres	4×5CN 2×4CN	4×5CN 2×4CN	6×5CN	6×5CN
Axial Ligands	Methanol/Water	Methanol/Ethanol	Water	Solvents/Nitrile
Exposure (hrs)	19.23	11.96	17.19	1.21
Disordered?	No	Yes	Yes	No
R_1 (%)	10.66	11.81	3.75	4.30

structure adopts square pyramidal geometry for all six Cu(II) centres. A notable difference between structures is the axially coordinated ligand. Cu(H_2L6) and Cu(H_2L9) “kinetic” structures both possess axially coordinated solvent molecules from the crystalizing solution, while these ligands have been substituted for water molecules in the “thermodynamic” structures. This indicates that the aqua ligand is the thermodynamically preferred ligand over the alcohols.

The crystal data were all collected on a Bruker D8 Venture Bio PHOTON III diffractometer and hence the exposure times reflect the quality of the crystal and the collection strategy employed. The crystals were generally poorly diffracting and hence long exposure times were employed to mitigate weak reflections. The author often “over collected” data with the opinion that data can always be omitted but not fabricated. A high redundancy or multiplicity in the data is beneficial because by averaging multiple measurements of each reflection during data reduction improves the signal to noise ratio and hence the accuracy of the integrated intensities. The structures were not so badly disordered, and the disorder could be modelled and was often due to co-crystalized solvent. The disorder present in Cu(H_2L9) “thermodynamic” is due to a single water molecule with about 70:30 site occupancy. Ultimately, the final value of R_1 is the best indicator of crystal quality.

Finally, the crystal structures allow physical, chemical, and biological properties of the compounds to be delineated. The various axial ligands highlight the Cu(II) centres’ ability to bind different ligands as the coordination sphere is dynamic in nature. The variable geometry of the Cu(II) centre permits diverse binding modes between the chelate and therapeutic protein target. The available coordination sites for the monomer allow labile aqua ligands to be substituted by phenolic residues present on the SARS-CoV-2 protein target. These phenolic tyrosine residues likely occupy the equatorial position in the square plane of the chelate such that overlap with the atomic $3d_{x^2-y^2}$ orbital is optimized and electronic delocalization promoted. The crystal structures also show that the ligands are involved with intermolecular interactions such as H-bonding, and these interactions may facilitate additional binding to the protein target.

The crystal structures also explain the observed solubility of the copper chelates. CuL5 is readily soluble and saturates in water at 3 mM; this is because there are large solvent-accessible voids and as water enters the lattice, the intramolecular stabilization is disrupted and monomers of the chelate are released into solution. Cu(H_2L6) saturates water at 760 μM while Cu(H_2L8) saturates water at 993 μM. The water solubility of these compounds can be attributed to solvent-accessible voids as well as H-bond donors and acceptors that are present at the surface of the metallocycle and are available to interact with water molecules entering the

lattice. The solubility difference between Cu(H_2L6) and Cu(H_2L8) can be ascribed to the functional group present on the aryl ring. The isopropyl group present in Cu(H_2L6) sterically blocks H-bonding between water molecules and the amide group more than the ethyl group present on Cu(H_2L8). The excellent water solubility of CuL5 can be attributed to the H-bond acceptor ability of the *N*,*N*-dimethylamide which does not sterically block the access of water molecules to the functional group. CuL10 is very poorly water soluble, and this can be attributed to the strong coordinating forces which result in the polymeric crystal structure observed.

The stability of the copper chelates can be rationalized by looking at the bond lengths found in the crystal structures. The Cu–N_{amide} bonds are consistently longer than 2 Å while the neutral donors N_{pyr} and $O_{carbonyl}$ have bonds to Cu(II) *ca.* 1.9 Å. It is unusual for anionic donors to have longer bonds than neutral donors and this reflects the electronic delocalization of the amidate negative charge into the C=O of the chelate. It is apparent that the amide containing ligand is weakly coordinated to Cu(II) and explains the instability of the complexes in the presence of various buffers. The available coordination sites at the copper centre are readily bound by the buffers and the weak Cu–N_{amide} bond is easily broken resulting in demetallation of the potential antiviral agents. The Cu(II) NNN amide pincers presented in this work are effortlessly synthesized as the metal ion occupies the pincer cleft almost instantly. The reactions run to completion in only a few hours and hence, the adage “easy come, easy go”, holds true.

References

(1) Groom, C. R., Bruno, I. J., Lightfoot, M. P. & Ward, S. C. (2016). Acta Cryst. B72, 171-179.

(2) Dhar, D.; Yee, G. M.; Markle, T. F.; Mayer, J. M.; Tolman, W. B. Reactivity of the Copper(III)-Hydroxide Unit with Phenols. *Chem. Sci.* **2017**, *8* (2), 1075–1085. https://doi.org/10.1039/C6SC03039D.

(3) Bailey, W. D.; Dhar, D.; Cramblitt, A. C.; Tolman, W. B. Mechanistic Dichotomy in Proton-Coupled Electron-Transfer Reactions of Phenols with a Copper Superoxide Complex. *J. Am. Chem. Soc.* **2019**, *141* (13), 5470–5480. https://doi.org/10.1021/jacs.9b00466.

(4) Lloyd, G. O.; Steed, J. W. Supramolecular Assembly in a Janus-Type Urea System. *Chem Commun* **2014**, *50* (12), 1426–1428. https://doi.org/10.1039/C3CC48603F.

(5) Hossain, S. M.; Prakash, V.; Mamidi, P.; Chattopadhyay, S.; Singh, A. K. Pyrene-Appended Bipyridine Hydrazone Ligand as a Turn-on Sensor for Cu^{2+} and Its Bioimaging Application. *RSC Adv.* **2020**, *10* (7), 3646–3658. https://doi.org/10.1039/C9RA09376A.

(6) Fu, L.; Liu, Y.; Pan, M.; Kuang, X.-J.; Yan, C.; Li, K.; Wei, S.-C.; Su, C.-Y. Accumulation of Versatile Iodine Species by a Porous Hydrogen-Bonding Cu(Ii) Coordination Framework. *J. Mater. Chem. A* **2013**, *1* (30), 8575. https://doi.org/10.1039/c3ta11157a.

(7) Higa, T.; Moriya, M.; Shimazaki, Y.; Yajima, T.; Tani, F.; Karasawa, S.; Nakano, M.; Naruta, Y.; Yamauchi, O. Synthesis and Characterization of Imidazolate-Bridged Polynuclear Copper Complexes. *Inorganica Chim. Acta* **2007**, *360* (10), 3304–3313. https://doi.org/10.1016/j.ica.2007.03.058.

(8) Bruker (2021). APEX4version 2021.4-1 Data Collection Software Which Includes SAINT Version 8.40B, SADABS-2016/2, and XPREP Version 2014/2. Bruker AXS Inc., Madison, Wisconsin, USA.

(9) Dolomanov, O. V., Bourhis, L. J., Gildea, R. J., Howard, J. A. K. & Puschmann, H. (2009). J. Appl. Cryst. 42, 339-341.

(10) Sheldrick, G. M. (2015). Acta Cryst. A71, 3-8.

(11) Sheldrick, G.M., Acta Cryst., 2015, C71, 3-8.

(12) Brandl, M.; Weiss, M. S.; Jabs, A.; Sühnel, J.; Hilgenfeld, R. C-H···π-Interactions in Proteins. *J. Mol. Biol.* **2001**, *307* (1), 357–377. https://doi.org/10.1006/jmbi.2000.4473.

(13) Lichtenberger, D. L.; Renshaw, S. K.; Wong, A.; Tagge, C. D. Investigation of Metal-d.Pi.-Butadiynyl-.Pi. Interactions in (.Eta.5-C5H5)(CO)2FeC.Tplbond.CC.Tplbond.CH Using Photoelectron Spectroscopy. *Organometallics* **1993**, *12* (9), 3522–3526. https://doi.org/10.1021/om00033a025.

(14) Lichtenberger, D. L.; Renshaw, S. K.; Bullock, R. M. Metal-Acetylide Bonding in (.Eta.5-C5H5)Fe(CO)2C.Tplbond.CR Compounds. Measures of Metal-d.Pi.-Acetylide-.Pi. Interactions from Photoelectron Spectroscopy. *J. Am. Chem. Soc.* **1993**, *115* (8), 3276–3285. https://doi.org/10.1021/ja00061a028.

Chapter 6

Conclusion

Seven novel ligands were synthesized in high yields and fully characterized by standard spectroscopic techniques, these are H_4L1 and H_4L4 – H_4L9. The synthetic methods for H_2L10 and H_2L11 were modified and yields significantly improved. Four novel Zn(II) chelates were synthesized, these are Zn(H_2L1), Zn(H_2L2), Zn(H_2L3), and ZnL5. It was shown that carboxylic acid functionalized arylamines produced off-target chelates and the desired mononuclear NNN amide metal pincer could not be synthesized with these ligands. The desired metal pincer was formed for ZnL5, but the Zn(II) pincers were unstable in water and could not be used for biological applications. Nine novel Cu(II) chelates were synthesized, three of these were off-target complexes incorporating carboxylic acid functionalized ligands, i.e., Cu(H_2L1), $Cu_2(H_2L2)_2$, and Cu_2(L3). The remaining six chelates are novel Cu(II) NNN amide pincers, CuL5 – Cu(H_2L11).

In silico methods showed that the metal pincers may favourably bind the RBD of SARS-CoV-2 and theoretically disrupt receptor recognition with ACE2. High-Throughput Virtual Screening docked > 100 000 metal chelates against the RBD and showed that the compounds may be designed to produce high docking-scores comparable to large libraries of natural compounds. However, these chelates were not synthetically feasible and so additional docking was performed to determine ideal substitution patterns for synthetically feasible compounds. The docking study and MD analysis showed that solvent-exposed residues Y489 and Y505 are the most likely binding sites.

Biophysical studies showed that the Cu(II) NNN pincers bind phenolic residues like tyrosine with a Gibbs free energy of about –24.3 kJ mol^{-1} at 37 °C. NMR studies of the peptide epitope corresponding to Y505 on the SARS-CoV-2 RBD showed that the chelates specifically target tyrosine. Ligand binding to the Delta variant RBD was observed by CD spectroscopy and a weak induced signal was produced, indicating that the copper complex was surface bound and that it may potentially function as an antiviral fusion inhibitor. Molecular docking and DFT was then used to identify that Y489 is the most likely target. The interaction between Cu(H_2L8) and the RBD was then quantified with fluorescence spectroscopy and showed that the copper complex binds the protein target with a Gibbs free energy of –28.5 kJ mol^{-1} at 37 °C. *In silico*

methods were then used to decompose this binding energy into its contributing terms. Cu(H_2L8) binds Y489 with a coordinating bond strength of –24.3 kJ mol^{-1} and additional interactions to G485 and N487 contributing –4.20 kJ mol^{-1} to the total Gibbs free energy. The exact coordination geometry at the metal centre and the protonation state of tyrosine could not be delineated. The Cu(II) NNN pincers studied here were generally unstable in biological systems and hence live virus cell culture data was never collected.

Finally, eleven novel X-ray crystal structures were solved. CuL2 “blue” and CuL2 “green” crystalized as dinuclear cage structures with solvatochromic properties. CuL3 was easily crystalized and formed a 2D metal-organic framework. The remaining eight X-ray structures were solved for CuL5 – CuL10, with “kinetic” and “thermodynamic” crystals solved for Cu(H_2L6) – Cu(H_2L9). The Cu(II) NNN pincers all formed metallocycle hexamers and the tensional integrity stabilizing the cyclic architecture was discussed in detail. The bonding interaction between metal centres and the bridging carbonyl moiety was delineated with DFT. Cu(II) NNN amide pincers found in the Cambridge Structural Database were analysed and a likely structural basis for metallocycle formation was presented.

This proof-of-concept study was a success, and no future work is planned for the Cu(II) NNN amide pincers. The Cu(II) ion may be substituted for another transition metal, such as Au(III), to afford better stability to the metal pincer, in which case, live virus cell culture data may be collected.

